



Monitoring and modeling physical weathering of marls and its effect on erosion, Draix-Bléone CZO.

Coline Ariagno

► To cite this version:

Coline Ariagno. Monitoring and modeling physical weathering of marls and its effect on erosion, Draix-Bléone CZO.. Applied geology. Université Grenoble Alpes [2020-..], 2022. English. NNT : 2022GRALU031 . tel-04064625

HAL Id: tel-04064625

<https://theses.hal.science/tel-04064625v1>

Submitted on 11 Apr 2023

HAL is a multi-disciplinary open access archive for the deposit and dissemination of scientific research documents, whether they are published or not. The documents may come from teaching and research institutions in France or abroad, or from public or private research centers.

L'archive ouverte pluridisciplinaire **HAL**, est destinée au dépôt et à la diffusion de documents scientifiques de niveau recherche, publiés ou non, émanant des établissements d'enseignement et de recherche français ou étrangers, des laboratoires publics ou privés.

THÈSE

Pour obtenir le grade de

DOCTEUR DE L'UNIVERSITÉ GRENOBLE ALPES

École doctorale : STEP - Sciences de la Terre de l'Environnement et des Planètes

Spécialité : Sciences de la Terre et de l'Univers et de l'Environnement

Unité de recherche : ETNA - Erosion torrentielle, neige et avalanches

Suivi et modélisation de l'altération physique des marnes de Draix et de son impact sur l'érosion

Monitoring and modeling physical weathering of marls and its effect on erosion, Draix-Bléone CZO.

Présentée par :

Coline ARIAGNO

Direction de thèse :

Peter VAN DER BEEK

Professeur, UGA

Caroline LEBOUTEILLER

chercheur, INRAE

Directeur de thèse

Co-encadrante de
thèse

Rapporteurs :

Maria Estela NADAL-ROMERO

CHARGE DE RECHERCHE, Instituto Pirenaico de Ecología

Mickael ATTAL

MAITRE DE CONFERENCES, The University of Edinburgh

Thèse soutenue publiquement le **2 décembre 2022**, devant le jury composé de :

Peter VAN DER BEEK

PROFESSEUR, Universität Potsdam

Maria Estela NADAL-ROMERO

CHARGE DE RECHERCHE, Instituto Pirenaico de Ecología

Mickael ATTAL

MAITRE DE CONFERENCES, The University of Edinburgh

Cédric LEGOUT

MAITRE DE CONFERENCES HDR, Université Grenoble Alpes

Eric LAROSE

DIRECTEUR DE RECHERCHE, CNRS délégation Alpes

Dimitri LAGUE

DIRECTEUR DE RECHERCHE, CNRS délégation Bretagne et Pays de la Loire

Directeur de thèse

Rapportrice

Rapporteur

Examinateur

Président

Examinateur

Remerciements

Difficile de tourner cette page de vie sans jeter un regard en arrière, simplement pour apprécier le chemin parcouru, penser aux compagnons d'aventures et s'assurer d'avoir tout donné et continuer à grandir. Si le projet de thèse a occupé l'essentiel de mon temps, ces trois années ont été agrémentées d'une multitude de petites expériences, toutes enrichissantes et stimulantes tant professionnellement que personnellement. J'aimerais ici partager ce flot de moments de vie qui ont aussi contribué à faire de ce doctorat une réussite pour moi.

Baignée dans le monde de l'enseignement depuis toute petite, j'ai été ravie et impressionnée de passer de l'autre côté du bureau, celui du tableau, et de pouvoir à mon tour transmettre ce que l'on m'avait donné. Mais que l'on ne s'y méprenne pas, j'ai aussi beaucoup reçu! Je me suis questionnée, interrogée et formée pour progresser avec les étudiants. Dans cette démarche, le Label RES m'a permis de suivre de nombreuses formations pédagogiques; de la classe inversée aux débats organisés, j'ai découvert des techniques et méthodes d'apprentissages tant innovantes pour les élèves que exigeantes pour l'enseignant.

Les conférences scientifiques (EGU, OZCAR-Terreno, GIS, visite à Potsdam), l'école d'été OZCAR ou la mobilité internationale à Boulder ont également été pour moi des aventures incroyables, qui m'ont sortie de ma zone de confort, ont porté mon cerveau à ébullition et m'ont permis de belles et surprenantes rencontres.

Et que serait cette thèse sans toutes ces rencontres, ces discussions et ces échanges !!? Mes rendez-vous hebdomadaires avec Caroline et Peter en sont le point d'orgue et vont assurément me manquer. Au début un peu impressionnée, j'ai vite pris plaisir à faire ces réunions, moments d'échanges privilégiés qui m'ont permis de profiter pleinement de l'expérience de mes deux mentors et d'approfondir continuellement mon travail. Peter, la distance n'a pas éméché ton assiduité à suivre ces réunions; tes conseils avisés, ta sérénité et ta bienveillance ont été des ingrédients des plus précieux pour chaque étape de ma thèse. Un immense merci pour l'acteur central que tu as été dans mon parcours depuis quelques années. Toujours pleine d'énergie et d'optimisme, Caro, tu as parfaitement complété ce duo. Même si le flux de tes bonnes idées, suggestions, fut parfois difficile à suivre (imaginez-vous, ça va encore plus vite que quand elle parle !!), tu m'as sans cesse poussé à donner le meilleur de moi-même et à prendre du recul pour approfondir toujours plus loin mes recherches. Mon esprit critique, ma compréhension de mon terrain et la clarté de mon discours ne seraient pas ce qu'ils sont sans ton suivi rapproché. Ce travail scientifique a toujours été accompagné de moments plus légers, de rires, de repas partagés, de complicité, de figues, de chaussettes et d'aventures ! Ces quelques mots sont trop peu pour vous exprimer toute ma gratitude...

Mon plaisir de retrouver mon terrain n'aurait pas été si fort sans la présence de Seb à Draix. Gardien de l'observatoire, tu m'as fait partager ton expérience sans compter et fait découvrir ton beau pays sous de multiples facettes. De nos footings dans les Terres noires aux discussions animées sur l'écologie, ces passages à Draix (toujours trop courts !) ont été des moments hors du temps, loin de ma vie grenobloise chronométrée, un grand merci pour cela !!

J'ai eu la chance d'évoluer dans une dynamique de travail et une atmosphère des plus agréable : ce sont toutes ces portes ouvertes, ces discussions de midi ou ces petites têtes venues m'encourager qui m'ont aussi donné envie de me lever tous les matins. Mentions particulières tout d'abord à Guillaume ; tant au bout d'une corde que pour tous les conseils scientifiques, je t'ai fait confiance, sans regret, et nos échanges engagés m'ont beaucoup fait grandir. A mon co-bureau Erwan, pour sa gaieté quotidienne et sans qui l'apprentissage de Python aurait été bien plus long et douloureux.

Je n'ai certainement pas été une des plus assidue aux rendez-vous des doctorants, pour les réunions comme pour les bières, mais j'ai apprécié tous les jours cette dynamique de groupe et cette entraide. Merci Suzanne pour l'énergie que tu mets pour entretenir ces liens! Marco et Mohammad, votre soutien pendant ces derniers mois a été des plus précieux, je vous souhaite tout le meilleur pour finir à votre tour cette aventure !

Besoin d'un petit coup de main technique ? Rien de plus facile avec notre équipe technique d'élite! Merci Hervé, Firmin et Alexis pour les conseils, la conception de mon pied de caméra et les récits d'aventures toujours aussi captivants. Merci à Christian sans qui mon vélo serait une épave, maintenant je sais ce qu'est une roue libre ! Je n'oublie pas non plus Nathaly qui m'a rendu la vie tellement plus facile dans la gestion de mes multiples missions.

Parmi ces missions, je retiens tout particulièrement mon séjour à Boulder, assurément un beau coin ces Rockies américaines ; en trail, en skis ou en grimpe j'en ai pris plein les yeux ! Je retiendrai avant tout les belles rencontres que j'ai faites, simples et touchantes, j'ai eu beaucoup de chance d'être bien entourée !

I would like to thanks all of you who made this trip unique!

To Ben, the guy who eat candy as fast as nobody else, for your French support, that was such a pleasure to have you around every days! To Albert for your great idea of the traverse, you can be proud of you, and for showing to me that couch activities and hiking with anvil skis for hours can goes together! To Irina for all our ski adventures and to have showed me that you can keep smiling even when you are suffering on the rock! To Frederico and Alicia for all the attention that you gave me, I was feeling like at home (or almost, just missing cheese).

To Greg for showing me how mathematics are easy, you can add a little lambda where ever you want! Modeling was such impenetrable for me but your classes and your help gave me the opportunity to turn a bit the light on in this obscure domain. Thank you so much! To Benjamin for the great runs that we did and for your amazing patience in front of a computer when I was close to play ultimate with my laptop! To Elisa who taught me how 'Perudo' is such a statistical game. To Scott for our great climbing time and to have been in for your first ski gully! To Brandee & Aaron for your inspired recipes and for drowning me in the American's world with the superbowl. To Abby, with your hat and your puffy jacket, I was feeling less alone frozen in the lab! To Josie, who code and speak faster than lucky luke, it reminded me every day what is the true English speaking!

J'ai également une pensée pour tous les enseignants et encadrants de stage qui m'ont accompagnés durant toutes ces années d'études. Ce projet de thèse n'était certainement pas un hasard, il est le fruit de nombreux choix et de beaucoup de soutien de la part du corps enseignant. Chaque étape et chaque brique a été nécessaire pour grandir et c'est leur passion, qu'ils ont su transmettre avec patience et abnégation, qui m'a toujours inspirée et orientée.

Parce que la déconnexion est un besoin essentiel pour bien travailler, je remercie tous les copains; compagnons de cordés, adeptes de jeu de société ou tout simplement de bonnes bouffées d'air et de rires m'ont été plus qu'indispensables pour revenir derrière le PC avec de la motivation!

Enfin je voudrais remercier toute ma famille pour l'intérêt qu'ils ont toujours porté à mon projet et les nombreux encouragements que j'ai reçu. Merci à mes grands-parents qui par leur savoir et leur sagesse m'inspirent chaque jour. Merci à mon petit frère, qui, inconsciemment, m'a toujours poussé à donner le meilleur de moi-même. Merci à mes parents sans qui rien n'aurait été possible. Votre soutien sans faille quelques soit mes échecs ou mes choix m'a permis de concilier, tout au long de mon parcours, sport et étude sans jamais me soucier de demain. J'ai grandi pas à pas, toujours épaulée et remplie de cette détermination que vous m'avez transmise. Cette thèse est aujourd'hui une réussite partagée.

C'est parce que le creux des vagues est parfois difficile à remonter toute seule que je dédie mes derniers mots à Kévin. Ton épaule a été mon repaire; tu m'as montré la voie et tu connaissais les obstacles, merci pour ta patience infinie.

Résumé

Les Badlands sont des zones géomorphologiquement actives, souvent peu végétalisées et escarpées, où l'altération et l'érosion sont intenses et très variables. L'Observatoire de la Zone Critique Draix-Bléone, SE France, situé dans les badlands constitués des marnes noires du Jurassique (appelés aussi ‘Terres Noires’), a permis d'enregistrer les changements morphologiques, les flux d'eau et de sédiments ainsi que les variations climatiques dans ces terrains depuis presque 40 ans. Le but de ce travail est d'étudier la variabilité spatiale et temporelle du régolithe (c.-à-d., la couverture de surface de particules fragmentées et mobilisables), d'identifier ses principales caractéristiques et de quantifier son impact sur la production sédimentaire à l'échelle du bassin versant. Ces résultats, qui s'appuient sur des données de terrain et l'analyse d'enregistrements de long-terme, ont été utilisés pour construire un modèle d'évolution de paysage capable de simuler l'évolution morphologique et la dynamique sédimentaire à l'échelle intra-annuelle, et de prédire la production de sédiments dans un contexte de changement climatique.

Mon analyse des enregistrements climatiques et sédimentaires sur plusieurs décennies montre un cycle d'hystérèse annuel en forme de ‘huit’, qui traduit la forte variabilité intra-annuelle des processus d'altération, d'érosion et de transport. Ce cycle d'hystérèse illustre en particulier la transition entre des conditions de type ‘transport-limited’ et ‘supply-limited’ qui s'opère au cours des mois d'été, et l'influence de l'intensité des pluies sur l'export sédimentaire estival. J'ai utilisé les jeux de données de température de sol et d'export sédimentaire de l'observatoire pour explorer différents processus de gélification et quantifier leur contribution respective au flux sédimentaire annuel. J'ai observé que le processus de fragmentation lié à la croissance de lentilles de glaces (frost-cracking) peut moduler les exports sédimentaires annuels et expliquer la part de la variabilité interannuelle des exports sédimentaires non-expliquée par la variabilité des précipitations. Cet indicateur de frost-cracking doit donc être pris en compte lors de la construction de modèle prédictifs.

J'ai également contribué à étendre le jeu de données de l'observatoire en échantillonnant et mesurant les caractéristiques du régolithe, à différentes saisons, dans le but de quantifier les processus d'altération physique. La granulométrie, caractérisée par le D50, augmente systématiquement dans les dix premiers centimètres des profils verticaux. Ainsi, le D50 a été identifié comme un bon proxy de l'altération du régolithe dans ces terrains marneux. Les mesures de D50 et de résistance de la surface du régolithe suivent un cycle saisonnier qui suggère que le régolithe est principalement produit (par les processus de frost-cracking) pendant la période hivernale et que le transport sédimentaire domine pendant la période estivale. Par ailleurs, l'analyse de la variabilité spatiale des caractéristiques du régolithe montre des différences d'épaisseur du régolithe selon l'orientation des versants, bien qu'aucune asymétrie morphologique n'ait été observée à l'échelle du bassin.

Finalement, j'ai développé un modèle d'évolution de paysage pour simuler les flux de sédiments à l'échelle du bassin, leur variabilité temporelle, et faire des prédictions

quantitatives sur les futurs changements morphologiques dans les badlands dans un contexte de changement climatique. J'ai utilisé la forme observée de la dynamique intra-annuelle des exports sédimentaires (cycle d'hystérose) et la répartition spatiale de l'épaisseur du régolithe, toutes deux résultant d'observations de terrains, comme critères de calibration du modèle. J'ai ainsi pu montrer que les fonctions de production et d'érosion dépendantes de l'épaisseur de sol sont nécessaires pour générer un régime de type 'supply-limited' dans la deuxième partie de l'année. L'intensité des pluies, combinée à un seuil d'entrainement des sédiments (aussi bien sur les versants que dans le réseau de drainage), est responsable de la relation non-linéaire observée entre les exports sédimentaires et les précipitations dans la première moitié de l'année. Un travail plus approfondi est encore nécessaire pour développer une méthode de calibration automatique et tester le modèle avec différents scenarii climatiques.

Abstract

Badlands are geomorphically active sites, with steep and sparsely vegetated slopes, where weathering and erosion are both intense and highly variable. The Draix Bléone-Critical Zone Observatory (CZO), SE France, is located in badlands developed on Jurassic black marls ('Terres Noires') and has permitted recording morphological changes, water and sediment fluxes, as well as climatic variations in these terrains since almost 40 years. The aim of this work is to explore the spatial and temporal variability of the regolith (i.e., the surface layer of fragmented mobilizable particles), identify its main characteristics and quantify its impact on catchment-scale sediment production. These results, based on field monitoring and analysis of long data records, is used to build a Landscape Evolution Model (LEM) that is able to simulate morphological evolution and sediment dynamics at intra-annual timescales, and predict sediment production in a context of climate change.

My analysis of decade-long sediment and climatic records shows an annual hysteresis cycle that displays a 'figure of eight' pattern, which demonstrates the high intra-annual variability of weathering, erosion and transport processes. In particular, this hysteresis cycle illustrates the transition from transport-limited to supply-limited conditions that occurs during summer months, and the influence of rainfall intensity on summer sediment export. I use historical datasets of soil temperature and sediment export from the Observatory to investigate different frost-weathering processes and quantify their contribution to the annual sediment export. I observed that the ice-segregation process modulates the variability in total sediment export that cannot be explained by interannual variations in rainfall (~30%) and thus should be taken in account when building predictive models.

I also contribute to expanding the Observatory dataset by sampling and measuring the characteristics of the regolith, in different seasons, in order to quantify physical weathering processes. Grain size, characterized by D₅₀, increases systematically in the upper ~10 cm of vertical profiles. Thus, D₅₀ has been identified as a good proxy of regolith weathering in these marls. Both D₅₀ and resistance measurements of surface regolith follow a seasonal cycle, suggesting that the regolith is mostly produced (by frost-weathering processes) during the winter period and that the summer period is dominated by sediment transport. Moreover, analysis of the spatial variability in regolith characteristics shows a potential difference between regolith thicknesses on hillslopes according to their aspect, even if no morphological asymmetry is observed at the catchment scale.

Finally, I develop a landscape evolution model to simulate catchment-scale sediment flux and its temporal variability, and make quantitative predictions on future morphological changes in these badlands in a context of climate change. I used the observed intra-annual pattern of sediment export (hysteresis cycle) and the spatial distribution of regolith thickness, both resulting from field observations, as calibration criteria for the model. I show that depth-dependant soil-production and -erosion functions are needed to generate a 'supply-limited' regime in the second half of the year and that rainfall intensity, combined with a threshold for sediment entrainment (both on hillslopes and in the drainage network), is responsible for the non-linear relation between sediment export and rainfall observed in the first part of the year. Further work is needed to develop an automatic calibration method and test the model under different climatic scenarios.

Table of content

Remerciements	1
Résumé	4
Abstract	6
Table of content	7
Introduction	10
Chapter I.....	23
I. Sediment export in marly badland catchments modulated by frost-cracking intensity, Draix-Bléone Critical Zone Observatory, SE France	23
I.1. Introduction	24
I.2. Study site	26
I.3. Methods.....	28
I.3.1. Data acquisition	28
I.3.2. Data Processing	30
I.3.2.1. Rainfall and sediment export	30
I.3.2.2. Temperature indicators.....	31
I.3.2.3. Uncertainties	32
I.4. Results.....	33
I.4.1. Seasonal variability in sediment export	33
I.4.2. Potential temperature control on sediment export.....	35
I.5. Discussion	39
I.5.1. Limitations of our study.....	39
I.5.2. Significance of the observed hysteresis cycle	41
I.5.3. Frost weathering as a major control on sediment production in the Draix-Bléone CZO	42
I.5.4. Implications for the erosional response to climate change	43
I.6. Conclusions	45
Appendices Chapter I	46
Chapter II.....	50
II. Seasonal dynamics of marly badlands illustrated by field records of hillslope regolith properties, Draix-Bléone CZO, SE France	50
II.1. Introduction	51
II.2. Context and methods	53
II.2.1. Study site	53
II.2.2. Plot measurements	55
II.2.3. Geophysical survey.....	57
II.2.4. Data processing: Water content, density, grain size and resistance.....	58
II.2.5. Geophysical and morphologic data processing.....	58
II.3. Results.....	59

II.3.1.	Relation between field measurements and state of the regolith	59
II.3.2.	Geophysical results.....	62
II.3.3.	Morphological analysis of the Moulin catchment.....	63
II.4.	Discussion	64
II.4.1.	Uncertainties related to field measurements	64
II.4.2.	A proxy of regolith weathering.....	64
II.4.3.	Can we identify a weathering front in black marls?.....	66
II.4.4.	Influence of aspect on weathering and morphology of the Moulin catchment....	67
II.4.5.	Perspectives: integrating regolith characteristics in landscape morphology analysis	
	68	
II.4.6.	Implications for modelling landscape evolution in badlands.....	69
II.5.	Conclusions	71
Appendices chapter II.....		72
Chapter III.....		76
III.	Modeling seasonal sediment dynamics and landscape evolution in a marly badland catchment, Draix-Bléone Critical Zone Observatory, SE France.	76
III.1.	Introduction	77
III.2.	Modeling framework	81
III.2.1.	Geomorphic process laws.....	81
III.2.1.1.	Soil production	81
III.2.1.2.	Hillslope transport.....	82
III.2.1.3.	II.1.3 Fluvial entrainment and transport	84
III.2.2.	Modeling strategy.....	85
III.2.2.1.	Initial model.....	87
III.2.2.2.	Including soil production and sediment availability.....	87
III.2.2.3.	Including rainfall intensity	88
III.3.	Model constraints and parameter values.....	89
III.3.1.	Fixed parameters.....	89
III.3.2.	Parameters constrained from Draix observatory records.....	91
III.3.3.	Calibrated parameters.....	92
Results		93
III.3.4.	Initial model.....	93
III.3.5.	Including soil production and sediment availability.....	93
III.3.6.	Including rainfall intensity and fluvial transport threshold.....	98
III.4.	Discussion	102
III.4.1.	The Draix model: a tool to reproduce observed sediment dynamics	102
III.4.1.1.	A simple model to validate the precipitation - sediment-export correlation	
	102	
III.4.1.2.	Non-local diffusion	102
III.4.1.3.	Impact of depth-dependent hillslope processes.....	103
III.4.1.4.	Modelling rainfall-intensity controls on sediment export.	103

III.4.2.	Limits of the model.....	105
III.4.3.	Modeling perspectives in a context of climate change.....	107
III.4.3.1.	Model adjustment based on field observation	107
III.4.3.2.	Developping an automatic calibration procedure	107
III.4.3.3.	Model predictions under climate change	108
III.4.3.4.	Application of the model beyond the Draix CZO	109
III.5.	Conclusion.....	110
	Appendice chapter III	112
	Discussion and conclusion.....	115
	Epilogue	121
	References.....	123

Introduction

'Chaque connaissance acquise, peut devenir le commencement d'une aventure, et j'aime à penser qu'il n'y a pas, en ce domaine, de conquête mais une quête infinie de savoir et d'explorations. Qu'un jour les jeunes agiront à leur tour. Qu'ils seront responsables de la nature, de la vie quotidienne, de leur bonheur et de celui des autres. De l'état de la Terre.' (Jean-Louis Etienne)

Motivations / enjeux de l'étude:

Les marnes..., mais qu'est-ce que c'est ? Combien de fois ai-je entendu cette question en réaction à l'énoncé de mon sujet de thèse ? Souvent végétalisées ou cultivées, les zones marneuses, et leurs homologues argileuses, passent souvent inaperçues dans nos paysages où nos regards sont plus facilement attirés par d'imposants reliefs rocheux. Pourtant, lorsque ces lithologies apparaissent, par le jeu de l'érosion, du relief ou de la déforestation, il est alors difficile de passer outre leurs aspects sculptés et disséqués. Mon parcours de sédimentologue m'avait laissé l'image d'une roche sans grand intérêt, très meuble mais qui permettait cependant de bien délimiter les contours des réservoirs grâce à ses propriétés imperméables. Après trois ans d'études plus approfondies sur cette formation et ses subtils changements au cours de l'année, je suis aujourd'hui convaincue de l'intérêt scientifique de ces terrains marneux et perçois désormais la nature complexe et 'vivante' de cette roche.

Connus sous le nom de 'Badlands', historiquement appelés 'mauvaises-terre' pour leur faible contribution à la production agricole, ces terrains sont d'incontournables laboratoires pour qui s'intéresse aux transferts sédimentaires (Nadal-Romero et al., 2018). Théâtre d'une érosion extrême, ces hauts de bassins versants dénudés deviennent alors des zones de production sédimentaire intense, clés de la dynamique sédimentaire continentale (Copard et al., 2018). Ce travail de thèse, positionné à la source de la chaîne sédimentaire, vise à mieux comprendre la dynamique saisonnière des processus physiques d'altération puis d'érosion des versants marneux. La fragilité du substrat marneux induit des changements morphologiques sur des échelles de temps très courts (mois/années) ce qui permet aux géomorphologues de suivre et de quantifier cette altération et les flux sédimentaires induits.

La production sédimentaire trouve sa source dans la transformation du profil vertical de sol sous l'effet de l'altération (S. P. Anderson et al., 2007). Depuis le substratum (roche mère saine) jusqu'aux sédiments de surface, une altération progressive ou segmentée par des fronts d'altérations est à l'œuvre, chaque profondeur étant le siège de divers mécanismes d'altérations physiques et chimiques (Figure 1 – échelle Locale). Résultat de cet incubateur, le régolithe est le substrat de surface composé de particules fragmentées facilement mobilisables et vouées à être transportées. Un des enjeux de ce travail de thèse sera d'identifier des indicateurs permettant de quantifier ces mécanismes d'altération physique.

L'altération chimique est aussi présente sur notre site d'étude (Cras et al., 2007; Soulet et al., 2021), mais les mécanismes physique d'altération prédominent largement dans les zones montagneuses, ce qui explique notre choix d'étude. La production de régolithe dans les badlands détermine la quantité de sédiments disponibles pour être transportés vers le réseau de drainage. Ce travail s'inscrit ainsi dans le cadre de la gestion des apports sédimentaires dans nos rivières et de leurs infrastructures associées. Les sédiments fins, dont les badlands sont un contributeur majeur (40% des apports fins de la Durance ; Copard et al., 2018), sont associés à des problématiques d'envasement de barrages et de réduction de la capacité des réservoirs (Annandale, 2014; Kondolf et al., 2014).

La disponibilité en sédiments fins le long des cours d'eau génère également des problématiques écologiques. L'impact sur la biodiversité et les habitats aquatiques lié au colmatage des lits de rivières par les sédiments fins (Mathers et al., 2017; Osmundson et al., 2002; Pitlick & Wilcock, 2001) reste une question discutée et essentielle pour la mise en place de plans de gestion cohérents et appropriés au regard de tous les usagers des rivières. Même si un certain verdissement des Alpes est actuellement observé (Carlson et al., 2017; Filippa et al., 2019), les multiples rapports du GIEC (IPCC reports) ne cessent d'alerter sur la perte de ressource en sol liée à l'érosion et sur la désertification en cours de nos paysages à l'échelle mondiale. Cette tendance engendre l'apparition de nouvelles zones actives d'érosion, disséminées et non connectées, qui feront l'objet de processus d'érosion et de transport accrus. Une meilleure connaissance des processus et mécanismes d'altération des sols dénudés, des quantités produites, de l'interaction sol-végétation, des facteurs de contrôle du ruissellement, des temps de transit sédimentaire, ...etc, paraît alors cruciale pour anticiper les changements à venir et leurs conséquences.

Témoin de l'intérêt porté à ces questions par les différents gestionnaires des rivières, des versants et des risques naturels (EDF, RTM, Syndicats de rivières, agriculteurs), l'observatoire Draix-Bléone a été créé en 1983 pour suivre l'érosion des versants de marnes noires et améliorer la prédiction des quantités exportées et l'estimation des stocks sur les versants.

Contexte scientifique

Du terrain...

Située à l'interface entre le milieu atmosphérique et la lithosphère, l'étude des sols, leur caractérisation et leur évolution, rassemblent différentes thématiques. Cette complexité se retrouve dans le concept de « zone critique », proposé en 2001 par le National Research Council et qui désigne l'enveloppe la plus externe de la Terre (Brantley et al., 2017). Cette 'pellicule' est le siège de multiples interactions physico-bio-chimiques entre différents milieux (solide, liquide, gazeux) et génère ainsi des phénomènes et des processus complexes. Par la présence de vie en surface, cette zone est précieuse, fragile et critique, au sens d'essentielle à la survie du vivant sur la planète. En 2007, la US National Science Fondation (NSF) soutient la création du premier réseau d'observatoires de la zone critique (White et al., 2015). Crée en 2015, le réseau d'observatoires français OZCAR (Observatoires de la Zone Critique ;

Application et Recherche) a pour objectif de faire le lien entre les diverses disciplines étudiant la zone critique, afin d'adopter une approche scientifique plus complète et intégrée des problématiques de surface et d'apporter des réponses globales sur les changements qui s'opèrent dans ces interfaces (Brantley et al., 2017; Gaillardet et al., 2018). Cette nouvelle communauté, plus alerte sur les interactions entre les différents compartiments de la zone critique, sera peut-être à même de mieux comprendre et de prédire les changements du système qui sont en marche. Au sein de l'infrastructure d'OZCAR, vingt et un observatoires, réseau de sites sentinelles, enregistrent, décrivent et modélisent la zone critique, chacun dans des contextes climatiques, géologiques et sociétaux distincts, et selon des échelles de temps différentes.

Partie intégrante du réseau OZCAR, l'observatoire Draix-Bléone enregistre depuis plus de 35 ans les processus hydrologiques et érosifs qui affectent les bassins versants de montagne (Draix-Bleone Observatory, 2015). Constitués de marnes du Jurassique moyen, plus communément appelés 'Terres Noires' (Antoine et al., 1995), les badlands de Draix sont des terrains d'étude privilégiés pour estimer les flux et les processus d'érosion et de transport de sédiments fins ou grossiers. Sensibles aux paramètres climatiques, ces terrains permettent d'explorer la variabilité spatiale et temporelle des processus d'altération et d'érosion. Le couvert végétal, inégal selon les bassins versants, est également source d'interrogation quant à son évolution et aux interactions qu'il induit sur les processus géomorphologiques.

Le site de Draix-Bléone...

Les différents bassins versants suivis de l'observatoire de Draix-Bléone couvrent un large spectre de taille et de couverture végétale qui permettent de capter et de comparer les processus érosifs à différentes échelles (Mathys, 2006; Mathys et al., 2003). Depuis le bassin du Laval (86 ha) à celui de la Roubine (0.1 ha), considéré comme une unité élémentaire, en passant par le bassin versant du Moulin (8 ha), ces espaces principalement dénudés sont tous instrumentés pour enregistrer les flux de charriage et de matières en suspension (Figure 2). L'érosion et les ravinements y sont intenses, à l'inverse du bassin du Brusquet (107 ha) où les débits solides sont nettement plus faibles que sur le Laval (Carrière et al., 2020), bassin de taille et de lithologie similaire, grâce au reboisement initié par le RTM à la fin du 19^{ème} siècle. L'estimation de cette charge sédimentaire solide est une donnée particulièrement rare sur le long terme tant elle nécessite des installations spéciales (ex: plages de dépôts) et un suivi régulier (mesure de volume après chaque crue via un relevé topographique de la plage de dépôt) (figure 3). Elle est pourtant essentielle pour l'estimation des taux d'érosion à l'échelle du bassin versant (~6 mm / an au Laval). La fraction fine des flux sédimentaires, quantité plus facile à obtenir, est ici obtenue en utilisant le débit (calculé à partir des données de hauteurs d'eau du limnigraphé) et la concentration du flux (mesuré par un turbidimètre et un prélevageur) (Figure 3).

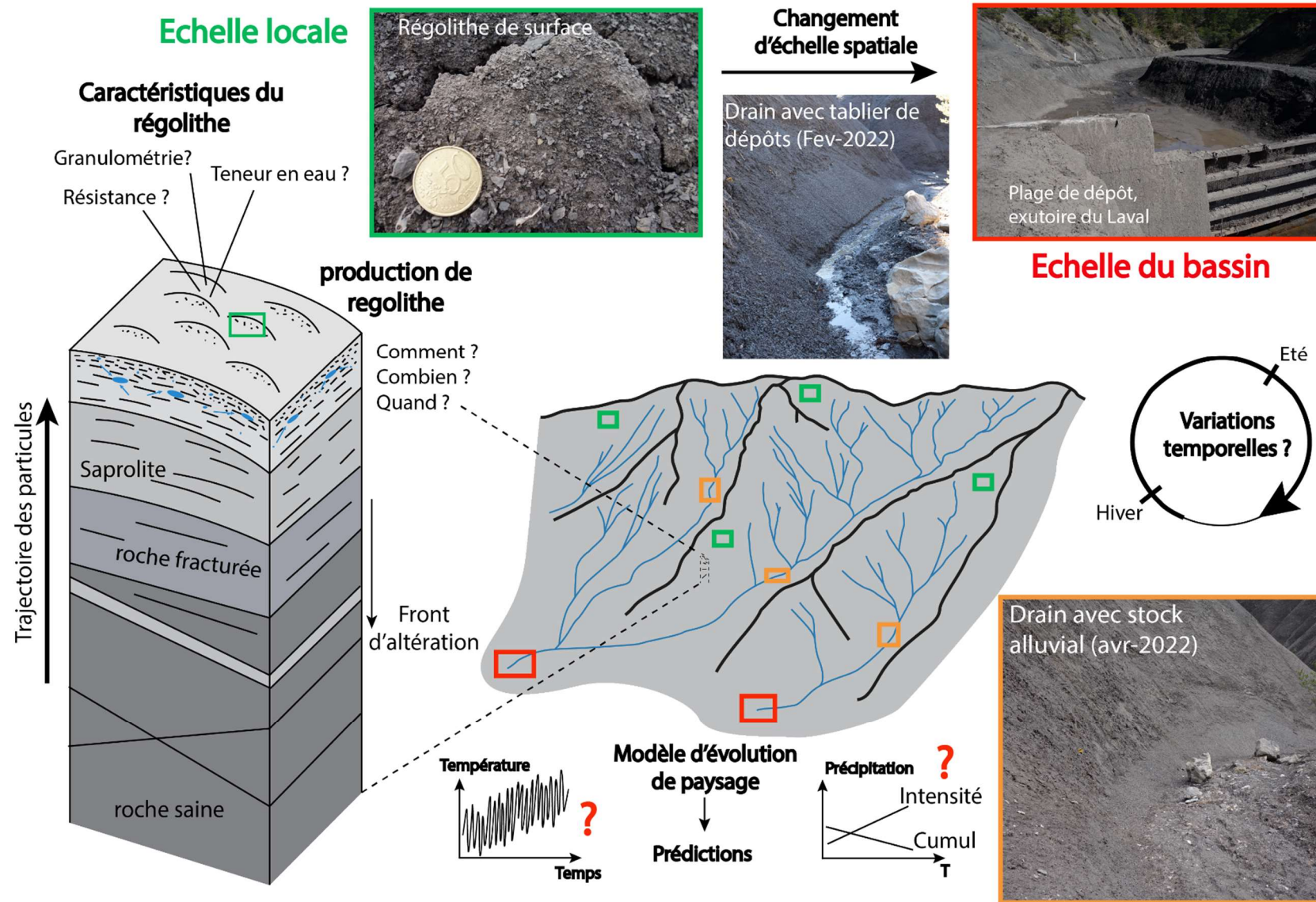


Figure 1: Description schématique du contenu et des principales questions qui ont motivé ce travail de thèse. Deux échelles seront traitées : 'A l'échelle locale' via des analyses de terrain et 'l'échelle du bassin' via la construction d'un modèle d'évolution de paysage.

...et ses problématiques...liées au processus chimiques d'altération

La présence de ces installations de mesures, couplée à un terrain très réactif sur de courtes échelles de temps, a fait émerger autour de l'observatoire un large panel de questions scientifiques ; depuis les interactions entre végétation et stabilisation des sols à la quantification des flux de matières solides, en passant par l'identification des principaux agents d'érosion sur les versants.

L'altération chimique des marnes, roche composée en partie de minéraux carbonatés (CaCO_3), soulève également un questionnement sur le rôle de ces badlands dans le cycle du carbone. Si la contribution significative des badlands aux flux de carbone organique particulaire des rivières a été démontrée (Copard et al., 2018), l'altération chimique des marnes est aussi un processus contributeur du flux de CO_2 vers l'atmosphère (Soulet et al., 2021). La forte corrélation entre température et émission de CO_2 issue des versants marneux amène ces problématiques au-devant de la scène dans le contexte de changement climatique actuel. Des études sur le rôle des communautés microbiennes sur les flux de carbone (en cours) et sur l'oxydation des minéraux de sulfure (Pye & Miller, 1990), notamment la pyrite (FeS_2), sont ainsi des perspectives de recherche pertinentes et nécessaires pour cerner de façon complète l'impact de l'érosion de ces bassins. Ce travail de thèse ne traitera pas de l'altération chimique des badlands de Draix et restera centré sur les mécanismes d'altération physique. Ce choix est motivé par la faible contribution de l'altération chimique, par rapport à l'altération physique, aux quantités totales de matières exportées par ces bassins (Cras et al., 2007).

....liées au couplage végétation / érosion

Par définition les badlands se réfèrent à des zones dénudées où la production sédimentaire est plus intense que dans les zones végétalisées (Gallart et al., 2013; Legout et al., 2013; Llena et al., 2021; Mathys et al., 1996; Poulenard et al., 2012). L'impact de cette couverture végétale sur l'hydrologie des bassins a notamment été mis en évidence par Cosandey et al. (2005). En s'appuyant sur les bassins de Draix, ils ont montré que le bassin reboisé du Brusquet enregistrait des pics de crues jusqu'à dix fois moins intenses, pour les événements les plus extrêmes, que ceux du bassin dénudé du Laval. Mallet et al. (2020) ont complété cette analyse en montrant que le type de couverture végétale influence la teneur en eau du sol, un des leviers du déclenchement du ruissellement. La diversité végétale joue également un rôle sur la structure des sols. Burylo et al., (2012) ont montré qu'une gestion appropriée des espèces végétales peut permettre de diminuer l'érosion et faciliter la restauration des sols. Avec des objectifs proches, Erktan et al., (2016) ont utilisé le carbone organique du sol, indicateur de la dynamique végétale, pour observer une stabilisation des sols le long d'un gradient de succession végétale, via la consolidation d'agrégats.

....liées à la dynamique sédimentaires des particules fines et du charriage

La sensibilité des marnes à l'altération mécanique et la désintégration de ces agrégats en particules fines fait également partie des problématiques traitées par l'observatoire Draix-

Bléone tant les concentrations en MES (Matières En Suspension) peuvent être très élevées lors des crues (jusqu'à 800 g/L). Plusieurs études relient la création de MES à la dynamique des crues : l'abrasion des agrégats lors des crues (Grangeon, 2012) ou l'abrasion et la fragmentation des marnes au sein des flux charriés (Bouteiller, 2011) induisent la production d'une granulométrie fine. La caractérisation des MES et leurs modes de formation permet de mieux cerner les temps de transit de ces flux solides et apporte une première estimation de leur répartition spatiale. La gestion des stocks de MES dans les rivières est un enjeu majeur pour le fonctionnement des infrastructures hydrauliques et la préservation des milieux aquatiques. Misset et al. (2021) et Navratil et al. (2010) observent en particulier que les lits des rivières en aval des bassins marneux peuvent stocker environ 80% de la masse moyenne annuelle de MES exportées. Si la mobilité des lits, pour les tronçons encore morphodynamiquement actifs, explique une part des flux de particules en suspension lors d'événements intenses (Misset et al., 2019b), la configuration des sources sédimentaires reste un facteur de contrôle majeur de la dynamique des MES (Misset et al., 2019a). Ces résultats confirment la nécessité d'un suivi quantifié du charriage et des particules en suspension des hauts de bassins versants, et notamment des zones de badlands, identifiées comme principal fournisseur en sédiments fins de la Durance (Copard et al., 2018). Les bassins de Draix équipés pour les mesures en continu des précipitations, des débits et des flux solides (suspension et charriages) (Figure 3) permettent une telle quantification du transport solide (Liébault et al., 2016). Esteves et al. (2019) ont ainsi montré que la dynamique des exports de MES était très variable selon les crues et ne faisait pas ressortir de tendance claire entre pluies, débits et MES. Mathys (2006) s'est attaché plus particulièrement à décrire la dynamique du transport solide à l'échelle évènementielle et les interactions entre flux liquides et solides lors de la formation des crues. Ces deux études mettent également en évidence une saisonnalité des exports sédimentaires, dictée par une saisonnalité des régimes de pluie, acteurs principaux de l'érosion des badlands marneux. Deux périodes se distinguent : la fin du printemps / début d'été qui se caractérise par de forts orages, courts mais intenses, et l'automne qui enregistre des événements de pluies longs (cumul de pluie élevé) mais de plus faible intensité. Mathys et al., (2005) ont montré que l'intensité de la pluie joue un rôle prépondérant dans l'arrachement des matériaux sur les versants et que la schistosité du substrat marneux renforce ou inhibe cette capacité érosive. A l'échelle du versant, les pluies intenses induisent donc une forte érosion mais ne permettent pas un transfert total des sédiments jusqu'à l'exutoire. L'analyse des transferts sédimentaires à l'échelle du bassin versant traduit un retard de la vague sédimentaire entre le pic d'érosion et le pic d'export ; les sédiments érodés sont d'abord stockés dans le réseau hydrographique après l'hiver et les pluies de printemps, pour être ensuite repris à l'automne par des événements aux cumuls plus élevés (Bechet et al., 2016; Mathys, 2006). En utilisant une comparaison d'images de laser-scanner terrestre sur une période de deux ans, Bechet et al. (2016) ont interprété ces processus d'érosion cycliques comme un excès de sédiments disponibles associé à des contraintes hydrauliques limitées (i.e. une capacité de transport réduite) au cours de la première partie de l'année (jusqu'à la fin du printemps). Une transition s'opère au cours de l'été entre ce régime, dit '*transport-limited*', et un régime '*supply-limited*', qui se caractérise à l'inverse par une capacité de transport théorique non atteinte, limitée par la disponibilité en sédiment dans le bassin (Tucker &

Whipple, 2002). Cette cyclicité saisonnière est induite par le renouvellement de matériel transportable au cours de l'hiver.

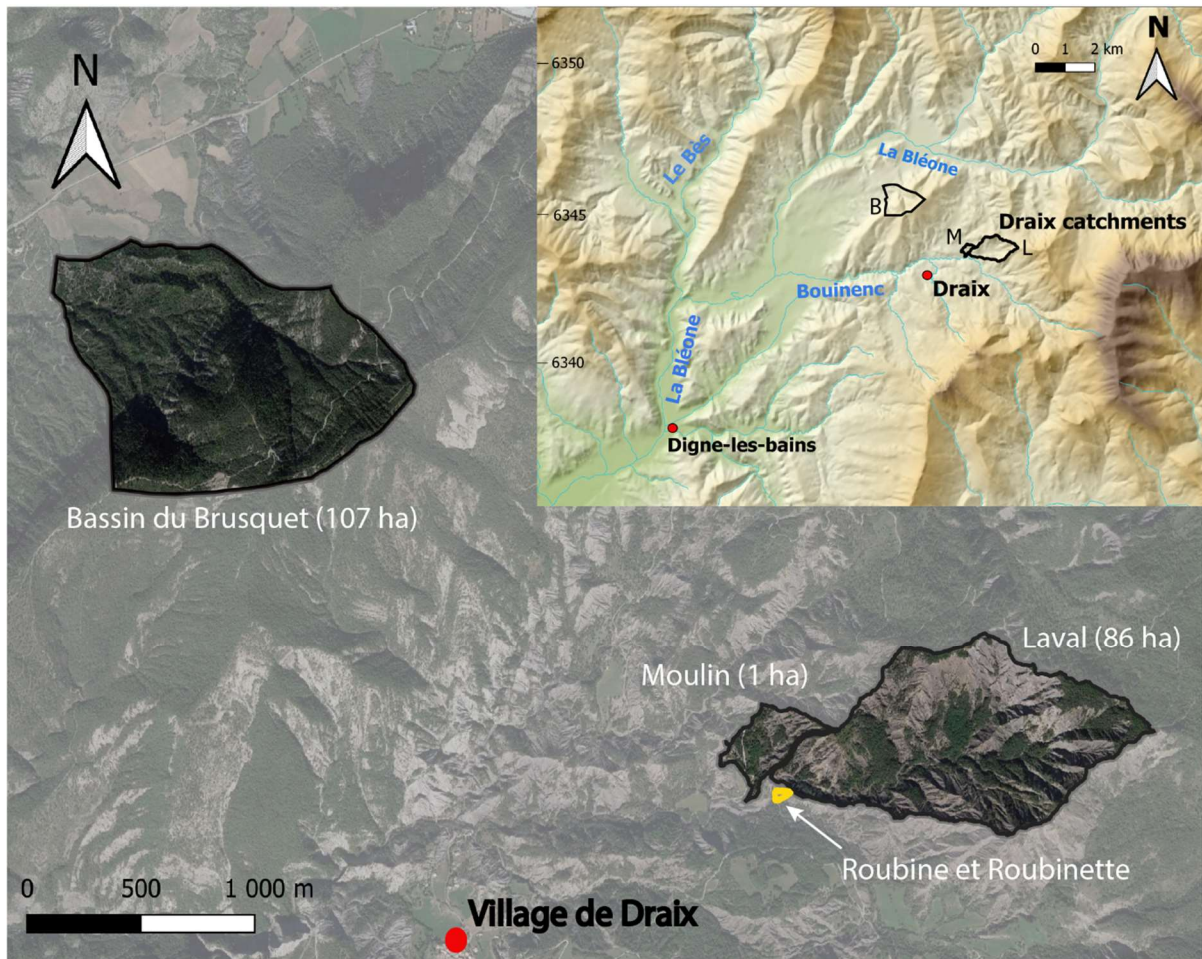


Figure 2: Image satellite (Géoportail) des bassins versants considérés de l'Observatoire de Draix-Bléone sur le site de Draix. L'encart précise la situation géographique de l'observatoire à l'échelle régionale (MNT RGEALTI IGN).

...liées aux processus de gélifraction et à la caractérisation du régolithe

De nombreuses études, sur l'observatoire Draix-Bléone ou sur des sites similaires, attribuent cette production de régolithe, résultat de l'altération du substratum qui mène à la formation d'un substrat fragmenté et ainsi facilement transportable en surface, aux processus de gélifraction (Nadal-Romero et al., 2007; Oostwoud Wijdenes & Ergenzinger, 1998; Regués et al., 1995; Rovéra & Robert, 2005). L'altération des marnes par la succession des cycles de gel-dégel est le processus de production de régolithe principalement considéré dans ces études. Le processus de 'fragmentation induite par la croissance de lentilles de glace' ('ice segregation'), testé sur plusieurs sites d'étude en zones de montagnes, a également été considéré dans la littérature (R. S. Anderson, 1998; Hales & Roering, 2007; Hallet et al., 1991; Rengers et al., 2020). Une description détaillée des mécanismes associés à ces deux processus et à leurs applications est fournie dans l'introduction du premier chapitre. Notre étude apporte une analyse quantitative de la contribution de ces processus d'altération par gélifraction, via l'utilisation de différents indicateurs de température, au flux sédimentaire totale. L'identification du processus de fragmentation comme acteur principale de l'altération

est une étape clé pour évaluer le volume de sédiments disponibles et mobilisables dans les bassins et ainsi prédire les quantités de sédiments exportés. La caractérisation du régolithe (rugosité, structure, résistance, granulométrie, capacité d'infiltration) devient alors nécessaire pour identifier les proxys de cette altération saisonnière. Bien que Bechet et al. (2015) aient observé l'érosion des marnes à l'échelle millimétrique via l'utilisation d'un laser-scanner terrestre sur un échantillon transporté, la majorité des études réalisent des mesures *in-situ*. Maquaire et al. (2002) ont mesuré la résistance des marnes via la pénétrométrie dynamique pour estimer l'épaisseur du régolithe, Mallet et al. (2020) s'est intéressé à l'état hydrique des sols marneux et différentes campagnes sur les bassins versants marneux espagnols ont mesuré la densité et la granulométrie du substrat (Nadal-Romero et al., 2007, 2008; Nadal-Romero & Regüés, 2010). Un état des lieux plus détaillé des connaissances sur ces méthodes est proposé dans l'introduction du deuxième chapitre. Notre étude ajoute une nouvelle caractéristique du régolithe, via la mesure de la granulométrie et le calcul du D50, aux connaissances existantes. La comparaison statistique des différentes mesures met ainsi en évidence le D50 comme proxy de l'altération saisonnière.

Cependant, la mesure, le suivi et la collecte de données d'altération et d'érosion des marnes restent souvent un challenge. L'altération rapide de la roche mère en régolithe, substrat friable et très poreux, rend particulièrement difficile l'installation de sondes dans le sol. Ces dernières sont régulièrement déchaussées ou enfouies, ce qui engendre un mauvais contact avec le sol, et fournissent alors des données erronées, voire discontinues. La structure en plaquettes de la marne rend également l'échantillonnage plus délicat et induit de l'incertitude dans les mesures (teneur en eau, granulométrie, etc. ; Ariagno et al., *in review*). Les installations pour les mesures de débit d'eau, de charriage ou de MES sont, elles, confrontées aux crues torrentielles des badlands. Très rapides, puissantes et extrêmement chargées en sédiments, celles-ci produisent souvent des dommages sur les systèmes de mesures, et parfois leur perte (Mallet, 2018; Mathys, 2006). Dans ce contexte, outre l'investissement matériel, un investissement humain est indispensable pour le suivi des dispositifs de mesures en place et l'analyse critique des données. C'est l'ensemble de ces données de terrain récoltées et validées (Draix-Bleone Observatory, 2015) au cours de 35 années de suivi qui représente la force et l'intérêt de l'observatoire Draix-Bléone. La continuité et la qualité des mesures ainsi que le respect de ces environnements sont les maîtres mots de ces dispositifs d'observation, sentinelles des changements en cours de la zone critique (White et al., 2015).

Le CZO de Draix-Bléone dans un contexte international

Les problématiques soulevées sur le site de Draix-Bléone sont reprises par bon nombre de badlands dans le monde, tant ces zones d'érosion actives induisent de rapides changements sur la morphologie des paysages. Depuis les plateaux de loess d'Asie (Higuchi et al., 2013; Jiao et al., 2011; Saha et al., 2020) aux étendues désertiques d'argilite ou de grès de l'Amérique du Nord (Kasanin-Grubin, 2013; Rawling et al., 2003), en passant par les bassins marneux d'Espagne (Nadal-Romero et al., 2007; Sole'-Benet et al., 1997), la lithologie des badlands varie mais les morphologies et la couverture végétale sont similaires et les quantités de sédiments exportés restent élevées. Plus proche géologiquement du site de Draix-Bléone, les

badlands du pourtour méditerranéen ont fait l'objet de plusieurs analyses et inter-comparaisons (Nadal-Romero et al., 2011, 2021) et deux grands types de badlands se distinguent selon les régimes climatiques (arides versus humides). De multiples facteurs géomorphologiques responsables de l'altération ou de l'érosion ont été étudiés et différentes approches méthodologiques ont été mises en place pour permettre l'estimation de la charge sédimentaire exportée (Nadal-Romero et al., 2011). Parmi les petits bassins versants expérimentaux répertoriés par Mallet (2020), les bassins instrumentés de Draix-Bléone se distinguent par la diversité des mesures en place. Les enregistrements long-terme de la charge sédimentaire, et ce à différentes échelles spatiales, intégrant MES et charriage, sont des données particulièrement rares et précieuses.

Au sein du réseau national OZCAR, l'observatoire Draix-Bléone est le seul implanté sur des badlands avec des problématiques d'érosion intenses et de transport court-terme.

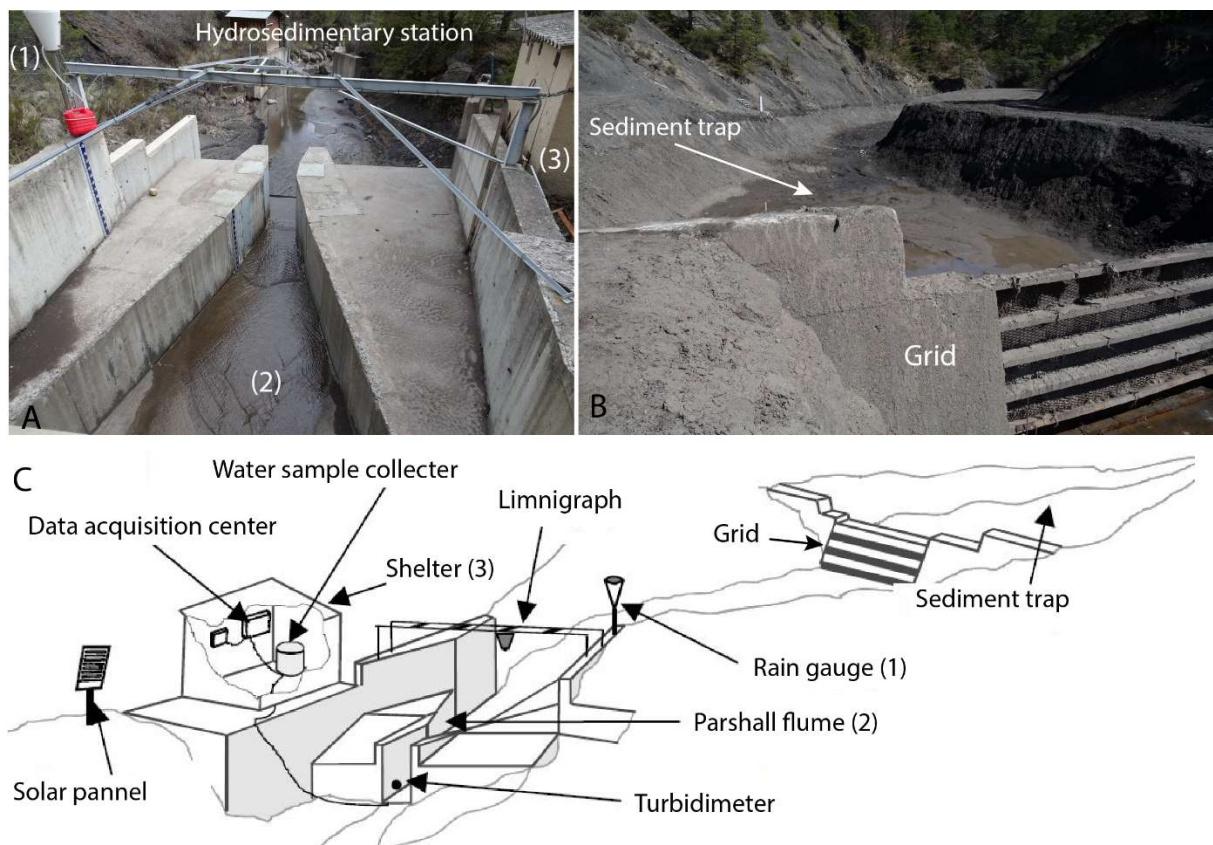


Figure 3: Hydrosedimentary station (A) and sediment trap (B- Avril 2022), both are part of the measure installations (C) situated at the outlet of the Laval catchment. Modified from Mathys (2006)

...aux modèles d'évolution de surface

Qu'on le veuille ou non, le passage du terrain à la modélisation est devenu inévitable et essentiel en géosciences tant il permet d'élargir les points de vue, aussi bien spatialement que temporellement. Quand la géologie de terrain met à l'honneur l'observation, les modèles peuvent apparaître comme des boîtes noires, lieu de complexes interactions qui tentent de reproduire les phénomènes et structures subtils et interconnectés de notre environnement.

Pourtant la puissance de ces outils est incontestée et les applications multiples. L'enjeu reste alors de ne pas perdre de vue l'origine des objets et/ou phénomènes à modéliser pour ne pas déconnecter 'géo' et 'sciences'.

Les modèles d'évolution de paysages (Landscape Evolution Models, LEM) s'attachent à reproduire l'évolution des morphologies de surface induites par l'interaction de multiples processus physiques et chimiques qui transforment et transportent des éléments de la lithosphère (Figure 1– échelle du bassin). De tel modèles numériques permettent de visualiser, tester et quantifier diverses dynamiques d'un système, via différentes combinaisons de paramètres d'entrée et selon différents forçages (climatiques, tectoniques, etc.) (Tucker & Hancock, 2010). La complexité de ces modèles réside dans la multitude des processus qui opèrent sur une même surface à des échelles de temps et d'espace qui leur sont propres (Coulthard, 2001). Les applications de ces modèles d'évolution de paysage sont multiples (van der Beek, 2013): analyse de la formation des terrasses glaciaires (Langston et al., 2015), couplage versants-rivière (Baartman et al., 2012) ou encore estimation du contrôle tectonique et structurale sur l'évolution des morphologies (van der Beek & Braun, 1999). En apportant une vision globale du bassin versant, les modèles d'évolution de paysages associent implicitement les différentes disciplines liées à la zone critique et permettent ainsi une meilleure représentation des processus, qui s'accompagne également d'une complexification de ces modèles.

Les changements observés en surface, synonymes de transferts de masse entre différentes entités du bassin versant, sont modélisés par des lois de transport géomorphologiques. Ces lois théoriques représentent le cœur même de la 'boîte noire', elles traduisent de façon mathématique l'érosion, induite par un ou plusieurs processus, des bassins versants à des échelles spatio-temporelle variables (Dietrich et al., 2003). Nous utiliserons une loi d'altération (transforme la roche saine en régolithe), qui décrit le ralentissement exponentiel de l'altération lorsque l'épaisseur de régolithe devient significative. Deux lois de transport seront utilisées ; une loi de diffusion non-locale qui permet l'érosion et le transport de particules sur les versants et une loi d'érosion fluviale dépendant de l'épaisseur des sédiments dans les chenaux. Une description plus détaillée des lois géomorphologiques utilisées dans notre modèle est proposée dans la partie 'II. Modelling framework' du 3ème chapitre.

Les bassins versants de l'observatoire de Draix-Bléone représentent un cadre idéal pour construire un modèle d'évolution de paysage : les différentes chroniques long-termes des grandeurs climatiques (précipitations, températures, etc.), les modèles numériques de terrain haute résolution et les relevés continus de la charge sédimentaire (MES et charriage) forment un jeu de données d'entrée et de calibration étoffé et varié. La connaissance détaillée de la dynamique du régolithe (Rovera et Robert, 2005; Bechet et al., 2016; Ariagno et al., 2022 et in review) et du transport sédimentaire dans ces bassins (Descroix & Mathys, 2003; Mathys, 2006) aide la phase de calibration du modèle. Les paramètres peuvent alors être estimés via des observations directes issues du terrain ou varier dans un intervalle de valeurs concret et défini par d'autres études. La dynamique annuelle des badlands induit des changements

morphologiques rapides et visibles sur de courtes échelles de temps. Cela permet une adaptation des protocoles et techniques de mesures ainsi que l'analyse de l'évolution des tendances érosives sur une échelle de temps humaine. La bonne connaissance des processus, le fait qu'ils soient rapides et donc mesurables à une échelle de temps humaine, et la disponibilité de données pour calibrer les lois géomorphologiques, nous permet d'utiliser le concept de 'natural experiment' proposé par (Tucker, 2009) pour construire notre modèle sur ce site.

L'utilisation et le développement de modèles numériques sur le site de Draix-Bléone permettent une valorisation dans leur ensemble des chroniques de mesures long-terme et une approche plus interdisciplinaire des problématiques scientifiques. Un historique des différents modèles appliqués aux badlands de Draix est proposé dans l'introduction du chapitre 3. Le modèle qui sera développé dans ce dernier chapitre est un intermédiaire entre les modèles d'évolution à l'échelle des temps géologiques (plusieurs millions d'années) qui font intervenir les forçages long-termes (tectoniques) (van der Beek & Braun, 1998; Bishop, 2007; Gilchrist et al., 1994) et les modèles événementiels qui nécessitent une connaissance précise des mécanismes physiques de l'écoulement sur de courtes échelles de temps (Mathys, 2006; Taccone, 2018).

Les problématiques scientifiques

Le contexte scientifique dense décrit ci-dessus met en lumière la nécessité de trouver des grandeurs capables de quantifier les exports sédimentaire, éléments indispensables pour prédire les évolutions de ces flux solides. Avec également des enjeux forts pour la gestion de la charge sédimentaire des rivières, notre étude s'intéresse au rôle de l'altération sur la variabilité temporelle à différente échelle des processus de production sédimentaire. Par la suite, l'objectif est d'intégrer ces connaissances dans un modèle d'évolution de paysage des bassins de l'observatoire de Draix-Bléone.

Notre travail se concentre donc autour de trois principales questions :

- Peut-on quantifier l'impact de l'altération sur la production sédimentaire, et en particulier sur la variabilité intra et interannuelle des exports ? Et quel est alors le processus d'altération sur les versants qui contribue le plus à la production sédimentaire et sur quelle échelle de temps intervient-il ?
- Comment suivre l'altération in-situ des marnes et peut-on identifier une grandeur mesurable, qui rende compte de cette altération, et qui puisse être utilisée pour alimenter les modèles numériques d'évolution ?
- Comment construire un modèle permettant de rendre compte de la dynamique intra-annuelle des exports sédimentaires, à partir de la compréhension des processus d'altération obtenue précédemment ?

Ces questions nous amènent à travailler à l'échelle du régolithe sur les versants des bassins (Figure 1). La première partie de ce manuscrit est consacrée à l'exploration des données de l'observatoire, et plus particulièrement des données de température de sol qui ont permis le calcul d'indicateurs d'intensité du processus de gélification. La comparaison de ces indicateurs de température au flux solide permet d'identifier la contribution des processus d'altération au flux sédimentaire, et en particulier d'estimer la part de la variabilité inter-annuelle de ces flux qui est liée à ces phénomènes thermiques. La variabilité intra-annuelle des exports sédimentaires a également été revisitée en utilisant les récentes périodes d'enregistrement (2003-2019) des données de pluie et d'export sédimentaire.

En parallèle, la nécessité de quantifier l'altération conduit aux problématiques du deuxième chapitre, qui rapporte les résultats de 11 campagnes de terrain réalisées sur des versants aux orientations et schistosités différentes. Plusieurs caractéristiques du régolithe ont été mesurées : résistance, teneur en eau et granulométrie, afin d'explorer leur interdépendance et d'extraire un indicateur quantitatif de l'altération du régolithe.

Le modèle d'évolution de paysage développé dans le chapitre trois traduit la volonté de spatialiser les processus d'altération et d'érosion à l'échelle du bassin afin d'apporter des prédictions quantitatives des exports sédimentaires. Les indicateurs et grandeurs

responsables de l'altération identifiés dans les deux premiers chapitres aideront à la construction et au développement du modèle.

Réalisé à partir de la topographie du bassin-versant du Laval, ce modèle s'attache à reproduire les processus d'altération saisonniers identifiés sur les versants et permet une analyse à l'échelle intra- et inter-annuelle, de la dynamique sédimentaire. A partir d'un modèle de départ simple, prédisant une relation linéaire entre pluie et exports sédimentaires, nous avons cherché à complexifier le modèle en utilisant comme indicateur de fiabilité la comparaison entre la dynamique des exports simulés et la variabilité intra-annuelle précédemment observée (cycle d'hystérèse - chapitre 1). Notre approche s'est attachée à simuler des processus et utiliser des critères de calibration issus d'observations de terrain (chapitre 2). Intégrer au modèle les observations et les processus identifiés dans les deux premiers chapitres est un des challenges de ce travail.

La modélisation du fonctionnement des badlands est une étape clé pour étudier l'impact de la variation des forçages climatiques telles que les températures ou la pluviométrie. La variabilité du régolithe et des exports sédimentaires sur de courtes échelles de temps fait des badlands l'un des environnements les plus sensibles aux rapides perturbations du climat à venir (Clarke & Rendell, 2010). Le modèle d'évolution de Draix-Bléone est donc une première brique pour tester l'impact d'une modification des températures et / ou du régime de pluie (Nadal-Romero et al, 2021), via différents scénarii climatiques, sur la production et les exports sédimentaires des badlands. La prédiction de ces changements est un enjeu majeur pour quantifier les flux solides et liquides des futurs événements extrêmes (Hirschberg et al., 2021) et estimer les risques pour les infrastructures et les populations en aval.

Chapter I

Sediment export in marly badland catchments modulated by frost-cracking intensity, Draix-Bléone Critical Zone Observatory, SE France

Ariagno, C., Le Bouteiller, C., van der Beek, P., & Klotz, S. (2022). Sediment export in marly badland catchments modulated by frost-cracking intensity, Draix–Bléone Critical Zone Observatory, SE France. *Earth Surface Dynamics*, 10(1), 81–96. <https://doi.org/10.5194/esurf-10-81-2022>

Abstract. At the interface between the lithosphere and the atmosphere, the critical zone records the complex interactions between erosion, climate, geologic substrate and life, and can be directly monitored. Long data records (30 consecutive years for sediment yields) collected in the sparsely vegetated, steep and small marly badland catchments of the Draix-Bléone Critical Zone Observatory (CZO), SE France, allow analysing potential climatic controls on regolith dynamics and sediment export. Although widely accepted as a first-order control, rainfall variability does not fully explain the observed inter-annual variability in sediment export. Previous studies in this area have suggested that frost-weathering processes could drive regolith production and potentially modulate the observed pattern of sediment export. Here, we define sediment-export anomalies as the residuals from a predictive model with annual rainfall intensity above a threshold as the control. We then use continuous soil-temperature data, recorded at different locations over multiple years, to highlight the role of different frost weathering processes (i.e., ice segregation versus volumetric expansion) in regolith production. Several proxies for different frost-weathering processes have been calculated from these data and compared to the sediment-export anomalies, with careful consideration of field data quality. Our results suggest that frost-cracking intensity (linked to ice segregation) can explain about half (47–64%) of the sediment-export anomalies. In contrast, the number of freeze-thaw cycles (linked to volumetric expansion) has only a minor impact on catchment sediment response. The time spent below 0 °C also correlates well with the sediment-export anomalies and requires fewer field data to be calculated than the frost-cracking intensity. Thus, frost-weathering processes modulate sediment export by controlling regolith production in these catchments and should be taken into account when building predictive models of sediment export from these badlands under a changing climate.

1.1. Introduction

Landscape erosion and its associated hazards, such as torrential floods, rockfalls, etc., are some of the visible consequences of the complex interaction between the Critical Zone and climate (e.g., Anderson et al., 2012). Regolith production is the result of a variety of processes, many of which are influenced by climate, and constitutes a critical first step in the source-to-sink sediment pathway (e.g. Dixon et al., 2009; Riebe et al., 2017). However, the impact of climate (change) on regolith production and ensuing landscape erosion remains difficult to quantify. In a context of rapid global climate change, how will sediment production be affected (e.g., Nearing et al., 2004; Hirschberg et al., 2021; Nadal-Romero et al., 2021)? How will dominant erosion processes evolve according to lithologies and climatic variations? How will vegetation evolve locally and will it amplify or reduce surface erosion? These questions, among others, motivate the study of soil weathering mechanisms and their sensitivity to climate (e.g., Nadal-Romero et al., 2018).

In badland areas, the interaction between erosion and climate is enhanced because of the absence of vegetation and the easily erodible lithologies. Following the general definition, “badlands” refers to “deeply dissected erosional landscapes, formed in soft-rock terrain, commonly but not exclusively in semi-arid regions and with sparse vegetation, that have a high drainage density of rill and gully systems and are dominated by overland flow” (Harvey, 2004). The widespread badland landscapes known as “Terres Noires” in the South-Eastern French Alps have been extensively studied because of their susceptibility to erosion, leading to high sediment export (e.g., Antoine et al., 1995). Over the last 35 years, several small catchments in these marly badlands have been monitored in the framework of the Draix–Bléone Critical-Zone Observatory (CZO), leading to a quantification of weathering and erosion through repeated measurements of sediment yield at the event scale (Mathys et al., 2003). Because of the ample availability of sediment and the efficient network connectivity (Jantzi et al., 2017), floods in these catchments can transport a very large quantity of sediment (Delannoy & Rovéra, 1996). As an example, during one flood event on 17/06/2014, 6390 tonnes/km² were exported and the suspended sediment concentration reached 440 g/l. Such sediment-laden floods can potentially cause significant damage to downstream infrastructure. Landscape changes are easily and rapidly observable in the Draix–Bléone catchments, but improved identification and understanding of the weathering processes in these marls are required to more accurately predict exported sediment volumes.

Several studies have addressed the characteristics and dynamics of regolith development in the marly badlands of the Draix-Bléone CZO and similar sites. The impact of water content, hydraulic conductivity and infiltration capacity of marls in the Draix-Bléone CZO on runoff generation and erosion was studied by Esteves et al. (2005), Mathys et al., 2005 and Mallet et al., 2018. Rovéra and Robert (2005) first investigated periglacial erosion processes in the Draix-Bléone CZO; they noted the marls’ sensitivity to frost weathering, in particular to freeze-thaw cycles, and the resulting faster ablation on north-facing compared to south-facing slopes. Working in the Central and Eastern Spanish Pyrenees, Regués et al. (1995) and Nadal-Romero et al. (2007) confirmed the important role of slope aspect in controlling the weathering of marls. By studying bulk density, surface mechanical resistance and moisture content, they highlighted a clear temporal and spatial variability in the regolith and inferred that weathering

in these catchments was mainly dependent on the number of freeze-thaw cycles occurring during the year. Based on a two-year time series of twelve high-resolution digital elevation models from a 0.13 ha catchment in the Draix-Bléone CZO, Bechet et al (2016) showed that erosion processes follow a seasonal cycle, with accumulation of loose regolith on slopes during winter followed by its transport from the slopes to the main gullies during summer. These authors inferred a yearly cycle between transport-limited conditions in spring to supply-limited conditions in autumn. However, Jantzi et al. (2017) used sediment-budget calculations from the larger Moulin and Laval catchments of the Draix-Bléone CZO (see below) to infer that sediment transfer is not immediate; they calculated a 3-year residence time for sediments in these catchments.

Overall, existing observations from the Draix-Bléone CZO and similar sites (e.g., Regués et al., 1995; Nadal-Romero et al., 2007) lead to consider frost-weathering as a potentially important process controlling regolith production in marly Alpine badlands. Several studies have explored this process in different geological contexts, employing theoretical, experimental and observational approaches. The two main frost-weathering processes considered in the literature are volumetric expansion of ice and ice segregation (e.g., Matsuoka, 2008). Volumetric expansion of ice can occur repeatedly during freeze-thaw cycles, whereas ice segregation occurs when liquid water migrates towards a locus of ice-lens growth. In cold and high Alpine environments, it appears that ice segregation controls rock weathering by widening rock fractures or “frost cracking” (R. S. Anderson, 1998; Matsuoka & Murton, 2008). The growth of ice lenses required for frost cracking has been argued to depend primarily on absolute temperature, water availability and temperature gradient (Hallet et al., 1991). Hales and Roering (2007) developed a numerical model to estimate soil temperature at different depths and defined a frost-cracking intensity indicator to quantify ice-driven mechanical erosion. In their model, frost cracking occurs when rocks are in the “frost-cracking window” (between -3 and -8 °C) and liquid water is available because either the surface or rocks at depth are above freezing point; the frost-cracking intensity depends on the temperature gradient in the frost-cracking window. Subsequently, Anderson et al. (2013) modelled rock damage by frost cracking using the above model, adding the distance that water must travel to reach the locus of potential frost cracking, and observed the impact on regolith production and hillslope evolution. Frost-cracking has thus been identified as the major control on rock weathering in high Alpine environments (Bennett et al., 2013; Delunel et al., 2010; Draebing & Krautblatter, 2019; Hales & Roering, 2007).

The above models have, however, not yet been applied in more temperate/humid climates and in soft lithologies. Two previous studies invoking frost weathering in these contexts (Rovéra and Robert, 2005; Nadal-Romero et al., 2007) only addressed the number of freeze-thaw cycles, and thus implicitly frost weathering by volumetric expansion. Additionally, the link between regolith production and sediment yield is known but remains difficult to quantify. Rengers et al. (2020) recently bridged this gap by studying plot-scale (22 m²) sediment accumulation and debris-flow channel filling patterns using repeat topographic surveys. They found a strong correlation between frost-cracking intensity and sediment production in a steep Alpine bedrock setting.

In this study, we develop a similar approach at the catchment scale (0.1-1 km²) in marly badlands, taking advantage of the exceptional long-term dataset available for the Draix-Bléone Observatory. At the catchment scale, sediment export is primarily driven by rainfall, particularly during high-intensity events (Mathys et al., 2003), but we hypothesize that frost-weathering processes can modulate sediment yield, even at this scale, by controlling regolith

production on hillslopes. Coupled to this first hypothesis, this study aims to highlight and quantify the main frost-weathering process in a setting of humid climate and soft lithology, by using high-resolution soil-temperature measurements (every 10 min.) from different locations. We compare calculated temperature indicators, including the number of freeze-thaw cycles, the time spent below 0 °C, the mean negative temperature and the frost-cracking intensity, during a winter season to the sediment-export anomaly (i.e., the residual of sediment yield that cannot be explained by rainfall variability) in the following year (e.g., for the 2007-2008 winter season, we used the sediment export for the year 2008). The goal of our study is threefold: (1) to confirm the seasonal variability of regolith supply by analysing monthly total sediment yield; (2) to quantify the role of frost-weathering processes in yearly sediment production; and (3) to identify the relevant weathering processes by statistical analysis of different proxy indicators.

1.2. Study site

The Draix-Bléone CZO is part of the French network for the study of the critical zone OZCAR (Gaillardet et al., 2018) and is specifically dedicated to the study of erosion and sediment transport in a mountainous region. Hydrological and sedimentary fluxes have been monitored on several catchments in this CZO since 1983 (Draix-Bleone Observatory, 2015). The Draix-Bléone CZO is situated in the Alpine foothills, 12 km northeast of the town of Digne in South-East France (Figure 4). The Draix catchments are drained by the Bouinenc stream, a tributary of the Bléone, which is itself one of the main tributaries of the Durance River. The geology is characterised by Mesozoic sediments that were folded and faulted during the Alpine orogeny (Lemoine et al., 1986; Lickorish & Ford, 1998). The Bouinenc catchment has a mountainous and Mediterranean climate. Due to its relatively high elevation (>800 m above sea level), the mountainous influence is responsible for cold winters with frequent frost. The Mediterranean influence leads to dry summers interspersed by intense thunderstorms. Annual rainfall is about 900 mm/yr (varying between ~600 and ~1300 mm/yr interannually) in Draix. The rainfall regime varies across seasons, with high-intensity rainfall events during spring/summer and lower-intensity but longer rainfall events in autumn. Only the main streams (Laval and Moulin) are permanent, although the Moulin shows very low discharge in summer; all tributary gullies are ephemeral. Snow fall occurs almost every year but in small amounts (<10 cm) and it melts quickly. The mean annual temperature is 10.3 °C, with an annual variability between mean daily temperatures of approximatively 0.5 °C in winter and 20 °C in summer. This study focuses on two instrumented catchments of the Draix-Bléone CZO: the Laval and the Moulin catchments, which have drainage areas of 0.86 and 0.10 km², respectively. Elevations range from 850 to 1250 m a.s.l. for the Laval and from 850 to 925 m a.s.l. for the Moulin catchment. Vegetation cover is 46% in the Moulin and 32% in the Laval catchment (Carriere et al., 2020). The catchments are underlain by thick Middle-Jurassic black marl series locally known as “Terres Noires”. Subtle changes in composition of the marls, with a limestone fraction varying according to stratigraphic level, have been observed (Brochot, 1997) but our study site is not affected by these variations. The dominant bedding dip is to the east in the Draix area. These black marls are susceptible to strong erosion and develop steep badland slopes (mean hillslope angles of 0.58 for the Laval and 0.40 for the Moulin catchment), with high drainage density and deeply incised gullies characterizing the catchment morphologies (Figure. 1C, D). Sediment transport occurs through gravitational processes on hillslopes, minor

landslides ($<1 \text{ m}^3$) and debris-flows in the upper network, and fluvial transport as bedload and suspended load in the main network. The Draix catchments record some of the highest observed specific sediment yields worldwide: average annual sediment yields are around 12,000 and 570 tonnes, equating to specific sediment yields of around 14,000 and 5,700 tonnes/km 2 /y, for the Laval and Moulin catchments, respectively. This sediment budget results from 22 floods per year on average (for the Laval), ranging between 13 and 45 floods / yr and associated with very heterogeneous sediment yields from 0 up to around 6500 t/km 2 per event (Smetanová et al., 2018). It has been shown that erosion is strongly focused in the unvegetated parts of these catchments; the specific sediment yield of the adjacent vegetated Brusquet catchment is two orders of magnitude smaller than that of the Laval catchment (Carrière et al., 2020). Considering only the unvegetated parts of the catchments as contributing to the sediment yield and the measured sediment density of 1700 kg/m 3 , the average erosion rate is around 8 mm/yr (Mathys, 2006).

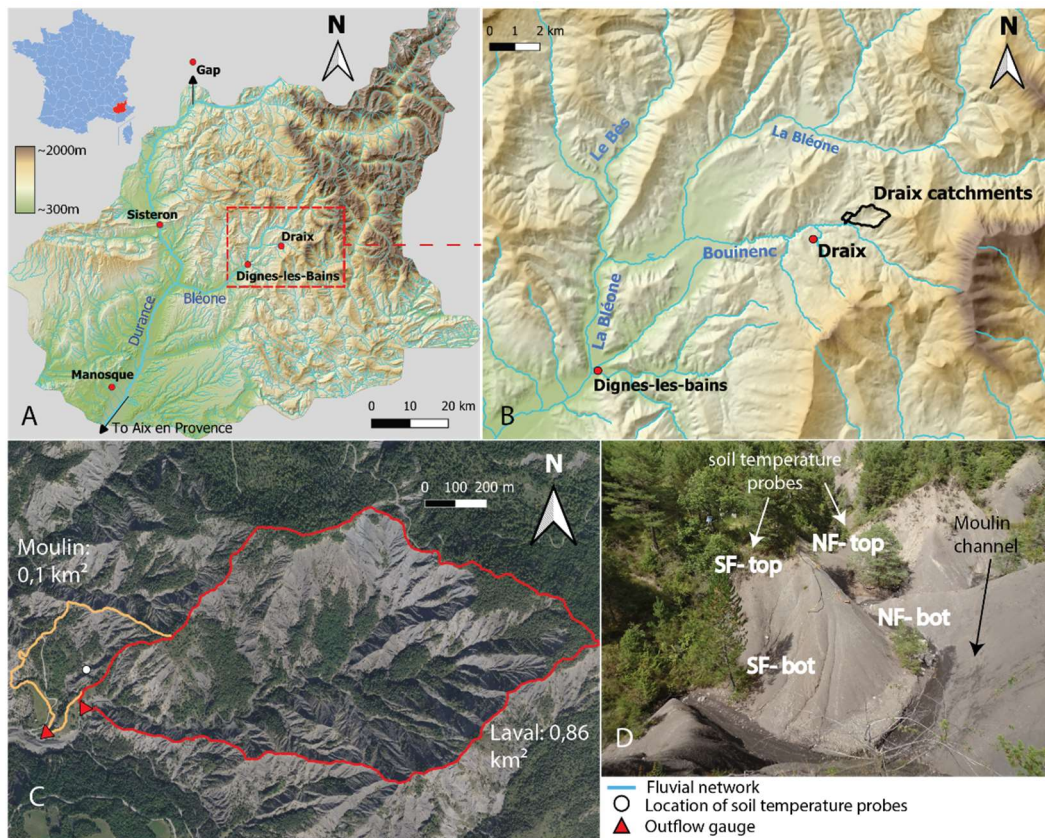


Figure 4: Geographic setting of Draix-Bléone Critical Zone Observatory. (A) Location within the 'Alpes de Hautes-Provence' department of southeast France (inset), red box shows location of B. Maps are from DEM RGEALTI IGN database; (B) Zoom on the Bouinenc catchment, black outlines show Moulin and Laval catchments. (C) Satellite image (Géoportail) of the Moulin and Laval catchments, showing location of outflow gauges and soil-temperature probes. (D) Setting of soil-temperature measurement sites, in a meander of the Moulin stream on north-facing (NF) and south-facing (SF) slopes at different locations (uphill and downhill) on the hillslopes.

I.3. Methods

I.3.1. Data acquisition

We use three types of datasets: rainfall, sediment yield and soil temperature. Monthly and annual rainfall values are obtained by summing the detailed event records measured with a tipping-bucket rain gauge located at the outlet of the Laval catchment (Figure 4C). Sediment yield is measured at the outlets of both the Laval and Moulin catchments, where hydro-sedimentary stations have been set up to monitor water discharge and both suspended load and bedload. Suspended sediment concentration is measured with automatic samplers and turbidimeters and suspended sediment flux is computed as the product of discharge and concentration, cumulated over a flood to obtain an event-scale yield. Bedload volumes are measured after each flood by topographic surveys of a sediment trap located immediately upstream of the station. Bedload volume is then converted into mass using a density of 1700 kg/m³, constrained by measurements in the sediment trap (Mathys, 2006). The raw data we use is therefore a series of event-scale sediment yield. An analysis of inter-event sediment export, assuming an inter-event concentration of 0.1g/L (respectively 1g/L) shows that flood export represents more than 99% (respectively 98%) of the total annual sediment export. Thus, sediment export (both as suspended load and as bedload) is considered negligible during low flow and we define the total sediment export as the monthly or yearly sum of the suspended load and bedload contributions during floods. For a few flood events, the suspended-load data is missing. In such cases, we reconstructed the event-scale suspended sediment yield based on the average proportions of suspended load and bedload, computed from multiple complete years of total load records. The proportions of suspended load and bedload in the Laval catchment are 74% / 26% for summer floods (May to September) and 57% / 43% for winter floods (October to April).

Soil temperature has been recorded continuously between August 2005 and December 2020, using several PT100 soil-temperature probes located on opposite slopes (867 m elevation) in an inner meander of the Moulin Creek (Figure 4C, D). The acquisition frequency was 10 minutes. We use the data from probes located in bare black marls at uphill and downhill locations on north- and south-facing slopes, respectively (i.e., four sites in total; Figure 4D), in order to explore variations in soil temperature due to differences in exposure (Rovéra & Robert, 2005). At each site, four probes are available to measure soil temperature at depths of 1, 6, 12 and 24 cm, respectively (Appendice 1), spanning the range of depths that has been reported for the weathered regolith in this area (Maquaire et al., 2002). In 2019, temperature-probe locations were modified to a single set of four probes located mid-slope on both the north- and south-facing slope. As our interest is focused on frost weathering, we specifically analysed soil temperatures during the winter season, from October 18th to March 31st. This period was chosen because negative soil temperatures are almost absent outside these dates; During the periods between April 1st and October 17th, we found that the time spent below 0 °C was on average less than 0.4% of the total time in a year and represents less than 4% of the time spent below 0 °C during the winter. The time spent in the frost-cracking window outside of the analysed winter period was null for most of the study years. We chose to start the winter season on October 18th because some yearly series miss temperature data for early October.

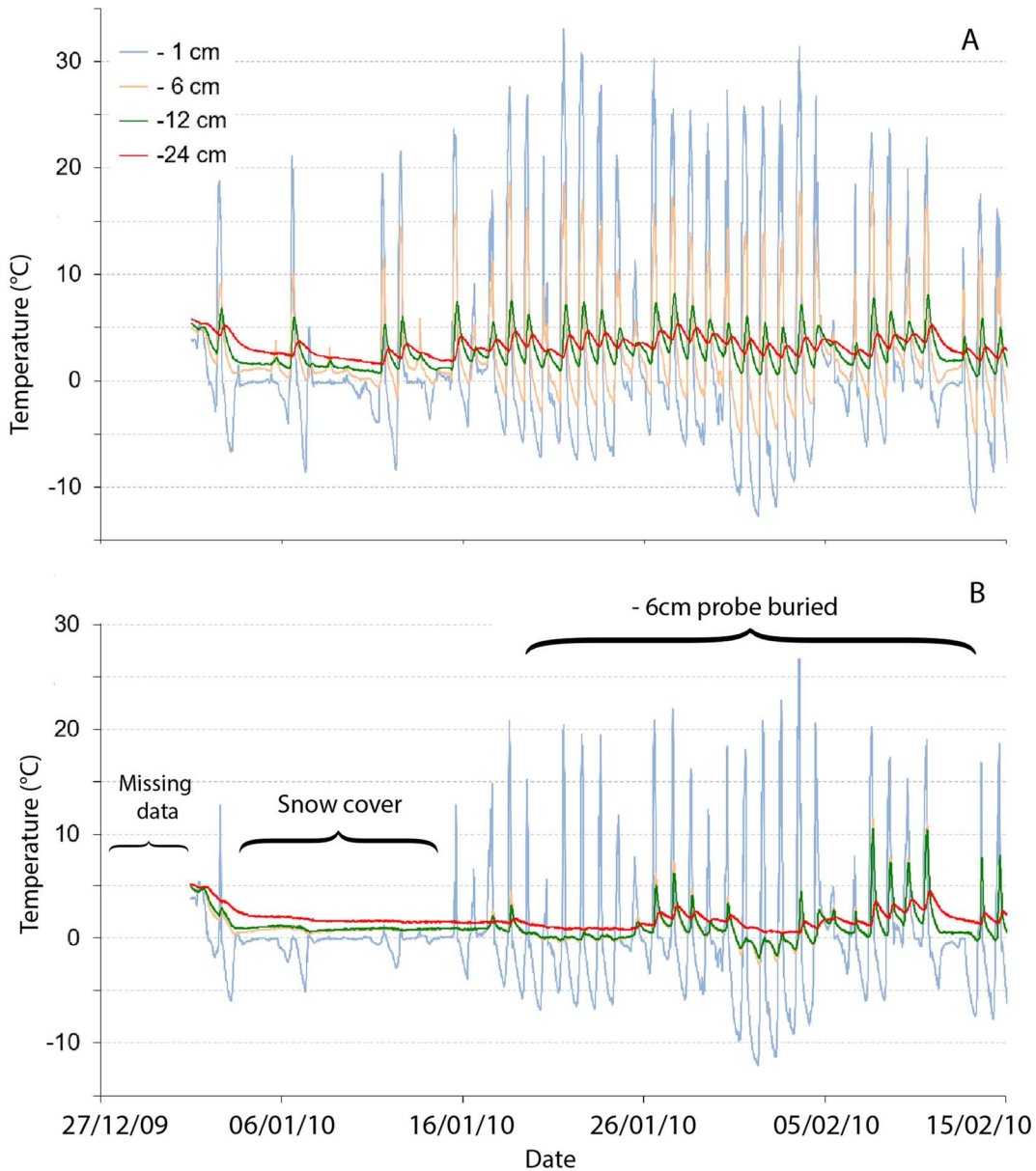


Figure 5: Exemple of raw temperature series (1 measurement every 10 min). (A) Typical soil-temperature series recorded with four probes at different depths (from south-facing uphill location; time scale as in B). (B) Example of soil-temperature series (from south-facing downhill location) biased because of climatic conditions (snow cover), buried or loosened probes. A full year of temperature measurements is shown in Appendix 1. High temperature values are observed at -1 cm even in winter when the black marls heat radiatively during sunny periods.

The soil-temperature dataset includes periods of missing or spurious data, due to probe malfunction, unearthing or burial. The relatively mobile nature of the marls leads to frequent displacement of probes, identified in the temperature records by similar temperatures between probes at different depths or anomalous daily temperature ranges (Figure 5). When these periods are longer than twenty consecutive days, the full season of data is rejected (i.e., 2005/2006, 2010/2011 and 2012/2013). When the missing period is shorter (for seasons 2011/2012, 2014/2015, 2015/2016), we searched for a relation between soil temperature and air temperature (recorded at the closest weather station) in order to reconstruct soil temperature during the missing time interval (Appendice 2 & 3). Over the eleven winter seasons used to calculate our temperature indicators, we reconstructed 56 days in this

manner, which represents around 3% of the total winter temperature dataset (see Appendix Table 1 for details). We found that a simple two-tier linear fit predicted soil temperature well for air temperature below 10 °C and soil temperature below 5 °C, with an inflection point around -4°C. The correlation breaks down for higher temperatures due to radiative heating effects; however, since our focus is on soil temperatures below 0 °C, the simple linear-correlation approach is sufficient. The presence of snow sets the soil temperature to ~0 °C (Figure 5) and thus perturbs the linear trend. Therefore, the regression was calibrated during snow-free periods only.

The soil temperature data has been recorded in the Moulin catchment but is regarded representative also of the adjacent Laval catchment that shares the same lithology. Sediment-yield data is available for both the Moulin and Laval stations (located 100 meters apart at the outlets of both catchments; Figure 4C) and our analysis of hysteresis cycles shows that both catchments have the same sediment dynamics (see Section I.3.1, Figure 7, Figure 8). Because of its reduced vegetation cover and larger area (0.86 km²), we consider that the Laval catchment is more representative for the analysis of the relationship between sediment yield and temperature indicators (Figure 6, Figure 7 and Figure 9 to Figure 12) than the much smaller Moulin catchment (0.089 km²). Moreover, the larger sediment export values from the Laval catchment are associated with smaller relative uncertainties. For these reasons, we focus our attention on the sediment-export data from the Laval catchment for our analysis.

I.3.2. Data Processing

I.3.2.1. Rainfall and sediment export

First, we compared monthly sediment export and monthly rainfall to understand the seasonal dynamics of sediment transport in the Laval and Moulin catchments (Figure 4, Figure 6). The analysis was performed for the period 2003 - 2020, during which sediment export was precisely recorded. In this time interval, rainfall amounts were summed for each month to obtain monthly rainfall. When gaps were present in the data (around 6% of the time), daily cumulative reconstitutions of these missing periods were possible thanks to the network of tipping-bucket rain gauges installed around the catchment. Monthly averaged rainfall intensity was also computed by averaging non-zero values of 5-minute constant time-step rainfall intensities. As established in previous studies (Bechet et al., 2016; Mathys et al., 2003), sediment export at the event scale is driven by rainfall intensity above a threshold. Therefore, we analysed the correlation between annual sediment export and annual rainfall, looking not only at total annual rainfall, but also at annual rainfall above several threshold values of intensity varying from 10 to 80 mm/h. For this correlation, we used the instantaneous intensities computed at the variable time steps of each tipping event. We selected this range of thresholds based on inferences from previous studies (Mathys, 2006) and then used the value providing the best correlation to predict annual sediment-export values. In order to overlap with the period where soil-temperature data were available, we used only data between 2005 and 2020 for the correlation between rainfall and annual sediment export. We define the sediment-export anomaly as the residual between measured sediment export in any year and the predicted value from this regression. With the aim of quantifying the impact of frost weathering on sediment production, and of identifying the most relevant frost-weathering process, our objective is to identify a controlling factor to explain this sediment-export anomaly.

I.3.2.2. Temperature indicators

With the aim of quantifying the impact of frost weathering on sediment production and of identifying the most relevant frost-weathering process, we selected four potential indicators of frost-weathering intensity and correlated them both with each other and with the sediment-export anomaly.

First, we computed the Frost Cracking Intensity Indicator (FCII) based on the model of Hales and Roering (2007), inspired by the segregation ice-growth hypothesis of Hallet et al. (1991). Because reliable data on soil moisture are very challenging to obtain in marly badlands, we considered, based on the work by Mallet et al. (2018), that the marls fulfil the moisture conditions needed for ice-lens growth during winter. Since we had access to direct soil-temperature measurements at different depths, we used these rather than the diffusive model based on air-temperature developed to predict soil temperatures in the original formulation of Hales and Roering (2007). The soil-temperature gradient was computed between the probes located at 1 cm and 24 cm depth. We summed temperature gradients during all time intervals when the surface temperature (probe at 1-cm depth) was within the frost-cracking window (between -3 and -8 °C) over a winter cycle, and used this number as a proxy for the frost-cracking intensity. Following Anderson et al. (2013), we express the FCII in units of temperature-time/length ($^{\circ}\text{C min}/\text{cm}$ in our case). The probes at 24 cm depth on the north-facing slope did not produce reliable data for almost all years considered; we therefore only computed FCII for the south-facing slope.

The second indicator counts the number of freeze/thaw cycles as a proxy for the efficiency of frost weathering by volume expansion. The raw temperature data include many insignificant temperature fluctuations around 0 °C, over very short periods that do not allow the formation of frost. We therefore applied a time threshold of 1 hour below 0 °C to count a freeze/thaw cycle. The same duration was considered as a threshold for temperature remaining above 0 °C to distinguish two freezing periods. We observed that increasing this threshold to more than 1 hour did not affect the number of freeze/thaw cycles significantly; above this threshold the number of cycles tended toward counting the daily temperature cycles.

The third indicator is the time spent at negative temperatures. We counted the number of 10-minute periods with negative temperature recordings at the 1 cm-depth probe and converted these into hours. Finally, the fourth indicator is the mean negative temperature, which was computed as the mean temperature value when it is below zero, again for the 1 cm-depth probe. The behaviours of these indicators were found to be very different between south-facing and north-facing sites, whereas they did not vary much between uphill and downhill sites. Therefore, we analysed them by averaging the value of the uphill and downhill indicators for each slope aspect. For the 2019-2020 winter season, only a single set of data per slope aspect was available, measured at a mid-slope location, and we use this in addition to the averaged temperature data from before 2019.

I.3.2.3. Uncertainties

We accounted for uncertainty in our analyses using the following procedures. We defined the uncertainty on the sediment-export anomaly resulting from the linear regression between rainfall and sediment export as the 2σ error on the sediment-export values predicted by the regression. Whereas the sediment-export and rainfall measurements are associated with uncertainties themselves, these are insignificant with respect to the uncertainty on the regression and were therefore not included in the analysis. For the temperature indicators, we defined the uncertainty around their mean value by the difference between the value of the indicator obtained at the uphill and downhill location on the same slope (i.e., north-facing versus south-facing).

To establish a relation between sediment-export anomalies and temperature indicators while accounting for these uncertainties in both parameters, we used weighted linear regression with the uncertainty in both independent and dependent variables as (inverse) weights (cf. York et al., 2004). Since a conventional R^2 is invalid in the presence of measurement errors (Cheng et al., 2014), we characterise the quality of the weighted regressions by a weighted correlation coefficient R^2_w computed from the weighted residual ($\text{Var}_{\text{res-w}}$) and weighted total ($\text{Var}_{\text{tot-w}}$) variance ($R^2_w = 1 - (\text{Var}_{\text{res-w}} / \text{Var}_{\text{tot-w}})$). The goodness-of-fit of the weighted correlation is expressed by the weighted sum of deviations from the best-fit line S , normalised by the degrees of freedom ($n-2$): $S_n = S / (n-2)$ (York et al., 2004). We also computed standard R^2 and p-values from an ordinary least-squares linear regression as these are more readily interpreted in terms of significance of the regression. Because of the apparent differences in correlations between the north-facing and south-facing slopes, we analysed correlations for both slope aspects separately.

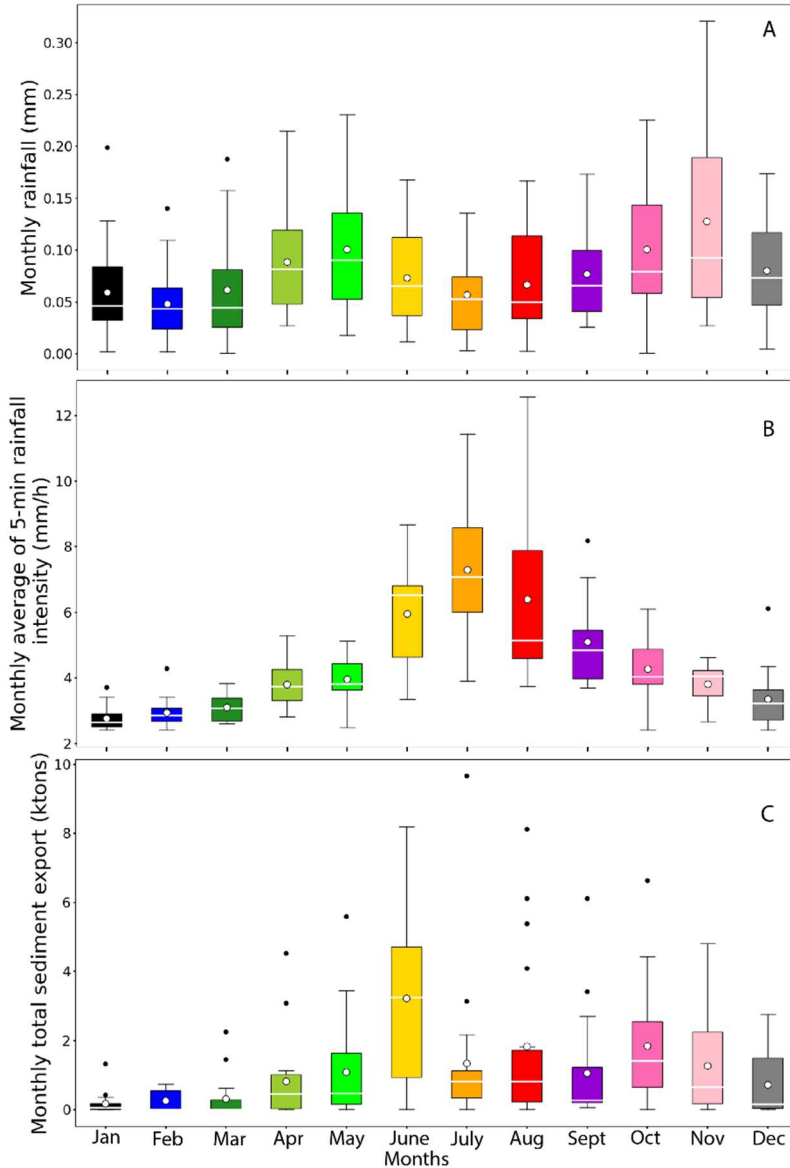


Figure 6: Boxplots of (A) monthly rainfall, B) Monthly average rainfall intensity computed at 5-minute time-steps and C) monthly total sediment export (i.e., bedload + suspended load) of the Laval catchment. White lines show median values and white dots indicate mean values. The first (Q_1 , 25%) and third (Q_3 75%) percentiles are indicated by the box limits, whiskers show $Q_1 - 1.5 \times IQR$ and $Q_3 + 1.5 \times IQR$ (inter-quartile range). Black dots are outlier values (i.e., with values $< Q_1 - 1.5 \times IQR$ or $> Q_3 + 1.5 \times IQR$).

1.4. Results

1.4.1. Seasonal variability in sediment export

Box plots of monthly precipitation, monthly rainfall intensity, and total sediment export (i.e., bedload and suspended load) recorded between 2003 and 2020 show high disparity between monthly averages and significant interannual variation for each month (Figure 6). Median monthly rainfall values are low in winter and summer and peak in spring and autumn, varying from ~ 50 mm in January-March to ~ 100 mm in October-November, with extreme values reaching ~ 300 mm in those months (Figure 6A). In contrast, the monthly average rainfall intensity (Figure 6B) shows a single peak in summer, with median values varying between ~ 2.7 mm/h in January up to ~ 7.5 mm/h in July. Monthly total sediment export also shows two peaks (late spring and autumn), with minimum and maximum values of median sediment export around 0 and 3.6 ktons in January and June, respectively. The variability in monthly total sediment export is high and extreme values reach almost 10 ktons in July.

For all three datasets, (i.e., rainfall, rainfall intensity and sediment export), higher monthly values are associated with higher variability (i.e., values for November, July and June, respectively). For total sediment export, most months show outlier values and distributions are skewed toward high values (mean > median). Rainfall boxplots show a larger spread between the first and third percentiles but more symmetric distributions.

Despite noticeable disparities between years (Figure 6, Appendix 4), mean values highlight a strong seasonal pattern in precipitation, rainfall intensity and sediment export, as previously observed (Mathys et al., 2003; Figure 7). In the Laval catchment, sediment export is low in winter and increases in spring to a peak in June, with an average monthly export of ~3.2 ktons that can be associated with a significant increase in average monthly rainfall intensity (~6 mm/h) (Figure 6B, Figure 7B), despite relatively low total rainfall during that month (<80 mm). Conversely, autumn months (October, November) are characterized by high total rainfall (>100 mm/month) but much lower rainfall intensity (<4.5 mm/h) and sediment export (<1.5 ktons/month). Thus, rainfall intensity appears to play a key role in triggering spring sediment export. Despite their difference in size, the monthly distribution of total sediment export is similar between the Moulin and Laval catchments (Figure 8): both show a major peak in June, amounting to ~20% of total yearly sediment export, with smaller peaks (~10%) in August and October. The monthly rainfall distribution shows a main peak in October-November, with a secondary peak in May. The spring rainfall peak (May) occurs one month earlier than the sediment-export peak (June) for both catchments.

Based on annual data records since 2005 and previous work (see Methods section), we established a correlation between rainfall intensity above a threshold and sediment export (Figure 9). An optimal correlation is obtained for a threshold of 50 mm/h ($R^2 = 0.86$), with most scatter occurring for cumulative rainfall (above threshold) values between 0 and 40 mm. This correlation was used to define the sediment-export anomaly as the residual between observed and predicted annual sediment-export values for each year.

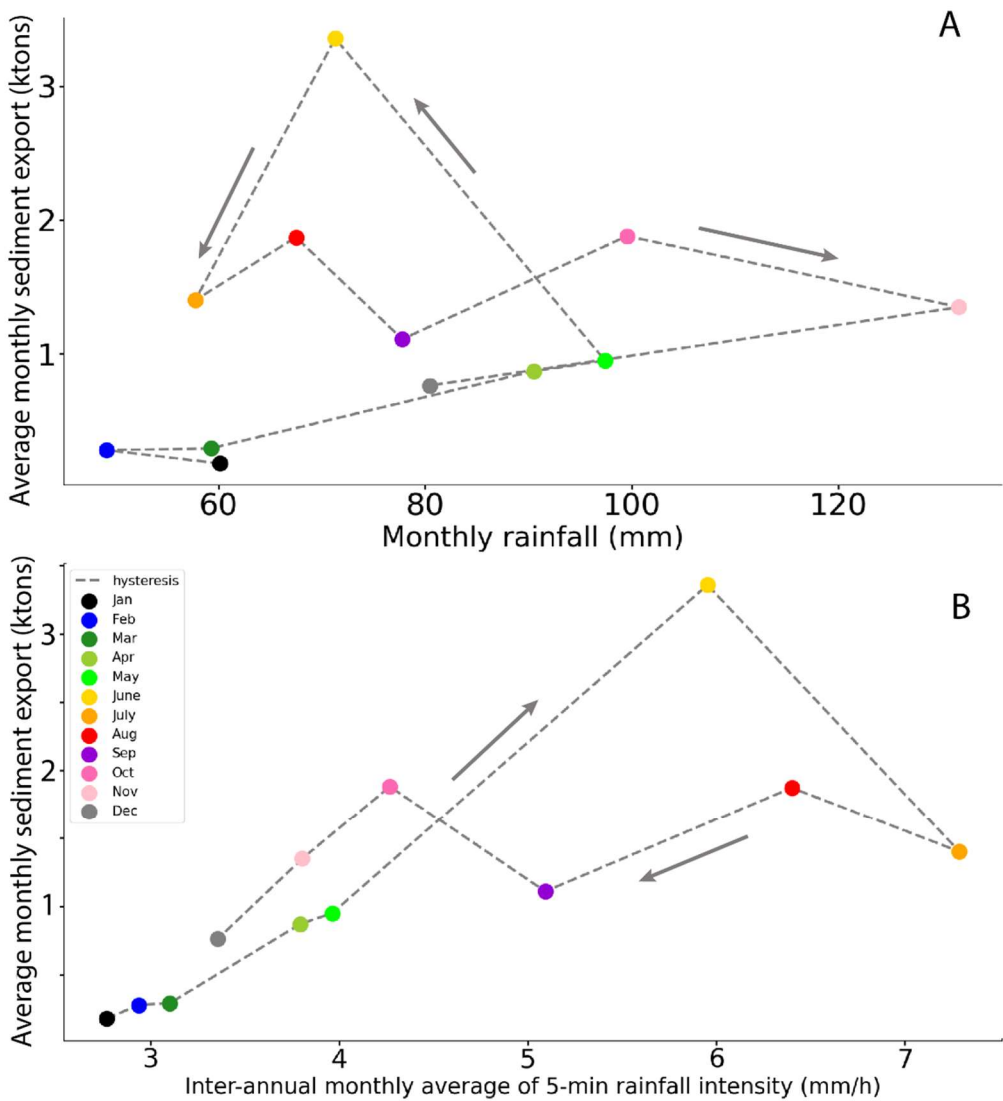


Figure 7: Hysteresis plot using interannual monthly average values from the Laval catchment between 2003 and 2020. (A) Monthly sediment export (ktons) versus monthly rainfall. Dashed line highlights the hysteresis cycle with two separate maxima: high sediment export and moderate rainfall in June versus high total rainfall and moderate sediment export in October/November (B) Monthly sediment export (ktons) versus monthly average rainfall intensity. Dashed line illustrate the hysteresis cycle with a maxima of sediment export in June preceding a stationary period with around 1.5 ktons of sediment export per month between July and November. A plot of all monthly rainfall averages is shown in Supplementary Figure 7.

1.4.2. Potential temperature control on sediment export

Daily temperature fluctuations in the bare marly soils that were monitored are significantly higher for the shallow (-1 cm) than for the deep (-24 cm) sensors (Figure 5). During summer, surface temperatures show a daily variability of ~ 40 °C (between $\sim 10\text{--}15$ °C at night and $\sim 50\text{--}55$ °C at midday), whereas the daily variability in winter averages around 20 to 30 °C depending on aspect. These daily variabilities decrease drastically with depth, fluctuating generally within 5 °C and 20 °C for the probes at -24 cm and -12 cm depth respectively, but can occasionally be

higher. The maximum daily temperature is reached asynchronously according to the exposure; in the north-facing hillslope, maximum temperature occurs in the morning (around 10 am), whereas in the south-facing slope it occurs late in the afternoon (around 4 pm). At the maximum depth (-24 cm), minimum soil temperatures during winter are negative on the north-facing slope but positive on the south-facing slope.

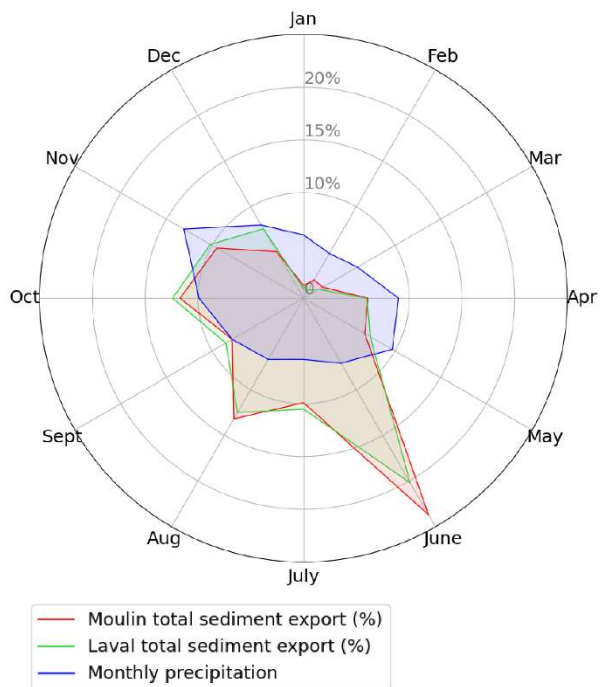


Figure 8: Comparison of the relative distribution of monthly sediment export for the Laval and Moulin catchments, together with relative monthly rainfall distribution.

with the other temperature indicators. Time below 0 °C is also strongly correlated with the number of freeze-thaw cycles / year ($R = 0.90$) on the south-facing slope. All of the correlations between temperature indicators are significant ($p < 0.05$) on the south-facing slope. On the north-facing slope, in contrast, no significant correlations between temperature indicators were found. Sediment-export anomalies correlate most strongly with frost-cracking intensity on the south-facing slopes ($R = 0.87$) but are also significantly correlated with time below 0 °C ($R = 0.77$). On the north-facing slope, the only significant correlation occurs between sediment-export anomaly and time below 0 °C ($R = 0.75$), but note that frost-cracking intensity was not calculated on the north-facing slope.

These correlation results led us to investigate how much of the variability in sediment-export anomalies can be explained by these different temperature indicators, taking into account the uncertainties on both measures (Figure 11, Figure 12). Results show that the weighted regression between frost-cracking intensity and sediment-export anomalies can explain 47% of the variance in the latter ($R_w^2 = 0.52$). The ordinary least-squares (OLS; i.e., unweighted) correlation is significant ($p = 0.005$) and only slightly deviates from the weighted regression (Figure 11). Based on this trend, the highest sediment-export anomalies appear to occur in years succeeding winters with strong (negative) frost-cracking intensity.

We calculated four different temperature indicators during the winter months, as explained in section 3.2.2, and compared these with each other as well as with the sediment-export anomaly obtained previously, in order to (1) assess the degree of co-variation between the different indicators, and (2) characterize the direction and strength of the relationship between the temperature indicators and the sediment-export anomaly. Overall, stronger correlations were found between temperature indicators on the south-facing slope than on the north-facing slope (Figure 10). Frost-cracking intensity, which was only computed on the south-facing slope, correlates strongly ($|R| > 0.67$)

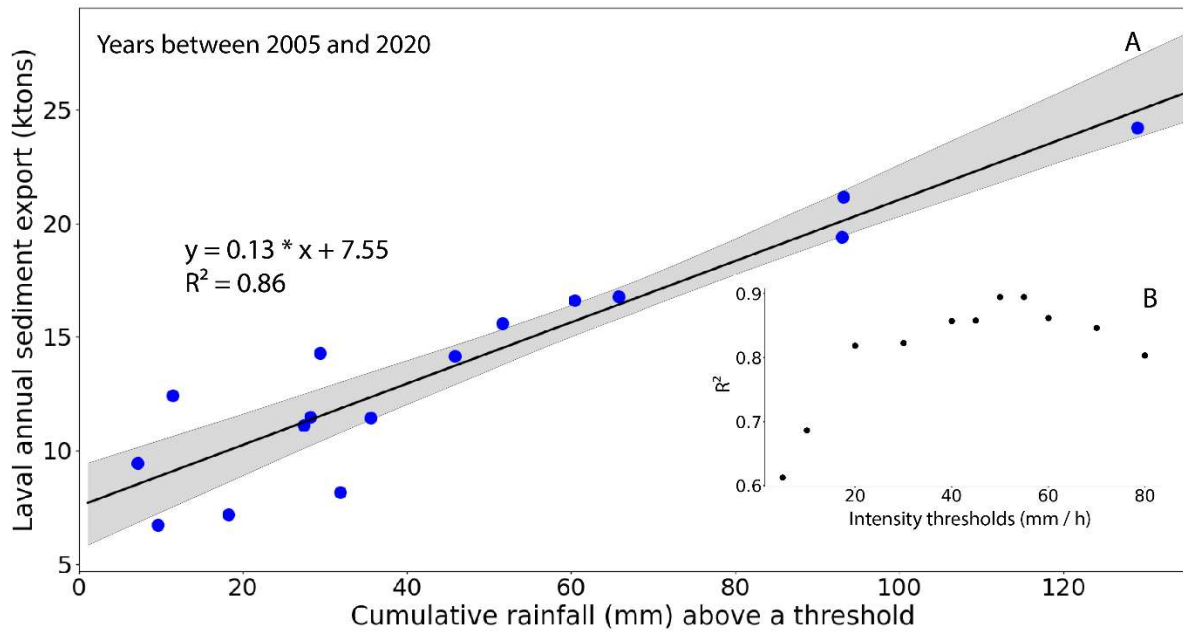


Figure 9: (A) Linear correlation between annual total sediment export from the Laval catchment and the cumulative rainfall above an instantaneous intensity threshold of 50 mm/h for the years 2005 to 2020 (blue dots). Regression line is in black; grey shaded area shows 95% confidence interval. Most outliers occur for low cumulative rainfall above the threshold (< 40 mm). (B) Coefficient of determination (R^2) between annual sediment export and annual rainfall above threshold for different intensity thresholds. Optimum correlations are found for threshold values between 50 and 55 mm/h.

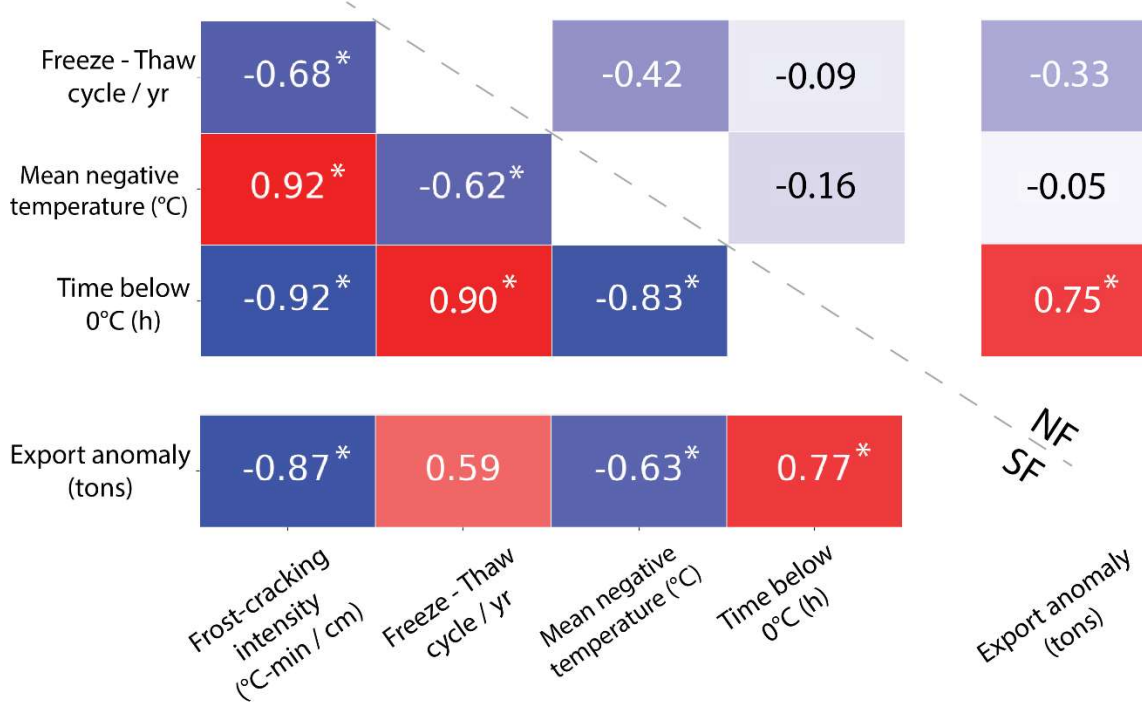


Figure 10: Correlation matrix between different soil-temperature indicators computed from all data points (using both uphill and downhill locations on the same slope); and between soil-temperature indicators and sediment-export anomaly (calculated using averages between uphill and downhill locations from the same slope). Lower-left and upper-right parts of the table report correlations for south-facing (SF) and north-facing (NF) slopes, respectively (note that frost-cracking intensity was not calculated for north-facing slopes; see text). Blue boxes show negative correlations and red boxes show positive correlations; values indicate correlation coefficient R and stars (*) indicate significant correlations (i.e., $p < 0.05$).

A significant positive relationship is also found between sediment-export anomalies and time below 0 °C on both the south-facing ($R_w^2 = 0.77$) and north-facing ($R_w^2 = 0.51$) slopes (Figure 12). In contrast, regressions between sediment-export anomalies and either the number of freeze-thaw cycles / year or the mean negative temperature are not significant on either slope and show an opposite trend between slopes (i.e., a positive correlation on one slope and negative on the other; Figure 12). This analysis suggests that both the frost-cracking intensity (where it can be calculated) and the time spent below 0 °C in a particular winter, which are strongly correlated (Figure 10, Appendix 5) are good predictors of sediment-export anomalies (deviations from sediment export predicted by rainfall over a threshold) in the following year.

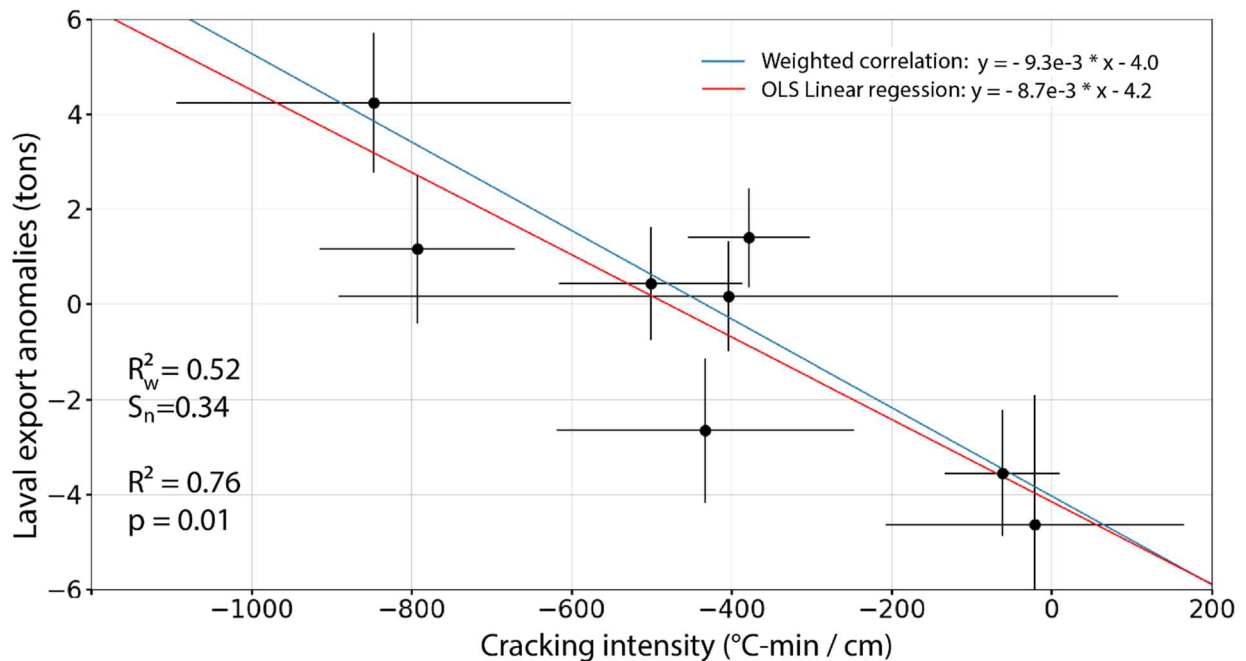


Figure 11: Regression analysis between sediment-export anomalies and frost-cracking intensity on the south-facing slope for the years 2007 - 2010, 2014, 2015, 2017 and 2020. Horizontal error bars refer to the difference between measurements at uphill and downhill locations (temperature measurements for 2017 were only available for the downhill location, thus uncertainty on frost-cracking intensity was computed as the average of the uncertainties from the others years); vertical error bars are $\pm 2\sigma$ uncertainty in export anomaly. Red line shows ordinary least-squares (OLS) linear regression; blue line shows weighted linear regression following York et al. (2004). Weighted determination coefficients R_w^2 and associated normalized goodness-of-fit indicator $S_n = S / (n-2)$ are indicated for the weighted regression. Standard R^2 and associated p -value indicate significance of the ordinary least-squares (unweighted) regression.

1.5. Discussion

1.5.1. Limitations of our study

Because of the strong annual and inter-annual variability in regolith cover and sediment export, long-term field measurements at high spatial and temporal resolution are required to characterise the dynamics of badland erosion. The Draix-Bléone CZO provides one of the few localities worldwide where such records exist. Similar datasets have been collected in the Araguas and Vallcebre basins of (Northern Spain) but cover significantly shorter periods (6-18 months; Regués et al, 1995; Regués and Nadal-Romero, 2013). However, uncertainties in both sediment-yield records and soil-temperature measurements are inevitable and difficult to estimate.

The interpretation of the hysteresis cycle (Figure 7) should integrate the variability in sediment export (Figure 6C). Although June shows the highest sediment export overall, this month is also characterised by the highest inter-annual variability in sediment export. This variability can be explained by the stochastic nature of precipitation, which occurs mainly due to storms during the spring and summer seasons. Thus, sediment-export values for June vary between 0 (no large rainfall events during the month) up to 8000 tons. The monthly data show that the highest sediment export can also occur in July (and more rarely in August) in some years. In order to smooth out such stochastic behaviour, we integrated sediment-export values over the full year following each investigated winter season.

The export-anomaly values that we computed are dependent on the linear regression with rainfall above a threshold (Section 1.3.1; Figure 6). Extreme values, such as the three years with >70 mm or more rainfall above the 50 mm/h threshold, have an important impact on the regression and thus on the export-anomaly values. Calculating uncertainties on the annual sediment export is challenging, but an order of magnitude of around 10% of the total sediment export can be estimated. This uncertainty is negligible compared to the uncertainties on sediment-export anomalies that we infer from the regression analysis. The uncertainty on annual rainfall is also considered negligible.

Soil-temperature probes have proven very difficult to maintain at the depths where they were installed in the soft, mobile marls of our study area. For this reason, we could only calculate frost-cracking intensity (which requires concomitant data from the -1 cm- and -24 cm-depth probes) for the south-facing slope and for only 7 years between 2005 and 2019 (Figure 11). We therefore searched for a temperature proxy that allows predicting frost-weathering intensity with less constraints on the data, and found that the time spent below 0 °C (for the -1 cm-depth probe) can be a useful indicator.

When assessing the predictive power of the different temperature indicators to explain sediment-export anomalies, we aimed to take into account the uncertainties in both variables (Figure 11, Figure 12) by employing weighted regression based on uncertainties (York et al., 2004). However, the uncertainties in temperature indicator values were computed from only two points, i.e., the measurements at the uphill and downhill locations of each slope aspect. Uncertainties on both variables should also be of the same order of magnitude to avoid biasing the weighted regression, whereas in our case, the relative uncertainties in the temperature indicators can be much larger than those in the sediment-export anomalies. For this reason, we also report the ordinary least-squares regression and associated significance (*p*-value).

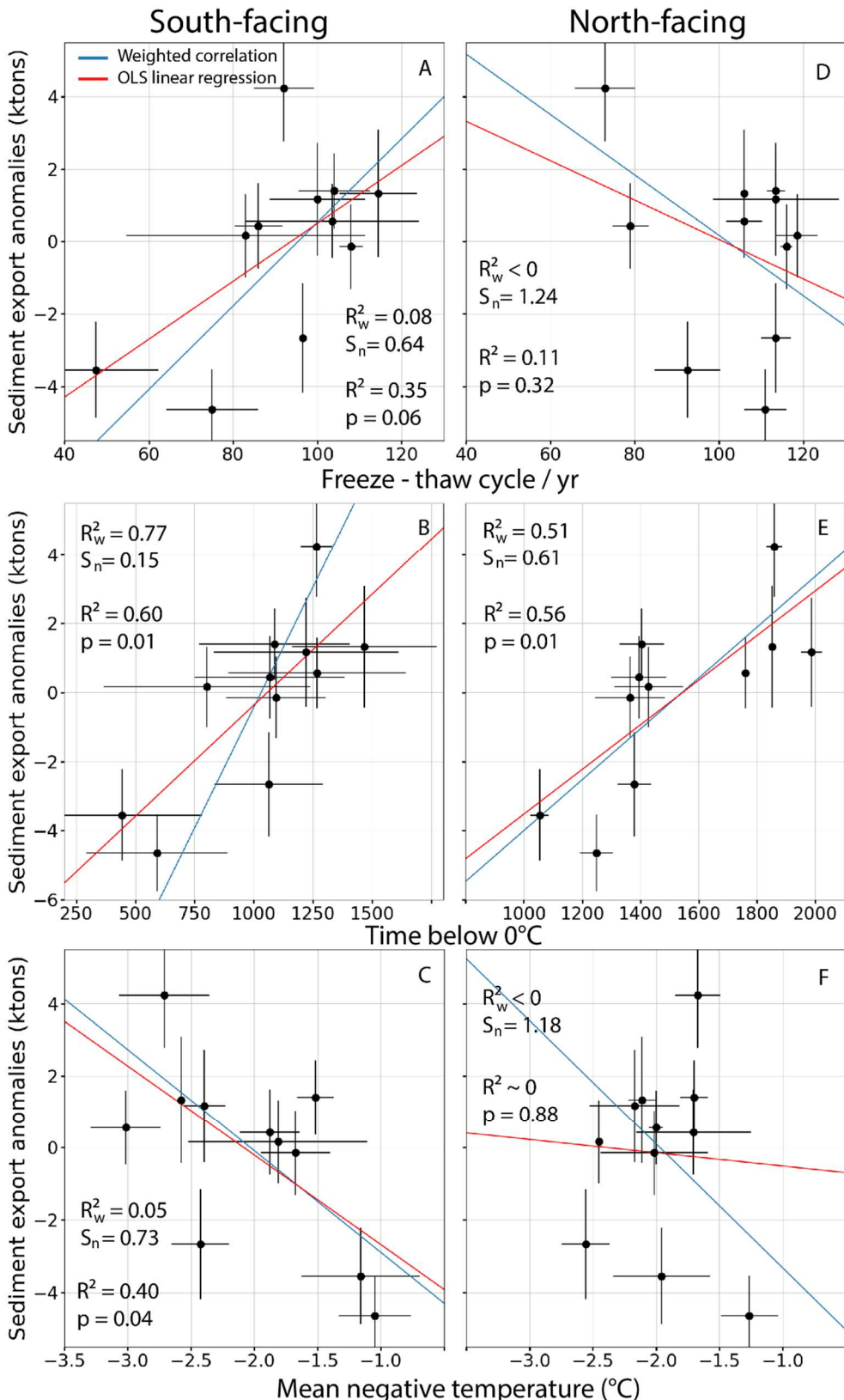


Figure 12: Linear regression analysis between sediment-export anomalies and (A, D) number of freeze-thaw cycles per year; (B, E) time spent below 0 °C; and (C, F) mean negative temperature. Left column shows regressions for south-facing slope and right column for north-facing slope. Error bars and red and blue regression lines are as in Figure 11. Weighted determination coefficients R_w^2 and associated normalized goodness of fit indicators S_n are indicated for each weighted regression. Standard R^2 and associated p -value indicate significance of the ordinary least-squares (unweighted) regressions.

1.5.2. Significance of the observed hysteresis cycle

Numerous studies have reported annual hysteresis cycles between rainfall or discharge on one hand, and sediment export on the other; these studies have commonly focused on large catchments, e.g. in the Andes or Himalaya (e.g., Andermann et al., 2012; Armijos et al., 2013; Tolorza et al., 2014; Li et al., 2021). For such large catchments, the annual hysteresis cycle is explained by the role of subsurface water storage (Andermann et al., 2012), dilution effects (Armijos et al., 2013) or variations in the contributive erosive area (Li et al., 2021). Hysteresis cycles for smaller catchments have generally been analyzed at the event scale, and have been interpreted in terms of the proximity of sediment sources and the spatio-temporal heterogeneity of rainfall (e.g., Klein, 1984; Buendia et al., 2016). More directly comparable to our results, several studies have been carried out in small ($< 15 \text{ km}^2$) Mediterranean badland catchments where climate can vary between arid to humid conditions. Llena et al. (2021) reported a seasonal sediment dynamic with lags between sediment production and sediment yield and highlighted the role of the channel network in the sediment transfer. Several catchments in Northern Spain that are very similar in size and lithology to our study site have been well studied and suspended sediment transport processes have been reconstructed at the event (Nadal-Romero et al., 2008; Soler et al., 2008) and seasonal scale (Nadal-Romero & Regués, 2010). Counter-clockwise and clockwise hysteresis loops in these catchments are associated to dry and wet seasons, respectively, and are inferred to be driven by infiltration and saturation processes on hillslopes.

The annual hysteresis cycle between rainfall amount and sediment export observed in the Draix-Bléone CZO (Figure 7A) presents two loops with successively anti-clockwise and clockwise patterns, reflecting the rapid seasonal changes in erosion regime in these badlands. We interpret the initial anti-clockwise hysteresis loop, with sediment export lagging behind precipitation in the first half of the year, to be due to the threshold in rainfall intensity required to generate erosion. The analysis of the annual hysteresis cycle between monthly average rainfall intensity and sediment export confirmed this interpretation; it is only with the high-intensity storms of late spring/early summer (June) that significant amounts of sediment are exported from the catchment (Figure 7B). The initial anti-clockwise hysteresis loop of Figure 7A thus indicates transport-limited conditions. In contrast, the clockwise loop characterising the second half of the year indicates supply-limited conditions, with the supply of mobile sediments running out after summer (Bechet et al., 2016). The hysteresis cycle between average rainfall intensity and sediment export highlights this lack of sediment supply during the summer: the mean rainfall intensity peak (July) lags behind sediment- export peak (June) and sediment export between July and October is steady at a lower value than the first half of the year (around 1.5 ktons per month), independently of rainfall intensity. A similar trend appears in the Moulin catchment, despite its much smaller catchment area (Figure 8). This seasonal pattern does not seem to change with recent climatic variations because it was already reported by Mathys et al. (2003), who analysed the seasonality of bedload yield based on Draix-Bléone observatory data between 1985 and 2003.

The annual pattern that we describe in Figure 7A characterizes the total sediment export, which is the sum of the suspended sediment and bedload yield. According to the observations of Mathys et al. (2006) and Liébault, 2017, highest export values for bedload occur during autumn. However, this trend is modified when adding the suspended load because the exported suspended-sediment mass can be up to four times higher than bedload-sediment mass during spring. A similar ratio has been observed in other catchments (Lana-Renault &

Regués, 2007; Rainato et al., 2017) and leads to the present result where late spring/early summer (more specifically, June) is the period that contributes most to the total sediment yield. Thus, sediment dynamics vary according to grain size: intense precipitation events during late spring/early summer mobilise the regolith produced during the winter, and suspended sediments are transported almost directly from the hillslopes to the catchment outlet. In contrast, coarser bedload sediments are deposited in gullies during these short intense events and are only exported by the lower-intensity but longer-duration rainfall events of the late summer and autumn (Figure 7). These dynamics suggest that suspended sediment storage is almost non-existent in the Moulin and Laval catchments, whereas bedload sediment can be stored for several months.

1.5.3. Frost weathering as a major control on sediment production in the Draix-Bléone CZO

The significant correlations between frost-cracking intensity or time below 0 °C and sediment-export anomalies imply that frost-weathering processes constitute a major secondary control on sediment export. While the main control on the yearly amount of sediment exported from the studied catchments is exerted by rainfall above a threshold (Figure 9), the efficiency of frost-weathering processes during the preceding winter, as expressed by the frost-cracking intensity indicator or the time below 0 °C, can explain about half of the residual from this trend (Figure 11, Figure 12). Together with the evidence for a transition from transport-limited to supply-limited conditions during the year discussed above, we interpret these results as indicating that frost-weathering processes modulate sediment export from the catchments by exerting a strong control on the production of mobilizable sediment. In particular, the lack of sediment supply during summer months inferred in the previous section argues against significant sediment production by solar-induced thermal stresses (e.g., Eppes et al., 2016), despite high daytime surface temperatures and large temperature variations in the marls during summer (Appendice 1).

These findings are consistent with those of Rengers et al. (2020), who found a strong positive correlation between the time spent in the frost-cracking window and sediment production feeding debris-flow channels on a small, steep plot in the Rocky Mountains of Colorado. The similar results between both studies, despite differing scales, lithologies and geomorphic settings, attest to the potential widespread control of frost-weathering processes on sediment production. Additionally, our results like those of Rengers et al. (2020) show a weak correlation between sediment production and the number of freeze-thaw cycles per year. As discussed in the introduction, freeze-thaw cycles are associated with volumetric expansion of ice, whereas frost-cracking is related to ice segregation. Thus, the migration of liquid water to loci of ice-lens growth appears to be a more efficient process of soil weathering than volumetric expansion, even in this temperate and moderate-elevation environment. Nadal-Romero et al. (2007) similarly concluded that frost-weathering processes play an important role in weathering of marly badlands in northern Spain; they also demonstrated significant variations between north-facing versus south-facing slopes. However, Nadal-Romero et al. (2007) focused their attention on freeze-thaw cycles and did not investigate frost-cracking, the quantification of which requires more data. Nonetheless, our studies concur in underlining the influence of frost-weathering processes on regolith development as well as important spatial variations between north- and south-facing slopes, supporting the theoretical predictions of Anderson et al. (2013).

Directly quantifying frost-cracking intensity (rather than inferring it from atmospheric temperature data) requires dense and high-quality field data, in particular concomitant soil-temperature data at multiple depths to quantify thermal gradients. Even in permanently monitored long-term observatories such as Draix-Bléone, such data may be rare. However, our study suggests that the time spent below 0°C, which correlates well with the frost-cracking intensity (Figure 10; Appendix 5), may be used as a simpler proxy to predict frost-weathering intensity. Our weighted regressions show that this indicator correlates well with the sediment export anomaly and captures the effect of frost-weathering processes on sediment production, even though uncertainties in the regression can be significant (in particular on the south-facing slope in our case). In contrast, neither the mean negative temperature nor the number of freeze-thaw cycles appear as reliable proxies to estimate frost weathering in this setting.

These correlations between sediment production computed during a winter season and sediment yield for the directly following year (spring to autumn), together with the strongly varying dynamics of transport during the year discussed in the previous section, favour the hypothesis of rapid sediment export from the studied catchments, in contrast to the 3-year residence time of sediments in these catchments inferred by Jantzi et al. (2017). In order to test this hypothesis, we performed correlations between the frost-cracking intensity in a particular winter season and the sediment-export anomaly of the first, second and third year after that season (i.e., in the last case, if we consider the 2006-2007 winter season for the frost-cracking intensity, we compare it to the sediment-export anomaly for 2010). In all configurations, the correlation is weaker than the direct annual correlation that we observed ($R^2 = 0.76$) and the correlation weakens with increasing residence time (Appendice 6); correlations for the years $n+2$ and $n+3$ are not significant. The ratio observed in sediment distribution during the spring/summer (74% suspended load / 26% bedload) and the rapid export of these fine sediments probably make the suspended load invisible in the estimation of sediment storage in the catchment, rendering the calculation of residence time complex. Thus, it appears that the Laval catchment has an efficient drainage system, with high connectivity and low sediment storage, which does not contribute significantly to the production / export balance. Similar short residence times have been observed, at a different scale, in a similar environment in northern Spain (Andres Lopez-Tarazon et al., 2011).

1.5.4. Implications for the erosional response to climate change

Due to their limited vegetation cover and soft lithology, badlands are sensitive areas that are directly exposed to climatic parameters and thus will respond quickly to even small climatic variations (e.g., Clarke and Rendell, 2010). In the context of anthropogenic climate change, weathering or erosion processes and hydrology will necessarily be modified: a positive or negative variation of one of these main operating processes could be balanced against others but could also be additive, thereby inducing important changes in morphology and sediment export in these landscapes.

Based on a review of multiple badland areas in the Mediterranean region, Nadal-Romero et al. (2021) have recently investigated the impact of climate change on these particular landscapes, taking into account different climatic drivers (rainfall amount, rainfall intensity, wetting-drying cycles, freeze-thaw cycles, soil moisture content, etc.). Their analysis predicts that for wet badlands such as Draix-Bléone, the expected increase in rainfall intensity should

increase erosion capacity on one hand, but that the expected increase in temperature should lower the number of freeze-thaw cycles, thereby reducing the efficacy of frost-weathering processes and decreasing sediment availability on the other hand. Considering the result from our study that frost-cracking intensity, and not freeze-thaw cycles, is the best indicator for sediment production by frost-weathering processes, the frost intensity rather than the number of frost days should present a better proxy to predict the evolution of sediment availability. However, the time spent below 0°C, identified here as a simple alternative proxy for frost-weathering intensity, will also be directly affected by an increase in temperature and similarly lead to a decrease in sediment production in a warming climate.

Recently, Hirschberg et al. (2021) have also shown that projected changes in precipitation and air temperature would lead to a reduction in both sediment yield and debris-flow activity in an Alpine catchment at moderate elevation (< 2000 m), because of the reduction in frost-weathering intensity. In general, expected changes in sediment production in temperate regions under a warming climate appear to have a counter-effect to the predicted increase in average rainfall amounts and intensities, which have been considered as “the most direct factors controlling erosional changes under climate changes” (Nearing et al., 2004). This complex interaction between sediment production and sediment transport underlines the necessity to account for the processes responsible for sediment production in longer-term predictions of sediment yield.

Finally, in addition to physical weathering processes that are discussed here, chemical and biological weathering processes also play an important role in rock weathering and will also be affected by precipitation and temperature changes (e.g., Brantley et al., 2011; Soulet et al., 2021). Additionally, erosion processes could be impacted by changes in the vegetation but these interactions are particularly complex to understand (Nearing et al., 2004). Therefore, climatic variations may change the balance between weathering and erosional processes as well as their timing, leading to complex positive or negative feedbacks on catchment erosion that remain difficult to predict.

I.6. Conclusions

Based on our analysis of sediment-yield records and soil-temperature data from the Draix-Bléone CZO and accounting for the inevitable uncertainties in our dataset, we show that frost-weathering processes modulate sediment export by controlling sediment production in these marly catchments. Our main conclusions are summarized below:

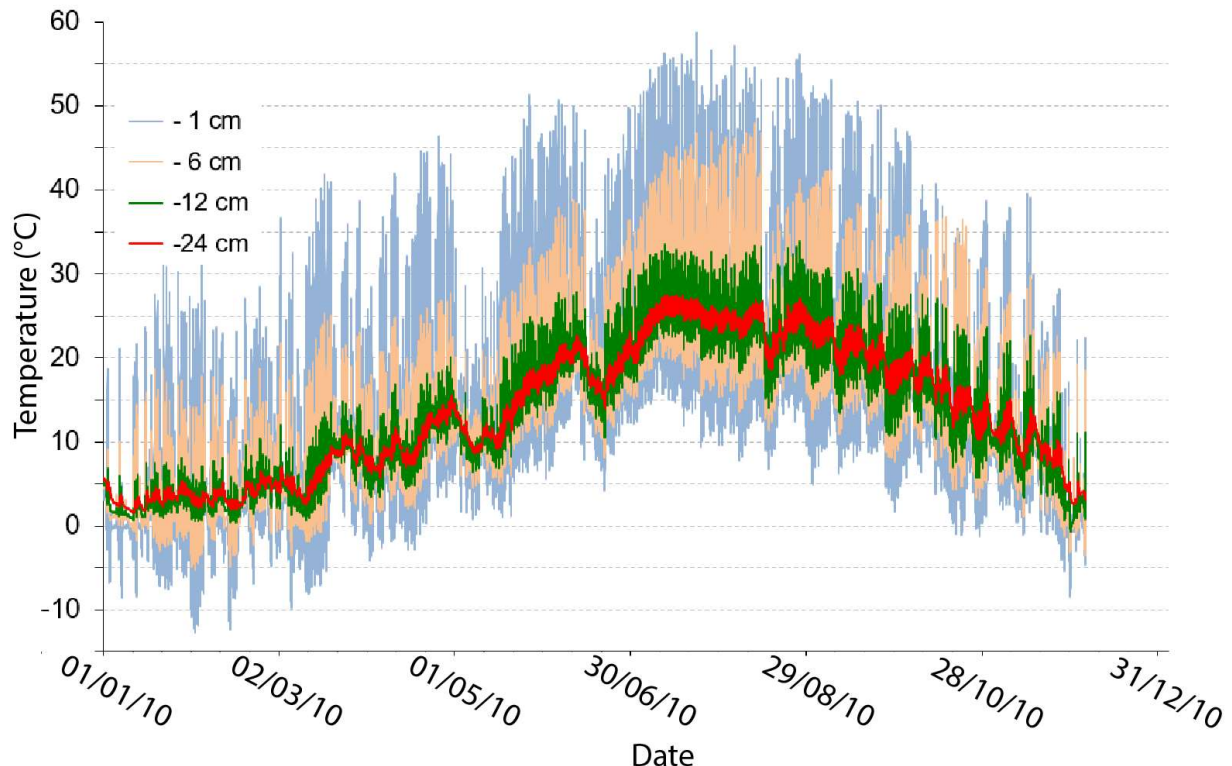
- Monthly total sediment export (suspended load and bedload) is highly variable and shows a seasonal pattern. The annual hysteresis cycle (Figure 7) shows an anti-clockwise pattern in the first half of the year (February-July), and a clockwise pattern later in the year (August-December), suggesting a spring / early summer transport-limited regime followed by a supply-limited regime during late summer and autumn in these catchments.
- Total annual sediment export is well correlated with rainfall above an intensity threshold; a threshold of 50 mm/h maximises the correlation (Figure 9).
- The frost-cracking intensity indicator, calculated following the Hales and Roering (2007) model, explains about half of the sediment-export anomaly (Figure 10), implying that the process of frost weathering through ice segregation strongly controls regolith production and modulates sediment export.
- The time spent below 0°C is an easier to measure and simpler proxy, and is also an indicator of frost-weathering intensity that correlates well with the sediment export anomaly (Figure 10). In contrast, neither the number of freeze-thaw cycles nor the average negative temperature during a winter season show significant correlations with sediment-export anomalies.
- South- and north-facing slopes show distinct behaviour with respect to frost-weathering processes, confirming observations from previous studies.
- Frost-weathering processes should be taken into account when building predictive models of sediment export under a changing climate. Under a warming climate, frost weathering should become less important, counteracting the increased sediment export expected from a stormier climate.

The long-term monitoring records available for the Draix-Bléone CZO catchments have allowed identifying frost-cracking by ice segregation as a major control on sediment production. Further assessment of the importance of this process would require similar studies in different environments (e.g., drier climates, more vegetated areas, higher elevation, etc.) and at different catchments scales. Field measurements of sediment export and soil-temperature are ongoing in the Draix-Bléone observatory and additional data could be incorporated to the present results in the next few years. In a context of global climate change, future measurements might illustrate the consequences of climate variations at human timescales on processes in the critical zone.

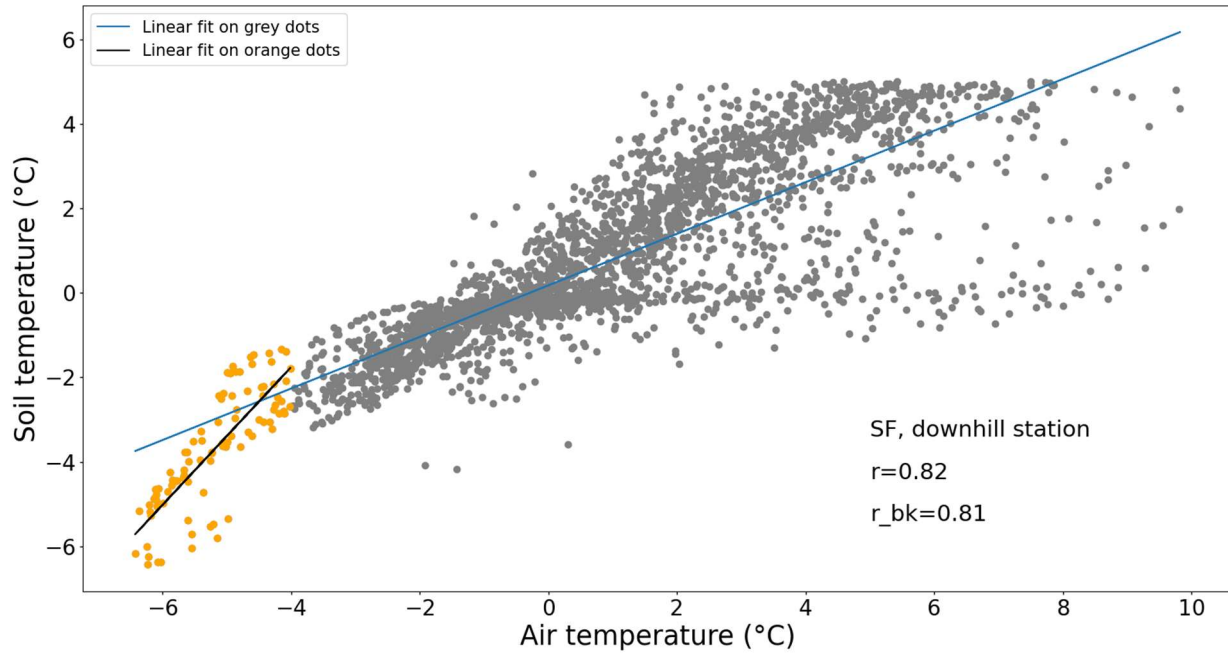
Appendices Chapter I

Depth of probes	Full winter period used in the analysis	Aspects	Hill location	Reconstructed periods
-1	2006/2007, 2007/2008, 2008/2009, 2009/2010, 2011/2012, 2012/2013, 2013/2014, 2015/2016, 2016/2017, 2019/2020	South-facing and North-facing	Uphill and Downhill	<p>2011/2012 SF uphill: 24/12 6h30 to 31/12 23h50</p> <p>2011/2012 all: 12/03 2h20 to 26/03 12h40</p> <p>2014-2015 SF: 7/12 11h10 to 11/12 18h30</p> <p>2015/2016 all: 4/11 18h00 to 7/11 8h40, 21/11 00h00 to 14/12 15h20, 27/12 4h00 to 29/12 18h20, 01/01 19h10 to 5/01 23h50</p>
-24	2006/2007, 2007/2008, 2008/2009, 2009/2010, 2013/2014, 2014/2015, 2016/2017, 2019/2020	South-facing only	Uphill (except for 2016/2017) and Downhill	No reconstruction possible

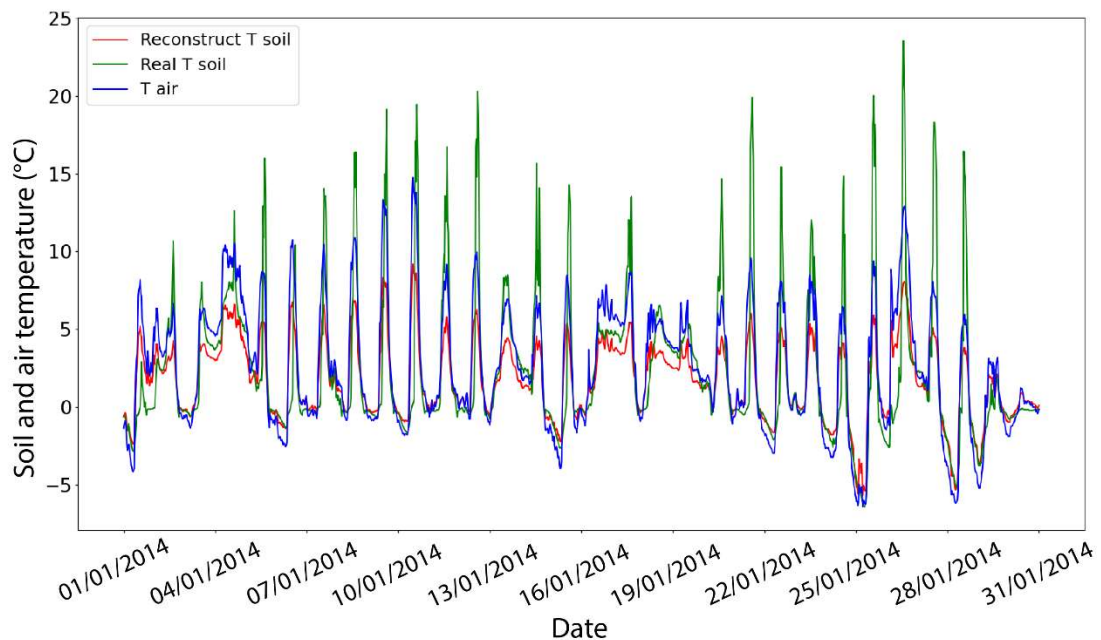
Appendice Table 1: Information about temperature dataset available between 2006 and 2020.



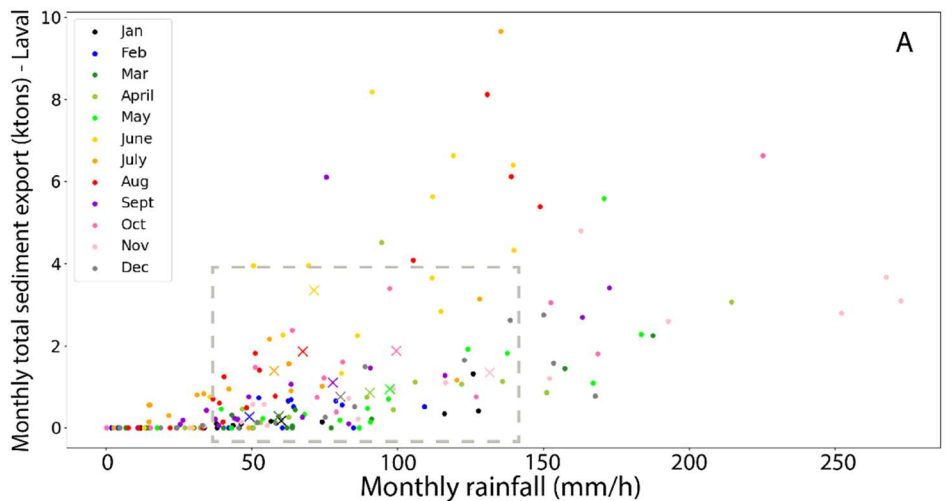
Appendice 1: Annual time series of raw temperature data from four different depth probes.



Appendice 2: Correlation between soil and air temperature measurements on south-facing slope (SF) downhill station between 01/01/2014 and 31/03/2014. Since we are interested in frost weathering, temperatures were cut off at 5 $^{\circ}\text{C}$ for soil temperature and 10 $^{\circ}\text{C}$ for air temperature. We note a two-tier linear relationship between soil and air temperatures, with a steeper correlation for very low air temperatures. We therefore set a threshold for air temperature (-4 $^{\circ}\text{C}$) and regress the data above and below that threshold separately (grey / orange dots and blue / black lines, respectively; correlation coefficients r and r_{bk} for the higher- and lower-temperature regressions are indicated). The threshold was determined independently for every year where temperatures needed to be reconstructed. Dots aligned along 0 \square soil temperature record snow cover; Such snow-cover periods were avoided as much as possible when determining the linear regression parameters.

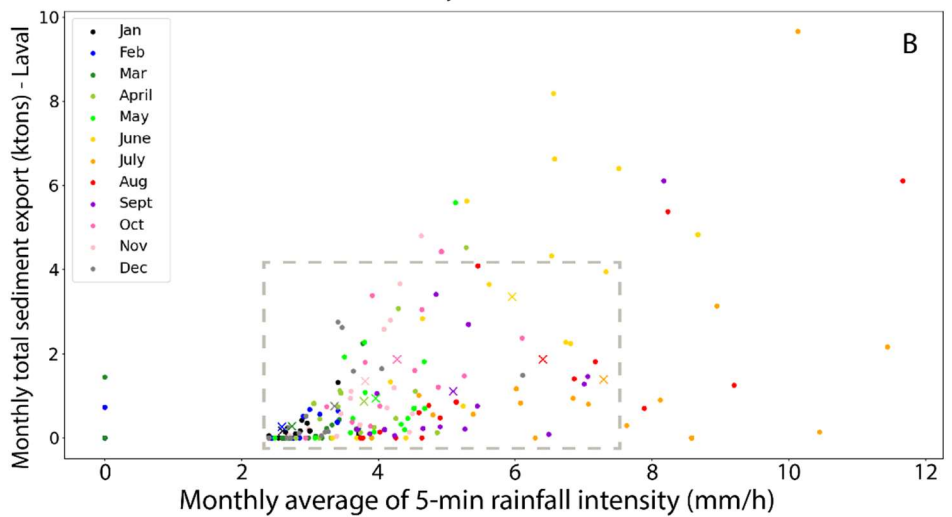


Appendice 3: Comparison of measured soil temperatures (green line) and reconstructed temperatures (red line) for a complete temperature series (January 2014). Note that the model is only calibrated for soil temperatures $< 5 ^{\circ}\text{C}$ (Supplementary Figure 2). Air temperature is also shown (in blue).

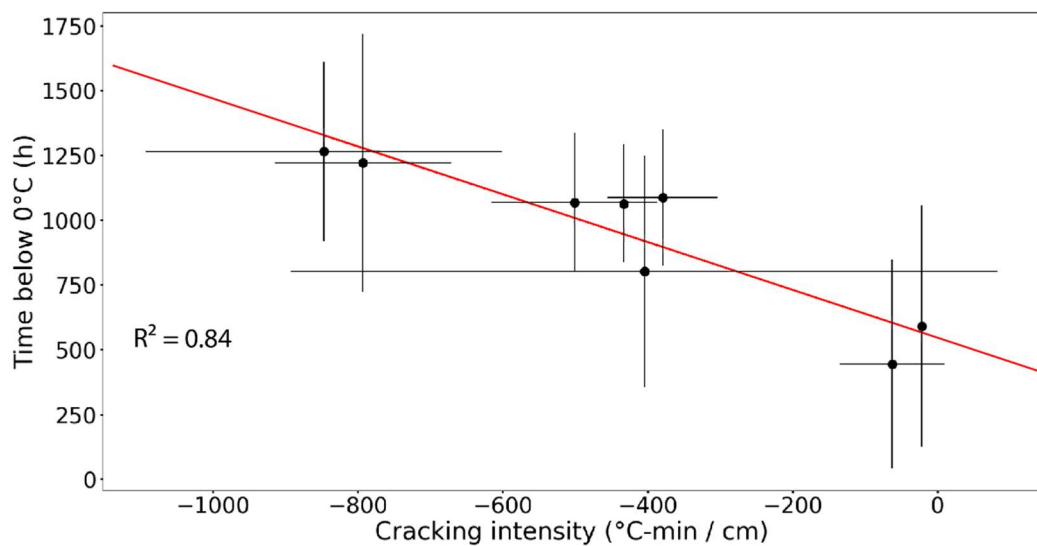


A

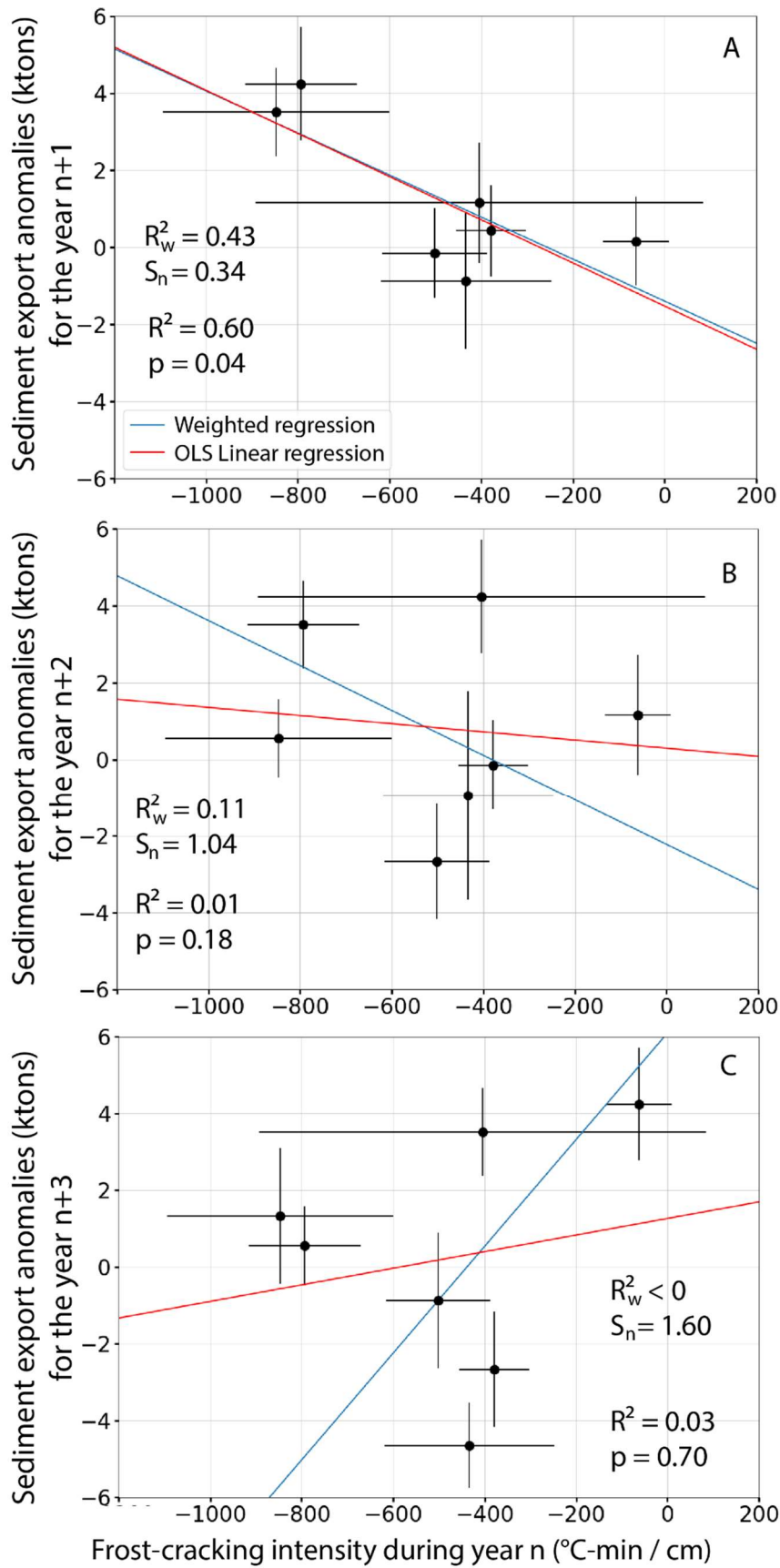
Appendice 4: Monthly sediment export (ktons) from the Laval catchment versus (A) monthly rainfall between 2003 and 2020. (B) Monthly average of 5-min rainfall intensity (mm/h). Dots are individual values for each month and crosses are interannual monthly averages over the analysed period. Dashed boxes show limits of Figure 4A, B.



B



Appendice 5: Regression analysis between frost-cracking intensity and the time below 0°C, the two temperature indicators that best predict the sediment export anomaly (Fig.7). Horizontal and vertical error bars refer to the difference between measurements at uphill and downhill locations (temperature measurements for 2017 and 2019 were only available for the downhill location; for these years the average difference for the other years was taken). Red line shows ordinary least-squares (OLS) linear regression giving a coefficient of determination $R^2 = 0.84$.



Appendice 6: Regression analysis between frost-cracking intensity on the south-facing slope for the years ($n =$) 2007 - 2010, 2014, 2015 and 2017 and the sediment-export anomalies of A) the year $n+1$, B) the year $n+2$, C) the year $n+3$ (See text for explanation). Horizontal error bars refer to the difference between measurements at uphill and downhill locations (temperature measurements for 2017 were only available for the downhill location, thus uncertainty on frost-cracking intensity was computed as the average of the uncertainties from the others years); vertical error bars are $\pm 2\sigma$ uncertainty in export anomaly. Red line shows ordinary least-squares (OLS) linear regression whereas blue line shows weighted linear regression following York et al. (2004). Weighted determination coefficients R^2_w and associated normalized goodness-of-fit indicator $S_n = S / (n-2)$ are indicated for the weighted regression. Standard R^2 and associated p -value indicate significance of the ordinary least-squares (unweighted) regression.

Chapter II

Seasonal dynamics of marly badlands illustrated by field records of hillslope regolith properties, Draix-Bléone CZO, SE France.

Ariagno, C., Pasquet, S., Le Bouteiller, C., van der Beek, P., & Klotz, S., in review. Seasonal dynamics of marly badlands illustrated by field records of hillslope regolith properties, Draix-Bléone CZO, SE France. *Earth Surfaces Processes and Landforms*

Abstract: Sparsely vegetated badlands are loci of intense erosion that is sufficiently rapid to have observable effects on human timescales. Characterizing and understanding the physical weathering processes in these settings are key to predict the temporal variability of regolith production and sediment flux, as well as their evolution under changing climate conditions. Here, we study intra-annual changes of hillslope properties and explore the relationship between production and transport of sediments in steep marly badland catchments of the Draix-Bléone Critical Zone Observatory (SE France), where decades-long monitoring records show rapid morphologic changes. There is evidence for seasonal dynamics of these badlands, but characterization and quantification of physical weathering processes have been lacking up to now. We explore this gap by monitoring key regolith parameters including grain size distribution (GSD), surface resistance, and water content in the regolith layer (surface to ~10 cm depth) at different locations, through repeated field surveys over a 2.5-year period. While water content appears to be directly controlled by the last previous rainfall event, the cyclic annual pattern in observed D50 suggests that loose and finely fragmented regolith is mainly produced and accumulates during the winter season, whereas sediment transport is dominant during spring-summer. This dynamic reduces regolith thickness and induces coarsening of hillslope surface material between early spring and autumn. Principal component analysis (PCA) highlights the strong correlation between resistance and GSD (characterized by D50). We therefore suggest that D50 provides the best proxy of regolith weathering in these marls. The spatial variability of the regolith was analysed through a geophysical profile, highlighting distinct behaviour depending on slope aspect. However, the distribution of slope angles is independent of aspect at the catchment scale. These results corroborate the strong annual dynamics of these catchments, where hillslopes and gullies are drained during spring and early summer high-intensity precipitation events, inducing high sediment yields.

Keywords: regolith weathering, field measurements, Near-surface geophysical survey

II.1. Introduction

Soil physical properties are a critical component for most ecosystems and result from the interaction between multiple erosion and weathering processes. As the interface between bedrock, biota and air, the soil is by nature one of the main elements of the Critical Zone and records its complex interactions. Here, we define soil as the weathered unconsolidated surface layer that is distinguishable from fresh rock as it is exposed to erosion and weathering processes. We therefore consider “soil” and “regolith” as synonyms. This layer contains the mobile products of bedrock transformation that can be transported into the stream network. The soil evolves on short timescales and modulates the variability of landscape morphology. However, the diversity of soils and climates render the relationship between soil characteristics and weathering mechanisms complex. Climate change may also affect the spatial and temporal patterns of weathering and soil production, thereby potentially perturbing sediment flux to rivers.

Determining and quantifying parameters that best describe the dynamics of the regolith in different geological contexts and under diverse climates remains a challenge. Physical soil properties can be approached by different viewpoints and need to be characterized carefully to serve the specific objectives of their study in different domains.

For agricultural purposes, the structure (packing, fragmentation, porosity, etc.) of the soil affects its fertility (Troeh, 2005; Ajdadi et al., 2016). In this domain, surface roughness is used as an indicator of soil quality and appears to be an important property because of its control on infiltration and runoff, which affect the susceptibility of the soil to erosion (Darboux et al., 2002; Bullard et al., 2018; Vázquez-Tarrío et al., 2017). Surface roughness is also closely related to grain size, which is an essential parameter controlling sediment transport both on hillslopes and in rivers (Howard, 1994; Piton et al., 2018; Haddad et al., 2022). In hydrology, the hydraulic capacity, porosity, water content and infiltration rate are key parameters to predict water storage and overland flow.

Soil properties and transport processes on hillslopes are also important in the study of mountain hazards, as their characterisation is required for understanding flash-flood and debris-flow triggering, landsliding or post-fire landscape response (Rengers et al., 2019; Nasirzadehdizaji & Akyuz, 2022). Finally, physical soil properties can affect chemical weathering, for instance by modifying porosity and thus increasing the weathering surface, or by affecting vegetation development. These interactions, initiated by the modification of soil properties, can lead to changes in the CO₂ flux between the atmosphere and soils (Soulet et al., 2021), as well as to vegetation segregation (Regué et al., 2000).

Associated to these varied fields of interest in soil properties, a wide range of techniques have been developed to characterize the regolith; ranging from laboratory analysis of field samples to high-resolution imagery of the soil (Schoeneberger et al., 2012; Tarolli, 2014; Bechet et al., 2015; Loyer et al., 2016) and geophysical tools to image the sub-surface (Tetegan et al., 2012; Pasquier et al., 2013).

The sparsely vegetated and strongly dissected landscape known as ‘Terres Noires’ in the south-eastern French Alps is characterised by rapid morphologic changes and interactions between hillslope and fluvial processes on short (intra-annual) time scales. Over the last 35 years, several small catchments in these marly badlands have been monitored in the framework of the Draix–Bléone Critical Zone Observatory (CZO), leading to enhanced knowledge of weathering mechanisms (Rovéra and Robert, 2005), sediment export (e.g.,

Antoine et al., 1995), and the relation between sediment production and export (Ariagno et al., 2022). The mountainous climate and easily erodible lithology induce a strong seasonal pattern in regolith formation and sediment export. During winter, regolith is formed mainly due to frost-cracking processes (Ariagno et al., 2022), leading to a heterogeneous surface and desiccation features, as also observed in similar Spanish badlands (Regués et al., 1995; Nadal-Romero & Regués, 2010). Spring flash floods induce a peak in sediment export (Mathys, 200; Ariagno et al., 2022). Because of the ample availability of sediment and the high network connectivity (Jantzi et al., 2017), the Draix-Bléone catchments record some of the highest observed specific sediment yields worldwide, with an annual value around 14,000 tonnes/km²/y for the Laval catchment (0.86 km²) and sediment concentrations that can reach 800 g/L (Draix-Bléone Observatory, 2015; Le Bouteiller et al., 2021). In this context, improving the understanding of the physical processes of soil production at the surface, as well as completing the characterization of the regolith and its temporal variability, is required to quantify sediment availability on hillslopes and predict more accurately the amount of sediment that will be transmitted to downstream fluvial areas.

The aims of this study are to synthesize the spatial and temporal variability of physical soil properties, and to identify a quantitative proxy representing the regolith state in the Draix-Bléone catchments. Our main hypothesis is that field measurements of regolith over time can identify such a quantitative proxy of the weathering state. To achieve this, we combine local (plot-scale) repeat field measurements over a 2.5-year period with a hillslope-scale geophysical survey. Our approach builds on similar work in subhumid badlands in the Central Pyrenees (Nadal-Romero et al., 2007, 2008; Nadal-Romero and Regués, 2010) that studied weathering using field measurements of bulk density, regolith moisture and surface mechanical resistance. These studies observed seasonal trends in the measured soil properties and highlighted slope aspect as a determining factor for weathering processes. Focusing on physical mechanisms, our study also addresses contrasts in slope aspect but includes grain-size measurements to the field dataset. Grain size depends primarily on the processes and degree of bedrock weathering. Although multiple techniques have been developed to measure grain size on hillslopes (Harvey et al., 2022), fully capturing this parameter remains complex. However, grain size is a key component to investigate sediment entrainment and motion on hillslopes (Michaelides & Martin, 2012; Sklar et al., 2017). Cohen et al. (2010) explored depth-dependant weathering functions using the grain-size variable D50 as a witness of change on hillslopes. Their modelling approach distinguished different weathering processes; ‘soil-weathering’ (i.e., the breakdown of large soil particles to smaller soil particles within the soil layer) and ‘soil-production’ (i.e., bedrock weathering into soil). Soil production functions such as the one of Heimsath et al. (1997) are commonly used in landscape evolution models but the parameters of these laws are both difficult to calibrate because of the lack of field data and supposed constant in time. Our work adds local-scale information on hillslope processes, providing qualitative and quantitative data about the temporal variability of soil production. Model calibration based on field measurement of weathering processes should improve the quality of estimated erosional output and thus improve model predictions under different climate scenarios.

The specific goals of this study are: (1) to analyse the seasonal evolution of each measured physical soil property and investigate potential relationships between these variables; (2) to identify a proxy regolith property that correlates with the observed intra-annual hysteresis in sediment export (Ariagno et al., 2022) and to highlight the weathering processes associated with this parameter; (3) to assess the spatial variability in regolith thickness and structure

using seismic measurements, and to discuss the relationship between aspect, slope and weathering processes on hillslopes; (4) to calibrate models of future evolution and their implications for predictions of sediment dynamics in the marly catchments of the Draix-Bléone CZO.

II.2. Context and methods

II.2.1. Study site

The Draix-Bléone CZO is part of the French network for the study of the critical zone OZCAR (Gaillardet et al., 2018) and is specifically dedicated to the study of erosion and sediment transport in a mountainous region. Hydrological and sedimentary fluxes have been monitored in several catchments of this CZO since 1983 (Draix-Bléone Observatory, 2015). The Draix-Bléone CZO is situated in the Alpine foothills, at elevations between 850 and 925 m a.s.l., 12 km northeast of the town of Digne-les-bains in southeast France (Figure 13A). The Draix catchments are drained by the Bouinenc stream, a tributary of the Bléone, which is itself one of the main tributaries of the Durance River. The bedrock geology is characterised by Mesozoic sediments that were folded and faulted during the Alpine orogeny (Lemoine et al., 1986; Lickorish & Ford, 1998). The Bouinenc catchment has a mountainous and Mediterranean climate due to its relatively high elevation (>800 m above sea level). The mountainous influence is responsible for cold winters with frequent frost, whereas the Mediterranean influence leads to dry summers interspersed with intense thunderstorms. Annual rainfall is about 900 mm/yr (varying between ~600 and ~1300 mm/yr interannually) in Draix. The rainfall regime varies across seasons, with high-intensity rainfall events during spring/summer and lower-intensity but longer rainfall events in autumn. Only the main streams of the Draix catchments (Laval and Moulin) are permanent, although the Moulin shows very low discharge in summer; all tributary gullies are ephemeral. Snowfall occurs almost every year but in small amounts (<10 cm) and it melts quickly. The mean annual temperature is 10.3 °C, with an annual variability between mean daily temperatures of approximatively 0.5 °C in winter and 20 °C in summer.

This study focuses on the Moulin catchment of the Draix-Bléone CZO (Figure 13B), which has a drainage area of 0.10 km², a vegetation cover of around 46%, and is entirely underlain by thick Middle-Jurassic black marl series. The dominant bedding dip is about 35° to the east in the Draix area. The catchment morphology is characterised by high drainage density and deeply incised gullies; the catchment is wide in its upper part and becomes narrower and concentrated around the main meandering channel in its lower part. Sediment transport occurs through gravitational processes on hillslopes, minor landslides (<1 m³) and debris flows in the upper drainage network, and fluvial transport as bedload and suspended load in the main drainage network. Considering only the unvegetated parts of the catchments as contributing to the sediment yield and the measured sediment density of 1700 kg/m³, the average erosion rate in the Moulin catchment is around 8 mm/yr (Mathys, 2006).

Based on previous studies of regolith characteristics (Esteves et al., 2005; Mathys, 2006; Mallet et al., 2018), we chose specific locations for recording regolith properties over several years. Slope aspect and bedding orientation have been identified as important factors controlling hydrological processes (e.g., infiltration and runoff; Esteves et al, 2005; Mathys et al, 2005). We test the influence of these factors on regolith production and evolution by

choosing four measurement plots of 1 m² each, all situated in the lower part of the catchment, encompassing a specific combination of these two factors:

- P1: east-facing slope (36°) and surface parallel to the bedding.
- P2: west-facing slope (32°) and surface perpendicular to the bedding.
- P3: north-facing slope (54°) perpendicular to the bedding.
- P4: south-facing slope (49°), perpendicular to the bedding.

The first two sites (P1, P2) are situated just north-west of the interfluve between the Moulin and the Laval catchments, on a small plateau above the main Moulin channel. P3 and P4 are located on both sides of a meander ridge in the Moulin channel. After the first year, we noted the anomalous behaviour of P3 (see results and discussion sections) and therefore added another plot with a lower slope angle (P3bis; 51°), which is placed in the meander upstream of the one containing P3 and P4.

The temporal analysis can be combined with quantitative measurements of the spatial variability in regolith thickness along a seismic profile. The geophysical transect is located between P3 and P4 through the meander ridge (Figure 14).

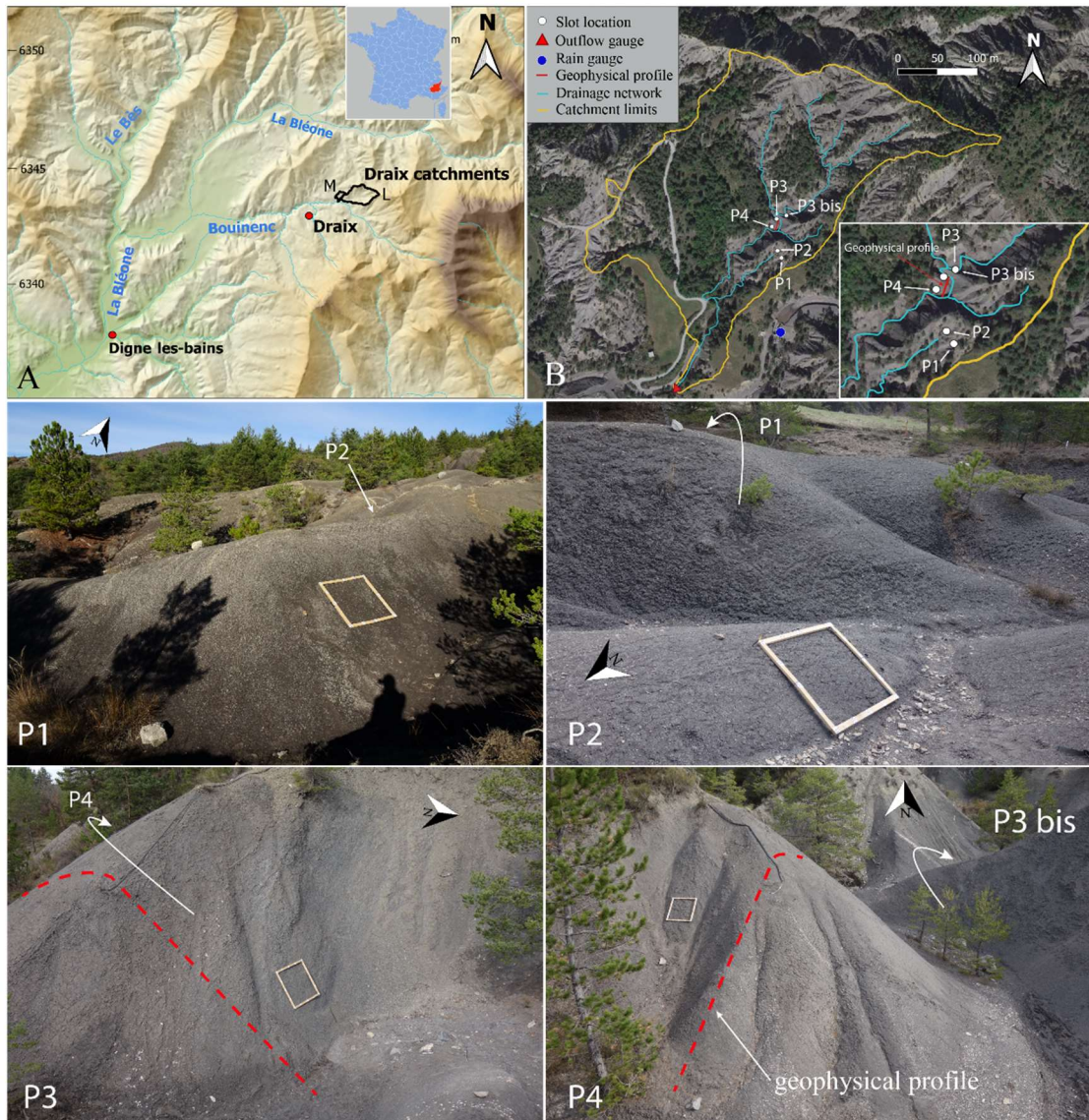


Figure 13: Geographic setting of the Draix-Bléone Critical Zone Observatory and of the measurement sites. (A) Shaded relief map (from the DEM RGEALTI IGN database) of the Bouinenc drainage basin and location of the monitored catchments (black outlines; L: Laval; M: Moulin). Inset shows location in France. (B) Satellite image (Google Earth) of the Moulin catchment. Inset shows a zoom on the measurement plots and the location of the geophysical profile. Lower images (P1-P4) are field photographs of the different measurement plots (wooden frame is 1 x 1 m); east-facing and parallel to the schistosity (P1); west-facing and perpendicular to the schistosity (P2), north-facing (P3); and south-facing (P4). Red dashed line shows the location of the geophysical profile.

II.2.2. Plot measurements

Data were collected four times per year to record the seasonal evolution and the impact of the temperature and precipitation regimes on regolith characteristics. We started the field measurements in November 2019 and repeated the campaigns in February/March, April and August for 2.5 years until March 2022 (total of 10 measurement campaigns, with one additional campaign for grain-size measurements, Appendix Table 2).

For each of the four plots and each campaign, we measured the resistivity in the field and collected samples for water content, density, and grain-size measurements in the lab. The

small-scale variability in water content and density was characterised by taking three different samples on each plot during each campaign, using metallic cylinders of 2.5-cm depth and 5-cm diameter. Because of the dryness of the marl surface, it was frequently difficult to catch the samples in the cylinder. Setting up the cylinder into the soil was also challenging for several campaigns (especially in spring and summer). Cylinder samples were stored in a watertight plastic bag for transport and weighed before being placed in an oven at 70 °C. They were weighed again three and six days later to ensure obtaining a steady dry weight.

Samples for grain-size measurements were collected from the upper 2.5 cm of soil (i.e., a similar height as the cylinder) at undisturbed locations adjacent to the plots. We used a trowel to avoid breaking particles and collected samples in a single move. Samples were stored in aluminium baskets for transport, dried for two days in the oven and weighed. Samples were subsequently sieved with 8 sizes of sieve: 8, 4, 2, 1, 0.4, 0.2 and 0.08 mm. Sieving was performed under water by hand, without shaking the sieve to avoid fragmentation of the grains. All sieves, each containing a part of the sample, were dried in the oven for two days and weighed; the grain size distribution was obtained by subtracting the weight of each sieve from the measurements. Because it was difficult to capture the fine fraction of the samples (<0.08 mm), we subtracted the sum of each dry fraction from the initial dry mass to obtain the weight of the fine fraction. All samples were sieved by the same operator to avoid uncertainty from the sieving process as much as possible. In order to assess the reproducibility of our grain-size measurements we sampled the plot P1 five times in May 2020. We also collected a vertical profile for grain-size analysis at each plot during the May 2020 campaign. To this end, we collected two or three cylinder samples at each depth. After each sample collection at a particular depth, we homogenised and cleaned the new surface (previous surface - thickness of the cylinder) before collecting the following sample.

A mini penetrometer was used to obtain resistance measurements from each plot. We randomly collected twenty measurements in each plot for each campaign to characterise the local-scale spatial variability in resistance.

The cumulative rainfall in the last 10 days before each campaign was obtained by summing the detailed event records, measured with a tipping-bucket rain gauge located at the outlet of the neighbouring Laval catchment, <500 m from the Moulin outlet (Figure 14).

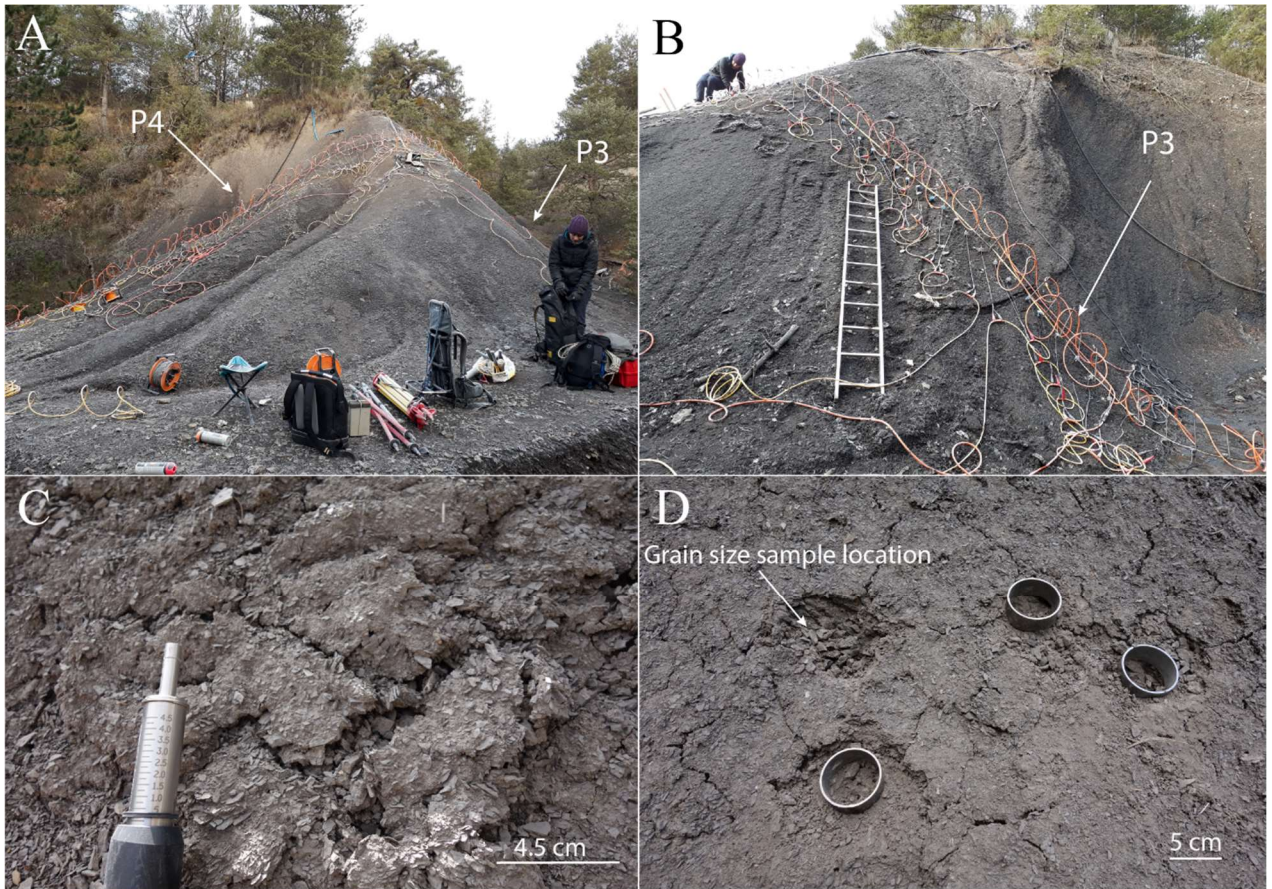


Figure 14: Field data collection. (A-B) Photos of the geophysical survey on a meander ridge of the Moulin main stream. Plots P3 and P4 are indicated on each side of the ridge. (C) Weathered regolith on north-facing plot P3 in March 2022 (Campaign 11). The mini-penetrrometer indicates very low resistance. (D) Water-content samples (cylinders) and grain-size sample on south-facing plot P4 in March 2022.

II.2.3. Geophysical survey

We collected geophysical data in December 2018 along a 24-m-long profile crossing the ridge separating the plots P3 and P4 (Figure 15). We generated seismic waves in the subsurface with the impact of a hammer on a high-density polyethylene plate placed on the ground. We repeated these shots at 25 locations spaced 1-m apart along the transect. For each of these shots, we recorded the seismic-wave propagation using 96 4.5 Hz geophones spaced 0.25-m apart and connected to four 24-channel Geometrics Geode seismic recorders. Total station surveying was carried out to accurately retrieve the locations and elevations of shots and geophones along the profile.

II.2.4. Data processing: Water content, density, grain size and resistance

We computed the volumetric water content (ϑ) using the measured cylinder weights:

$$\vartheta = \frac{\rho_s}{\rho_w} * \frac{m_h - m_d}{m_d} \quad (1)$$

With m_h and m_d the mass of the humid and dry samples respectively, ρ_s the dry sample density and ρ_w water density (1 g cm^{-3}). The reported water content is the mean of the three samples collected for each plot/campaign. The uncertainty is the highest value between either the mean of the uncertainty calculated for each sample, or the standard deviation of the water content of the three samples.

From the same samples, we computed the dry sample density ρ_s in g/cm^3 :

$$\rho_s = \frac{m_d}{V_c} \quad (2)$$

The value of D50 was computed by linear interpolation between the two cumulative masses (associated to sieve size) that bracket the D50 mass. The uncertainty associated with the D50 value is set by taking $\Delta m_d = 0.1 \text{ g}$ for each sieve (implying $\Delta m_{d_total} = 0.8 \text{ g}$). From the five samples collected at the same plot and time we infer that the D50 value is reproducible to within 0.3 mm (Appendice Table 2).

To obtain the resistance value for each plot/campaign we computed the mean of the 20 measurements. We assigned a value of 5 to measurements that were out of the mini penetrometer bounds (max = 4.5 units). In winter and early spring, the regolith was sometimes crusty at the surface with loose and fragmented material underneath. With the pressure on the crust, the mini-penetrometer pierced the crust suddenly; we thus record the value required to pierce the crust. The uncertainty associated with this measurement is the standard deviation of the 20 measured values.

The cumulative rainfall (D-10) was calculated because we observed that volumetric water content appeared significantly influenced by short-term weather conditions preceding the campaigns. Several observation periods preceding the campaigns, varying between 5 and 20 days, were tested, and the 10-day period was chosen based on the best correlation with volumetric water content.

We performed statistical analyses on this dataset, including a multivariate linear regression, using the sklearn-PCA python package.

II.2.5. Geophysical and morphologic data processing

Collected seismic data were processed using seismic-refraction tomography to estimate the P-wave velocity (Vp) in the subsurface. We initially picked first arrival times on each of the 96 traces of the 25 recorded shot gatherers with a sufficiently high signal-to-noise ratio. These first arrival times were then inverted using the seismic-refraction tomography module of the

pyGIMLI python library (Rücker et al., 2017), where the inversion domain corresponds to a triangular mesh with constant velocity cells through which rays are traced using a shortest-path algorithm. The velocity in each cell is solved with a generalized Gauss-Newton inversion, which starts with an initial model consisting of a velocity field that increases linearly with depth. The subsurface velocity distribution is updated at each iteration in order to decrease the discrepancy between estimated and observed travel times. We followed the inversion strategy proposed by Pasquet et al., 2016 and ran 135 separate inversions with different combinations of regularization parameters and starting models. This allowed us to estimate uncertainties in the velocity distribution along the profile.

We used a 50-cm resolution digital elevation model (DEM) acquired during a lidar survey in 2015 to extract slope and aspect for each pixel of the Moulin catchment, using Qgis-SAGA algorithms. Slope is computed with the Horn formula, in the direction of the steepest descent with units of degrees. The aspect value indicates the direction in which slopes are facing according to the definition of the azimuth (0°: North, 90°: East). We delimited unvegetated areas using vegetation maps extracted from aerial imagery by previous authors (Vallauri, 1997). We used a vegetation cover shapefile to obtain a clipped DEM of bare parts of the catchment, which we used for the morphological analyses.

II.3. Results

II.3.1. Relation between field measurements and state of the regolith

Appendice Table 3 provides a synthesis of all the collected field measurements. We used Principal Component Analysis (PCA) on the four parameters measured in the plots (D50 of grain size distribution, density, resistance, water content) together with the D-10 cumulative rainfall, in order to remove redundancy in the dataset and assess which parameter best explains the variability of the measurements. The main axes of the variable correlation plot (Figure 15A) explain 74% of the variability in the dataset. The resistance plots close to the F1 axis, indicating that it contains a major part (~50%) of this variability. Moreover, the projection of the resistance on the F1 axis indicates that the resistance is well explained by the PCA. The right angle observed between water content and D50 in the variable correlation plot (Figure 16A) implies a lack of correlation between these two parameters. The correlation matrix (Figure 16B) indicates the strength of the linear correlations between each of the measured and computed parameters. The cumulative D-10 rainfall and the volumetric water content show a positive correlation with each other ($r = 0.43$) and a negative correlation with D50 and resistance. The strongest correlations are found between D50 and resistance ($r = 0.69$) and between cumulative D-10 rainfall and resistance ($r = -0.56$).

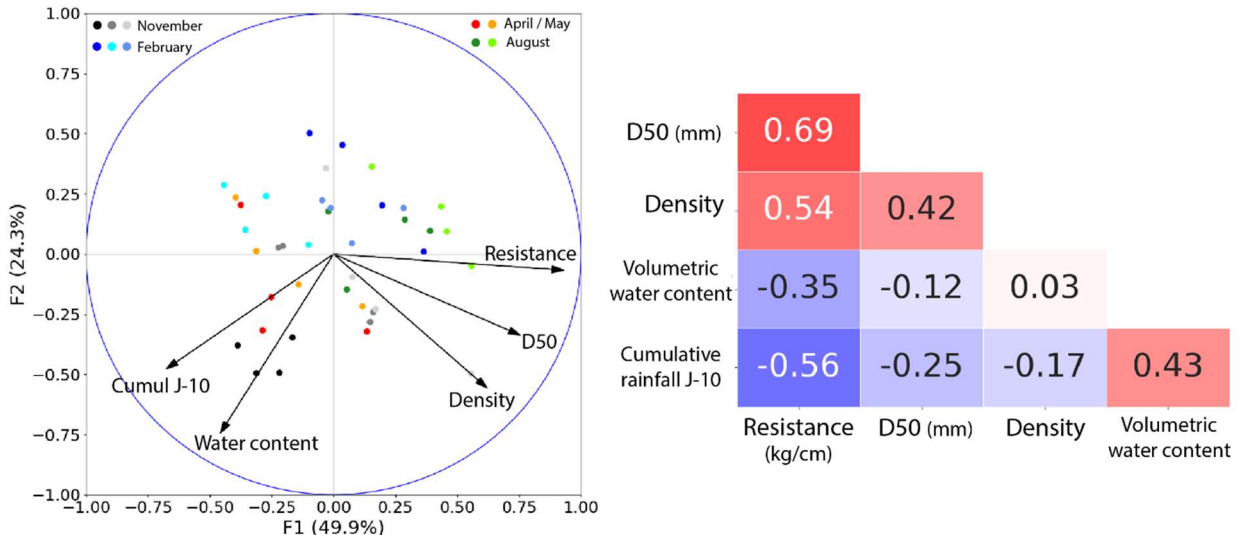


Figure 15: (A) Result of the Principal Component Analysis shown on a variable correlation plot. (B) Correlation matrix between the five parameters of the PCA. Blue boxes show negative correlations and red boxes show positive correlations; values indicate the correlation coefficient R.

Multivariate linear regression analysis shows that around 55% of the variability in resistance is explained by D50 and water content (Appendice Table 3). Figure 16A shows the positive linear trend between resistance and D50. This figure also shows some variability between the different plots: P3 and P4 are situated in the extreme parts of the regression while measurements from P1 and P2 are spread out along the trend.

The temporal evolution of the mean D50 and the mean resistance values present a similar sinusoidal trend (Figure 16B, Figure 16C), reaching their highest values at the end of summer (August) and minimum values during winter (February). There is also a significant spread between the different plots during any campaign. For practically all campaigns, smallest values were measured on the south-facing slope (P4) whereas the highest values were measured on the north-facing slope (P3). After one seasonal cycle (one year) of measurements, we suspected P3 values to be anomalous. To confirm this hypothesis, we sampled another north-facing slope site close by (P3bis). Thus, we analysed data and computed mean values only with P1, P2 and P4 (and P3bis when available); see the discussion for justification of this choice. A significant difference is observed between the February campaigns, with a significantly higher value for both parameters measured in February 2020 compared to February 2021; D50 measured in February 2022 is intermediate between these. The temporal evolution of regolith water content is presented in Appendix 8.

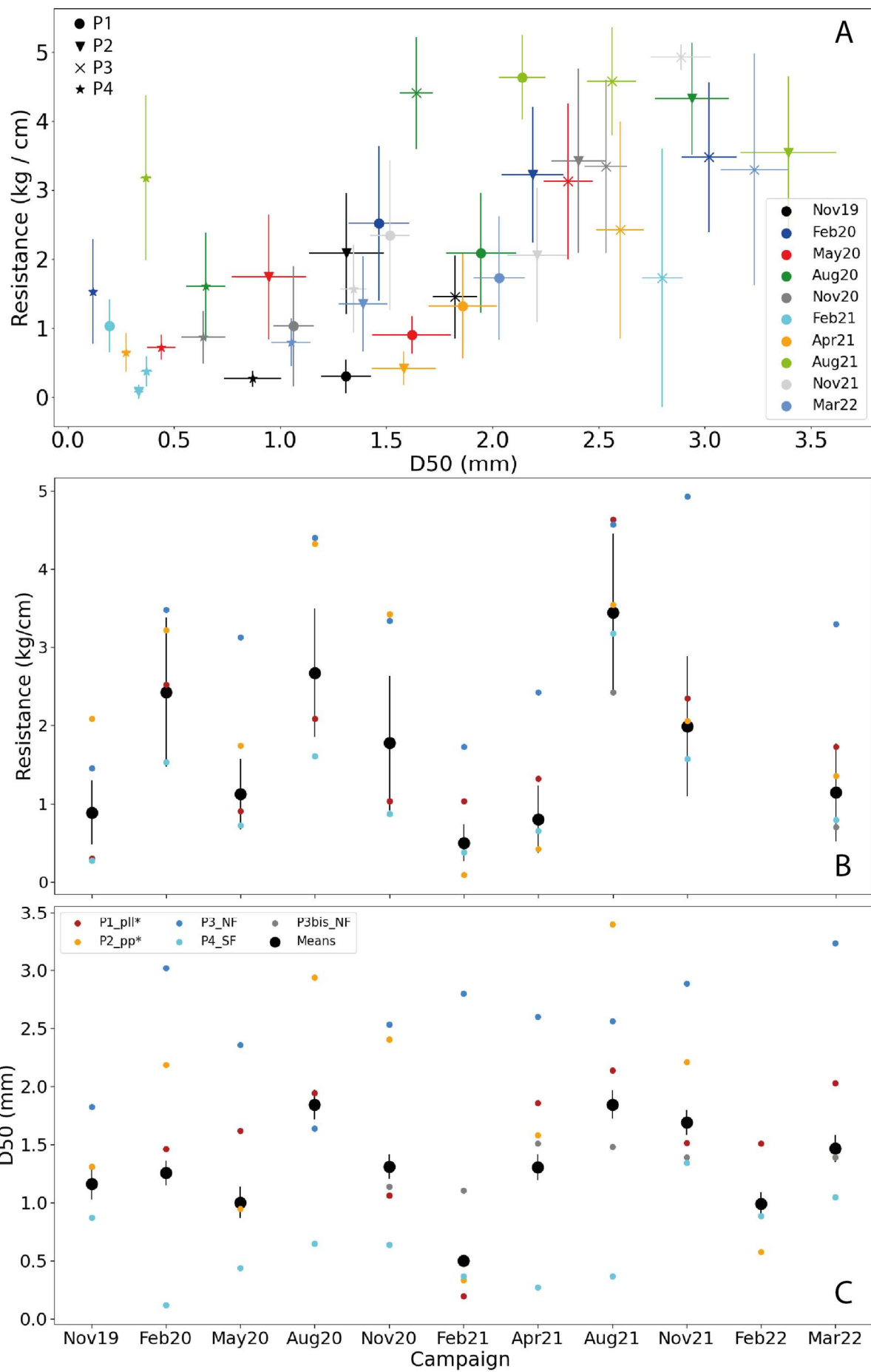
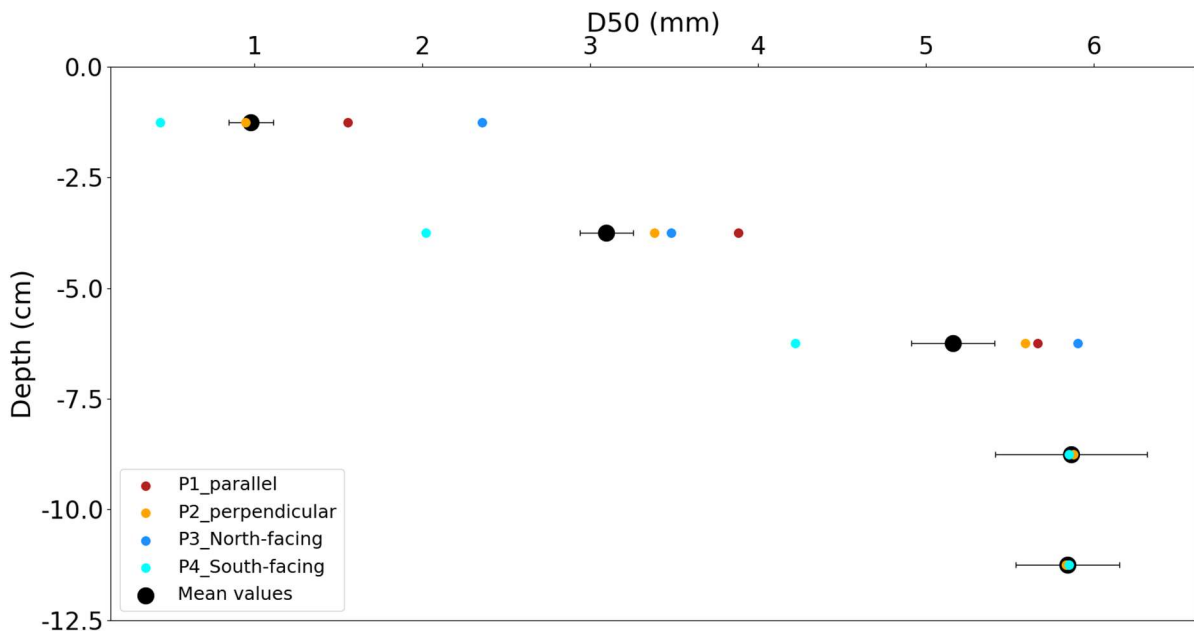


Figure 16: Covariation of grain size and resistance measurements. (A) Positive correlation between resistance and D50, using the whole dataset. Markers illustrate the spatial variability (four sites) and colours show the temporal variability (10 campaigns). (B-C) Temporal evolution of the resistance and D50, respectively. Coloured dots show plot values; black dots are the mean of three or four plots (P1, P2, P4, (P3bis)) for each campaign, with bars indicating the standard deviation.

The samples from the vertical profile (Figure 17) show a rapid increase in D50 in the first 8 cm below the surface and reach a stable value of ~5.5 mm in the deeper part (8 to 12.5 cm). The mean D50 varies between 1.0 and 5.9 mm. Note that the south-facing plot (P4) always shows the smallest D50, regardless of depth. Below 8 cm depth, D50 values are similar between the plots P4 and P2; we could not sample P1 and P3 at these depths because the regolith was too consolidated.



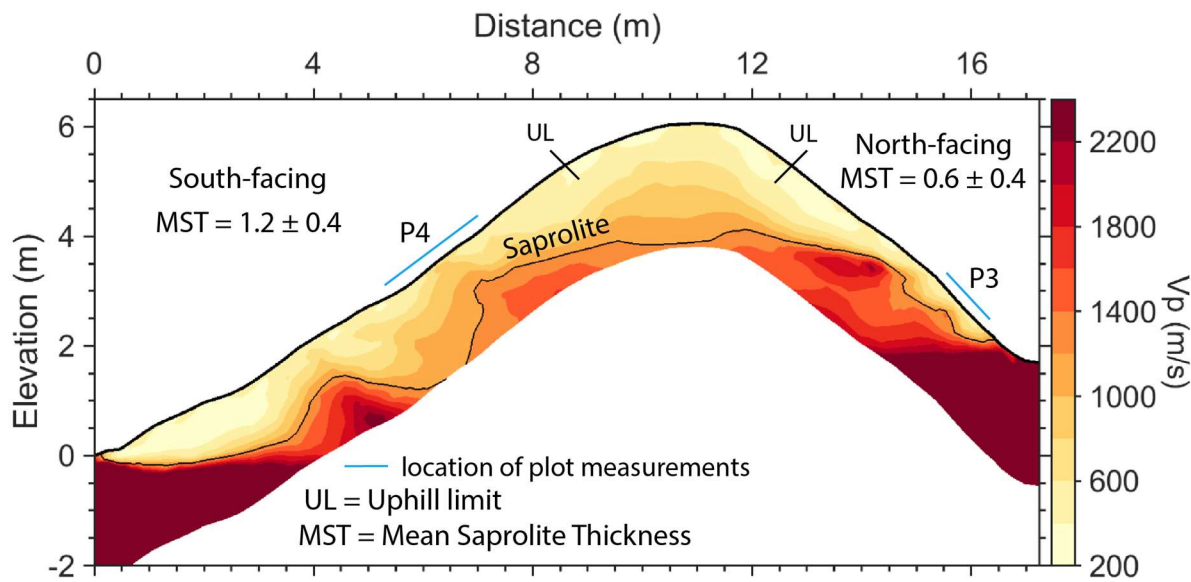


Figure 18: Seismic-velocity profile of the sampled meander ridge in the Moulin catchment. Black line indicates 1200 m/s velocity contours, reported in the literature as the limit between saprolite and fractured bedrock. Reported mean saprolite thicknesses (MST) are the mean depth of the black line from the base of the hillslope to the uphill limit (UL) indicated.

II.3.3. Morphological analysis of the Moulin catchment

Using only the unvegetated area of the Moulin catchment (0.038 km^2), we compared the slope frequency for four slope-aspect classes (North-, East-, South- and West-facing; Figure 19). The resulting distribution is unimodal and similar for all slope aspects, with modal slopes around 0.9. Mean values are slightly lower; 0.85 for North- and South-facing slopes and 0.83 for East- and West-facing slopes. Cumulative frequency curves show a slight difference between Nord-South and East-West directions between slope values of 0.5 and 1.0, arguing in favour of slightly steeper North- and South-facing slopes compared to East- and West-facing slopes.

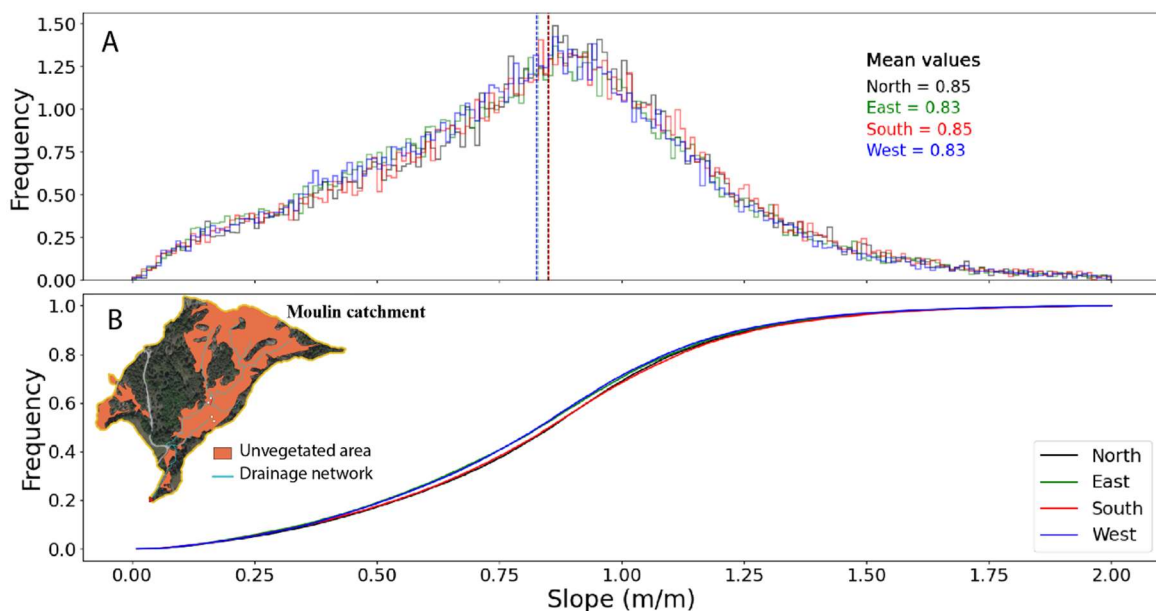


Figure 19: Morphological analysis of the Moulin catchment. (A) Histogram of slope frequency according to slope aspect. Vertical dashed lines show mean slope for each aspect class. Bin size is 0.01 m/m . (B) cumulative slope frequency for each aspect class. Inset shows map of the Moulin catchment with the unvegetated area mask (orange) used for the analysis.

II.4. Discussion

II.4.1. Uncertainties related to field measurements

The characteristics of the marly lithologies, including their softness and flaky grain shape, lead to uncertainties during both sampling and laboratory analyses. We aimed to estimate these uncertainties by taking multiple samples (cf. sections 2 and 3). Controlling the cylinder-sample volume was particularly difficult in the non-cohesive slope material. In particular, the strong preferred orientation of the marl grains induced an irregular surface at the base of the cylinder.

Grain-size samples incorporate aggregate grain-sizes with up to centimeter-sized particles that disaggregate upon contact of water. Our sample processing used a single operator and a similar procedure in order to reduce these uncertainties. Sampling necessarily induced some fragmentation, the effect of which on the measured grain-size distribution is impossible to quantify. We therefore took care to sample the same quantities of regolith in the same manner during each campaign, both at the surface and at depth (cf. section 2). Samples were not subsampled to avoid segregation bias. Results from the reproducibility assessment validate the protocol and quantify the uncertainties (Appendice 7).

The resolution of geophysical measurements is closely linked to the spacing between geophones and the seismic wavelength (e.g., Scott et al., 2017). For seismic refraction analysis, resolution is highest at the surface and decreases with depth. Lateral resolution is about half the geophone spacing close to the surface (i.e., 0.125 m) and vertical resolution is about a tenth of the wavelength (i.e., less than 0.4 m in the shallow, low velocity materials). Although mean saprolite depths on both south- and north-facing slopes are only slightly higher than the vertical resolution limit, they are sufficiently different to interpret them in terms of spatially variable weathering intensity.

II.4.2. A proxy of regolith weathering

Looking at the dependency between measured field variables is a common analysis and several studies have noticed a positive correlation between water content and resistance or between density and D50 (e.g., Regüés et al., 1995; Nadal-Romero et al., 2007; Anderson et al., 2013). The PCA shows that ~50% of the variability in the dataset is related to the resistance. Although this variable is associated with significant uncertainties, due to the sensitivity of the micro penetrometer to small spatial variations in the regolith surface, it is well correlated with both D50 and water content, which are independent of each other (Figure 15). Water content itself is correlated with D-10 cumulative rainfall. As shown by the depth profiles, D50 can be related to the state of fragmentation of the regolith. Therefore, the resistance of the regolith is explained by its state of weathering (D50) and humidity (water content and cumulative rainfall). The multivariate regression confirms that D50 and water content have a significant impact on the resistance and explain more than half of its variability. As D50 shows a clear seasonal variability (Figure 16C), the temporal variability of the dataset can be explained by seasonal weathering dynamics combined with high-frequency variability of the humidity, linked to precipitation.

The seasonal variability of D50 thus implies a seasonal variability in the state of weathering of the surface regolith layer. The temporal variation in resistance and D50 (Figure 16) may also shed light on the relationship between weathering and sediment export. Ariagno et al. (2022) have shown recently that frost-cracking during winter is the main control on sediment production in the Draix catchments. This study also highlighted an annual hysteresis cycle in sediment export from these catchments, with a peak in sediment export in June for a moderate amount of rainfall, contrasting with a peak in cumulative rainfall linked to moderate sediment export during autumn. The sinusoidal trend observed in D50 and resistance provides physical support for these inferences: the regolith is more fragmented, finer and less resistant during the winter; spring rainfall events will thus easily mobilize this regolith and export it as sediment in a transport-limited regime. As the easily mobilizable top layer of regolith is removed, the surface becomes coarser and more resistant, as indicated by our measurements at the end of the summer. This situation corresponds to a supply-limited regime, in which sediments are more difficult to detach and transport. However, the transition between both regimes is not sharp, as illustrated by comparing our D50 measurements over time with the depth profiles (Figure 16, Figure 17): the surficial regolith at the end of summer is still significantly finer-grained than the material at depth. It is therefore weathered material that corresponds to the removal of <2.5 cm from the surface (depth of the sample cylinder), consistent with estimates of sediment export from the catchment (Ariagno et al., 2022). The timing of the transition between these two regimes is also controlled by the distribution of rainfall events over spring and summer.

Moreover, two anomalies need to be highlighted and discussed: (1) the particularly high D50 and resistivity values of the P3 samples; and (2) the anomalous measurements during winter 2020 (Feb20) compared to the following winters (Feb21 and, for D50, Feb22).

In comparison to plots P1, P2 and P4, which show a clear seasonality in D50 and resistance (Figure 16), the P3 plot shows less variability, a less predictive pattern in changes and overall higher values of resistance and D50. In contrast to the other plots, this slope also shows significant sediment deposition at its base. A possible explanation for these anomalies could be the slope angle of $\sim 53.5^\circ$, which is steeper than that of the three other plots and may prevent sediment accumulation on this hillslope. Thus, the lack of regolith could be due to dry-ravel transport operating on this relatively steep slope. However, regolith formation has been observed elsewhere on hillslopes with similar aspect and slope angles. An additional explanation could be that, in addition to the steep slope on the P3 plot, steeper slopes above it might contribute to enhancing dry ravel at this location and continuously remove any regolith produced. A reduced intensity of weathering processes on this north-facing slope could be an alternative explanation. However, we have no field arguments to support this hypothesis and it goes against previous studies showing that weathering processes are enhanced on north-facing slopes (Nadal-Romero et al., 2007; Anderson et al., 2014).

To avoid the potential specific characteristics of this site, we added a second sample on a north-facing slope (P3bis) to the dataset from November 2020. Data from this plot are much more coherent with that from plots 1, 2, and 4, confirming that weathering processes are not significantly different on north-facing slopes. In light of these observations, we choose to not

take in account the records of P3 in the calculated mean values but to include data from P3bis when available.

The second anomaly is the high value of D50 measured on all plots in February 2020 compared to February 2021, with intermediate values measured in February 2022. The resistance shows a similar pattern, although it was not measured in February 2022. The higher values of D50 and resistance at the end (Feb20) than at the beginning (Nov19) of the winter is interpreted as a lack of weathering of the regolith. As frost-cracking has been inferred to be the main physical weathering process in this catchment (Ariagno et al., 2022), we computed the frost-cracking intensity indicator (FCI) for both winters, following the approach of Ariagno et al. (2022). Between the campaigns of November 2019 and February 2020, we found a FCI of about -11 °C min/cm on south-facing slopes, whereas for the same period during the winter 2020-2021 and 2021-2022 the FCI is about -411 °C min/cm and -866 °C min/cm, respectively. These large differences imply significantly less intense frost-weathering processes in the first winter of our campaign (Nov19-Feb20) compared to the other two.

Moreover, because precipitation above a threshold is the main driver of erosion in these badlands (Mathys, 2006; Ariagno et al., 2022), we also looked at the distribution of rainfall over these two winters. In the 2019-2020 winter season, nine rainfall events (as defined by Mathys, 2006) were recorded, with a cumulative rainfall of 278 mm. In the following winter (2020-2021), seven events were recorded, with a cumulative rainfall of 113 mm. These records suggest that, in addition to reduced sediment production, the 2019-2020 winter was also characterised by significant rainfall, which would have driven slope erosion during this winter season. Together, these observations explain the anomalous value of D50 found between November 2019 and February 2020: limited frost-weathering combined with more entrainment of regolith by rainfall induced an absence of regolith fining during this season.

II.4.3. Can we identify a weathering front in black marls?

In the denuded marly badlands of Draix-Bléone, where 8 mm/yr of erosion are recorded and a supply-limited regime occurs during part of the year (Bechet et al., 2016; Ariagno et al., 2022), estimating the regolith thickness is determinant to predicting sediment export. We observed a rapid increase of D50 in the first centimetres below the surface, indicating rapidly diminishing fragmentation of the regolith with depth. This trend can be interpreted in two different ways.

The trend of D50 values is consistent with an exponential increase in weathering intensity towards the surface. Taking D50 as a proxy, this can be expressed as:

$$D50_{(h)} = D_{inf} * \left(1 - \exp\left(\frac{-h}{h^*}\right)\right)$$

where D_{inf} is the D50 value of unweathered rock [mm], h is depth in the soil [mm] and h^* is the soil decay depth [mm].

The exponential decline of weathering intensity with depth ('soil production function') has been well documented (e.g., Gilbert, 1877; Heimsath et al., 1997) but there are fewer studies quantifying soil-weathering rates (Wells et al., 2006; Yoo & Mudd, 2008). Cohen et al. (2010) explored the relation between the bedrock–weathering (soil-production) function and the soil-weathering function. They showed that the soil-weathering function controls the distribution of the soil grading down the profile, but that soil-surface properties were controlled by the integrated degree of weathering and thus by the soil-production function.

However, our results can also be interpreted as a linear increase of D50 with depth in the top seven centimetres of the soil. This depth would indicate a boundary below which the regolith is characterised by another weathering state, illustrated by a constant value of D50. From a penetrometry survey, Maquaire et al. (2002) also found a first boundary between 6 and 12 cm depth, depending on the location of the resistance profile. The impossibility to collect grain-size samples below 7 cm depth in the P2 and P4 plots can also be interpreted as indicating a resistance boundary at that depth. In both cases, these results confirm the presence of a fragmented regolith at the surface at the end of the winter / early spring (May 2020) with a first weathering front around 7 cm depth.

Additionally, the geophysical survey provides continuous data and images a deeper weathering front, whereas the field measurements represent point observations that are below the resolution of the geophysical survey. Depending on lithology, climate, humidity and chemical weathering (Dixon, Heimsath, Kaste, et al., 2009), the development and limits of the saprolite layer are difficult to predict and not uniform between study sites (Befus et al., 2011; Holbrook et al., 2014). Here, the lower weathering front of the saprolite layer ($VP < 1200$ m/s; Figure 18), as set by Flinchum et al. (2022), can be compared to the resistance boundary on hillslopes found by Maquaire et al. (2002) at around 45 to 65 cm depth (transition toward a more compact saprolite). As the mean saprolite thickness (MST) between north and south-facing slopes is about 0.9 m (thus, in the same order of magnitude than reported by Maquaire et al. (2002)), it appears reasonable to set the saprolite weathering front with the $VP = 1200$ m/s reported by Flinchum et al., (2022), even on marly hillslopes

II.4.4. Influence of aspect on weathering and morphology of the Moulin catchment.

Both the field measurements and the geophysical survey indicate, at different scales, a distinct state of weathering between slopes of different aspects. At the plot scale, D50 on the south-facing slope (P4) is always smaller than on the north-facing slope (P3 or P3bis), even when slope-angles are similar (P3bis). These observations are different from other studies: working on similar badlands in northern Spain, Nadal-Romero et al. (2007) recorded markedly more active regolith weathering on north-facing slopes, as indicated by differences in regolith properties (bulk density, resistance, frost activity, geochemistry). In a more temperate climate, the Gordon Gulch watershed (Colorado) has been well studied and contrasts in vegetation, rock weathering and moisture content have been found between north- and

south-facing slopes, with enhanced weathering on north-facing faces subject to long period of snow cover (Anderson et al., 2014).

Previously, we developed arguments that could explain the particularly thin regolith layer on the P3 plot (Section II.4.2). However, our results between P4 and P3bis are still opposite to previous studies, although the distinct behaviour between aspects is reduced. Further field measurements on other north-facing slopes would be needed to compare our study site with other locations. These aspect distinctions are also found at a larger scale as demonstrated by the geophysical survey: the weathering front of the saprolite is deeper on the south-facing ($MST = 1.2$ m) than on the north-facing ($MST = 0.6$ m) slope at this site. Although we know that the north-facing slope site is probably influenced by its high slope angle, this complementary continuous method confirms the difference in regolith and saprolite thickness between these two slopes of opposite aspect.

To extend the spatial analysis from the hillslope to the catchment scale and put the observed contrast between opposite-facing slopes into context, we analysed the morphology of the Moulin catchment. Within the Moulin catchment (Figure 14B), the main drainage is not located symmetrically inside the catchment; a wider vegetated area is present on the north side of the channel (i.e., dominated by south-facing slopes). However, the distribution of slopes throughout the catchment does not highlight a significant difference between aspects (Figure 18). Thus, the morphology of the ridge that we sampled in a meander of the Moulin catchment, which was clearly steeper on its north-facing than on its south-facing slope, cannot be related to a more general morphologic trend over the catchment (Appendice 9).

Several studies have reported asymmetries between north- and south-facing slopes. At a global scale, Pelletier et al. (2018) documented the slope-aspect controls on critical zone processes, modelling the topographic asymmetry of catchments as a function of latitude and elevation. They showed that pole-facing hillslopes tend to be steeper than other slopes at low latitudes and that this pattern reverses (i.e., pole-facing slopes are less steep) around 50° N. Elevation modulates this changeover latitude by lowering its value for higher elevations. In particular, the change in steeper-slope aspect for elevations around 1 km (the elevation of the Moulin catchment) occurs between $45\text{--}50^{\circ}$ N (Draix latitude: 44.1° N). Being located in this transition zone may explain the lack of a clear asymmetry in slope aspect that we observed for the Moulin catchment (Fig 6). Similarly, Anderson et al. (2013) did not observe a marked asymmetry in slope steepness in the Gordon Gulch catchment. In contrast, Nadal-Romero et al. (2007) noticed an asymmetry at the catchment scale with a stronger expansion of badlands on shady slopes than slopes with sunny aspects. These observations are consistent with the model of Pelletier et al. (2018) as the Spanish badlands studied by Nadal-Romero et al. (2007) are located at lower latitude and elevation than the Draix catchments.

II.4.5. Perspectives: integrating regolith characteristics in landscape morphology analysis

Although our field measurements show consistent trends, match with the observed sediment-export cycle (Figure 7A) and confirm the results of previous studies on weathering processes

in these badlands, field observations need to be continued and extended to better understand which processes drive the spatial heterogeneity of the regolith and what are the consequences of this heterogeneity.

First, to more fully assess the potential contrast between weathering on north- and south-facing slopes, a larger dataset of D50 on north-facing slopes would be required. As discussed above, sediment accumulation might be prevented and non-local diffusion by dry ravel increased above a threshold hillslope angle, inducing transient sediment deposition at the base of hillslopes. This hypothesis needs to be tested by looking at regolith characteristics on similarly inclined hillslopes elsewhere in the catchment. Coupled measurements of slope and regolith characteristics throughout the catchment (using the resistance, which is much less time consuming to measure than D50) could allow to define a slope threshold for sediment entrainment on hillslopes. In parallel, mapping transient sediment deposits at the base of hillslopes might help to understand which parameters drive this phenomenon, a first step necessary to identify the associated weathering processes. Although slope angle is undoubtedly one of these key parameters, slope aspect may also play a role by influencing soil temperature, humidity or exposure to solar energy.

Tracking the location of sediment deposits could also help to explain the observed asymmetry of the position of the main channel in the Moulin catchment (Figure 14B) as well as the adjacent Laval catchment, with the main channel of both catchments clearly shifted toward the south. Johnstone et al. (2017) showed that '*the asymmetry in the position of the thalweg within mainstream valleys is positively correlated with asymmetry in the length of fans...*'. Further study of these catchments is required to establish a potential relationship with sediment production and transport, or vegetation development, as a function of slope aspect.

At smaller scales, Bechet et al. (2015, 2016) investigated the change in hillslope and regolith characteristic using terrestrial laser scanning. Similar studies could improve the quantification of regolith surface roughness over time, which could provide another proxy of the weathering state.

The results of the geophysical survey are complementary to our field measurements and provide support for active erosional removal of regolith on the hillslope where the P3 plot is located, leading to a thinner saprolite layer. Performing additional surveys on longer and steeper slopes could further clarify the impact of aspect on regolith thickness. In particular, it would be interesting to confirm the particular behaviour of the P3 site by looking at other north-facing slopes, in order to test whether slope angle or aspect is the prime parameter affecting regolith thickness.

II.4.6. Implications for modelling landscape evolution in badlands

With the rapid growth of digital elevation models and numerical analysis tools, landscape-evolution models have become key tools to investigate the drivers of spatial and temporal variability in erosion rates, combine and test hypotheses and explore quantitative predictions (e.g., Tucker & Hancock, 2010). The development of numerical models of badland evolution

provides significant promise for a better understanding of the rapid erosion processes operating in them, the interaction with vegetation and the long-term evolution of erosion rates (e.g., Gallart et al., 2013). With their long-term dataset of climate variables and sediment yield, the catchments of the Draix-Bléone observatory are prime candidates to further develop and test landscape evolution models for badlands. Detail studies like this one, focusing on various compartments of the landscape (hillslopes, crests, channels, etc...), help to better understand phenomena and processes that control the morphological evolution and provide field data to constrain values of the main parameters identified. Modelling the seasonal cyclicity of the regolith state we demonstrate here requires developing landscape models with sub-annually varying erosion/weathering processes and, therefore, sub-annual time-steps. The identification of a weathering proxy and its quantification (Ariagno et al., 2022) allow to calibrate the parameters of the soil-production function (Heimsath et al., 1997) based on field data. Model calibration based on field measurements of weathering processes should improve the quality of the estimation erosional output and thus improve the prediction of the model under different climate scenarios. Moreover, it would allow adjusting the model to a specific area in a physically meaningful way.

II.5. Conclusions

Based on our field measurements and statistical analyses, and accounting for the inevitable uncertainties in our dataset, we show that D50 is a good proxy to characterise the state of regolith weathering in the Draix badlands.

Both soil resistance and D50 follow a seasonal weathering dynamic: small values of these parameters are found during the winter, when the regolith is particularly fragmented and crumbly, while high values are recorded at the end of the summer, when mobile regolith has been washed from the hillslopes by the intense spring/early summer rainfall events. This cyclicity of D50 is consistent with the intra-annual hysteresis in sediment export observed by Ariagno et al. (2022). A small D50 value implies availability of easily detached sediment on hillslopes for transport in the drainage network. In contrast, the highest values imply a less-weathered regolith that was exposed to the surface due to the removal of the more mobile sediment above it. Moreover, the frost-weathering intensity indicator, shown to predict sediment production in the Draix catchments (Ariagno et al., 2022), can explain field measurements of D50 that do not conform to the seasonal trend.

In contrast to the seasonal cyclicity, the dynamics of the water content show a high-frequency (daily) variability. Independent to the D50, this variable is highly correlated to the cumulative rainfall in the previous ten days.

Although further studies on aspect influence are needed to confirm the results obtained here, both discrete (field samples) and continuous (geophysical survey) measurements highlight the spatial variability of the weathered layer thickness and show a distinct behaviour of the regolith between the south-facing and north-facing slopes studied. However, this trend is not visible at the catchment scale, as the morphological analysis of the denuded area of the Moulin catchment shows a similar slope distribution independent of aspect.

Our field measurements over a 2.5-year period allow identifying seasonal dynamics in the state of the regolith, but an extended dataset would allow to confirm the observed cyclic trend and to better identify anomalous years. Conducting another geophysical survey and adding additional regolith samples of north-facing slopes at different locations would be needed to conclude on the impact of aspect on hillslope weathering and sediment production. In a context of the greening trends in the Alps (Carlson et al., 2017; Filippa et al., 2019), the development of the vegetation cover might also affect the morphology of badlands catchments and perturb the ongoing sediment dynamics. Finally, field laboratories like the Draix-Bléone observatory are determinant to improve model prediction under different climate scenarios, as they allow a solid calibration of parameters based on field measurements or long-term datasets and record changes at human timescales.

Appendices chapter II

This Supporting information contains two tables with the field campaign schedule (Appendice Table 2) and the complete dataset of the recorded variables (Appendice Table 3). Table S3 reports the detailed results of the multivariate regression.

Field-measurement analyses are completed with the D50 reproducibility assessment results (Appendice 7) and the temporal variation of the water content (Appendice 8). Appendix 9 shows the morphological analysis of the total (vegetated and bare) Moulin area.

Date	Grain size (P1 - P4)	Grain size P3bis_NF	Grain size vertical profil	Resistance	Water content	Geophysic
15-nov-19	x			x	x	
17-Feb-20	x			x	x	
12-May-20	x		x	x	x	
31-Aug-20	x			x	x	
17-nov-20	x	x		x	x	
12-Feb-21	x	x		x	x	
19-Apr-21	x	x		x	x	
2-Aug-21	x	x		x	x	
29-nov-21	x	x		x	x	
20-Feb-22	x	x		x	x	

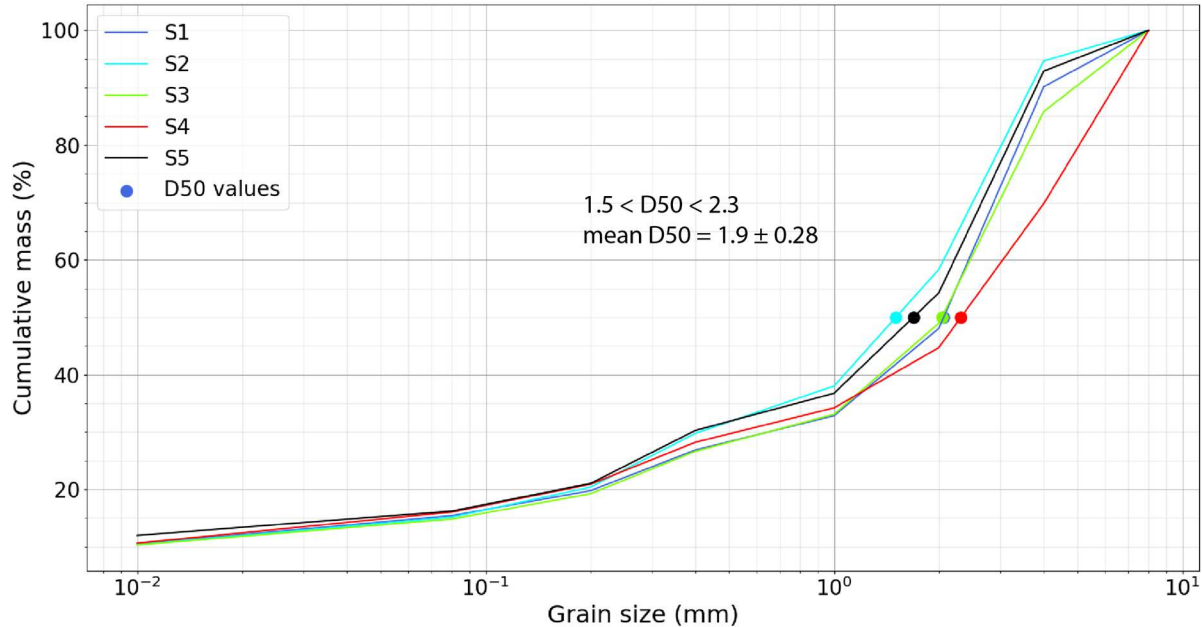
Appendice Table 2: Chronology of the field campaigns and associated data acquisition

campaigns	Plot location	GSD50 (mm)	error GSD50	Resistance	error resistance	Water content ϑ	error ϑ	Density	error density	cumul rainfall j-10 (mm)	error cumul
nov-19	P1	1.31	0.12	0.3	0.24	0.2	0.01	1.81	0.11	68.8	0.2
nov-19	P2	1.31	0.18	2.09	0.87	0.21	0.01	1.7	0.1	68.8	0.2
nov-19	P3	1.82	0.1	1.46	0.61	0.15	0.01	1.69	0.1	68.8	0.2
nov-19	P4	0.87	0.13	0.27	0.12	0.19	0.01	1.68	0.1	68.8	0.2
Feb-20	P1	1.46	0.14	2.52	1.12	0.04	0.01	1.26	0.08	3.2	0.2
Feb-20	P2	2.19	0.14	3.22	0.98	0.07	0.01	1.48	0.09	3.2	0.2
Feb-20	P3	3.02	0.13	3.48	1.08	0.07	0.01	1.73	0.11	3.2	0.2
Feb-20	P4	0.12	0.01	1.53	0.75	0.03	0.01	1.45	0.09	3.2	0.2
May-20	P1	1.62	0.19	0.91	0.27	0.14	0.01	1.51	0.09	62.2	0.2
May-20	P2	0.95	0.18	1.75	0.9	0.2	0.02	1.56	0.1	62.2	0.2
May-20	P3	2.36	0.11	3.13	1.13	0.09	0.01	1.89	0.12	62.2	0.2
May-20	P4	0.44	0.07	0.73	0.18	0.08	0.01	1.3	0.08	62.2	0.2
Aug-20	P1	1.95	0.17	2.09	0.87	0.17	0.01	1.67	0.1	2.2	0.2
Aug-20	P2	2.94	0.17	4.32	0.81	0.06	0.01	1.6	0.1	2.2	0.2
Aug-20	P3	1.64	0.08	4.4	0.81	0.07	0.01	1.66	0.1	2.2	0.2
Aug-20	P4	0.65	0.09	1.61	0.77	0.09	0.02	1.7	0.1	2.2	0.2
nov-20	P1	1.06	0.09	1.03	0.87	0.16	0.01	1.43	0.09	16.2	0.2
nov-20	P2	2.4	0.13	3.42	1.33	0.16	0.02	1.67	0.1	16.2	0.2
nov-20	P3	2.53	0.1	3.34	1.25	0.18	0.02	1.65	0.1	16.2	0.2
nov-20	P3bis	1.14	0.1							16.2	0.2
nov-20	P4	0.64	0.1	0.87	0.38	0.15	0.01	1.53	0.09	16.2	0.2
Feb-21	P1	0.2	0.01	1.03	0.39	0.14	0.01	1.34	0.08	38.2	0.2
Feb-21	P2	0.33	0.02	0.09	0.1	0.11	0.02	1.15	0.07	38.2	0.2
Feb-21	P3	2.8	0.09	1.73	1.87	0.12	0.01	1.16	0.07	38.2	0.2
Feb-21	P3bis	1.11	0.09							38.2	0.2
Feb-21	P4	0.37	0.03	0.38	0.22	0.06	0.02	1.51	0.09	38.2	0.2
Apr-21	P1	1.86	0.16	1.32	0.76	0.09	0.02	1.61	0.1	68.8	0.2
Apr-21	P2	1.58	0.15	0.42	0.25	0.09	0.01	1.36	0.08	68.8	0.2
Apr-21	P3	2.6	0.11	2.42	1.57	0.05	0.01	1.86	0.11	68.8	0.2
Apr-21	P3bis	1.51	0.1							68.8	0.2
Apr-21	P4	0.27	0.02	0.65	0.28	0.06	0.02	1.32	0.08	68.8	0.2
Aug-21	P1	2.14	0.11	4.63	0.61	0.01	0.01	1.78	0.11	2.6	0.2
Aug-21	P2	3.4	0.23	3.54	1.1	0.02	0.01	1.77	0.11	2.6	0.2
Aug-21	P3	2.56	0.12	4.57	0.78	0.03	0.01	2.13	0.13	2.6	0.2
Aug-21	P3bis	1.48	0.13	2.43	1.12					2.6	0.2
Aug-21	P4	0.37	0.03	3.18	1.19	0.01	0.01	1.75	0.11	2.6	0.2
nov-21	P1	1.52	0.09	2.35	1.08	0.13	0.02	1.77	0.11	8	0.2
nov-21	P2	2.21	0.14	2.06	0.97	0.13	0.02	1.95	0.12	8	0.2
nov-21	P3	2.89	0.14	4.93	0.18	0.13	0.02	2.31	0.14	8	0.2
nov-21	P3bis	1.39	0.1							8	0.2
nov-21	P4	1.35	0.06	1.57	0.63	0.05	0.01	1.39	0.09	8	0.2
Feb-22	P1	1.51	0.19							25.6	0.2
Feb-22	P2	0.58	0.06							25.6	0.2
Feb-22	P3									25.6	0.2
Feb-22	P3bis	1.04	0.07							25.6	0.2
Feb-22	P4	0.89	0.05							25.6	0.2
mars-22	P1	2.03	0.12	1.73	0.9	0.1	0.01	1.65	0.1	8.6	0.2
mars-22	P2	1.39	0.12	1.35	0.69	0.08	0.01	1.48	0.09	8.6	0.2
mars-22	P3	3.23	0.16	3.3	1.67	0.05	0.01	1.42	0.09	8.6	0.2
mars-22	P3bis	1.39	0.1	0.71	0.57					8.6	0.2
mars-22	P4	1.05	0.09	0.8	0.35	0.05	0.01	1.77	0.11	8.6	0.2

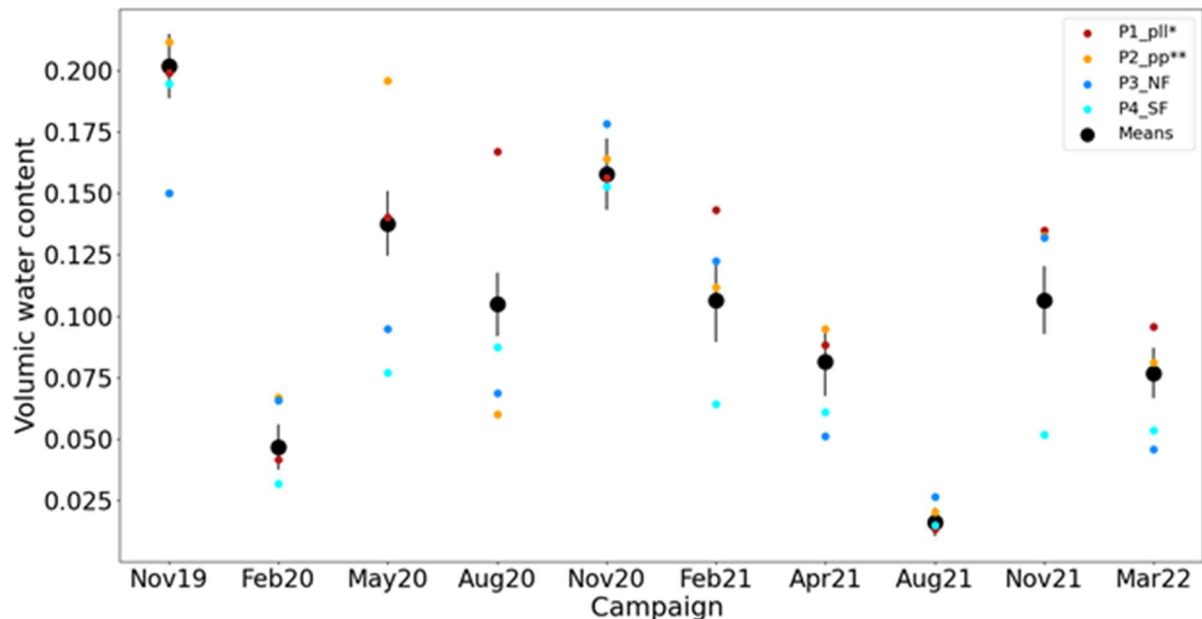
Appendice Table 3: Field measurements dataset

	<i>coef</i>	<i>Std error</i>	<i>t</i>	<i>P > t </i>	[0.025	0.975]
<i>constant term</i>	1.17	0.42	2.77	0.01	0.30	2.04
<i>D50 (mm)</i>	0.93	0.19	4.88	0.00	0.54	1.32
<i>water content θ</i>	-6.58	2.71	-2.43	0.02	-12.15	-1.01

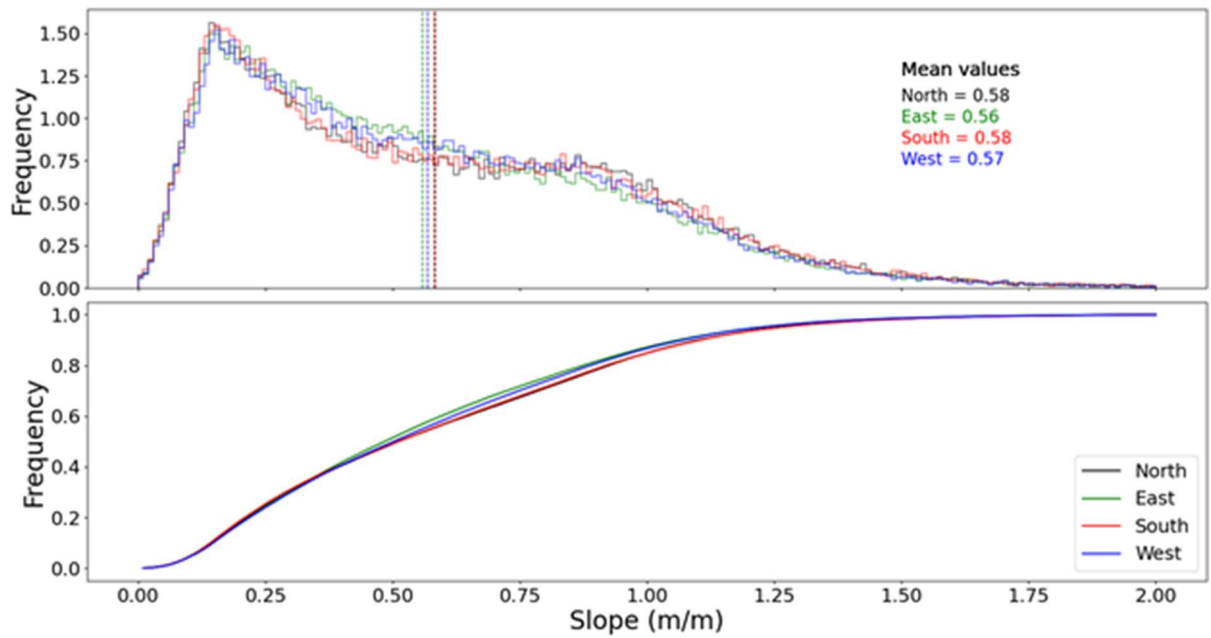
Appendice Table 4: Multivariate regression results (Ordinary Least Squares (OLS) methods) between D50, water content and resistance. Coefficient of determination $R^2 = 0.54$ and the goodness of fit of the regression (F-statistic) = 15.80



Appendice 7: Reproducibility test for grain-size measurements. Five samples were collected from plot P1 during campaign Y; the plot shows the grain-size distribution and resulting D50 for these 5 samples.



Appendice 8: Temporal evolution of the water content of field samples. Coloured dots show single-plot values; black dots are the mean of three plots (P1, P2, P4) for each campaign. *pll: parallel to bedding, **pp: perpendicular to bedding.



Appendice 9: Morphological analysis on the total area of the Moulin catchment. (A) Histogram of slope frequency according to slope aspect (colours). Vertical dash line show mean slope of each aspect interval. Bins size is 0.01. (B) Cumulative frequency of the slope for each aspect.

Chapter III

Modeling seasonal sediment dynamics and landscape evolution in a marly badland catchment, Draix-Bléone Critical Zone Observatory, SE France.

Abstract: Badlands are particularly sensitive components of the critical zone where weathering, erosion and transport processes can be observed on human time-scales. Within the Draix-Bléone Critical Zone Observatory (CZO), SE France, water and sediment (both bedload and suspended load) fluxes and climatic drivers have been recorded for more than 35 years, making it an ideal natural laboratory to develop a landscape-evolution model (LEM) for badland evolution calibrated with field data. Based on these records and existing knowledge on the sediment dynamics of these marly catchments, the aim of this study is to develop a LEM that is able to reproduce the observed intra-annual sediment-flux variability, in particular the transition from transport-limited to supply-limited conditions that occurs during summer. Our model predicts soil thickness and sediment export at monthly timescales, thereby providing potential links between “classical” LEM that run at long time scales and event-scale models, and simulating the physical processes driving the sediment dynamics in these catchments at their relevant timescale. We use the annual hysteresis cycle between rainfall and sediment export recorded in the Draix catchments as a quantitative indicator of the adequacy of the model. First, we model the supply-limited regime observed in the second half of the year in the badlands, illustrated by an clockwise loop in the annual hysteresis pattern, using depth-dependent hillslope regolith production and erosion laws. Next, we express the impact of rainfall intensity, identified as the main trigger of sediment motion both on hillslopes and in the drainage network, in order to reproduce the observed non-linear relation between sediment export and rainfall during the first part of the year (illustrated by an initial anti-clockwise loop in the hysteresis cycle). Parameter calibration is performed using average annual sediment export and soil depth in specific compartments of the catchment. The model successfully reproduces the hysteresis pattern but further work is needed on the calibration to obtain consistent magnitudes of sediment export. This new landscape evolution model appears to be a relevant tool to model observed annual morphology changes in badlands and to predict badland evolution in a context of climate change.

III.1. Introduction

Sediment-yield prediction is a major issue for natural-hazard assessment and hydraulic infrastructure management, especially in the current context of rapid climate change. Landscape evolution models (LEM) play a key role in this challenge, allowing exploration of multiple hypotheses and long-term simulations. Hillslope weathering controls sediment availability for erosion and transport (e.g., Anderson et al., 2013; Ariagno et al., 2022), while fluvial processes control sediment transport, drainage network development and long-term landscape incision (e.g., Howard, 1994; Lague, 2014; Whipple & Tucker, 1999). Landscape-evolution modeling helps understanding the interactions between hillslope and fluvial erosion (Willgoose et al., 1991) and quantifying their contribution to the amount of sediment exported (e.g., Tucker & Slingerland, 1997). In the current context of climate change and global warming, the occurrence or the amplitude of extreme events is expected to intensify, but the potential effects on sediment export from catchments are complex and remain insufficiently understood (Burkett et al., 2005).

Badlands constitute some of the most sensitive components of the Critical Zone where weathering, erosion and transport are intense and affect landscape morphology at human time scales (e.g., Nadal-Romero et al., 2018). Geomorphologists have long considered these areas as particularly rich natural laboratories because “badlands appear to offer in a miniature spatial scale and a shortened temporal scale many of the processes and landforms exhibited by more normal fluvial landscapes, [...]” (Howard, 1994). These erosional landscapes are commonly unvegetated and develop in easily eroded lithologies, forming deeply dissected landforms. These characteristics can intensify some erosion processes (overland flow, physical weathering, etc...) and render some others insignificant (e.g., tree-throw, root-related weathering). Landscape evolution models might thus be particularly relevant tools for badlands as they can be more easily focused on specific processes and calibrated based on direct measurements in badland catchments. Such models add a quantitative level of interpretation and multi-spatial and -temporal scale characterization of slope forms, drainage density and sediment yield where, in most cases, only interpretation or qualitative information are available (Howard, 1997). The widespread badland landscapes known as ‘Terres Noires’ in the southeastern French Alps have been extensively studied because of their susceptibility to erosion, leading to high sediment export (e.g., Antoine et al., 1995). Over the last 35 years, several small catchments in these marly badlands have been monitored in the framework of the Draix–Bléone Critical Zone Observatory (CZO), leading to a quantification of weathering and erosion through repeated measurements of sediment yield (Draix-Bléone Observatory, 2015) (Figure 20).

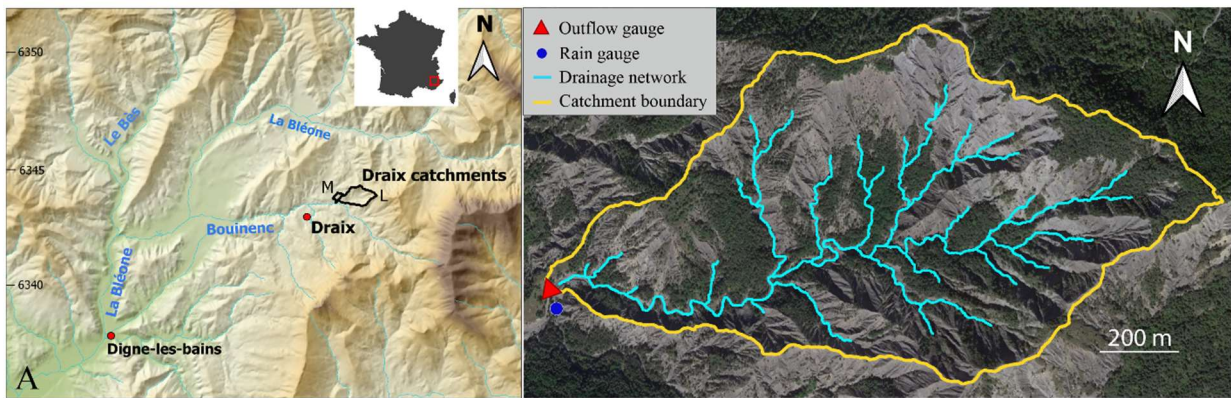


Figure 20: Geographic setting of the Draix-Bléone Critical Zone Observatory and its catchment sites. (A) Shaded relief map (from the RGEALTI DEM; IGN database) of the Bouinenc drainage basin and location of the monitored catchments (black outlines; L: Laval; M: Moulin). Inset shows location (red box) in France. (B) Satellite image (Google Earth) of the Laval catchment showing the main drainage network (cyan outlines) as defined in our model (i.e. drainage areas $>10,000 \text{ m}^2$).

Few catchment-scale models have been developed for the Draix-Bléone CZO. Mathys et al. (2003) aimed to reproduce and quantify the particularly strong erosion pulses, initiated by rainfall events and hydrologic transfer, observed in the badlands. They used a hydro-sedimentary model operating at the event scale ("Erosion des Torrents en Crue" (ETC); Brochot & Meunier, 1996), which combined hillslope sediment production and fluvial transport processes, to simulate water and sediment fluxes during floods. Based on the Telemac-Sisyphe modeling platform, Taccone (2018) developed a physically based model of the Laval catchment using hydraulic transfer equations, and including both hillslope and fluvial erosion processes, in order to simulate the hydrosedimentary response to individual flood events. Although these models do not predict the topographic evolution of the catchments, the separation of the different landscape components comprises an approach that is similar to landscape-evolution modeling.

The variability in vegetation cover in the different catchments of the observatory has inspired modeling studies to evaluate the effect of vegetation on erosion rates. The modeling results of Mathys et al. (2003) showed that vegetation considerably reduces sediment yield by rendering each of the erosion and weathering processes less efficient. Lukey et al. (2000) used a physically based, spatially distributed sediment-transport model (SHETRAN) to evaluate the effect of catchment reforestation on runoff and erosion. However, this model was also focused on hydraulic processes and did not capture how geomorphic processes drive landscape evolution over time. Recently, Carriere et al. (2020) filled this gap by using a landscape-evolution model to simulate the impact of vegetation on erosion of the Draix catchments. The model coupled hillslope and fluvial erosion functions to assess changes in the catchment morphology at multiple-year timescales, according to the distribution of vegetation cover. Carriere et al. (2020) showed that the reduction of erosion by vegetation is due mainly to a decrease in diffusivity (i.e., in soil erodibility) rather than to a decrease in runoff. The model developed in this paper is built on similar erosion functions (hillslope diffusion and fluvial erosion), with the addition of a soil production function, and strives to reproduce the intra-annual dynamics of the catchment based on the seasonal variability of regolith properties (Ariagno et al., in review).

The frame of this model is derived from several observational studies, which report distinct behavior of mountainous Mediterranean badlands between seasons. In these badlands, frost-weathering processes act as the major driver of soil generation during winter (Anderson et al., 2013; Ariagno et al., 2022; Nadal-Romero et al., 2007; Regués et al., 1995). Rainfall, and especially rainfall intensity, is generally recognized as the main driver of erosion in these marly catchments (Mathys et al., 2003). Very few rainfall events occur during this first part of the year and mobilizable materials accumulate on hillslopes, leading to a transport-limited regime (Bechet et al., 2016). However, field observations also report continuous dry-ravel processes occurring during winter (Liébault et al., 2022), inducing transient sediment deposits at the bases of hillslopes. This process moves sediment from steep hillslopes to channels and may affect sediment export during spring floods. Mathys (2006) and Ariagno et al. (2022) showed that the peak in sediment export occurs in late spring / early summer and can be related to an increase in rainstorm and rainfall intensity. Autumn is marked by longer and less intense rainfall events leading to moderate sediment export (in which bedload is more important; Liébault et al., 2022) because of the reduced availability of sediment on hillslopes and in gullies. These observations illustrate the transition from a transport-limited regime to a supply-limited regime (Bechet et al., 2016) during the year.

Such detailed knowledge on the dynamics of the Draix catchments has emerged, principally, owing to the available long-term dataset of climatic and sediment-yield records. Additionally, studies on specific processes have added understanding of the yearly sediment cycle, including the sensitivity of erosion to rainfall intensity (Mathys et al., 2003), the importance of frost weathering (Ariagno et al., 2022), and bedload versus suspended-load transport (Liébault, 2017). Combining the long-term dataset with these specific studies allow placing tight constraints on landscape-evolution model calibration at both inter-annual and intra-annual timescales.

Our modeling study focuses on the 0.86 km² Laval catchment, which is mainly unvegetated (68%) and situated between 850 m and 1250 m elevation. The Laval catchment shows steep slopes in its upper part and more gentle slopes, with some vegetated areas, close to the main channel. Rainfall, discharge and sediment flux (both suspended and bedload) have been monitored since 1983 with a dense network of rain gauges around the catchment, a Parshall threshold, and a large deposit area at the outlet, respectively. The average annual sediment budget of the Laval catchment is about 13300 t, equating to a specific sediment yield of around 15500 t km⁻² (for the period 2006-2021 except 2013). The seasonal dynamics detailed above is based on these records (Figure 21; Ariagno et al., 2022) and, as the processes behind these results are well described and understood, a main objective of our modeling is to assess which processes are necessary and sufficient to reproduce this hysteresis cycle. Our hypothesis is to test a limited number of physical process to reproduce sediment export patterns.

Starting from the well-known relation between sediment yield and rainfall (Nearing et al., 2004; Sun et al., 2016), we have added to the model, step by step, the main physical erosion components observable in the Draix catchments in order to replicate the intra-annual sediment dynamics. Each modeling step pursues intermediate goals: (1) Confirm the first-order control of rainfall on sediment export in this area; (2) Test how depth-dependant erosion functions can be used to model a supply-limited regime; and (3) explore the role of rainfall intensity in triggering sediment transfer on hillslopes and through the drainage network. The LEM we develop allows predicting sediment export and the response of

erosional processes to climate change perturbations. At a larger scale, the Draix LEM enhances the pertinence of coupled field measurements and modeling, especially for model calibration. As the interest in the response of badlands to global change is growing (Nadal-Romero et al., 2021), we aim for this model to become a relevant tool for investigating responses and feedbacks to small changes in climate variables that could easily be adapted to other badlands in the world.

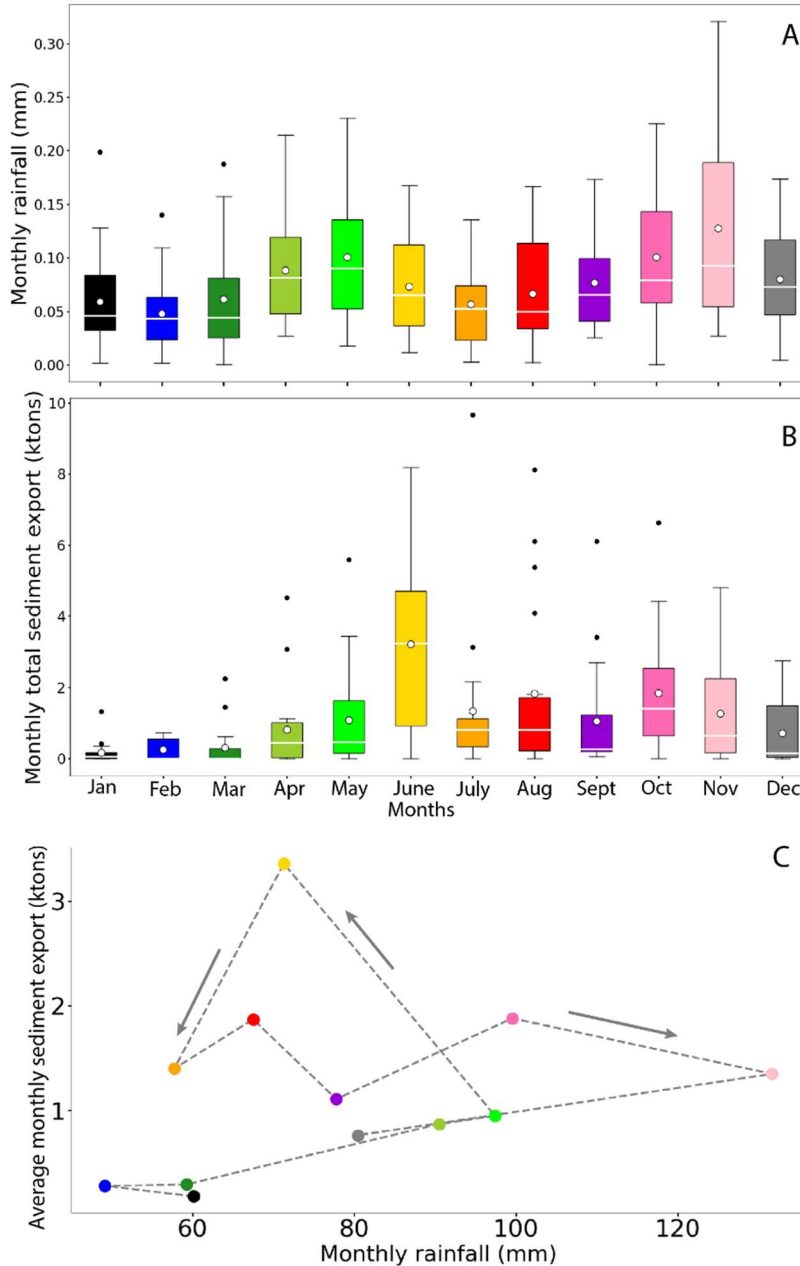


Figure 21: Main precipitation and sediment-transport dynamics of the Laval catchment (modified from Ariagno et al., 2022). Box plots of (A) monthly rainfall and (B) monthly total sediment export (i.e., bedload + suspended load) of the Laval catchment. White lines show median values, and white dots indicate mean values. The first (Q_1 , 25 %) and third (Q_3 , 75 %) quartiles are indicated by the box limits, and whiskers show $Q_1+1.5$ IQR and $Q_3+1.5$ IQR (IQR: interquartile range). Black dots are outlier values . (i.e., with values $< Q_1-1.5$ IQR or $> Q_3+1.5$ IQR). (C) Hysteresis plot of monthly sediment export versus monthly rainfall using interannual monthly average values from the Laval catchment between 2003 and 2020 (dots colored according to month, as in (B) and (C)). The dashed line highlights the hysteresis cycle with two separate maxima: high sediment export and moderate rainfall in June versus high total rainfall and moderate sediment export in October–November.

III.2. Modeling framework

We use the open-source python toolkit ‘Landlab’ (Hobley et al., 2017), which offers tools to combine multiple geomorphic laws on 2D regular grids or digital elevation models (DEM). In our landscape evolution model, spatial variables, called ‘fields’ (like topography, soil depth, sediment flux), are affected by different functions describing physical processes, called ‘components’.

III.2.1. Geomorphic process laws

We make use of three geomorphic laws, which focus on the main physical mechanisms of weathering and erosion identified in the Draix badlands (Figure 22). Two of these laws operate on hillslopes: the soil-production function (i.e., conversion of bedrock into soil or regolith; Figure 22A) and the transport-length diffusion (TLD) law for hillslope transport (Figure 22B). The third process, fluvial erosion and transport, is based on the stream-power law with alluvium conservation and operates in the drainage network of catchments (Figure 22C).

III.2.1.1. Soil production

The weathering and fragmentation of fresh rock into soil was conceptualized by Gilbert (1877; see Humphreys & Wilkinson, 2007 for a review). He noticed in particular that frost action was reduced as a regolith layer accumulated. This initial step of rock disintegration and transformation was first modeled by Ahnert (1966) as an exponential decay function:

$$P = \frac{\partial z}{\partial t} = P_0 * \exp\left(-\frac{h}{h_p^*}\right) \quad (1)$$

Where P is the soil production rate (i.e., the rate of bedrock disintegration to soil) and P_0 is the maximum soil production rate. z is the elevation of the bedrock-soil interface considering no uplift. The soil thickness (h) and the characteristic weathering depth (h_p^*) in the exponential express the gradual increase in weathering efficiency with the decrease in regolith thickness ($P = P_0$ for $h = 0$). Rock weathering is limited by temperature changes and biology (e.g., roots) in the case of mechanical weathering, and by water and oxygen availability in the case of chemical weathering. In both cases, these controls are less active at depth. Thus, a deep bedrock/soil interface induces a decrease in both physical and chemical weathering efficiency. However, soil thickness is not homogeneous across landscapes as ridges, hillslopes and gullies are affected differently by erosion processes and there are multiple potential sources of variance (animal burrowing, bedrock heterogeneity, etc.). Indirectly, topographic inflections (divergent or convergent topography) also affect soil production, as regolith depth tends to increase with decreasing curvature (Heimsath et al., 1999), therefore limiting weathering efficiency. Several studies have tested and confirmed this relationship with field data, in particular by measuring in-situ produced cosmogenic ^{10}Be concentrations to show the inverse relationship between weathering rate and soil depth (Heimsath et al., 1997, 2000; Small et al., 1999). Different mathematical forms have been proposed for the soil-production function, like the ‘humped’ production function (Ahnert, 1977; Anderson, 2002). This peaked function describes a maximum weathering rate under a non-zero soil depth combined with an

exponential decrease below this point. This approach was considered based on the argument that a shallow thickness of regolith can effectively hold water at the bedrock surface and thus enhance the weathering processes of rock (Gilbert, 1877). We choose to use the exponential decay function because it is consistent with field measurement on our site (Ariagno et al., in review). A historical and extended discussion of this function can be found in Tucker & Hancock (2010).

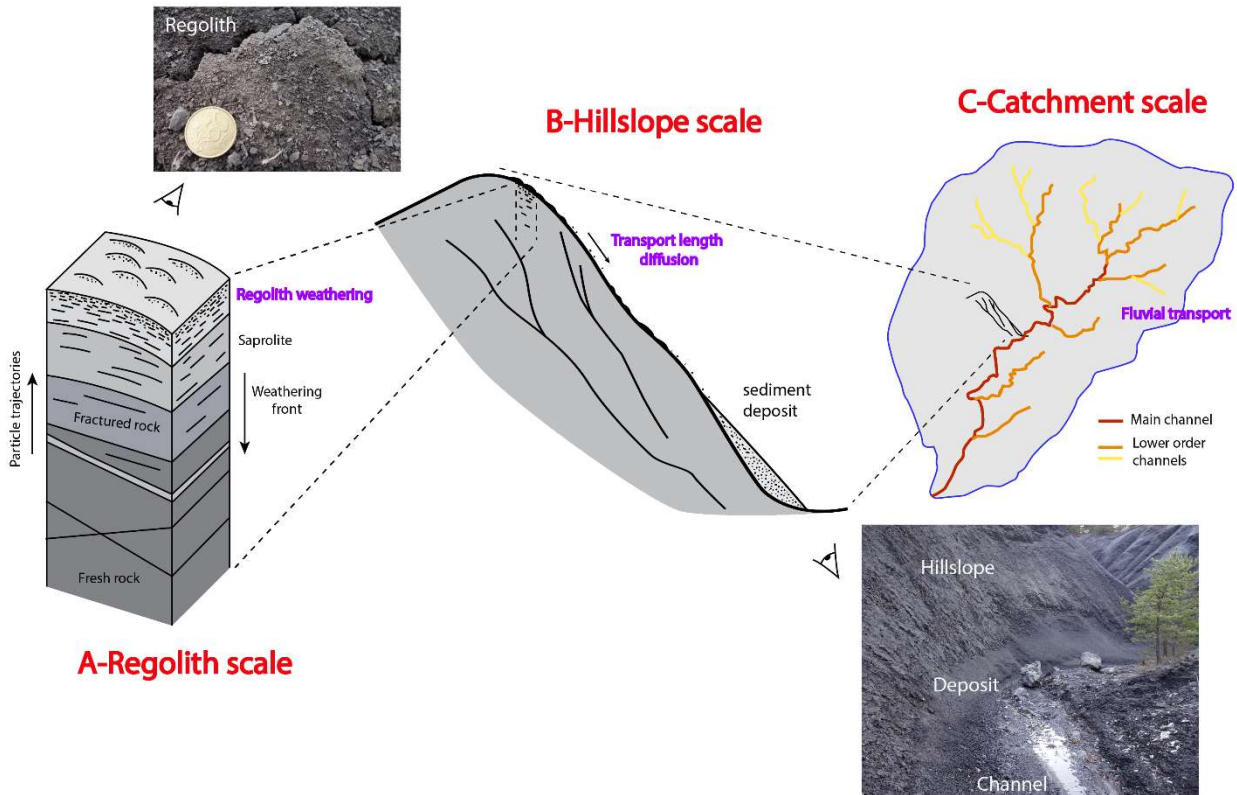


Figure 22: Sketch of the geomorphic processes included in the model. The regolith scale (A) illustrates the soil production function: bedrock is gradually chemically and physically weathered at depth and becomes increasingly fragmented toward the surface. Loose and mobilizable particles at the top of the rock column constitute the regolith (or soil) layer. The associated field photo (top left) shows the grain-size on the surface (millimeter-scale particles). The non-local diffusion function acts at the hillslope scale (B), transferring particles from hillslopes to the channels. Dry-ravel processes induce transient sediment deposits. Finally, the fluvial transport law (C) models erosion of sediments in the channels, and their transport from low order channels to the outlet passing through the main channel. The lower-right photo shows transient sediment deposits at the base of a steep hillslope and in the channel. The photo also shows the hillslope-channel coupling; flows in the channel entrain sediment and erode the basal-slope deposits during successive floods.

III.2.1.2. Hillslope transport

The temporal and spatial variability of regolith thickness on hillslopes results from a continuous competition between input and output. On hillslopes, the input of the system is the regolith created by bedrock weathering and incoming sediment flux due to diffusion, while the output is sediment that is transported outside of the plot by the diffusive hillslope processes (biologic, rain splash, dry ravel, etc.). The dynamic balance of regolith thickness on hillslopes can be described with a mass conservation equation for soil thickness, h :

$$\rho_s \frac{\partial h}{\partial t} = -\rho_r \frac{\partial z}{\partial t} - \rho_s \nabla \cdot \vec{q}_s \quad (2)$$

Where ρ_s and ρ_r are the bulk densities of soil and bedrock, respectively, and \vec{q}_s is the soil flux vector (Dietrich et al., 1995).

(Davis, 1892) and (Gilbert, 1909) were the first to associate the sediment flux q with the local gradient and Culling (1963) mathematically formalized this hillslope-transport relation: $q_s = -K_d \nabla z$ where K_d is the diffusion coefficient [L^2 / T]. This linear slope-dependent sediment transport law is widely used in numerical models of landscape evolution (Dietrich et al., 2003; Heimsath et al., 1999; Kirkby, 1971; Tucker & Hancock, 2010; Tucker & Slingerland, 1997). However, more elaborate versions of this law have been proposed in order to, for instance, express the effect of soil thickness on local diffusion. Johnstone & Hilley (2015) suggested to take into account the underlying lithological properties by adding a sediment-depth dependency:

$$q_s = -K_d \left| \frac{dz}{dx} \right| \left(1 - e^{-\frac{h}{h_d^*}} \right) \quad (3)$$

Where h is the sediment thickness and h_d^* is a characteristic soil depth for which erosion decreases to (1/e) of its maximum value. Thus, this equation describes a supply-limited regime when soil resources are limited.

The linear diffusion model is also not well adapted to describe sediment transport on steep hillslopes, with high spatial variations in curvature, such as in badlands (Roering et al., 1999). Whereas the linear model represents slow and continuous hillslope transport processes, a non-linear model can integrate episodic events such as shallow landsliding, which are characteristic of steep slopes. In this non-linear slope-dependent model, hillslope sediment flux, induced by diffusion processes, rapidly increases when the gradient approaches a critical value (Anderson, 1994; Roering et al., 1999), which is more appropriate to describe badlands dynamics.

This local description of diffusion processes is adapted to slow morphological changes and implies a long simulation duration to reach topographic equilibrium. The local non-linear diffusion model is therefore not ideal to represent slope-transport processes in Draix, as the bare hillslopes and cohesive lithology inhibit soil creep and increase overland flow, while the steep slopes enhance dry-ravel processes. This latter process is especially intense during winter when frost weathering is active, fragmenting and detaching particles from bedrock, which are immediately transported downslope on high-gradient slopes. Dry-ravel processes can be observed on the catchment hillslopes during the cold period and lead to formation of transient sediment deposits at the bases of hillslopes (Figure 22). These observations lead us to consider the ‘non-local’ non-linear diffusion approach developed by Carretier et al., (2016). Given that the variation in slope elevation is defined by the balance between erosion (E_h), with a similar form of equation (3), and deposition (D), these authors proposed a non-linear form of the deposition function. A minor modification has recently been made to this formulation (Shobe et al., 2022) to avoid dependency on the grid resolution dx :

$$D = \frac{q_s (1 - |S/S_c|^2)}{\lambda} \quad (4)$$

Where D the local deposition rate [L / T], q_s is the incoming sediment flux per unit width [L^2 / T], $S = (\frac{dz}{dx})$ is the local slope [L/L], S_c is the critical slope [L/L], and λ is a sediment-transport length scale that cannot be smaller than dx . As the deposition rate depends on both the slope and the critical slope, this formulation tends to local diffusion equation for small slopes ($S \ll S_c$) and ‘non-local’ sediment bypass for $S \sim S_c$; particles can travel a large distance before redeposition on cells with slopes close to the critical slope. The detachment rate is thus proportional to the local gradient and the flux q_s integrates sediments that have been detached locally as well as sediments that have been eroded upslope (Carretier et al., 2016). The transition between local and non-local diffusion is found for intermediate slopes, where the travel distance is gradient-dependent. For a sufficiently long run duration (as instance 10,000 yr), the final topography on a 2-D model grid is similar between the local and non-local non-linear diffusion models.

Finally, we choose to use this transport-length diffusion law (later called TLD) both for winter dry ravel process and for summer hillslope transport induced by rainsplash and overland flow.

III.2.1.3. II.1.3 Fluvial entrainment and transport

Several mathematical descriptions for fluvial incision and transport have been proposed but the most commonly used is the stream-power incision model (Howard, 1994; Howard & Kerby, 1983; Tucker & Slingerland, 1997; Whipple & Tucker, 1999), which defines bedrock channel erosion rate ‘ E ’ as a power-law function of slope S and drainage area A , the latter being a proxy for discharge:

$$E = K_f A^m S^n \quad (5)$$

where m and n are positive constants controlled by the mechanics of the dominant erosion processes; the ratio m/n falls into a narrow range near 0.5 ($0.35 < m/n < 0.6$; Snyder et al., 2003; Whipple & Tucker, 1999; Wohl & David, 2008). K_f is the fluvial erosion coefficient [$\text{L}^{1-2m} \text{T}^{-1}$], which integrates the effect of substrate resistance, climate, channel width, etc. At the extreme opposite to the bedrock channel incision, there is the fully alluviated channel, made up of non-cohesive sediment. This transport-limited system is characterized by unlimited loose material and a rate of change in bed, which depend of a sediment transport capacity. Laws taking in account sediment cover predict a sediment transport capacity as a function of local variables (slope, discharge, grain size) (Howard AD. 1980; Smith & Bretherton, 1972; Tucker & Bras, 1998; Tucker & Hancock, 2010; Willgoose et al., 1991). However, both model, the stream-power incision and transport-limited model (alleviated), are not adapted for mixed rivers, which means simultaneous treatment of the bedrock incision and sediment transport. Shobe et al. (2017) reviewed several existing models that attempt to couple sediment transport and bedrock erosion. These authors concluded that, while these models differ in their applicability to different spatial and temporal scales, overall they are not adapted to model mixed bedrock-alluvial landscape evolution. The SPACE model (Shobe et al., 2017) that we use, established from the approach of Davy & Lague (2009), Lague (2010), and Zhang et al.

(2015), is developed to overcome this lack of mixed model. This erosion-deposition sediment model solves the spatial and temporal changes in sediment flux and alluvial thickness by employing local analytical solutions. Thus, Shobe et al. (2017) added sediment parameters to the basic stream-power law (5), and dealt with the balance between sediment thickness (fully alluviated channel) and bedrock exposure (bare channel). The entrainment rate of sediment E_s is expressed as follows:

$$E_s = \left(K_s q_w S^n - \omega_{cs} \left(1 - e^{-\frac{\omega}{\omega_{cs}}} \right) \right) \left(1 - e^{-\frac{h}{h_f^*}} \right) \quad (6)$$

Where K_s is a sediment erodibility parameter [L^{-1}], q_w is water discharge per unit channel width (commonly computed as $q_w = k_q A^m$, with k_q subsumed into K_s). ω_{cs} [m/yr] is a threshold stream power required for sediment entrainment, such that entrainment / erosion is zero when stream power is below the chosen threshold (Shobe et al., 2017). The existence and relevance of such a threshold have been debated (e.g., Lague et al., 2005; Snyder et al., 2003; Tucker, 2004). Shobe et al. (2017) developed an optional exponential expression for the threshold stream power, which modulates the sediment entrainment with an exponential decline as the ratio ω / ω_{cs} decreases allowing a smooth transition close to the threshold (Kirchner et al., 1990; Wilcock & McArdell, 1997). h is the sediment thickness and h_f^* is a characteristic sediment thickness that can be seen as a reach-scale bedrock roughness length-scale [L]. The ratio h / h_f^* expresses the ability of sediment to cover the rough bedrock surface. Where this ratio is high ($h \gg h_f^*$ and $1 - e^{-h/h_f^*} \rightarrow 1$), E_s is similar to the classic stream-power law (5) including a threshold stream-power term. The exponential term allows (1) reducing fluvial erosion when sediment thickness in the channel is reduced (allowing modeling a channel-bed supply-limited regime) and (2) ensuring a smooth transition between sediment-mantled and bedrock channels. Note that we made the choice to consider all mobile material, soil and sediment, as one unique type of material. This is the reason why we use the variable h to describe soil thickness on hillslopes, and sediment thickness in alluvial streams.

SPACE also integrates a sediment-deposition law that depends on the sediment concentration in the water column c_s and the effective sediment settling velocity V (Davy and Lague, 2009):

$$D_s = c_s V \quad (7)$$

V describes the fall velocity of the sediment particles, which is often related to the grain size. We set a small V in our model to limit deposition in the drainage network.

III.2.2. Modeling strategy

Ariagno et al. (2022) highlighted the seasonal variability in sediment export from the Laval catchment (Figure 21). They showed that sediment and water fluxes follow an annual hysteresis cycle, which was interpreted as reflecting both the transition from a transport-limited to a supply-limited regime during the year (Bechet et al., 2016), which is visible as a clockwise loop in the second half of the annual hysteresis cycle, and the rainfall-intensity driven transport-limited regime, which is visible as a counter-clockwise loop in first half of the

annual hysteresis cycle. The goal of this study is to develop a landscape-evolution model that is able to account for this intra-annual variability of sediment fluxes in such a catchment. This objective will be assessed by measuring the ability of the model to reproduce the observed annual hysteresis cycle, which is a good indicator of this variability. The model is based on an annual cycle (Figure 23) with two main periods identified (winter/summer). Rainfall events, which drive erosion and sediment transport, occur mainly during the summer and are characterized by their durations and intensities.

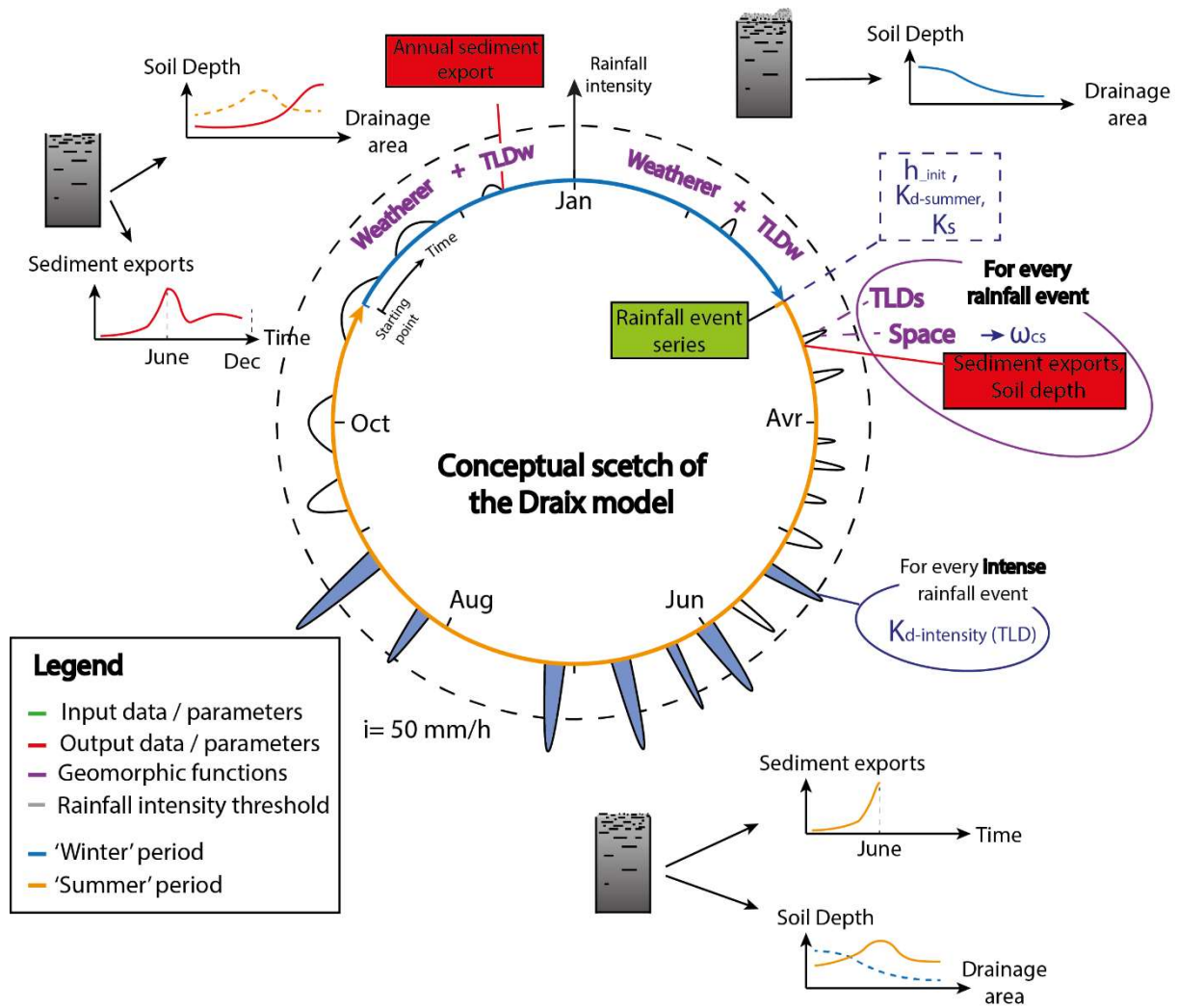


Figure 23: Summary sketch of the Draix landscape-evolution model. The blue ('winter') and orange ('summer') parts of the circle represent an annual cycle with a soil-production and an erosion phase during winter and summer, respectively. These two phases are modeled using different combinations of weathering and erosion processes (purple text). Field data (green box) and output variables (red boxes) are shown on the temporal cycle. Small black peaks indicate successive rainfall events with different durations (width) and intensities (height). The main parameters of the geomorphic law (blue box and text) are initialized for each year. The dashed black circle illustrates the intensity ($> 50 \text{ mm/h}$) above which the diffusive coefficient of the TLD ($K_{d\text{-summer}}$) component will be increased ($K_{d\text{-intensity}}$) for these specific rainfall events (blue peaks). After each rainfall event, values of sediment export and soil depth are recorded (purple ellipse). Small sketches situated around the main circle illustrate the annual evolution of soil depth and state of the regolith. The associated plots illustrate the expected evolution of sediments export and soil-depth distribution in the catchment (where dash lines represent the pattern of the previous plots).

We wish to simulate as closely as possible the real dynamics of the badlands by incorporating these seasonally variable processes. We run simulations for each year for which we have data (2006 to 2021 without 2013); however, the total duration of each simulation is slightly longer than one year as it includes the beginning of the winter season starting in the previous year. During the cold periods, only soil production and slope transport occur (i.e., we do not run fluvial erosion during this winter phase), even though a few rainfall events often occur before the end of February. These events are included in the summer phase in order to consistently predict sediment-export amounts at the end of the year. Similarly, the ‘summer’ simulation phase and thus the rainfall event series include November and December rainfall events, which are considered as the beginning of the winter.

We start with a basic model that includes hillslope and fluvial transport (but no soil production) and predicts a linear relation between mean monthly sediment exports and cumulative rainfall over the modeled fourteen-year period. We add components stepwise to this initial model to simulate the identified processes acting on the catchment and identify which are required to reproduce the main characteristics of the observed hysteresis cycle. We record model-predicted monthly sediment export and soil depth at the end of each month for each year, and compute inter-annual monthly averages of sediment export to compare with the hysteresis cycle reported by Ariagno et al. (2022). Soil-depth records will be used to calibrate hillslope-process (regolith production and slope transport) parameters. The initial conditions and parameter calibration for each step are discussed below.

III.2.2.1. Initial model

In an initial calibration step, we run the transport-length diffusion (TLD) and the fluvial erosion (SPACE) component for every rainfall event of each year. The time step for the erosion processes is the duration of the rainfall event (measured as a fraction of a year). We set the initial soil depth at $h_{init} = 10$ m to exclude soil-depth-dependent processes and ensure transport-limited conditions throughout the year at this stage. In contrast, we clear the main channels (with a drainage area $> 10,000$ m²) from soil so as to ensure hillslope-channel coupling. This succession of processes, including only the TLD and SPACE components, will be called ‘summer simulation phase’ as it captures the behavior of the spring, summer and autumn period in the Laval catchment (Figure 23). In this stage, the TLD is used to simulate diffusion by rain splash or overland flow and the corresponding parameter will be called K_{d_summer} .

III.2.2.2. Including soil production and sediment availability

The second step aims to reproduce the supply-limited regime observable at the end of the year in the Draix catchments. This regime is clearly illustrated by a rainfall peak in November (>120 mm on average) associated with only moderate sediment export (<1.5 kton). Thus, we integrate a finite availability of mobile sediment by dropping the initial soil thickness from 10 m to 0 and adding the soil-production (exponential weatherer) component in the winter

period (Ariagno et al., 2022; Nadal-Romero et al., 2007; Regués et al., 1995). This winter simulation phase also incorporates diffusion (TLD) to simulate the dry-ravel processes observed in the field during winter (Figure 23). Thus, the value of the diffusion coefficient K_{d_winter} for the winter TLD (dry ravel) is lower than the value of the erodibility parameter K_{d_summer} for the summer TLD (overland flow erosion). The justification for this lower value comes from: (1) for a given duration, dry ravel (winter diffusive process) is less efficient than rainfall-driven overland flow (summer diffusive process) to transport sediment on hillslopes, and (2) winter dry ravel process is activated in the model during a much longer interval than summer overland flow erosion (i.e. total duration of the winter phase versus sum of rain event durations). The cold period includes the time when frost weathering is most efficient (mid-November to end-February; Ariagno et al., 2022) and is divided in 105 daily time steps to reproduce the daily alternation between regolith production (frost at night) and dry ravel (during the day). This winter phase is run before and separately from the summer phase and the state of the topography, bedrock and soil depth at the end of the winter loop is used as the initial condition for the summer loop. To calibrate the model with this new value K_{d_winter} , we used the predicted evolution of soil depth. Thus five compartments of the Laval catchment were defined in order to check their sediment dynamics (Figure 26A). We divided the ‘hillslopes’ compartment in three categories: (1) the ‘steep slopes’ compartment, where $S > S_c$ and drainage area $A < 1000 \text{ m}^2$, which should be strongly affected by the TLD; (2) the ‘interfluves’ compartment, which embodies areas with small drainage area ($A < 8 \text{ m}^2$) and normal slope ($S < S_c$), and for which regolith characteristics were recently monitored over a two-year period (Ariagno et al., in review); (3) the ‘regular slopes’ compartment, which includes all areas with $8 \text{ m}^2 < A < 1000 \text{ m}^2$ and $S < S_c$. The drainage network is divided into two compartments: (4) the intermediate channels compartment which regroups areas with $1000 \text{ m}^2 < A < 10,000 \text{ m}^2$; and (5) the main channel with a drainage area $> 10,000 \text{ m}^2$. Soil depth in each of these compartments is recorded after the winter period and after each rainfall event.

III.2.2.3. Including rainfall intensity

The initial anti-clockwise part of the hysteresis cycle has been attributed to the increase in rainfall intensity recorded in late spring – early summer (Ariagno et al., 2022). Therefore, a third simulation stage adds a rainfall-intensity condition to the model, in order to better simulate the effect of rain splash, rain-drop size, etc. The observed increase in sediment export in the hysteresis cycle is thus considered the consequence of these physical mechanisms, which increase the detachment and movement of soil particles (Figure 23; Martínez-Murillo et al., 2013; Mathys et al., 2005). From the raw rainfall dataset, we computed maximum rainfall intensity for every selected rainfall event. During the summer phase, we enhance K_{d_summer} , leading to a new value $K_{d_intensity}$, when the maximum rainfall intensity of the event is higher than an intensity threshold $i = 50 \text{ mm/h}$, following the threshold set by Ariagno et al. (2022). Note that due to the discretization of the rainfall data record, this actually corresponds to a threshold of 48 mm/h (i.e., four tipping per minute).

The threshold for sediment entrainment ω_{cs} in the fluvial geomorphic law (SPACE) will also be calibrated to enhance the relative contribution of extreme rainfall event (Tucker, 2004). This

additional parameter is needed to highlight the physical processes, related to the increase in rainfall intensity, which lead to a strong non-linear response between rainfall and sediment exports. Including a sediment-entrainment threshold induces a decrease in the annual sediment export. We thus calibrate the erosion coefficient K_s together with the sediment entrainment threshold ω_{cs} to maintain a realistic annual sediment export. Therefore, in this step, we will use a higher K_s higher than in step two (II.2.2).

III.3. Model constraints and parameter values

The three geomorphic laws used in our model have a fairly large number of parameters (Table 1), which render the calibration phase complex. We therefore chose to fix some of the parameter values based on previous knowledge and analyses from our study site. Other parameter values were obtained from Draix observatory records or from calibration.

III.3.1. Fixed parameters

The topography is extracted from a 50-cm resolution digital elevation model (DEM) constructed from a 2015 lidar survey. Post-processing was conducted to fill voids (e.g., ensuring flow-path continuity) and decrease the resolution (i.e., increase the pixel size) in order to decrease the simulation duration. Thus, the model uses a grid of 2x2 m cells. Catchment boundaries are closed for water and sediment fluxes except for the outlet cell, which is set as a fixed boundary (water and sediment flow through it but no deposition occurs on this cell). The flow paths are computed using the FlowDirector and FlowAccumulator landlab components (Hobley et al., 2017), which use the steepest-slope algorithm. Drainage routing is run once at the beginning of the year but is not updated after each rainfall event, as the topography does not change significantly over the duration of the simulation (1 year). To account for evapotranspiration and deep infiltration effects, event runoff rate is defined by multiplying the event rainfall rate (cumulative rainfall divide by event duration), assuming that runoff duration is similar to rain duration, with the mean annual runoff coefficient $r_c = 0.38$, set by Mathys (2006) for the Laval catchment. The spatialized discharge field, used in the fluvial transport law, is then computed for each event as the product of the drainage area field and the event runoff rate.

Because we focus on the intra-annual dynamics, we run the model over a period of one year and we set the initial soil depth to zero every year. This procedure makes the model sensitive to the initial condition, in particular for soil depth, which is one of the most important variables we followed. However, on these badlands, the steady state do not exist because of the inter-annual variability in erosion and sediment yield. Thus, the initial forced conditions are designed to make sure that all the simulations share the same initial condition and therefore produce results that can be compared in terms of influence of the parameters that change from one year to the next (e.g., precipitation, number of events, temperature).

The regolith production function, ‘Exponential Weatherer Integrated’ in Landlab, simulates the winter production phase in our model. We set the maximum production rate (P_0) at 0.05

m/yr such that the resulting winter weathering produces an amount of regolith that is comparable to the annual erosion rate in the catchment (8 mm/yr), assuming that there is a balance between annual soil erosion and production. Similarly, the characteristic soil-production decay depth (Eq. 1) is set to $h_p^* = 0.1$ m (Table 1) based on regolith profile observations (Ariagno et al., in review). We do not take into account the potential change in density from bedrock to regolith in the component (SPACE, ‘large scale-eroder’) and thus keep the expansion factor as zero (default value).

In the transport-length diffusion component, the critical slope is set to $S_c = 1.4$ m/m based on field measurements (regolith is unstable on steeper slopes; Ariagno et al., in review) and previous morphometric analysis (Carriere et al., 2020). The critical slope prevents local deposition on hillslopes when the threshold is passed. This unusual high slope-threshold value can be explained by the cohesive lithology of marls, which creates aggregates that remain on the hillslopes, and the angular shapes of marly regolith fragments. The characteristic soil depth for diffusion (h_d^*) is chosen similar to the characteristic soil-production decay depth, i.e., 0.1 m. The transport-length scale was fixed as the grid cell ($\lambda = dx = 2$ m).

For the fluvial erosion component (SPACE, ‘large-scale eroder’), we prevent bedrock erosion by setting a small value of $K_r = 10^{-7}$ m⁻¹ since we assume that this process is not significant at the time scale of our simulation (not set to 0 because of numerical constraint). We simplified the model by setting sediment porosity and the fraction of permanently suspendable fines in bedrock to zero. We use “classic” values for the stream-power law exponents; $m = 0.5$ and $n = 1$ (Snyder et al., 2003; Whipple & Tucker, 1999; Wohl & David, 2008). We set the value of several parameters based on the study of Carriere et al. (2020), as the study area is the same. The alluvial depth scale h_f^* is fixed to 0.1 m. The settling velocity is taken as 10⁻⁴ m/yr, based on suspended particle sizes, leading to low deposition rates in the channels.

Parameter	Value	Units or dimensions	Short description
Exponential Weatherer integrated			
P	-	m/yr	Soil production rate
h	-	m	Soil thickness
P_0	0.05	m/yr	Maximum soil production rate
h_p^*	0.1	m	Characteristic soil depth (soil production)
Transport length diffusion			
K_d	-	m ² /yr	Diffusion coefficient (Eq 3)
K_{d_winter}	0.01	m/yr	Winter diffusion coefficient
K_{d_summer}	0.1	m/yr	Summer diffusion coefficient
$K_{d_intensity}$	50	m/yr	Intensity diffusion coefficient
h	-	m	Soil thickness
h_d^*	0.1	m	Characteristic soil depth (hillslopes transport)
E_h	-	m/yr	Locale erosion rate
D	-	m/yr	Local deposition rate

S	-	m/m	Slope
Sc	1.42	m/m	Critical slope
λ	2	m	Sediment-transport length scale
q_s	-	m^2/yr	Sediment flux per unit width
i	48	mm/h	Intensity threshold
SPACE			
Es	-	m/yr	Entrainment rate of sediment
h_f^*	0.1	m	Characteristic sediment thickness for fluvial transport
K_s	0.01 - 0.17- 0.5	m^{-1}	Sediment erodibility parameter
K_r	0	m^{-1}	Bedrock erodibility parameter
q_w	-	m^2/yr	Water discharge per unit channel width
ω_{cs}	0 - 30	m/yr	Threshold for sediment entrainment
ω_{cr}	0	m/yr	Threshold for bedrock erosion
Ds	-	m/yr	Deposition rate
V	1.0E-4	m/yr	Sediment settling velocity
cs	-	-	Sediment concentration in the water column
ff	0	-	Fraction of fine sediment
ϕ	0	-	Porosity
r_c	0.38	-	Annual runoff coefficient for Laval catchment

Other notations

Mass conservation equation

ρ_s	-	[M / L ³]	Bulk density of soil
ρ_r	-	[M / L ³]	Bulk density of bedrock
q	-	[L ² / T]	Soil flux vector
z	-	[L]	Elevation

Stream Power Law

e	-	[L / T]	Channel bedrock incision rate
K_f	-	[L ^{1-2m} T ⁻¹]	Erodibility coefficient
A	-	[L ²]	Drainage area
S	-	[L/L]	Slope
m	-	-	Area exponent of the stream power law
n	-	-	Slope exponent of the stream power law

Table 1: parameter values and notations. Note that the unit of K_d is from the Eq 3 where the units of $K_{d\text{-winter}}$ / $K_{d\text{-summer/intensity}}$ are from the equation of Shobe et al. (2017)

III.3.2. Parameters constrained from Draix observatory records

We use detailed rainfall records, measured with a tipping-bucket rain gauge located at the outlet of the Laval catchment, to generate unique rainfall event series for each year. The method for extracting rainfall events from the raw rainfall dataset is based on the protocol described by Mathys (2006) (Appendice 10). We used records from the 2006-2021 period,

excluding 2013 because the rainfall dataset for that year contained too many gaps. 43 rainfall events per year were extracted on average, with a minimum of 28 events for 2006 and a maximum of 61 events for 2018. From these rainfall-event series, we extracted three variables characterizing each event, which will be used in the model to define a realistic input discharge field (used to compute the fluvial erosion in SPACE): (1) the duration of the rainfall event; with a mean event duration of 726 min and extreme values of 3 and 6790 min; (2) the cumulative rainfall, varying between 1.0 and 152.2 mm with an average of 18.8 mm; and (3) the maximum instantaneous rainfall intensity; ranging from 1.5 to 180 mm/min. The intensity value retained for each event is the value of the maximum instantaneous intensity observed over the duration of the rainfall event.

Sediment yield is measured at the outlet of the Laval catchment, where a hydro-sedimentary station has been set up to monitor water discharge, suspended sediment load and bedload. Suspended sediment concentration is measured with automatic samplers and turbidimeters and suspended sediment flux is computed as the product of discharge and concentration, cumulated over a flood to obtain an event-scale yield. Bedload volumes are measured after each flood by topographic surveys of a sediment trap located immediately upstream of the station. Bedload volume is converted into mass using a density of 1700 kg/m³, constrained by measurements in the sediment trap (Mathys, 2006). The raw data we use is therefore a series of event-scale sediment yields. We compute monthly sediment-export values by summing the flood records for each month, as sediment export is considered negligible during low flow. The sediment-export amounts considered here thus comprise both suspended load and bedload. For a few flood events, data on either suspended load or bedload was missing. In such cases, we reconstructed the event-scale suspended sediment yield based on the average proportions of suspended load and bedload, computed from multiple complete years of total load records (see Ariagno et al., 2022 for details).

III.3.3. Calibrated parameters

The sediment erodibility coefficient (K_s) in the alluvial transport law (Eqs. 6, 7), the entrainment threshold (ω_{cs}) and the diffusion coefficients ($K_{d\text{-winter}}$ and $K_{d\text{-summer}}$) in the Transport-Length Diffusion law (Eqs. 3, 4) are the main parameters that we calibrate in the model. The model is particularly sensitive to K_s , as this parameter controls sediment transport through the drainage network and the amount of sediment ultimately exiting the model during the simulation. As the dominant diffusion processes differ for each season, the value of $K_{d\text{-winter}}$ was allowed to vary between 0.1 and 1 m/yr and the value of $K_{d\text{-summer}}$ vary between 1 and 5 m/yr. In order to simulate intense rain-splash erosion and overland flow during high-intensity rainfall events, we include an increased diffusivity, $K_{d\text{-intensity}}$, during these events in the third step of the modelling procedure. The value of $K_{d\text{-intensity}}$ is allowed to vary between 40 and 100 m/yr.

The sediment threshold entrainment ω_{cs} is first set to 0 to simplify the model. In the third phase, we allow non-zero values to better account for a non-linear sediment-transport response to rainfall intensity and calibrated the threshold value based on simulated sediment exports. Here we use a manual calibration procedure, with a step-by-step progression that

aims to optimize both the mean annual sediment export and the intra-annual variability in soil depth across the catchment.

Results

III.3.4. Initial model

For our initial model, which combines the SPACE and TLD components during the summer phase with an unlimited hillslope regolith supply, the simulated monthly sediment export is strongly linearly correlated with the monthly rainfall ($R^2 = 0.93$; Figure 24). In such a purely transport-limited modeling setup, both the highest monthly rainfall (~120 mm) and the highest monthly simulated sediment export (~2000 t) occur in November. The model-predicted annual sediment export best matches the observed mean annual sediment export recorded between 2006 and 2021 (13260 t) for transport-parameter values of $K_s = 0.01 \text{ m}^{-1}$ and $K_{d\text{-summer}} = 1 \text{ m/yr}$. We also checked that the hillslope and fluvial components were correctly coupled with transfer of sediment from hillslopes to the main drainage network respecting conservation of volumes (see Appendix 11).

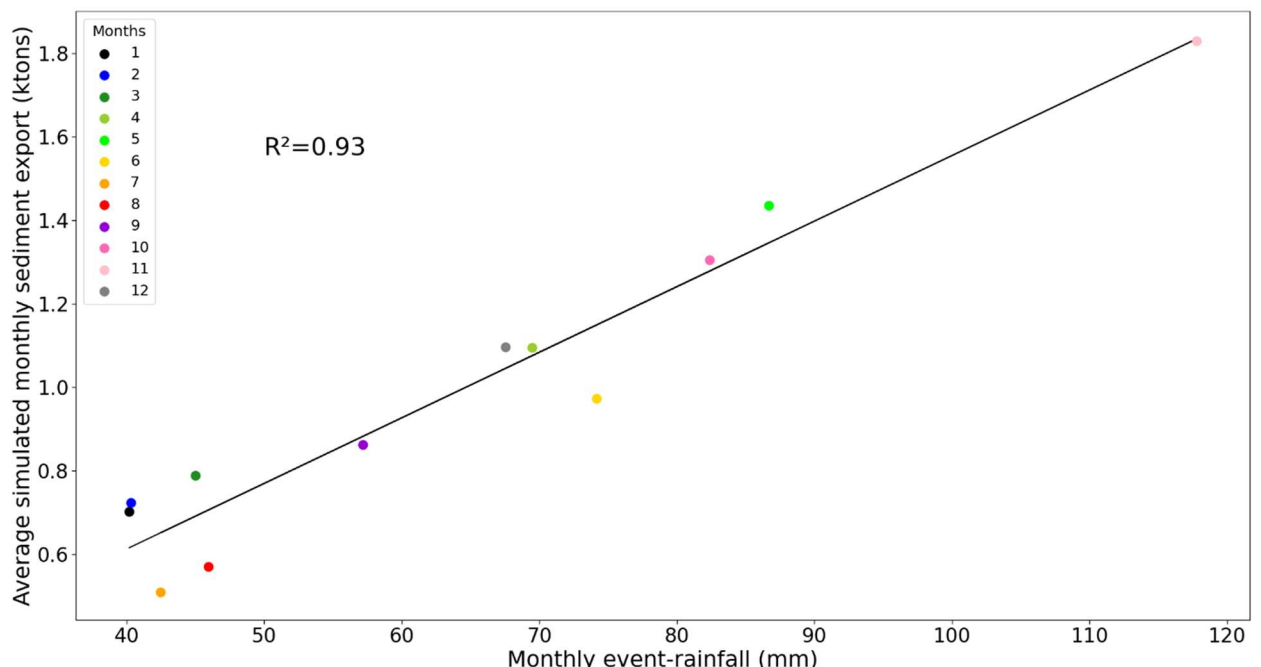


Figure 24: Monthly simulated sediment export versus cumulative monthly event-rainfall using interannual monthly average values from the Laval catchment between 2003 and 2021 (except 2013). The strong linear correlation ($R^2 = 0.93$) is highlighted (black line). Note that here, the monthly rainfall (x axis) is computed as the sum of event rainfall during the month, and is therefore slightly lower than the total monthly rainfall reported by Ariagno et al. (2022).

III.3.5. Including soil production and sediment availability

Next, we incorporate the winter simulation phase in the model; regolith is now produced, in limited amounts, by winter weathering. This part requires the calibration of the new

parameter $K_{d\text{-winter}}$ based on two criteria: mean annual sediment export and soil depth. This phase also implies (1) an adjustment of K_s to maintain annual export close to observed values and spatio-temporal trends in the drainage network; (2) a new calibration of $K_{d\text{-summer}}$. These changes affect the hysteresis pattern between rainfall and sediment export, with the appearance of a supply-limited regime at the end of the year.

We tested several combinations of K_s - $K_{d\text{-winter}}$ to minimize the difference between average annual records (~ 13300 t) and simulated annual sediment export of the Laval catchment. $K_{d\text{-summer}}$ was fixed to 5 m/yr during this calibration; this number is justified below. For each parameter combination, the model is run for 15 years (2006 to 2021, except 2013) and we compute the difference between observed and simulated mean annual sediment export. Results are shown in Figure 25. Annotations in the grid show the simulated mean annual sediment export and color indicates the difference between observed and simulated values. The best combination of K_s - $K_{d\text{-winter}}$ is found for $K_s = 0.1$ m $^{-1}$ and a $K_{d\text{-winter}} = 0.01 - 0.1$ m/yr (black box).

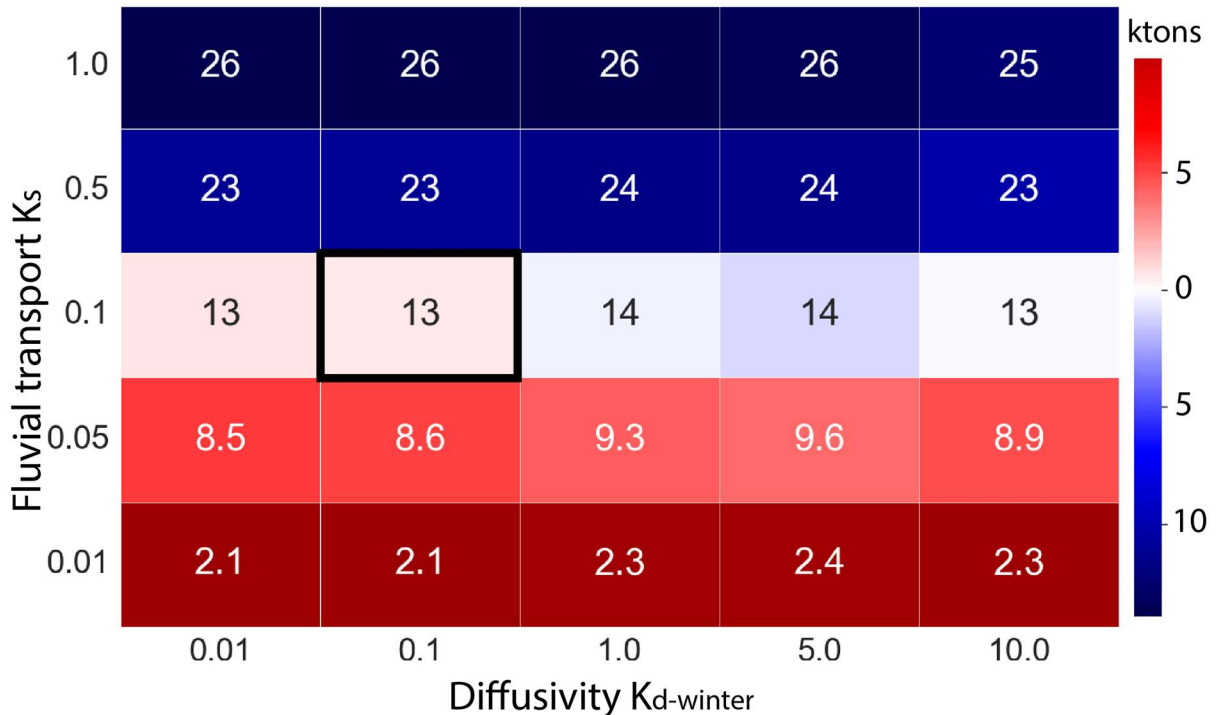


Figure 25: Calibration matrix between the fluvial transport coefficient K_s and the diffusion coefficient $K_{d\text{-winter}}$. Numbers indicate the cumulative annual sediment export predicted by the model (in kton); colors indicate the difference between the real (~ 13.3 kton) and simulated sediments exports. Red implies a deficit of sediment produced by the model while blue means an excess of model sediment export compared to the field records. Black box indicates the couple of parameter values chosen in the model.

Running the model with the previously calibrated values for K_s and $K_{d\text{-winter}}$ induces an incomplete transfer of sediment from the intermediate to the main channels (Fig. 25A). In contrast, Ariagno et al. (2022) showed, based on field data, that sediment residence time is not more than one year in the Laval, which implies that there is no storage of sediment in the drainage network at the end of the year. Thus, we increase the fluvial transport parameter to

$K_s = 0.17 \text{ m}^{-1}$ in order to predict an average sediment thickness in the main channel that is higher than in the intermediate channels at the end of each year (Figure 26B). Sediment thickness in channels and soil depth on hillslopes show different trends; while soil depth on hillslopes decreases constantly during the year, the main channel overall records a constant sediment thickness with a slight increase at the end of the year.

Soil depth on steep hillslopes ($\sim 1.1 \text{ cm}$) decreases quickly during the first rainfall events of the year and then decreases slowly to zero. The interfluves show a similar trend with less erosion overall (from $\sim 1.25 \text{ cm}$ to 0.24 cm). Most hillslopes (the ‘regular slopes’) record less erosion, with a constant decrease in soil depth over the year (from $\sim 1.4 \text{ cm}$ to $\sim 0.75 \text{ cm}$). The higher erosion observed on interfluves compared to regular slopes is due to the diffusion process, which enhances erosion on convex slopes.

Because the addition of a winter period, i.e., of a soil production period, modified the seasonal sediment dynamics, the summer diffusivity K_{d_summer} has also been recalibrated by comparison with the soil depth in the main compartments (Figure 27). The average erosion rate in the Laval catchment is around 6 mm/yr , when the annual sediment yield is attributed to homogeneous erosion from the whole catchment or 8 mm/yr when considering that only non-vegetated areas are eroded. Overall, soil depth decreases with increasing summer diffusivity, except for regular slopes for small K_{d_summer} . Interfluves show rapid and strong erosion with increasing K_{d_summer} , such that no soil is left at the end of the year for high K_{d_summer} , while soil depth on regular slopes decreases slowly with the increase of K_{d_summer} . The soil depth recorded from the simulations at the end of the year on the regular slopes compartment (probably a mixture of vegetated and unvegetated hillslopes) matches with the catchment erosion magnitude for $K_{d_summer} \leq 10 \text{ m/yr}$. However, a value of $K_{d_summer} = 10 \text{ m/yr}$ induces much more erosion on the interfluves and overestimates even more the erosion on the total catchment. Thus, among the five values of K_{d_summer} tested, we observed that the soil depth spatial and temporal trends, checked by looking at the three different compartments, are most consistent with observed erosion rate for $K_{d_summer} = 5 \text{ m/yr}$. This value of the summer diffusivity is higher than in the previous phase (5 versus 1 m/yr), which is consistent with the decreasing sediment availability for this modeling phase.

The combination of a limited initial soil depth and depth-dependent erosion functions produces supply-limited conditions at the end of the year and results into a seasonal hysteresis pattern of simulated sediment export against rainfall (Figure 28A). The rainfall peak in November ($\sim 110 \text{ mm}$) induces roughly a similar sediment export than in the original model (Figure 21) but the relative contribution of spring peak and November peak are not well captured. While both July and August are characterized by low export ($\sim 750 \text{ t}$) and rainfall ($\sim 45 \text{ mm}$) values, the winter period (January, February) shows higher sediments export ($\sim 1700 \text{ t}$) than in the real data ($\sim 300 \text{ t}$; Figure 21). The model simulates maximum sediment export around April-May ($\sim 2250 \text{ t}$) with a linear trend between export and rainfall in the early spring, as in the first setup of the model (Figure 24), but sediment exports decrease at the end of the year, illustrating the expected supply-limited regime.

We also compare the model results in the case where $K_{d_summer} = K_{d_winter}$, calibrated previously (Figure 25; $K_{d_winter} = 0.1 \text{ m/yr}$). As expected when diffusion processes are increased, monthly,

and thus annual, sediment export increase but the general shape of the hysteresis is not affected by the value of $K_{d\text{-summer}}$ (Appendice 12).

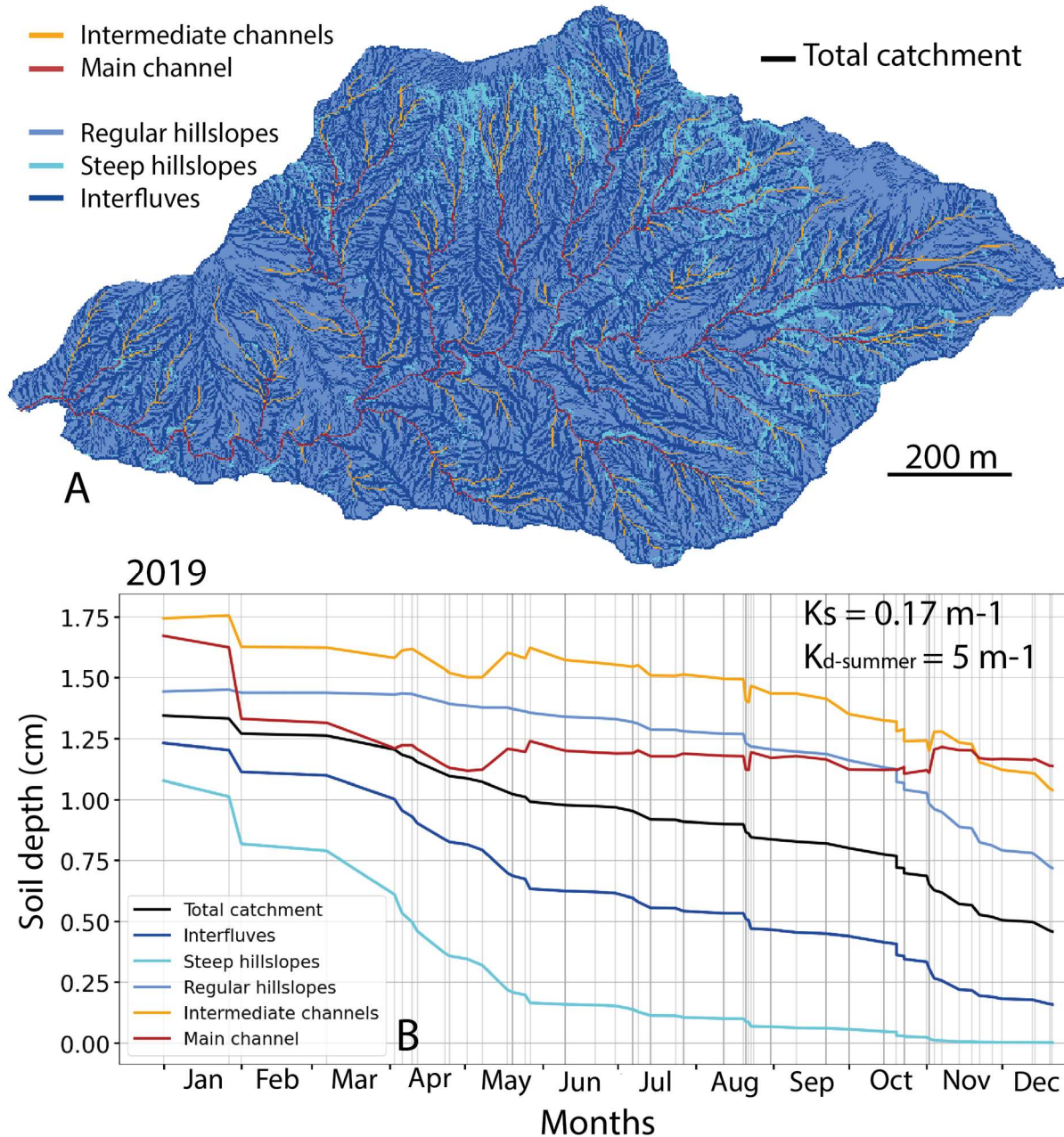


Figure 26: A) Map of the Laval catchment showing the different compartments tracked in the model and separated on the basis of slope and drainage area (A). Blue colors show hillslopes whereas orange and red show the drainage network. The quantitative definition of these compartments is given in the text. B) Predicted evolution of soil depth over one year (2019) in the different compartments of the catchment. Colors refer to the compartments shown in A; the black line shows the average soil depth for the whole catchment. The soil depth at the end of the winter constitutes the initial soil depth shown here. Vertical lines represent single rainfall events. Darker grey lines highlight the events with a rainfall intensity above 50 mm/h. Soil depth evolution records are shown for with $K_s = 0.17 \text{ m}^{-1}$ and $K_{d\text{-summer}} = 5 \text{ m/yr}$.

The high inter-annual variability of monthly cumulative rainfall and sediment export recorded at Draix, highlighted by previous studies (Ariagno et al., 2022; Mathys, 2006), is also seen in the annual rainfall-event series and simulated sediment exports (Figure 28B). Despite the

illustrated variability, two distinct trends emerge from the model predictions (Figure 28B; grey dashed lines): the first part of the year (January to May) induces higher sediment export than the second part of the year (June to December) for similar monthly rainfall amounts.

Therefore, the incorporation of a depth-dependent condition in the erosion laws of the model leads to simulate a clockwise hysteresis trend between rainfall and exports in the second half of the year, evidence for a supply-limited regime. However, the anti-clockwise loop of the original hysteresis (Fig. 2) is not reproduced by the model, meaning that erosion processes in the first part of the year are not correctly simulated, which motivates the next modeling step.

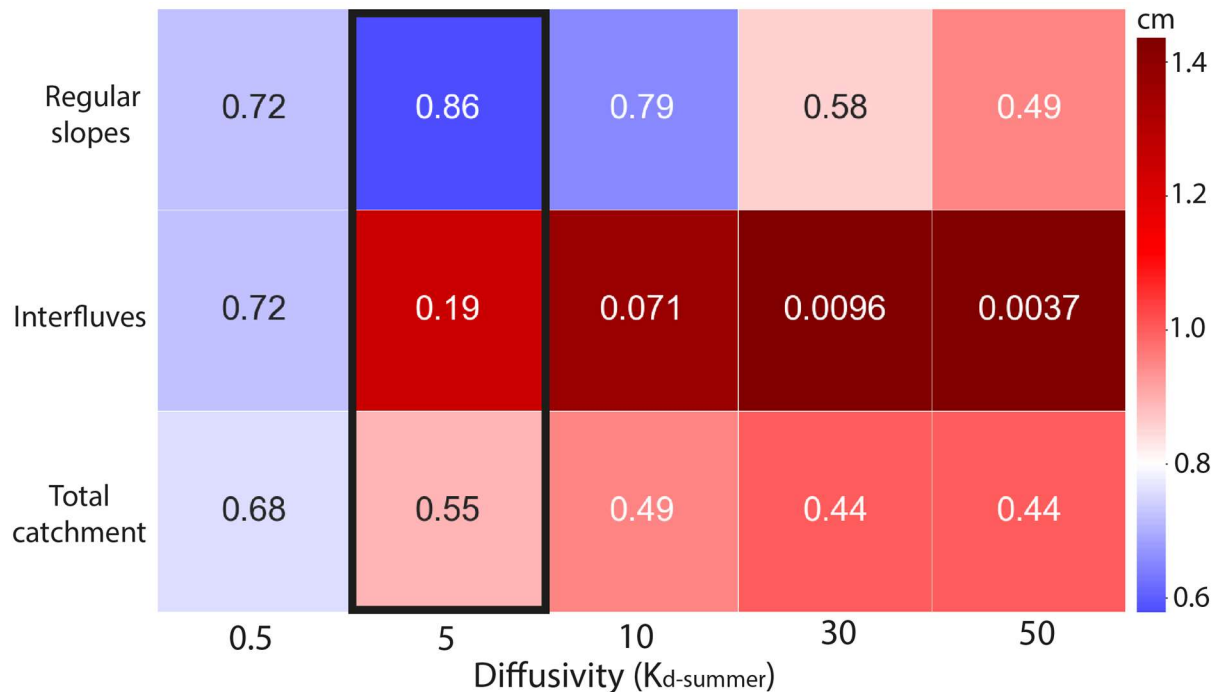


Figure 27: Calibration matrix for the diffusivity coefficient during the summer loop ($K_{d\text{-summer}}$). Numbers indicates the soil depth (cm) at the end of the year in the different compartments while colors show the difference between the initial and the final soil depth (i.e. the depth removed). Red shades indicate an excess of erosion compared to the average annual erosion (~8 mm) recorded in the Laval catchment, based on the long-term sediment-export dataset. Blue shades indicate a deficit of erosion compared to the reference value.

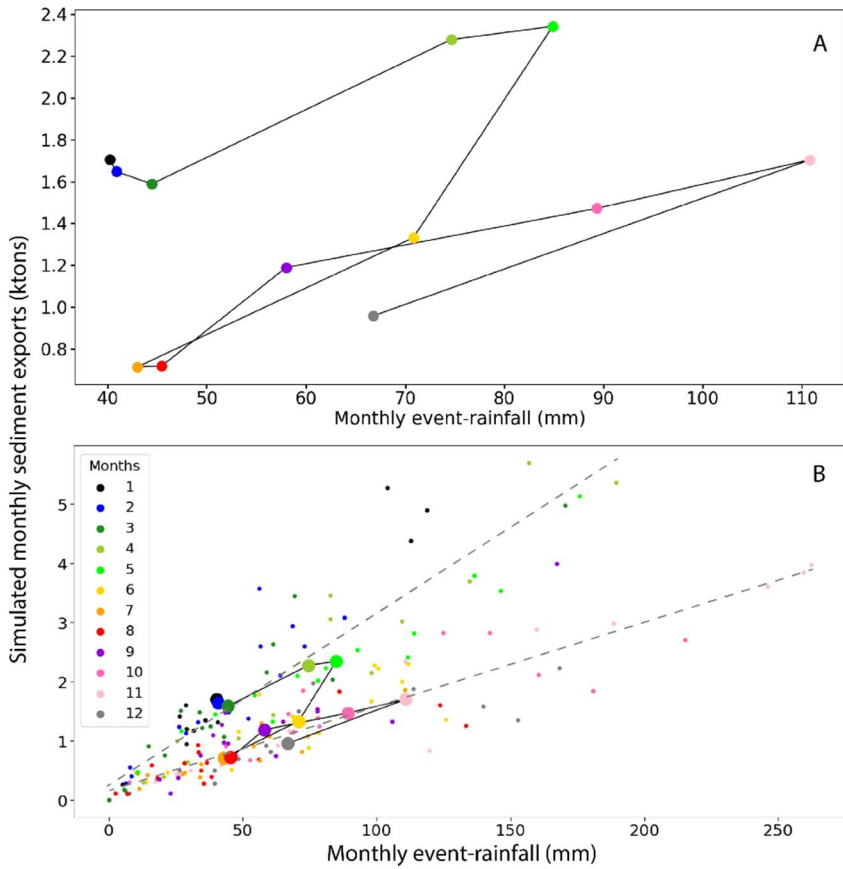


Figure 28: Hysteresis plot of monthly sediment export versus monthly cumulative event rainfall, simulated with depth-dependent soil production and transport laws. A) Inter-annual average of monthly simulated values. The hysteresis cycles illustrates two separate maxima: moderate rainfall and high sediment export in May versus high rainfall and moderate sediment export in November. Solid black line shows the hysteresis cycle with $K_{d\text{-winter}} = 0.1 \text{ m/yr}$ and $K_{d\text{-summer}} = 5 \text{ m/yr}$. B) Individual monthly values (small colored dots) illustrating the variability of the results. Large dots are the average monthly values as shown in A for $K_{d\text{-summer}} = 5 \text{ m/yr}$. Dashed grey lines highlight two separate seasonal trends: winter and early spring months (Jan.-May) induce higher

sediment exports than summer and autumn months (Jun.-Dec.), expressing the transition from a transport-limited to a supply-limited regime.

III.3.6. Including rainfall intensity and fluvial transport threshold

This third stage is designed to insert sensitivity to rainfall intensity in the model in order to account for the non-linear relation between rainfall and sediment export observed in the Draix catchment (Fig. 2). We pursue this goal by: (1) modulating summer hillslope diffusivity according to rainfall intensity; (2) adding a non-zero sediment entrainment threshold in the fluvial system, and consequently adjust the couple $K_s - \omega_{cs}$ to maintain consistency with the recorded mean annual sediment export; and (3) calibrating the diffusivity coefficient $K_{d\text{-intensity}}$ to enhance the diffusion processes during extreme events and reproduce the anti-clockwise hysteresis loop observed during the first half of the year.

Concerning the second point, we use a similar approach as for the calibration between K_s and $K_{d\text{-winter}}$, and calibrate the entrainment threshold (ω_{cs}) based on the difference between simulated and observed annual sediment exports (Figure 29). There is a tradeoff between combinations of $K_s - \omega_{cs}$; three of the tested combinations (0.17 - 2; 0.3 - 10; 0.5 - 30) give consistent results in terms of annual sediment export (~13.3 kton). The evolution of the hysteresis cycle have been analyzed for these three combinations but we will only discuss the results for $(K_s, \omega_{cs}) = (0.5, 30)$ because the higher threshold value emphasizes the trends that emerge. With this calibration, the evolution of soil depth during 2019, which is one of the years that record the highest number of rainfall events, shows an incomplete transfer of the sediment from hillslopes to the main channel (as in the previous modeling phase). Because

sediment transfer should be at least confirmed for this year, we slightly increase K_s from 0.5 to 0.6 m^{-1} (i.e., discuss the results for $(K_s, \omega_{cs}) = (0.6, 30)$) to avoid sediment storage in the drainage network. This change induces an increase of the mean annual sediment export, from 14.4 to 16.4 ktons.

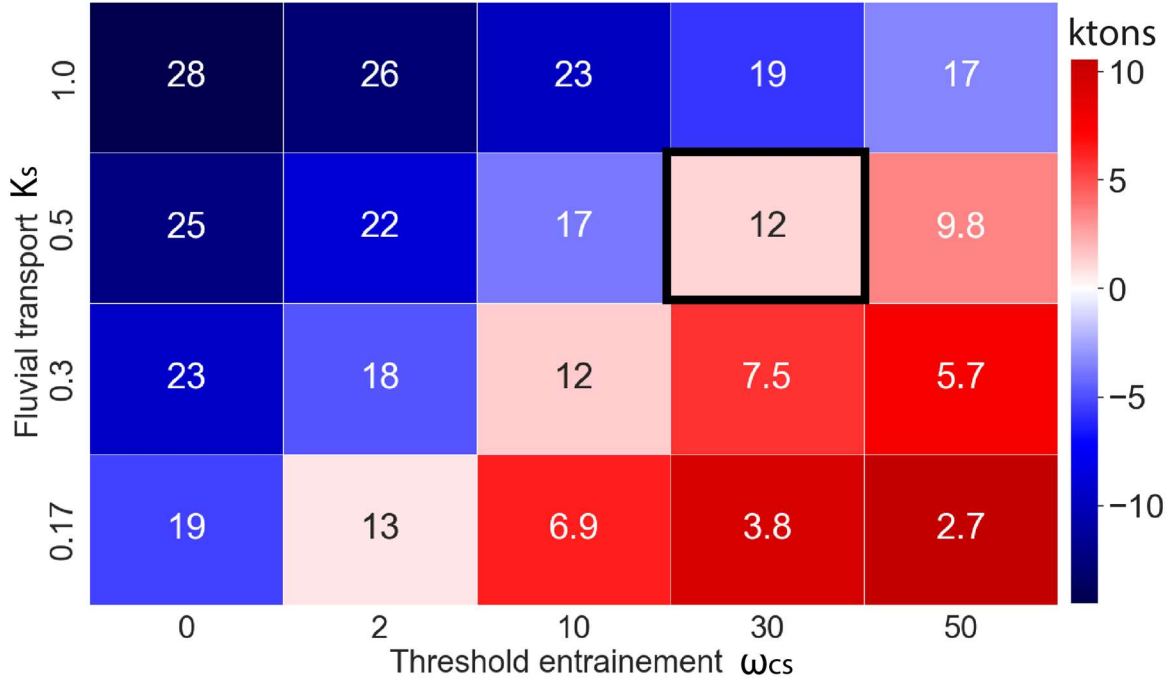


Figure 29: Calibration matrix between fluvial transport coefficient K_s and the sediment entrainment threshold ω_{cs} . Numbers indicates the total sediment export at the end of the year (in kton) while colors show the difference between real (~ 13.3 kton) and simulated sediments export. Red implies a deficit of sediment exported by the model while blue means an excess of model sediment export compared to the field records. Black box indicates the parameter combination chosen to run the model with the entrainment threshold.

Next we compare three configurations: (1) with an increased hillslope diffusivity for high intensity events, but no entrainment threshold in the fluvial system, (2) with an increased hillslope diffusivity for high intensity events and with an entrainment threshold in the fluvial system, and (3) same with an increased $K_{d\text{-intensity}}$.

The introduction of an intensity threshold to increase the diffusive coefficient $K_{d\text{-summer}}$ does not induce the expected change in the shape of the hysteresis cycle by itself: the spring export peak do not show an anticlockwise loop. The strong increase of the sediment export is mainly due to the increased of the K_s (i.e., from 0.17 to 0.6 m^{-1} ; Figure 28A, Figure 30A). The associated soil-depth evolution (Figure 30D) shows strong erosion in all compartments at the beginning of the year, with a particularly rapid loss of material in the channels ($\sim 1 \text{ cm}$ in the first two months). From June, channel sediment thickness increases significantly, but does not reach its initial value ($\sim 1.5 \text{ cm}$), before decreasing more gradually from October. In overall, hillslopes record an acceleration of erosion starting in March (i.e., a loss of soil depth), which is less significant for regular slopes than for interfluves. Note that the integration a fluvial sediment entrainment threshold alone does not induce the expected changes on the hysteresis cycle either. The sediment exports are reduced, and in particular, for the autumn months, but the spring anticlockwise loop does not appear.

The addition in the model of a sediment entrainment threshold ($\omega_{cs} = 30$ m/yr), combined with an increased diffusion coefficient $K_{d\text{-intensity}} = 40$ m/yr for the high-intensity events (mostly in summer), produces an anti-clockwise loop during spring months (Figure 30B), resembling the observed hysteresis cycle (Figure 21). However, the sediment export peak is still in May (~1.8 kton) as in Figure 28A and November export peak (~1.6 kton) remains high, which is in contradiction with the observed hysteresis (Figure 21). Thus, the association of a fluvial sediment entrainment threshold and an increased hillslope diffusivity for high-intensity events induces the correct hysteresis pattern (one anticlockwise loop, followed by a clockwise loop) but does not reproduce the observed magnitudes. Soil depth predictions for this calibration (Figure 30E) show a strong increase of sediment thickness in channels from June, becoming higher than the initial thickness. While sediment thickness in the intermediate channels slightly decreases at the end of the year, it is continuously increasing, albeit more slowly, in the main channels. In contrast with interfluves and steep hillslopes, regular hillslopes show a slight increase in soil depth until June/July and then decrease during the rest of the year.

The $K_{d\text{-intensity}}$ value becomes critical to enhance the sediment export in June; a value of $K_{d\text{-intensity}} = 100$ m/yr leads to a hysteresis cycle that shows almost similar characteristic to the observed one (Figure 30C). However, the difference between spring sediment export (May, June; ~2 kton) and autumn sediment export (October, November; ~1.6 kton) remains much smaller in the model predictions than in the observations. For this last calibration, the soil-depth evolution (Figure 30F) shows a similar pattern in all compartments as in the previous one (Figure 30E), but with twice as much variability for the channels.

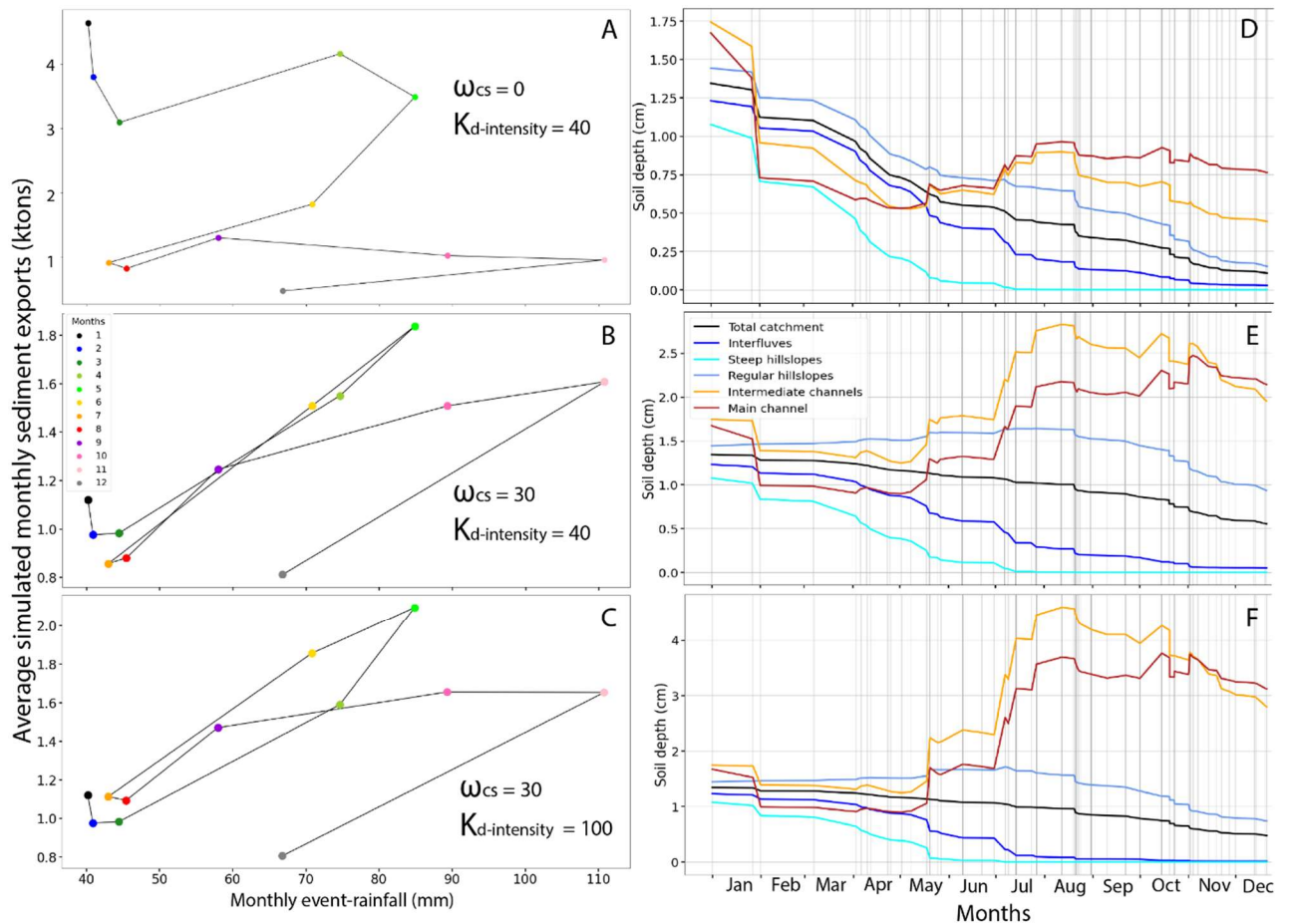


Figure 30: Hysteresis cycle and soil-depth evolution predicted by different combinations of the sediment entrainment threshold (ω_{cs}) and the diffusivity coefficient during intense rainfall events $K_d\text{-intensity}$. Fluvial sediment erodibility parameter $K_s = 0.6 \text{ m}^{-1}$. A-B-C) Hysteresis plots of simulated sediment export (kton) versus monthly cumulated event rainfall (mm), using inter-annual monthly average values. Compared to the previous simulated hysteresis loop (Figure 28A); A) the strong increase of the winter monthly sediment export is due to the increase of K_s . The two separate peaks for sediment export in May and rainfall in November remain clear; B) The spring loop becomes anticlockwise, which express the effect of rainfall intensity. Autumn sediment export is more significant compared to the spring peak. May records the highest sediment export; C) With an increase of the diffusivity coefficient $K_d\text{-intensity}$ from 40 to 100 m/yr, the spring sediment-export peak becomes dominant as expected (Figure 21). D-E-F) Soil-depth evolution in different compartments for one year (2019); D) Without sediment entrainment threshold ω_{cs} , the peak sediment thickness in the channels does not exceed the initial sediment thickness; E) With the addition of a sediment entrainment threshold $\omega_{cs} = 30 \text{ m/yr}$, sediment thickness in channels starts to increase whereas soil depth on regular slopes stabilizes and then decreases. The peak in sediment thickness in channels is slightly higher than the initial sediment thickness; F) With a higher diffusivity during extreme rainfall events ($K_d\text{-intensity} = 100 \text{ m/yr}$), soil depth on regular hillslopes increases until June / July and then decreases as the channels are filling. Sediment thickness in channels is twice higher at the end of the year than in the initial state.

III.4. Discussion

III.4.1. The Draix model: a tool to reproduce observed sediment dynamics

III.4.1.1. A simple model to validate the precipitation - sediment-export correlation

We explore, for the first time, the combination between non-local hillslope diffusion (TLD) and fluvial erosion with alluvium conservation (SPACE) in a landscape evolution model in order to simulate the interaction between hillslope and channels processes. We observe a clear transfer of solid sediment from upstream to downstream compartments, which shows the suitability of this association (Appendice 11). In particular, the model reproduces a key field observation: channels are filled with sediment from hillslopes by dry ravel processes early in the year (i.e., sediment thickness increases), and are washed out by floods (i.e., sediment thickness decreases) during late spring to autumn. Steep hillslopes, (i.e., with slopes higher than the critical slope), are particularly impacted by the non-local diffusion and record more erosion at the end of the year.

A linear relation between sediment export and rainfall at annual timescales is generally expected (Giménez et al., 2012). However, such a simple linear relation fails to illustrate the complexity of the observed sediment dynamics in the Draix catchments. Our initial model (II.3.1 & III.1) reproduces the first-order control of rainfall on erosion rate found for the marly catchments of Draix (Mathys, 2006; Ariagno et al., (2022). Thus, it translates the behaviour of a catchment in a constant transport-limited regime, where sediment availability is unlimited and where sediment export is controlled only by the amount of rainfall. In that case, sediment yield would be easily predicted with climatological station records.

III.4.1.2. Non-local diffusion

We have shown through different setup that the Transport Length Diffusion component is an efficient tool to model rapid sediment transfers from hillslopes, and in particular steep hillslopes, to the channels at their base. This process is even more relevant for badlands, where high rate of erosion are recorded and where the dissected and sharp landscape enhances the dry ravel phenomenon and rainfall-induced slope destabilization. We have modulated the intensity of this diffusion process by introducing different values with the erodibility coefficient K_d , according to the season, because hillslope erosion is dominated by different physical processes: dry ravel in winter; rainsplash and overland flow in summer. We found that sediment export is not very sensitive to $K_{d-winter}$, which only induces small variations of the order of 1 kton (Figure 25). However, the distribution of sediment across the catchment is strongly affected by winter diffusion, even for a small value of $K_{d-winter}$. At the end of winter, the modeled soil depth is distributed heterogeneously in the different compartments (Figure 26A), which highlights that this diffusion process induces morphological changes over short

time scales and represents a first process driving annual sediment dynamics in these catchments.

Like the winter diffusion, the summer diffusion enhances this initial separation between hillslopes and the drainage network: applying the TLD for each rainfall event results into thinning hillslope regolith down and supplying material to channels. As expected, steep slopes record the strongest soil loss because the process is focused on these areas. However, hillslopes with gradients lower than the critical slope threshold can temporarily store sediments arriving from steep slopes uphill. Such sediment transfer from steep to gentle slopes induces the increasing soil depth in the regular hillslopes compartment (Figure 26A) for relatively small values of $K_{d\text{-summer}}$. For larger values of $K_{d\text{-summer}}$, the erosion term exceeds the deposition term and regolith thickness is decreased on all slopes.

III.4.1.3. Impact of depth-dependent hillslope processes

Rendering hillslope erosion dependent on soil thickness leads to a slowdown of soil erosion, particularly on steep hillslopes, when soil depth approaches zero (Figure 26B). The limitation of the initial soil thickness in the summer loop by only considering soil produced during the winter period (0.0134 m on average) aims to induce a supply-limited condition in the annual sediment-export trend. The hysteresis cycle with two clockwise loops that we obtained (Figure 28A) illustrates the lack of sediment availability at the end of the year. The monthly variability of simulated sediment export and event-rainfall (Figure 28B) clearly highlights the two trends, each associated to a seasonal loop. Between January and May, the excess of mobile sediment in the catchment induces a transport-limited system where sediment export increases linearly with the increase of rainfall. Summer and autumn (from June to December) show less sediment export for overall higher rainfall, as the supply of mobile sediment runs out after the spring. We conclude from this experiment that the use of depth-dependent geomorphic transport laws, coupled with a limited production of regolith, can explain the observed transition from a transport-limited to a supply-limited regime in the Laval catchment.

However, the difference between the spring and autumn sediment-export peaks is lower in the model than in the observed data. The transition between the two loops (corresponding to the months of July, August and September) also shows (1) particularly low sediment-export values and (2) a positive linear correlation between rainfall and sediment export during autumn. These predictions are significantly different from the observed hysteresis loop (Figure 21), which records high sediment-export values during summer and no correlation between sediment export and rainfall in autumn.

III.4.1.4. Modelling rainfall-intensity controls on sediment export.

We hypothesize that rainfall intensity, identified as the driver of the spring sediment-export peak (Ariagno et al., 2022), enhances diffusion processes on marly hillslopes (Mathys et al., 2005). We therefore introduced an increased diffusivity coefficient during intense rainfall

events, $K_{d\text{-intensity}}$, to account for the fact that such events are extremely efficient in mobilizing hillslope sediments, and may therefore induce the observed late-spring peak in sediment export. However, increasing the summer diffusivity for high intensity rainfall does not induce the expected pattern in the simulated hysteresis cycle (Figure 30A). The associated simulated soil-depth records in the different compartments of the catchment (Figure 30D) show that including this intensity threshold tends to accelerate sediment transfer from interfluves to regular slopes and channels. This input of mobile material in the channels is then transported during floods, which explains the increase in sediment export during the spring months. However, high predicted sediment export during the months January to March in this model are inconsistent with the observations. This model behavior is explained by (1) high sediment availability on hillslopes at the end of winter – these sediments are easily mobilized by one significant rainfall event; (2) the increased fluvial erosion coefficient K_s , which leads to efficient sediment transport through the drainage network. Autumn sediment export mainly results from the mobilization of sediment that was temporarily stored in the (low order) channels, as hillslopes run out of sediment after this intense spring period of erosion.

The setting of an entrainment threshold ω_{cs} is critical for inducing the initial anti-clockwise loop in the observed hysteresis cycle (Figure 30B); the entrainment threshold leads to a strongly non-linear relation between rainfall and sediment export and a dominant contribution of extreme events.

The evolution of soil depth in the different compartments of the catchment for this final model setup (Figure 30E) shows the effect of the different parameters on the sediment dynamics. The sediment transit is enhanced by the high value of $K_s = 0.6 \text{ m}^{-1}$ used here. The introduction of a higher $K_{d\text{-summer}}$ ($K_{d\text{-intensity}}$) for events above a threshold intensity (i.e., $i = 50 \text{ mm/h}$) increases erosion on steep hillslopes, induces deposition on regular slopes and lead to an excess of sediment in the drainage network that cannot be washed out immediately. This behavior is illustrated by the ‘bump’ in sediment thickness in the channels during late spring/summer, which depends of the magnitude of $K_{d\text{-intensity}}$ (Figure 30D). For a couple $K_s - \omega_{cs} = 0.6 - 30 \text{ m}^{-1}\text{-m/yr}$, the anti-clockwise loop does not appear for $K_{d\text{-intensity}} < 35 \text{ m/yr}$. A slightly higher $K_{d\text{-intensity}}$ value of $\sim 40 \text{ m/yr}$ induces the expected transport-limited loop shape but with sediment export peaking in May and decreasing rapidly during summer (Figure 30B). Then, the increase of $K_{d\text{-intensity}}$ above 40 m/yr (Figure 30C) tends to increase the summer sediment export, since rainfall of high intensity mostly occur in summer in studied period (2006-2021).

We found that the predicted peak of sediment export in spring was particularly smaller than in the observed hysteresis (Figure 21) with the value of $K_{d\text{-intensity}} = 100 \text{ m/yr}$ and stay similar for the highest value that we tested (i.e., $K_{d\text{-intensity}} = 150 \text{ m/yr}$). The sediment-export peak, recorded in May with the parameter combination $K_s - \omega_{cs} = 0.6 - 30 \text{ m}^{-1}\text{-m/yr}$, is explained by the strong increase of sediment thickness in the channels (Figure 30E-F), starting in May. The lower rate of erosion during the first part of the year along with sediment storage on regular hillslopes induces this intense and rapid transfer of sediment when the threshold is passed, i.e., when rainfall intensity is sufficient to induce rapid hillslope diffusion.

Finally, we conclude that it is the combination of an increased hillslope diffusivity for high intensity events, and a fluvial entrainment threshold, which allows simulating a similar spring sediment exports trend.

Previous studies have shown that rainfall intensity is a main driver of the sediment-export peak during the spring (Ariagno et al., 2022; Mathys et al., 2005). In this landscape evolution model we developed, the simple addition of an intensity-dependent hillslope diffusivity coefficient does not induce any change in the sediment-export dynamics. Including an entrainment threshold (ω_{cs}) in the fluvial process law is also needed to make the model more sensitive to the rainfall intensity, and thereby to increase sediment export during the summer months in comparison to the early spring and autumn. The integration of a threshold for fluvial entrainment is a required condition to reproduce the observed hysteresis pattern. This parameter affects sediment export during extreme events if sufficient sediment is available in the upstream part of the catchment, which explains the required coupling of the entrainment threshold and the intensity-dependant hillslope diffusivity coefficient.

III.4.2. Limits of the model

Although our final model succeeds in reproducing some of the first-order observations on sediment dynamics in the Laval catchment, in terms of the hysteresis loop in sediment export and the intra-annual evolution of soil depth, it does contain simplifications that limit its application. Since we were particularly interested in the intra-annual dynamics, we run the model over a period of one year and we reinitiate the initial soil depth every year. This setup allows to simplify the model but render the comparison of simulated soil depth with field measurements in winter and at the end of autumn (Ariagno et al., in review) less direct, as the model underestimates erosion during these periods.

Although we demonstrate that the transport-length diffusion (TLD) component is a relevant and useful tool for short time-scale simulations, our landscape-evolution model is mostly sensitive to the fluvial-transport law (SPACE). The calibration of K_d for the winter period (Figure 25), based on the recorded annual sediment export, indicates a weak sensitivity to this parameter, showing a change of only 1 kton in the simulated sediment export (e.g. 7%) for a three-orders-of-magnitude variation in $K_{d-winter}$ values (0.01 to 10 m/yr). In contrast, even a small change in the fluvial transport coefficient K_s is sufficient to cause a significant increase or decrease in the simulated sediment exports. This limit can be overcome by looking at the distribution of soil depth over the catchment (Figure 26B, 8) as the TLD component induces transfer of sediments within the hillslope compartments. We used the regolith thickness to calibrate $K_{d-summer}$ because this thickness has been estimated in the Laval catchment with several approaches by previous studies (Malet et al., 2003; Ariagno et al., in review). This calibration with the soil depth could be difficult on catchments that are less studied and lack measurements of soil thickness.

Increasing hillslope diffusivity should be associated with an increase in sediment export, as this parameter controls the efficiency of hillslope erosion and sediment transport. This causal

relationship is observed most of the time except for high values of K_d during the winter period (increasing $K_{d-winter}$ from 5 to 10 m/yr, with a fixed $K_{d-summer} = 5$ m/yr and no threshold on rainfall intensity). In that case, the average yearly sediment export decreases by up to 1 kton, depending on the value of the fluvial transport coefficient. The analysis of soil-depth distribution in the catchment shows a strong increase of sediment thickness in the drainage network and, in particular, in the main channels where sediment thickness becomes higher than in the low order channels at the end of winter. However, rainfall events also induce more transport from channels to the outlet when more mobile material is available, which leads to a higher loss of soil depth when $K_{d-winter} = 10$ m/yr. Moreover, we made several tests but neither an increase of sediment erosion coefficient K_s nor an increase of the summer diffusivity results in an inversion of the trend. Thus, there might remain unidentified coupling effects between processes in the model and a deeper analysis of the model is needed to understand them.

The final setup of the model (Figure 30C) reproduces the general trend of the observed hysteresis cycle, with two successive loops in opposite directions. This result implies that the model incorporates the main processes active in the catchment (soil production, hillslope diffusion, and fluvial erosion) necessary to reproduce observations. However our quantitative predictions of monthly exports do not match exactly with the observed values (as an example, the modelled June sediment export is one of the highest (~1.8 kton) but is still significantly smaller than the observed value (> 3 kton). The simulated sediment export also displays two characteristics that are not consistent with the field data: (1) the sediment export during autumn is too high compared to the spring export peak; (2) sediment export during July and August is particularly low and closer to the winter-month exports than those of the autumn months.

The detailed analyse of the final simulated hysteresis cycle (Figure 30C) reports several trends that our calibration phase did not improve:

First, the relatively high predicted sediment export during autumn (September to November), which increased with the integration of the entrainment threshold (Figure 30B), questions the transition of the system toward a supply-limited regime observed at the end of the year in the previous model setup (Figure 28A). Several arguments might explain this result: (1) the average transport capacity of the fluvial system is strongly decreased with ω_{cs} (with K_s unchanged), thus the supply-limited regime is not fully reached at the end of the year; (2) the increase of $K_{d-intensity}$, responsible for the increase in sediment hillslope production in May, strongly increases sediment thickness in the channels from late spring to the end of the summer (Figure 30E); (3) the low amount of rainfall during the summer is insufficient to wash all the sediment out of the channels. This mobile sediment, stored in the drainage network, is then available for fluvial entrainment during autumn, when longer events and higher total amounts of rainfall are recorded. This excess of sediment in the channel at the end of the summer also results in an incomplete transfer of the mobile sediment out of the catchment for $K_s < 0.6 \text{ m}^{-1}$ (i.e., in December, sediment thickness in the low order channels is still slightly higher than in the main channel).

Secondly, the model predicts very low sediment exports in July and August (Figure 21), which is not consistent with the observed trend of constant export in summer/autumn in the original hysteresis.

At this stage, it is not clear whether these observations have to be related to an incomplete calibration, that could still be improved, or to the structure of the model itself, which could fail to capture some key processes for sediment dynamics (Figure 21).

III.4.3. Modeling perspectives in a context of climate change

III.4.3.1. Model adjustment based on field observation

In the course of field measurements to characterize the regolith and its seasonal variability in the marly Badlands of Draix (Ariagno et al., in review), we have found that the median grain-size of regolith fragments (D50) constitutes a good proxy for regolith weathering. Vertical profiles of D50 showed an exponential relationship between regolith weathering and regolith depth, such that a decrease in regolith depth through erosion corresponds to an increase of surface D50. Seasonal changes of surface D50 can then be converted to soil-depth changes and compared to the simulated soil-depth evolution. This calibration of the model by field measurements would allow to better constrain the diffusive coefficient value K_d , which controls hillslope erosion. However, only two annual cycles of D50 (each with four soil measurements) are available for 2020 and 2021. The small dataset of regolith measurement does not currently allow representing the full inter-annual climatic variability and limits potential comparison with the model predictions. But the simulated soil depth of the interfluves, which is an area similar to those monitored by Ariagno et al. (in review), shows an intra-annual variation in soil depth of about 1 cm. This magnitude is similar to the variation inferred from our D50 measurements and thus confirms that the model is a relevant tool to predict sediment dynamics on hillslopes. Expanding the field dataset of D50 measurements might help adjusting the coefficient of the transport-length diffusion (TLD) component to modulate hillslope erosion in the model.

Several studies relate maximum event discharge to the sediment export peak (Aich et al., 2014; Esteves et al., 2019; Sander et al., 2002). Landscape evolution models, such as the one developed here for Draix, consider the average event characteristics (event duration, total runoff, etc.) and do not model the internal flood dynamics. This approach might explain our difficulties to reproduce the sediment export dynamics at the intra-annual scale. Non-linear relations between mean and maximum discharge, and between discharge and sediment entrainment, could lead to an underestimation of sediment export for the flashiest events, i.e. summer storm floods.

III.4.3.2. Developping an automatic calibration procedure

The model parameter calibration was complex because of the number of parameters involved. The manual and step-by-step calibration of the parameters used in this study was needed to better understand the interactions between hillslope and fluvial erosion processes and their

effect on sediment dynamics. However, the development of an automatic calibration methodology might improve the model by exploring more possible parameter combinations. This study already identified and worked on two calibration criteria: the shape of the hysteresis curve based on sediment-export records (maintain the observed magnitude of the solid flux at the outlet) and the soil depth/ sediment thickness evolution according to the specific compartment of the catchment. For now, our manual calibration makes it difficult to fulfil closely these two main conditions. Other criteria could be added to this calibration phase, including the total annual sediment export or the ratio between spring and autumn export peaks, in order to simulate more closely the characteristics and the response of the catchments for every season. Automatic methods might help to more clearly relate specific questions to parameter variations, thus improving the previous results by better fitting the criteria used and helping to extend the model to other areas by simplifying and reducing the time required for the calibration phase.

III.4.3.3. Model predictions under climate change

Understanding and reproducing the real sediment dynamics of these marly catchments allows developing predictions for future sediment-export dynamics in a context where climatic variables will be perturbed. The forecast global climatic warming will lead to shorter and less intense winter periods, and thus decrease the soil-production capacity of these areas (Hirschberg et al., 2021). As previously shown (Ariagno et al., 2022), interannual variations in sediment export from the Laval catchment can be linked in part to sediment production by winter weathering, quantified by the Frost-Cracking Intensity indicator (FCI). In the present model, we have used a constant maximum regolith production rate for the winter season (P_0). Further development of this model would entail adjusting P_0 in the model according to the seasonal FCI: the annual availability of mobile sediment at the end of the winter would then depend on the intensity and duration of the cold period. This component would allow simulating the interannual variability of the winter weathering and its effect on sediment export. A better approximation of this variability would also improve the future sediment export predictions in a context of climate change.

A counter-effect to decreasing winter weathering intensity due to warming could arise from modifications to the rainfall regime (both in amount and intensity) widely considered ‘the most direct factors controlling erosional changes under climate changes’ (Nearing et al., 2004). In the region of Draix-Bléone badlands, Nadal-Romero et al. (2021) report that rainfall intensity should increase, leading to an increase in erosion capacity. The landscape-evolution model developed here can be a tool to test the effect of climate change on sediment export from Mediterranean badlands. Therefore, this study contributes to reducing the uncertainties in the relation between climate forcing and badland response, in a context where the main climatic variables driving badland erosion (precipitation, temperature,...etc) (Nearing et al., 2004; Vicente-Serrano et al., 2017) remain subject to significant uncertainties.

III.4.3.4. Application of the model beyond the Draix CZO

The Draix CZO is an ideal natural laboratory to perform field experiments and measurements that allow constraining a relatively elaborate landscape-evolution model. This site combines long-term records of sediment export and a quickly evolving morphology, providing sufficient constraints for developing a quantitative and process-based model. In our case, the existing long-term field dataset provides both the input for the model (rainfall timeseries) and the calibration data (sediment export). However, such datasets are rare and imply a sustained budgetary and human investment. Thus, is it possible to translate this LEM to other geographic contexts and what would be the components to adjust?

The specific intra-annual dynamics of the marly badlands studied here, with two distinct periods highlighting different erosional and weathering processes, probably limits the model to this particular geological setting. Soft rocks with soil cover are crucial to run this model.

The Draix model could probably be extended to area where weathering and transport phases are rapid and dominant in the sediment dynamics. The well-known Spanish badland catchments of Araguas and Vallcebre (Nadal-Romero et al., 2007; Regués & Gallart, 2004; Regués & Nadal-Romero, 2013) might be good candidates to test the model, as the lithology and climate in these catchments are similar to that in Draix. Moreover, these monitored catchments have sufficient climatic records and partial sediment datasets, which could help in the parameter calibration.

The current version of the model uses rainfall-event series as model inputs, which restricts the field areas to monitored catchments where such precise climatological records are available. The development of rainfall simulators opens new possibilities to extend the used of the LEM to new and less studied field areas. As an example, a Landlab component (alled 'PrecipitationDistribution', built using Poisson rules (Eagleson, 1978), can generate a random storm series with different characteristics (storm and interstorm duration, intensity, etc.).

III.5. Conclusion

The well-developed field dataset of the Draix-Bléone CZO and the sensitivity of badlands to climate change were the catalyst for developing a landscape evolution model specifically for this area. Our model provides an intermediate approach between event-scale models, describing precisely the event characteristics, and long-term landscape-evolution models, which simulate landscape development on timescales of thousands to millions of years. Here, we focused on an intra-annual time scale, using detailed climatic and erosion records. Based on field observations from multiple sources and precise characterization of the seasonal sediment dynamics of the Laval catchment, we increased the complexity of the model by adding, step-by-step, depth-dependent conditions and rainfall intensity conditions.

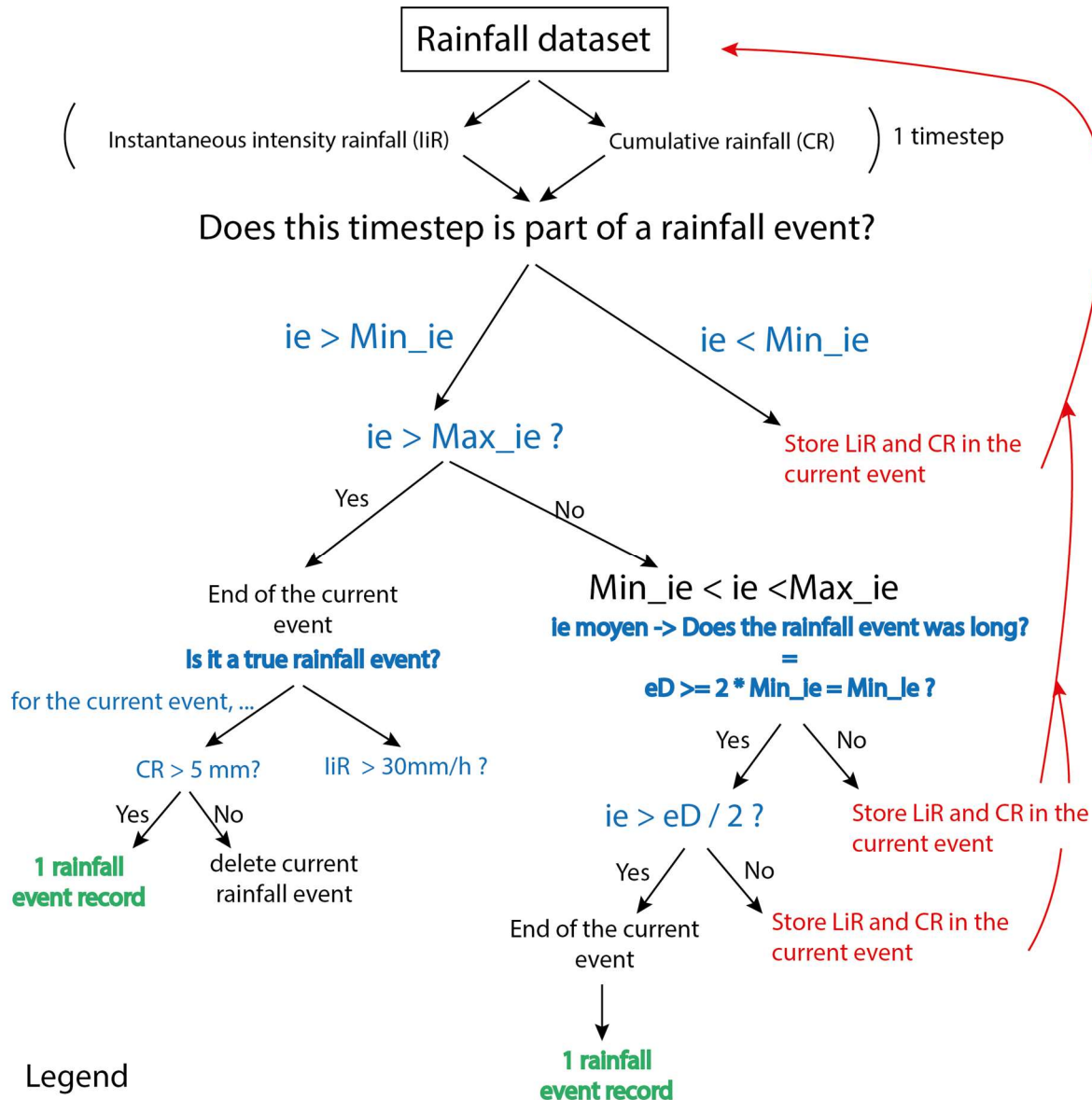
The linear dynamics between sediment export and rainfall highlighted by the initial model confirms the control of rainfall on erosion in marly catchments, which is illustrated by the sediment yield. By integrating depth-dependant soil production and hillslope diffusion, our model is able to reproduce the transition from a transport-limited to a supply-limited system observed at a yearly timescale by several studies. This behaviour makes clearer two seasonal patterns, passing from a simple linear relationship between rainfall and sediment export to a hysteresis cycle with two distinct regimes between spring and autumn. We used a non-local diffusion law to simulate the rapid transfer of sediment from hillslopes to the drainage network observed in the field. This novel component appears crucial to model the variable distribution of erosion within the catchment at the annual scale and has been calibrated based on field estimates of soil depth.

The observed sediment export peak occurring in late spring, triggered by increasing rainfall intensity, is not initially reproduced by the model. When the effect of the rainfall intensity is modeled by an increase of the hillslope diffusivity, sediment transfer between compartments of the catchment is enhanced. Only the addition of a sediment entrainment threshold coupled to the rainfall intensity threshold in hillslope diffusivity allows the anticlockwise loop of the hysteresis cycle appear during the transport-limited regime in the first part of the year. However, this calibration does not induce a complete transfer of sediment, as part of the sediment remains stored in the low order channels. However, the diffusivity coefficient remains difficult to calibrate in a complex and dense drainage network as occurs in badlands, which can cause unexpected feedbacks in some configurations. Although this non-local diffusion law is particularly useful for landscape-evolution models at these short timescales, further testing and simulation should be performed to enhance the overall understanding of this component.

Therefore, the model is able to simulate qualitatively both the temporal trend of sediment export and the spatiotemporal trend of soil depth in the catchment, but still requires improvement to simulate quantitative trends (Appendice 13). The final simulated hysteresis cycle reproduces the crucial characteristic of the real sediment dynamics, which suggests that

our model can be a reliable tool to explore sediment flux predictions under climate change. This could be done using different climatic scenarios to adapt the soil production according to the duration and intensity of the annual cold period or to modify the intra-annual rainfall dynamics.

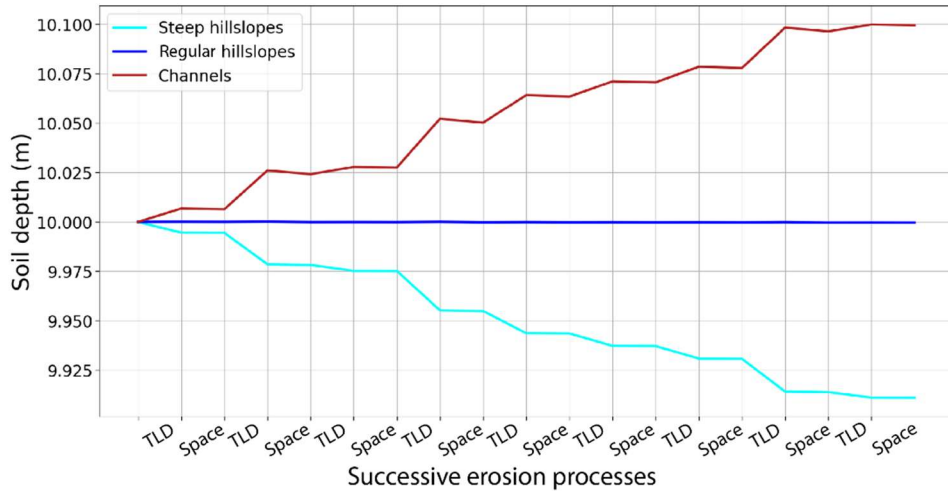
Appendice chapter III



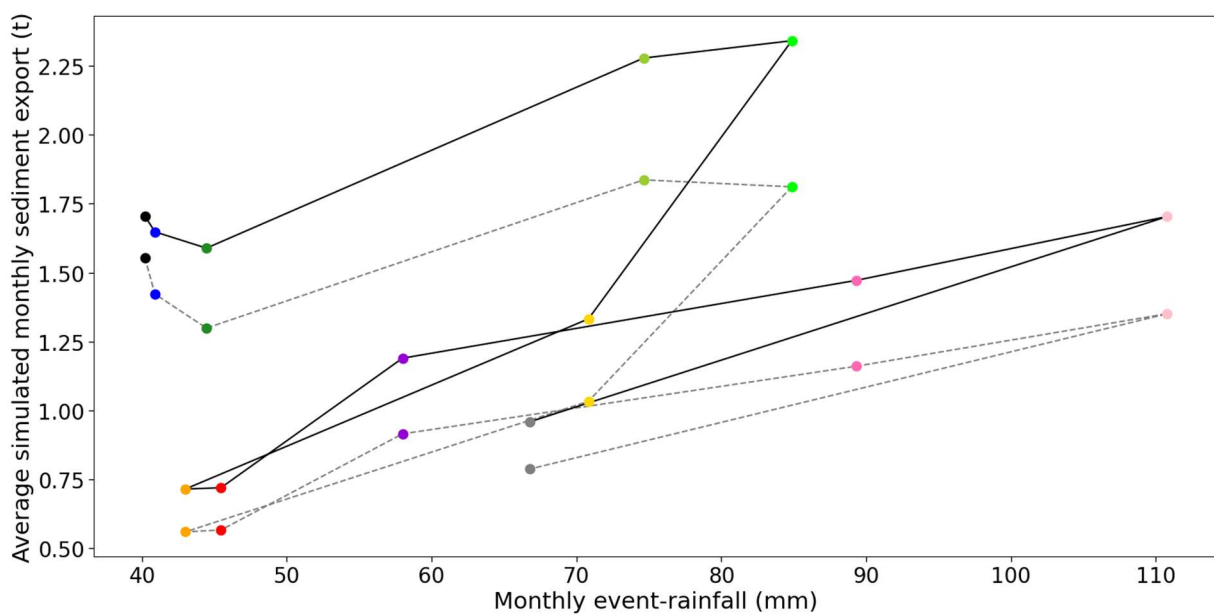
$\text{Minimum inter-event (Min_ie)} = 60 \text{ min}$
 $\text{Maximum inter-event (Max_ie)} = 720 \text{ min}$
 $\text{Minimum time for a long-event (Min_le)} = 120 \text{ min}$

Appendice 10: Sketch of the method to extract rainfall event from raw rainfall dataset (from Mathys, 2006). *If the duration of the inter-event is smaller than the minimum time of an inter-event (Min_ie), the event is still ongoing. If this inter-event duration is long enough (Max_ie), Mathys, (2006) set two conditions: the cumulative rainfall of the event should be >5 mm or the instantaneous rainfall intensity should be >30 mm/h. If one of these conditions is fullfilled, a rainfall event is created. On the other hand, for intermediate inter-event duration (between a minimum inter-event and a maximum inter-event time), if the event duration is less than twice the*

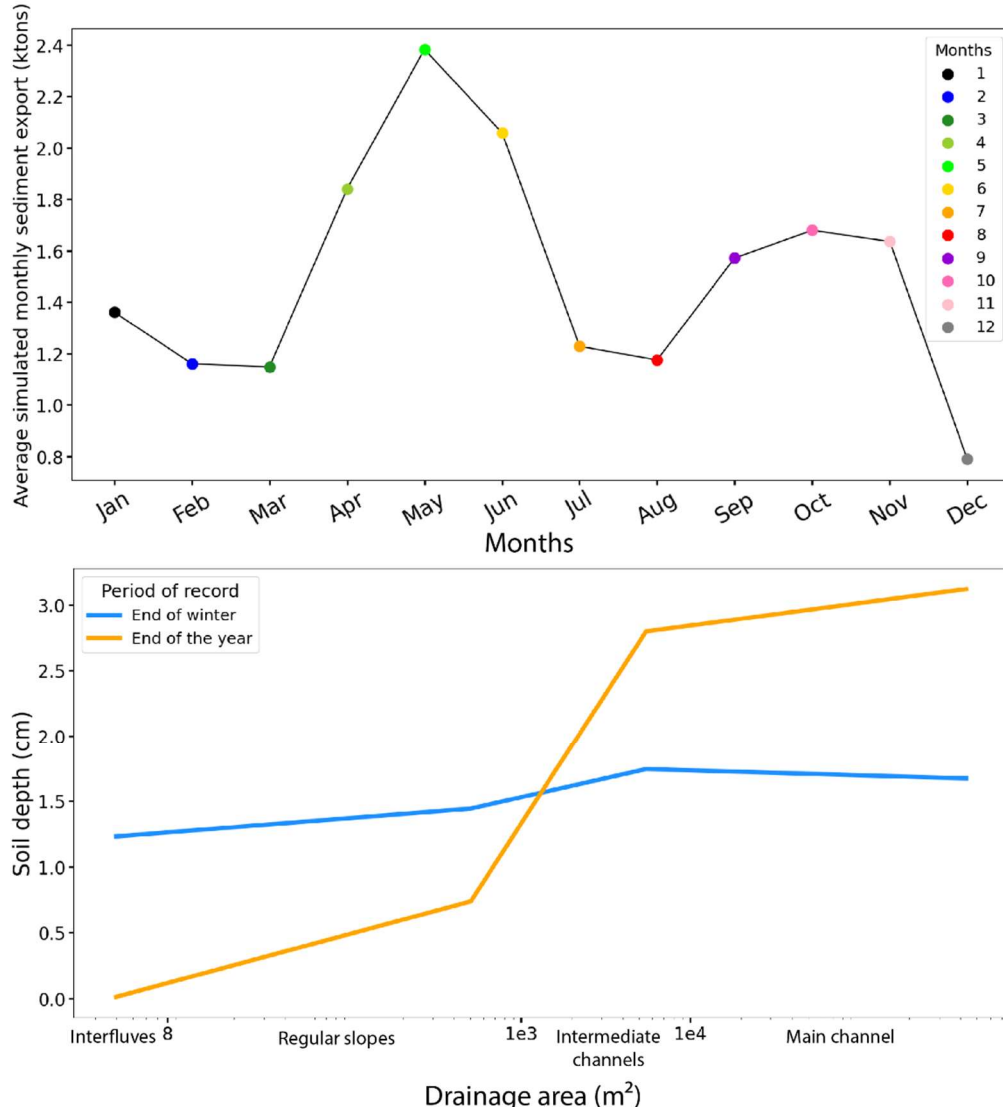
minimum inter-event duration, the ongoing rainfall event continues. However, if the event duration is more than twice the minimum of inter-event duration and that the latter one is superior to half of the event duration, the rainfall event is finished.



Appendice 11: Soil depth variation caused by successive diffusion and fluvial erosion events (TLD and Space), for three different compartments of the catchment. Steep hillslopes ($A < 10^4 \text{ m}^2$, $S > S_c$), normal hillslopes ($A < 10^4 \text{ m}^2$, $S > S_c$), and channels ($A > 10^4 \text{ m}^2$). The non-local diffusion component (TLD) mainly affects the steep hillslopes (i.e., soil depth decreases), and sediments are directly transferred to the channels (i.e., soil depth in channels increases). The fluvial transport law (SPACE) transports sediment in the channels (i.e., soil depth decreases) but induce no change on hillslopes. Regular hillslopes are practically unaffected by diffusion.



Appendice 12: Hysteresis plot, using Inter-annual average of monthly simulated values, of monthly sediment export versus monthly cumulative event rainfall, simulated with depth-dependent soil production and transport laws. The hysteresis cycles illustrates two separate maxima: moderate rainfall and high sediment export in May versus high rainfall and moderate sediment export in November. Dashed grey line shows the simulation result with a constant value of the diffusivity coefficient K_d (i.e., $K_{d-winter} = K_{d-summer} = 0.1 \text{ m/yr}$). Solid black line shows the hysteresis cycle with $K_{d-winter} = 0.1 \text{ m/yr}$ and $K_{d-summer} = 5 \text{ m/yr}$. This latter hysteresis loop is shifted up, implying an overall increase in sediment export.



Appendice 13: Quantitative predictions of the model for simulated sediment exports and soil depth on the Laval catchment. A) Using inter-annual average of monthly-simulated values. Two peaks of sediment export are observed over an annual cycle. B) Soil depth versus drainage area after the soil production period (blue line) and at the end of the year (orange line). The regolith dynamic induces a transfer of soil from hillslopes to channels.

Discussion and conclusion

« Seule une meilleure compréhension du monde qui nous entoure permettra de répondre aux interrogations et aux angoisses de l'ensemble des hommes »

(Pierre Joliot-Curie)

Principales conclusions et contributions...

[...sur la dynamique sédimentaire des bassins versants de Draix-Bléone CZO](#)

Fort de sa longévité, l'observatoire Draix-Bléone a permis l'acquisition d'une connaissance fine du fonctionnement des bassins versants marneux au travers de multiples études. La continuité des mesures de terrain (flux liquides et solides), la mise en place d'instruments plus performants () ou l'installation de nouveaux équipements (sondes de température de sol, géophones, ...) permettent respectivement de construire des tendances de long-terme, d'affiner ou d'améliorer les résultats et d'apporter de nouveaux éléments d'interprétation pour valider, ou non, les précédentes conclusions. C'est dans cet esprit que les données de flux sédimentaires ont été comparées aux précipitations afin de redéfinir quantitativement la dynamique sédimentaire intra-annuelle des 15 dernières années, qui avait été mise en lumière précédemment par Mathys (2006) et Bechet et al. (2016). Cette étape de revalorisation et de validation de précédents résultats reste nécessaire dans un contexte où les changements climatiques en cours induisent de profondes modifications des régimes érosifs.

Une des premières contributions de ce manuscrit s'inscrit donc dans cette démarche de validation scientifique et met en avant la variabilité intra-annuelle des exports sédimentaires via un cycle d'hystérèse. La première moitié de l'année, illustrée par une boucle anti-horaire de l'hystérèse, traduit un régime non-linéaire entre exports sédimentaires et précipitations avec un pic d'export en fin de printemps pour un cumul de pluie modéré. L'intensité des pluies devient un facteur indispensable pour retrouver un régime en 'transport-limited', c'est-à-dire une relation linéaire entre pluie et exports sédimentaires. La boucle horaire de l'hystérèse, dessinée par les mois d'automne, illustre le comportement d'un bassin en régime 'supply-limited'; la capacité de transport, due aux longs événements pluvieux, excède largement la disponibilité sédimentaire.

Les données long-terme de l'observatoire ont également mis en évidence une relation linéaire entre les exports sédimentaires annuels et le cumul de pluie au-dessus d'un certain seuil

d'intensité (50mm/h). Cette relation a conduit à définir une anomalie d'export, correspondant à la quantité de sédiment exportés qui ne peut pas être expliquée par la variabilité des précipitations.

... à l'échelle du régolithe

Implanté depuis 2003 sur les versants du bassin du Moulin, le réseau de sondes de température de sol n'avait jusqu'ici pas été exploité. La critique, longue et fastidieuse, de ces données de terrain sur les sols marneux dénudés est une première contribution de notre travail et permettra par la suite une plus large utilisation de ces chroniques.

L'implantation des sondes de températures à différentes profondeurs a permis de calculer des gradients de température dans le sol et ainsi de définir l'indicateur de gélification, aussi appelé 'frost-cracking intensity' et issu de la fragmentation de la roche sous l'effet de la croissance des lentilles de glace, proposé par (Hales & Roering, 2007). Parmi plusieurs indicateurs potentiels de gélification (temps moyen en dessous de 0°C, temps passé sous 0°C, nombre d'alternances gel-dégel), le frost-cracking intensity est le mieux corrélé à l'anomalie d'export, dont il explique plus de 50% de. La fragmentation du régolithe par croissance de lentilles de glace semble donc être le processus dominant responsable de la production sédimentaire dans ces bassins et régule, de façon indirecte, presque un tiers des exports sédimentaires annuels. Cependant, les difficultés liées à l'acquisition d'un tel jeu de données (maintenance régulière du réseau de sondes) font qu'il est rarement possible de pouvoir calculer cet indicateur. Notre étude fait également ressortir un indicateur alternatif, 'le temps passé sous 0°C', plus facile à acquérir pour expliquer l'anomalie d'export sédimentaire.

Ce travail de thèse a été rythmé par des campagnes de terrain saisonnières afin de caractériser le régolithe à différentes échelles spatio-temporelles. Via un tamisage en laboratoire des échantillons de marnes, nous avons montré que le D50, valeur médiane de la granulométrie de l'échantillon, était un bon proxy de l'état d'altération du régolithe. La cyclicité du D50 est également cohérente avec les variations intra-annuelles dessinées par l'hystérèse des exports sédimentaires. La fragmentation du régolithe en hiver par frost-cracking induit l'observation de faibles valeurs de D50. Avec un transport actif des sédiments mobilisables lors des événements pluvieux estivaux, le régolithe laisse apparaître une surface de moins en moins altérée au cours de l'été, synonyme d'une granulométrie plus grossière et donc d'un D50 plus élevé lors des campagnes de mesures fin Août. L'Indicateur de Frost-Cracking (FCI) nous a également permis d'identifier une année moins propice à la production sédimentaire et ainsi d'expliquer la valeur anormale du D50 obtenue à la fin de l'hiver 2020. Cette corrélation entre les deux indicateurs pourrait permettre à l'avenir de prédire l'état du régolithe sans passer par le tamisage, étape très chronophage de l'analyse.

Localisées selon des orientations et une schistosité variable, les placettes d'échantillonnage ont par ailleurs été pensées pour analyser la variabilité spatiale du régolithe. Plusieurs de nos résultats indiquent une altération différente entre les versants sud et les versants nord. Si le FCI n'a pu être calculé en face nord, l'indicateur de temps passé en dessous de 0 °C montre

des valeurs significativement différentes entre les deux orientations. Les valeurs de D50 issues des relevés en versant nord ne nous paraissent pas assez exhaustives pour conclure à une réelle différence de production sédimentaire entre versants sud et nord. En revanche, les résultats obtenus sur le versant sud enregistrent les valeurs de D50 les plus faibles, correspondant à une forte altération du régolithe.

A l'échelle décimétrique, l'interprétation du profil géophysique révèle une différence d'épaisseur non négligeable entre les deux orientations tandis qu'à l'échelle du bassin, aucune asymétrie des zones dénudées n'a été observé. Ce travail d'analyse de la variabilité spatiale du régolithe n'aura donc pas abouti à la quantification précise de l'impact de l'orientation sur les processus de production de régolithe mais des pistes de travail seront proposées pour étoffer le jeu de données de terrain et ainsi valider ou non nos premières observations.

[... du modèle d'évolution de paysage construit sur le site de Draix-Bléone.](#)

Construit à partir de notre analyse du terrain et de notre compréhension du système étudié, le modèle d'évolution de paysage ('Landscape evolution model', LEM) doit être un outil pour prédire les évolutions morphologiques des badlands marneux dans un contexte de changement climatique. Bien que le travail de prédition n'ait pu être mené faute de temps, le modèle réalisé reproduit le cycle d'hystérèse issu d'observations, preuve de sa capacité à rendre compte de la variabilité intra-annuelle de la dynamique sédimentaire. Cette cohérence entre observations et modélisations valide le choix des lois géomorphologiques d'altération, de diffusion et d'érosion fluviale utilisées pour simuler les processus physiques à l'œuvre dans les bassins versants.

Plus particulièrement, en utilisant une loi de diffusion non-locale et dépendante de l'épaisseur de sol (TLD), nous avons simulé, à l'échelle d'un cycle annuel, les transferts de sédiments entre différents compartiments d'un bassin (crêtes, versants, chenaux...). Les variations spatiales du régolithe enregistrées et le régime de type 'supply-limited' simulés en fin d'année valident donc la pertinence de ce processus de diffusion rapide, plus adapté aux systèmes agissant sur de courtes échelles de temps. Par ailleurs, cette loi de diffusion a été utilisée comme levier pour simuler l'impact de l'intensité des pluies sur le détachement des particules, et donc indirectement sur l'export sédimentaire. En plus de cette diffusion augmentée par les pluies intenses, nous avons montré que l'instauration d'un seuil d'entraînement des particules dans le réseau hydrographique était nécessaire pour qu'un export sédimentaire accru ait lieu, lors d'événements intenses, et induise la relation non-linéaire entre pluie et export sédimentaire (c.-à-d., la boucle antihoraire de l'hystérèse) observée dans la dynamique annuelle des bassins.

Perspectives

[Sur le terrain](#)

Faute de données de terrain suffisamment continues ou étoffées, nous n'avons pas réalisé de comparaison sur l'intensité de la gélification en fonction de l'orientation des versants (nord

ou sud). Apporter une attention toute particulière au fonctionnement et à l'implantation des sondes de température en face nord pourrait permettre de calculer un indicateur de 'frost-cracking' sur ces versants. De la même façon, de nouvelles campagnes de terrain sont nécessaires pour valider le jeu de données des D50 en face nord. L'extension spatiale des mesures de D50 pourrait également intégrer le gradient d'altitude comme possible facteur de contrôle de la gélification. De tels travaux permettraient (1) de comparer la sensibilité à la gélification des badlands par rapport à d'autres types de terrain (plus végétalisés, à lithologie différente, etc.), (2) de quantifier précisément la contribution de chaque versant à la production sédimentaire du bassin et ainsi d'améliorer l'estimation des exports sédimentaires. Une complexification du modèle d'évolution serait alors possible en ajustant l'intensité de l'altération, responsable de la production de sol, en fonction des différentes orientations, et éventuellement des altitudes, des versants.

Les analyses et relevés de terrain témoignent de la disparité spatiale et temporelle du processus de 'dry ravel'. Une cartographie des tabliers en fin d'hiver, l'estimation du volume de ces dépôts par relevés topographiques puis la corrélation de ce processus de diffusion avec les cycles de gel-dégel ou avec les températures de l'air sont autant de pistes pour quantifier plus précisément les masses sédimentaires impactées par ce processus et leur temporalité. Ces informations pourraient être intégrées au modèle d'évolution du paysage afin d'améliorer la description des transports sédimentaires pour les mois d'hiver et du printemps.

Réalisé avant le début de ce travail de thèse sur des zones marneuses dénudées, le profil géophysique apporte une information plus continue, à l'échelle du versant, de l'état d'altération du régolithe. Reproduire cette expérience sur des versants de différentes orientations et pour différents types de surface (c-à-d., marnes nues, prairies, arbuste, forêt) permettrait (1) de valider nos premières conclusions sur les profondeurs des horizons d'un sol marneux, (2) d'apporter une information plus spatialisée de ces horizons, (3) de corrélérer la variabilité spatiale du régolithe de sub-surface à des éléments géomorphologiques ou biologiques de surface.

Le profil vertical de D50 réalisé au printemps 2020 apporte une image détaillée de l'altération du régolithe. Reproduire un travail similaire à la fin de l'hiver ou à la fin de l'été permettrait d'explorer un peu plus la variabilité temporelle de la formation du régolithe *in situ*. La caractérisation du régolithe via de nouveaux outils est également un axe de travail potentiel pour définir d'autres paramètres indicateurs de l'état d'altération du régolithe, moins chronophages à obtenir que le D50. L'utilisation d'un laser scanner portable est à tester dans le but apporter une estimation précise de la rugosité du régolithe, paramètre qui pourrait facilement se substituer à la granulométrie. Par ailleurs, des relevés photographiques, couplés à l'échantillonnage du régolithe, ont été réalisés sur chaque placette et lors de chaque campagne de terrain. L'aspect très chronophage du traitement des images et de la réalisation de modèles 3D n'a pas permis d'aboutir à des analyses exploitables mais les données sont disponibles pour poursuivre une quantification de la rugosité via la photogrammétrie.

Pour tenter de quantifier la production de régolithe à partir d'un état d'altération modéré et défini, nous avons également mis en place une expérience de 'nettoyage' du régolithe sur une parcelle d'un 1 m² au niveau d'une crête du versant de la Roubinette. Les relevés de photogrammétries réalisés avant et après l'expérience ont ensuite été utilisés pour calculer le volume de sédiment évacué, volume pouvant être considéré comme celui du régolithe produit entre deux expériences. Les données recueillies devraient apporter de premières informations qualitatives sur la densité et la vitesse de fracturation du régolithe de sub-surface. La quantification précise du régolithe produit via cette expérience pourrait être couplée aux données ponctuelles de terrain dans l'objectif d'améliorer l'estimation de la variabilité spatiale et temporelle de la production sédimentaire de ces badlands marneux.

En élargissant un peu plus l'horizon

Notre travail ne s'est pas intéressé à l'impact du couvert végétal sur l'altération et l'érosion des badlands. Nos recherches ont plus particulièrement traité les versants dénudés mais la progression des zones végétalisées observée dans les bassins nous oblige à nous interroger sur la nature des interactions entre l'‘inerte’ et le ‘vivant’ dans un contexte de changement climatique. Un des futurs challenges du projet ClimBad (CLIMATE impact on BADland erosion) sera de quantifier le couplage entre végétation et érosion, en s'intéressant notamment aux rétroactions induites par la végétation sous des climats propices à l'érosion (p.ex., pluies de plus forte intensité).

Des géophones à l'écoute du bruit sismique ont été installés à l'exutoire du bassin du Laval. Encore dans leur phase de calibration, ils devraient apporter une estimation de la charge sédimentaire exportée. Étendre ce dispositif plus haut dans le bassin, à des confluences stratégiques ou à la sortie de zones plus ou moins végétalisées, permettrait d'apporter des détails sur la temporalité de la vague sédimentaire observée et d'estimer des temps de transits dans le bassin. Par ailleurs, cela permettrait d'élargir, à un bassin plus grand, les observations sur le transit d'une vague sédimentaire obtenues avec des chaînes d'érosion dans le lit du Moulin (Liébault et al., 2022). Même si ces installations ne captent pas le flux de matière en suspension, leur utilisation à différentes échelles permettrait de subdiviser le flux solide selon des caractéristiques précises du bassin et ainsi d'améliorer l'estimation de la production et de l'érosion globale de chaque compartiment du bassin.

Les résultats obtenus sur les processus d'altération par le gel ou sur la dynamique intra-annuelle des sédiments dans les badlands trouvent un réel intérêt pour la gestion des cours d'eau en aval. Les quantités de sédiments fins en transit, les variations temporelles de ces flux et l'impact des apports sédimentaires sur la dynamique globale des rivières sont des préoccupations récurrentes nécessaires pour préserver une continuité durable et écologique des cours d'eau. Construit pour prédire les exports sédimentaires (fins et grossiers) des zones fortement contributrices, notre modèle pourra servir d'outil décisionnel aux gestionnaires d'infrastructures hydrauliques pour anticiper les arrivées de matériaux en fonction de la temporalité des événements dans un contexte d'évolution du forçage climatique.

En modélisation

Même si le modèle réalisé donne de premiers résultats encourageants, la mise en place de méthodes de calibration plus automatiques paraît indispensable pour étendre le champ d'action du modèle à de nouveaux jeux de données d'entrée. Cette étape sera facilitée par notre étude manuelle qui a fait ressortir les paramètres les plus sensibles du modèle.

Faute de temps, certains résultats de terrain n'ont pas été suffisamment exploités lors de la calibration ou de la simulation des différentes phases du modèle. Une des prochaines étapes consistera à ajuster le taux maximum de production (P_0) en fonction de l'intensité des phénomènes de gélification annuels. Pour cela une relation entre P_0 et l'indicateur de frost-cracking doit être investiguée. Cette adaptation sur les processus de production sédimentaire devrait induire une amélioration de l'estimation des flux solides annuels et de la variabilité inter-annuelle.

L'objectif in fine du modèle d'évolution de Draix-Bléone est de pouvoir prédire la réponse sédimentaire des badlands selon différents forçages climatiques en entrées. Via l'utilisation de modèles climatiques régionaux (RCM) disponibles en ligne (programme CORDEX), notre modèle permettra de tester les effets, cumulés ou non, des changements dans les cumuls, les durées et les intensités des précipitations, ainsi que dans les températures hivernales, sur la dynamique sédimentaire. Les conséquences et les rétroactions possibles entre les variations de températures (responsables de la gélification) et ces modifications du cycle hydrologique seront particulièrement nécessaires pour la prédiction des exports sédimentaires. Les récentes avancées pour affiner la résolution des RCM (Pichelli et al., 2021) ouvrent de multiples possibilités de comparaisons, comme par exemple appliquer des précipitations seulement sur une partie du bassin ou encore comparer la réponse sédimentaire entre deux bassins proches mais de nature, d'orientation ou de couvert végétal différents.

Finalement, ce modèle pourra être appliqué à d'autres bassins de l'observatoire afin d'ajuster les prédictions d'exports sédimentaires de ces badlands en fonction des caractéristiques de chacun des bassins. Élargir l'utilisation du modèle à d'autres badlands, qui ne possèdent pas autant de données disponibles, comme par exemple les badlands marneux espagnols, pourrait être envisagé en forçant le modèle par des simulateurs de pluie (Tucker & Bras, 2000). Cette utilisation étendue du modèle permettrait d'analyser la réponse du modèle dans un contexte géographique complètement différent.

Epilogue

Je ne pouvais pas finir cette thèse sans mentionner l'incroyable chance que j'ai eu de travailler sur l'Observatoire de Draix-Bléone. Concentrées sur un même lieu, animées par un désir de rigueur et de découvertes, les recherches scientifiques menées au cœur des badlands sont le reflet de notre détermination à comprendre et à vivre en harmonie avec notre environnement. La continuité des chroniques de mesures, et donc implicitement des études menées, s'inscrit dans le patrimoine géologique, déjà exceptionnel, de cette région. L'interaction entre les diverses disciplines de la zone critique est également une incroyable richesse; elle forge naturellement des liens entre nous, scientifiques de tous horizons, induit un sentiment d'appartenance à une communauté tournée vers un même objectif et pousse à investiguer toujours plus loin les mécanismes de notre système Terre. Les bassins de Draix-Bléone laissent aussi la place à l'expérience et donc à l'erreur ou à l'échec, chose encore pas toujours reconnue et acceptée en science me semble-t-il. Face à cela, le terrain est toujours source d'inspiration et de nouvelles idées pour nos recherches et sa proximité nous permet d'adapter rapidement nos méthodes et mesures. J'ai aimé passer du temps dans ces ravinés, explorer leurs contours sinuieux, écouter le bruit des marnes qui dégringolent, observer les cristaux de glace du régolithe, griller comme dans un four dans ce décor lunaire et essayer de comprendre (bon sang de bon soir !) la logique de la formation du régolithe.

Pourtant quelque chose coince, quelque chose me titille... quelque chose qui n'est pas en phase avec la rigueur scientifique que j'ai apprise pendant ces trois dernières années. Quelle ne fut pas ma surprise la première fois que j'ai découvert mon terrain d'étude : « tiens, un piquet métallique, deux piquets, des câbles (et même des rouleaux de câbles!), des tuyaux de plastiques... ? » La science est à l'œuvre, ou plutôt ETAIT à l'œuvre, et bon: « on ne sait jamais, on relancera peut-être la manip »... Mais après 1 an, 2 ans ou 15 ans d'attente, le plastique s'est décomposé en micro particules, les câbles sont corrodés, le métal est rouillé et les marnes les ont rejetés, rien n'est réutilisable. Aujourd'hui, sous couvert de la science, nous polluons négligemment le haut d'un bassin versant, supposé sauvage, et premier garant de la qualité de nos rivières et de nos océans. Ce sont pourtant bien les géosciences qui permettent d'observer la dégradation de la biodiversité et les effets du changement climatique. Alors pourquoi ne pas rester cohérent dans notre démarche scientifique et mettre autant d'énergie à la désinstallation qu'à l'installation du matériel expérimental ? Combien de fois l'ai-je écrit ce mot 'cohérent' dans mon manuscrit... ? Mais cela ne suffit pas de l'écrire dans un papier, il faut le rester jusqu'au bout pour vraiment le saisir. Adopter une démarche responsable, ou tout simplement respectueuse, envers notre objet (et outil) de travail ne peut que rendre nos objectifs scientifiques plus pertinents et compréhensibles. Bruno Latour disait: « *Le sol ... est inappropriate. On lui appartient, il n'appartient à personne* », alors inutile de vouloir le coloniser dans ses moindres espaces. Certains diront que je suis insistante et que ce ne sont que des miettes, des détails perdus dans le flot de déchets produits chaque jour dans le monde. Peut-être..., mais alors je ne vois plus l'intérêt de discuter de la couleur ou de l'épaisseur du trait de mon graphique ou d'écrire un paragraphe sur les effets du changement climatique si par ailleurs je me fiche de ces « détails ».

Une autre incohérence me vient à l'esprit quand je pense à l'avenir de l'observatoire. L'intérêt des chroniques climatologiques ou sédimentaires long-termes et leur caractère exceptionnel n'est plus à démontrer dans un contexte de réchauffement climatique où l'évolution des tendances est scrutée à la loupe. Pourtant après presque 40 ans d'enregistrement, les mesures de charriages vont s'arrêter : « trop chères »... Je n'ai sûrement pas toutes les ficelles pour comprendre cette décision, et je ne doute pas que certains arguments font sens. Mais pourquoi l'intérêt scientifique intemporel ne prime-t-il pas sur l'aspect financier ou administratif du moment... ? Comme souvent, nous attendons des nouvelles technologies qu'elles nous sauvent, mais le temps presse, les caisses sont vides alors que le système alternatif en place ne fait que balbutier ses premières données.

Enfin, au travers de plusieurs rencontres et expériences de vulgarisation, j'ai pris conscience de l'intérêt et de la curiosité que suscitent nos travaux de recherche. En cela, je pense que l'Observatoire est une interface extraordinaire pour communiquer, partager, transmettre, écouter et recevoir. L'équipe de l'Inrae en charge du site de Draix, et en particulier Seb Klotz, sont les garants de cette activité aujourd'hui, et j'espère que ses missions perdureront demain.

Mais je ne ferais pas de science si je n'avais pas confiance en elle et en ses acteurs. La prise de conscience semble réelle dans la recherche, les choses bougent et des initiatives comme 'Ma Terre en 180 minute' donnent un élan d'espoir.

« Quand on commence à agir, l'espoir est partout. Alors, au lieu d'attendre l'espoir, cherchez l'action. » (Greta Thunberg)

References

- Ahnert, F. (1966). The role of the equilibrium concept in the interpretation of landforms of fluvial erosion and deposition.
- Ahnert, F. (1977). Some comments on the quantitative formulation of geomorphological processes in a theoretical model. *Earth Surface Processes*, 2(2–3), 191–201. <https://doi.org/10.1002/esp.3290020211>
- Aich, V., Zimmermann, A., & Elsenbeer, H. (2014). Quantification and interpretation of suspended-sediment discharge hysteresis patterns: How much data do we need? *CATENA*, 122, 120–129. <https://doi.org/10.1016/j.catena.2014.06.020>
- Ajdadi, F. R., Gilandeh, Y. A., Mollazade, K., & Hasanzadeh, R. P. (2016). Application of machine vision for classification of soil aggregate size. *Soil and Tillage Research*, 162, 8–17. <https://doi.org/10.1016/j.still.2016.04.012>
- Andermann, C., Bonnet, S., Crave, A., Davy, P., Longuevergne, L., & Gloaguen, R. (2012). Sediment transfer and the hydrological cycle of Himalayan rivers in Nepal. *Comptes Rendus - Geoscience*, 344(11–12), 627–635. Scopus. <https://doi.org/10.1016/j.crte.2012.10.009>
- Anderson, R. (2002). Modeling the tor-dotted crests, bedrock edges, and parabolic profiles of high alpine surfaces of the Wind River Range, Wyoming. *Geomorphology*, 46, 35–58. [https://doi.org/10.1016/S0169-555X\(02\)00053-3](https://doi.org/10.1016/S0169-555X(02)00053-3)
- Anderson, R. S. (1994). Evolution of the Santa Cruz Mountains, California, through tectonic growth and geomorphic decay. *Journal of Geophysical Research: Solid Earth*, 99(B10), 20161–20179. <https://doi.org/10.1029/94JB00713>
- Anderson, R. S. (1998). Near-surface thermal profiles in alpine bedrock: Implications for the frost weathering of rock. *Arctic and Alpine Research*, 30(4), 362–372.
- Anderson, R. S., Anderson, S. P., & Tucker, G. E. (2013a). Rock damage and regolith transport by frost: An example of climate modulation of the geomorphology of the critical zone. *Earth Surface Processes and Landforms*, 38(3), 299–316. <https://doi.org/10.1002/esp.3330>
- Anderson, R. S., Anderson, S. P., & Tucker, G. E. (2013b). Rock damage and regolith transport by frost: An example of climate modulation of the geomorphology of the critical zone. *Earth Surface Processes and Landforms*, 38(3), 299–316. <https://doi.org/10.1002/esp.3330>
- Anderson, S. P., Hinckley, E.-L., Kelly, P., & Langston, A. (2014). Variation in Critical Zone Processes and Architecture across Slope Aspects. *Procedia Earth and Planetary Science*, 10, 28–33. <https://doi.org/10.1016/j.proeps.2014.08.006>
- Anderson, S. P., von Blanckenburg, F., & White, A. F. (2007). Physical and Chemical Controls on the Critical Zone. *Elements*, 3(5), 315–319. <https://doi.org/10.2113/gselements.3.5.315>
- Andres Lopez-Tarazon, J., Batalla, R. J., & Vericat, D. (2011). In-channel sediment storage in a highly erodible catchment: The River Isabena (Ebro Basin, Southern Pyrenees). *Zeitschrift Fur Geomorphologie*, 55(3), 365–382. <https://doi.org/10.1127/0372-8854/2011/0045>
- Annandale, G. W. (2014). Reservoir sedimentation Sustainable water supply, climate change and reservoir sedimentation management: Technical and economic viability. In *Reservoir Sedimentation*. CRC Press.

- Antoine, P., Giraud, A., Meunier, M., & Van Asch, T. (1995). Geological and geotechnical properties of the “Terres Noires” in southeastern France: Weathering, erosion, solid transport and instability. *Eng. Geol.*, 40(3–4), 223–234. [https://doi.org/10.1016/0013-7952\(95\)00053-4](https://doi.org/10.1016/0013-7952(95)00053-4)
- Ariagno, C., Le Bouteiller, C., van der Beek, P., & Klotz, S. (2022). Sediment export in marly badland catchments modulated by frost-cracking intensity, Draix–Bléone Critical Zone Observatory, SE France. *Earth Surface Dynamics*, 10(1), 81–96. <https://doi.org/10.5194/esurf-10-81-2022>
- Ariagno, C., Pasquet, S., Le Bouteiller, C., van der Beek, P., & Klotz, S. (in review). Seasonal dynamics of marly badlands illustrated by field records of hillslope regolith properties, Draix-Bléone CZO, SE France. *Earth Surface Processes and Landforms*.
- Armijos, E., Crave, A., Vauchel, P., Fraizy, P., Santini, W., Moquet, J.-S., Arevalo, N., Carranza, J., & Guyot, J.-L. (2013). Suspended sediment dynamics in the Amazon River of Peru. *Journal of South American Earth Sciences*, 44, 75–84. <https://doi.org/10.1016/j.jsames.2012.09.002>
- Baartman, J. E. M., van Gorp, W., Temme, A. J. A. M., & Schoorl, J. M. (2012). Modelling sediment dynamics due to hillslope–river interactions: Incorporating fluvial behaviour in landscape evolution model LAPSUS. *Earth Surface Processes and Landforms*, 37(9), 923–935. <https://doi.org/10.1002/esp.3208>
- Bechet, J., Duc, J., Jaboyedoff, M., Loyer, A., & Mathys, N. (2015). Erosion processes in black marl soils at the millimetre scale: Preliminary insights from an analogous model. *Hydrology and Earth System Sciences*, 19(4), 1849–1855. <https://doi.org/10.5194/hess-19-1849-2015>
- Bechet, J., Duc, J., Loyer, A., Jaboyedoff, M., Mathys, N., Malet, J.-P., Klotz, S., Le Bouteiller, C., Rudaz, B., & Travelletti, J. (2016). Detection of seasonal cycles of erosion processes in a black marl gully from a time series of high-resolution digital elevation models (DEMs). *Earth Surface Dynamics*, 4(4), 781–798. <https://doi.org/10.5194/esurf-4-781-2016>
- Beek*, P. V. D., & Braun, J. (1998). Numerical modelling of landscape evolution on geological time-scales: A parameter analysis and comparison with the south-eastern highlands of Australia. *Basin Research*, 10(1), 49–68. <https://doi.org/10.1046/j.1365-2117.1998.00056.x>
- Befus, K. m., Sheehan, A. f., Leopold, M., Anderson, S. p., & Anderson, R. s. (2011). Seismic Constraints on Critical Zone Architecture, Boulder Creek Watershed, Front Range, Colorado. *Vadose Zone Journal*, 10(4), 1342–1342. <https://doi.org/10.2136/vzj2010.0108er>
- Bennett, G. L., Molnar, P., Mc Ardell, B. W., Schlunegger, F., & Burlando, P. (2013). Patterns and controls of sediment production, transfer and yield in the Illgraben. *Geomorphology*, 188, 68–82. <https://doi.org/10.1016/j.geomorph.2012.11.029>
- Bishop, P. (2007). Long-term landscape evolution: Linking tectonics and surface processes. *Earth Surface Processes and Landforms*, 32(3), 329–365. <https://doi.org/10.1002/esp.1493>
- Bouteiller, C. L. (2011). Dégradation des sédiments marneux et suspensions hyperconcentrées [Phdthesis, Université de Grenoble]. <https://tel.archives-ouvertes.fr/tel-00603000>
- Brantley, S. L., McDowell, W. H., Dietrich, W. E., White, T. S., Kumar, P., Anderson, S. P., Chorover, J., Lohse, K. A., Bales, R. C., Richter, D. D., Grant, G., & Gaillardet, J. (2017). Designing a network of critical zone observatories to explore the living skin of the terrestrial Earth. *Earth Surface Dynamics*, 5(4), 841–860. <https://doi.org/10.5194/esurf-5-841-2017>
- Brantley, S. L., Megonigal, J. P., Scatena, F. N., Balogh-Brunstad, Z., Barnes, R. T., Bruns, M. A., Cappellen, P. V., Dontsova, K., Hartnett, H. E., Hartshorn, A. S., Heimsath, A., Herndon, E., Jin, L., Keller, C. K., Leake, J. R., McDowell, W. H., Meinzer, F. C., Mozdzer, T. J., Petsch, S., ... Yoo, K. (2011). Twelve testable hypotheses on the geobiology of weathering. *Geobiology*, 9(2), 140–165. <https://doi.org/10.1111/j.1472-4669.2010.00264.x>

- Brochot, S., & Meunier, M. (1996). Un modèle d'érosion des torrents en crue (ETC). *Ingénieries Eau-Agriculture-Territoires*, 6, 9–18. <https://hal.archives-ouvertes.fr/hal-00476079>
- Buendia, C., Vericat, D., Batalla, R. J., & Gibbins, C. N. (2016). Temporal dynamics of sediment transport and transient in-channel storage in a highly erodible catchment. *Land Degradation & Development*, 27(4), 1045–1063. <https://doi.org/10.1002/ldr.2348>
- Bullard, J. E., Ockelford, A., Strong, C. L., & Aubault, H. (2018). Impact of multi-day rainfall events on surface roughness and physical crusting of very fine soils. *Geoderma*, 313, 181–192. <https://doi.org/10.1016/j.geoderma.2017.10.038>
- Burkett, V. R., Wilcox, D. A., Stottlemeyer, R., Barrow, W., Fagre, D., Baron, J., Price, J., Nielsen, J. L., Allen, C. D., Peterson, D. L., Ruggerone, G., & Doyle, T. (2005). Nonlinear dynamics in ecosystem response to climatic change: Case studies and policy implications. *Ecological Complexity*, 2(4), 357–394. <https://doi.org/10.1016/j.ecocom.2005.04.010>
- Burylo, M., Rey, F., Mathys, N., & Dutoit, T. (2012). Plant root traits affecting the resistance of soils to concentrated flow erosion. *Earth Surface Processes and Landforms*, 37(14), 1463–1470. <https://doi.org/10.1002/esp.3248>
- Carlson, B. Z., Corona, M. C., Dentant, C., Bonet, R., Thuiller, W., & Choler, P. (2017). Observed long-term greening of alpine vegetation—A case study in the French Alps. *Environmental Research Letters*, 12(11), 114006. <https://doi.org/10.1088/1748-9326/aa84bd>
- Carretier, S., Martinod, P., Reich, M., & Godderis, Y. (2016). Modelling sediment clasts transport during landscape evolution. *Earth Surface Dynamics*, 4(1), 237–251. <https://doi.org/10.5194/esurf-4-237-2016>
- Carriere, A., Le Bouteiller, C., Tucker, G. E., Klotz, S., & Naaim, M. (2020). Impact of vegetation on erosion: Insights from the calibration and test of a landscape evolution model. 45, 1085–1099.
- Cheng, C.-L., Shalabh, & Garg, G. (2014). Coefficient of determination for multiple measurement error models. *Journal of Multivariate Analysis*, 126, 137–152. Scopus. <https://doi.org/10.1016/j.jmva.2014.01.006>
- Clarke, M. L., & Rendell, H. M. (2010). Climate-driven decrease in erosion in extant Mediterranean badlands. *Earth Surface Processes and Landforms*, 35(11), 1281–1288. <https://doi.org/10.1002/esp.1967>
- Cohen, S., Willgoose, G., & Hancock, G. (2010). The mARM3D spatially distributed soil evolution model: Three-dimensional model framework and analysis of hillslope and landform responses. *Journal of Geophysical Research: Earth Surface*, 115(F4). <https://doi.org/10.1029/2009JF001536>
- Copard, Y., Eyrolle, F., Radakovitch, O., Poirel, A., Rimbault, P., Gairoard, S., & Di-Giovanni, C. (2018). Badlands as a hot spot of petrogenic contribution to riverine particulate organic carbon to the Gulf of Lion (NW Mediterranean Sea). *Earth Surface Processes and Landforms*, 43(12), 2495–2509. <https://doi.org/10.1002/esp.4409>
- Cosandey, C., Andréassian, V., Martin, C., Didon-Lescot, J. F., Lavabre, J., Folton, N., Mathys, N., & Richard, D. (2005). The hydrological impact of the mediterranean forest: A review of French research. *Journal of Hydrology*, 301(1), 235–249. <https://doi.org/10.1016/j.jhydrol.2004.06.040>
- Coulthard, T. J. (2001). Landscape evolution models: A software review. *Hydrolog. Process.*, 15, 165–173.
- Cras, A., Marc, V., & Travi, Y. (2007). Hydrological behaviour of sub-Mediterranean alpine headwater streams in a badlands environment. *Journal of Hydrology*, 339(3), 130–144. <https://doi.org/10.1016/j.jhydrol.2007.03.004>

- Culling, W. E. H. (1963). Soil Creep and the Development of Hillside Slopes. *The Journal of Geology*, 71(2), 127–161. <https://www.jstor.org/stable/30066150>
- Darboux, F., Davy, Ph., Gascuel-Odoux, C., & Huang, C. (2002). Evolution of soil surface roughness and flowpath connectivity in overland flow experiments. *CATENA*, 46(2–3), 125–139. [https://doi.org/10.1016/S0341-8162\(01\)00162-X](https://doi.org/10.1016/S0341-8162(01)00162-X)
- Davis, W. M. (1892). The Convex Profile of Bad-Land Divides | Science. <https://www.science.org/doi/10.1126/science.ns-20.508.245.a>
- Davy, P., & Lague, D. (2009). Fluvial erosion/transport equation of landscape evolution models revisited. *Journal of Geophysical Research: Earth Surface*, 114(F3). <https://doi.org/10.1029/2008JF001146>
- Delannoy, J.-J., & Rovéra, G. (1996). L'érosion dans les Alpes occidentales: Contribution à un bilan des mesures et des méthodes. *Revue de Géographie Alpine*, 84(2), X8-101.
- Delunel, R., van der Beek, P. A., Carcaillet, J., Bourlès, D. L., & Valla, P. G. (2010). Frost-cracking control on catchment denudation rates: Insights from in situ produced ^{10}Be concentrations in stream sediments (Ecrins–Pelvoux massif, French Western Alps). *Earth and Planetary Science Letters*, 293(1–2), 72–83. <https://doi.org/10.1016/j.epsl.2010.02.020>
- Descroix, L., & Mathys, N. (2003). Processes, spatio-temporal factors and measurements of current erosion in the French southern Alps: A review. *Earth Surface Processes and Landforms*, 28(9), 993–1011. <https://doi.org/10.1002/esp.514>
- Dietrich, W. E., Bellugi, D. G., Sklar, L. S., Stock, J. D., Heimsath, A. M., & Roering, J. J. (2003). Geomorphic transport laws for predicting landscape form and dynamics. *Geophysical Monograph Series*, 135, 103–132. <https://doi.org/10.1029/135GM09>
- Dietrich, W. E., Reiss, R., Hsu, M.-L., & Montgomery, D. R. (1995). A process-based model for colluvial soil depth and shallow landsliding using digital elevation data. *Hydrological Processes*, 9(3–4), 383–400. <https://doi.org/10.1002/hyp.3360090311>
- Dixon, J. L., Heimsath, A. M., & Amundson, R. (2009). The critical role of climate and saprolite weathering in landscape evolution. *Earth Surface Processes and Landforms*, 34(11), 1507–1521. <https://doi.org/10.1002/esp.1836>
- Dixon, J. L., Heimsath, A. M., Kaste, J., & Amundson, R. (2009). Climate-driven processes of hillslope weathering. *Geology*, 37(11), 975–978. <https://doi.org/10.1130/G30045A.1>
- Draebing, D., & Krautblatter, M. (2019). The efficacy of frost weathering processes in alpine rockwalls. *Geophysical Research Letters*, 46(12), 6516–6524. <https://doi.org/10.1029/2019GL081981>
- Draix-Bleone Observatory. (2015). Observatoire hydrosédimentaire de montagne Draix-Bléone [Data set]. Irstea. [ASCII]. Irstea. <https://doi.org/10.17180/OBS.DRAIX>
- Eagleson, P. S. (1978). Climate, soil, and vegetation: 2. The distribution of annual precipitation derived from observed storm sequences. *Water Resources Research*, 14(5), 713–721. <https://doi.org/10.1029/WR014i005p00713>
- Eppes, M. C., Magi, B., Hallet, B., Delmelle, E., Mackenzie-Helnwein, P., Warren, K., & Swami, S. (2016). Deciphering the role of solar-induced thermal stresses in rock weathering. *GSA Bulletin*, 128(9–10), 1315–1338. <https://doi.org/10.1130/B31422.1>
- Erktan, A., Cécillon, L., Graf, F., Roumet, C., Legout, C., & Rey, F. (2016). Increase in soil aggregate stability along a Mediterranean successional gradient in severely eroded gully bed ecosystems: Combined effects of soil, root traits and plant community characteristics. *Plant and Soil*, 398(1), 121–137. <https://doi.org/10.1007/s11104-015-2647-6>

- Esteves, M., Descroix, L., Mathys, N., & Marc Lapetite, J. (2005). Soil hydraulic properties in a marly gully catchment (Draix, France). *CATENA*, 63(2–3), 282–298. <https://doi.org/10.1016/j.catena.2005.06.006>
- Esteves, M., Legout, C., Navratil, O., & Evrard, O. (2019). Medium term high frequency observation of discharges and suspended sediment in a Mediterranean mountainous catchment. *Journal of Hydrology*, 568, 562–574. <https://doi.org/10.1016/j.jhydrol.2018.10.066>
- Filippa, G., Cremonese, E., Galvagno, M., Isabellon, M., Bayle, A., Choler, P., Carlson, B. Z., Gabellani, S., Morra di Cella, U., & Migliavacca, M. (2019). Climatic Drivers of Greening Trends in the Alps. *Remote Sensing*, 11(21), Article 21. <https://doi.org/10.3390/rs11212527>
- Flinchum, B. A., Holbrook, W. S., & Carr, B. J. (2022). What Do P-Wave Velocities Tell Us About the Critical Zone? *Frontiers in Water*, 3. <https://www.frontiersin.org/article/10.3389/frwa.2021.772185>
- Gaillardet, J., Braud, I., Hankard, F., Anquetin, S., Bour, O., Dorfliger, N., Dreuxy, J. R. de, Galle, S., Galy, C., Gogo, S., Gourcy, L., Habets, F., Laggoun, F., Longuevergne, L., Borgne, T. L., Naaim-Bouvet, F., Nord, G., Simonneau, V., Six, D., ... Zitouna, R. (2018). OZCAR: The French Network of Critical Zone Observatories. *Vadose Zone Journal*, 17(1), 180067. <https://doi.org/10.2136/vzj2018.04.0067>
- Gallart, F., Pérez-Gallego, N., Latron, J., Catari, G., Martínez-Carreras, N., & Nord, G. (2013). Short- and long-term studies of sediment dynamics in a small humid mountain Mediterranean basin with badlands. *Geomorphology*, 196, 242–251. Scopus. <https://doi.org/10.1016/j.geomorph.2012.05.028>
- Gilbert, G. K. (1877). Report on the geology of the Henry Mountains (Utah). In Report on the geology of the Henry Mountains (Monograph, p. 212) [U.S. Geographical and geological survey of rocky mountains region]. U.S. Government printing office. <https://doi.org/10.3133/70039916>
- Gilchrist, A. R., Kooi, H., & Beaumont, C. (1994). Post-Gondwana geomorphic evolution of southwestern Africa: Implications for the controls on landscape development from observations and numerical experiments. *Journal of Geophysical Research: Solid Earth*, 99(B6), 12211–12228. <https://doi.org/10.1029/94JB00046>
- Giménez, R., Casalí, J., Grande, I., Díez, J., Campo, M. A., Álvarez-Mozos, J., & Goñi, M. (2012). Factors controlling sediment export in a small agricultural watershed in Navarre (Spain). *Agricultural Water Management*, 110, 1–8. <https://doi.org/10.1016/j.agwat.2012.03.007>
- Grangeon, T. (2012). Etude multi-échelle de la granulométrie des particules fines générées par érosion hydrique: Apports pour la modélisation [Phdthesis, Université de Grenoble]. <https://tel.archives-ouvertes.fr/tel-00875975>
- Hales, T. C., & Roering, J. J. (2007). Climatic controls on frost cracking and implications for the evolution of bedrock landscapes. *Journal of Geophysical Research*, 112(F2), F02033. <https://doi.org/10.1029/2006JF000616>
- Hallet, B., Walder, J. S., & Stubbs, C. W. (1991). Weathering by segregation ice growth in microcracks at sustained subzero temperatures: Verification from an experimental study using acoustic emissions. *Permafrost and Periglacial Processes*, 2(4), 283–300. <https://doi.org/10.1002/ppp.3430020404>
- Harvey, E. L., Hales, T. C., Hobley, D. E. J., Liu, J., & Fan, X. (2022). Measuring the grain-size distributions of mass movement deposits. *Earth Surface Processes and Landforms*. <https://doi.org/10.1002/esp.5337>

- Heimsath, A. M., Chappell, J., Dietrich, W. E., Nishiizumi, K., & Finkel, R. C. (2000). Soil production on a retreating escarpment in southeastern Australia. *Geology*, 4. [https://doi.org/10.1130/0091-7613\(2000\)28<787:SPOARE>2.0.CO;2](https://doi.org/10.1130/0091-7613(2000)28<787:SPOARE>2.0.CO;2)
- Heimsath, A. M., Dietrich, W. E., Nishiizumi, K., & Finkel, R. C. (1997). The soil production function and landscape equilibrium. *Nature*, 388(6640), 358–361. <https://doi.org/10.1038/41056>
- Heimsath, A. M., E. Dietrich, W., Nishiizumi, K., & Finkel, R. C. (1999). Cosmogenic nuclides, topography, and the spatial variation of soil depth. *Geomorphology*, 27(1–2), 151–172. [https://doi.org/10.1016/S0169-555X\(98\)00095-6](https://doi.org/10.1016/S0169-555X(98)00095-6)
- Higuchi, K., Chigira, M., & Lee, D.-H. (2013). High rates of erosion and rapid weathering in a Plio-Pleistocene mudstone badland, Taiwan. *CATENA*, 106, 68–82. <https://doi.org/10.1016/j.catena.2012.11.005>
- Hirschberg, J., Fatichi, S., Bennett, G. L., McArdell, B. W., Peleg, N., Lane, S. N., Schlunegger, F., & Molnar, P. (2021). Climate change impacts on sediment yield and debris-flow activity in an alpine catchment. *Journal of Geophysical Research: Earth Surface*, 126(1), e2020JF005739. <https://doi.org/10.1029/2020JF005739>
- Hobley, D. E. J., Adams, J. M., Nudurupati, S. S., Hutton, E. W. H., Gasparini, N. M., Istanbulluoglu, E., & Tucker, G. E. (2017). Creative computing with Landlab: An open-source toolkit for building, coupling, and exploring two-dimensional numerical models of Earth-surface dynamics. *Earth Surface Dynamics*, 5(1), 21–46. <https://doi.org/10.5194/esurf-5-21-2017>
- Holbrook, W. S., Riebe, C. S., Elwaseif, M., L. Hayes, J., Basler-Reeder, K., L. Harry, D., Malazian, A., Dosseto, A., C. Hartsough, P., & W. Hopmans, J. (2014). Geophysical constraints on deep weathering and water storage potential in the Southern Sierra Critical Zone Observatory. *Earth Surface Processes and Landforms*, 39(3), 366–380. <https://doi.org/10.1002/esp.3502>
- Howard, A. D. (1980). Thresholds in river regimes. <https://doi.org/10.4324/9781003028697>
- Howard, A. D. (1994). A detachment-limited model of drainage basin evolution. *Water Resources Research*, 30(7), 2261–2285. <https://doi.org/10.1029/94WR00757>
- Howard, A. D. (1997). Badland Morphology and Evolution: Interpretation Using a Simulation Model. *Earth Surface Processes and Landforms*, 22(3), 211–227. [https://doi.org/10.1002/\(SICI\)1096-9837\(199703\)22:3<211::AID-ESP749>3.0.CO;2-E](https://doi.org/10.1002/(SICI)1096-9837(199703)22:3<211::AID-ESP749>3.0.CO;2-E)
- Howard, A. D., & Kerby, G. (1983). Channel changes in badlands. *GSA Bulletin*, 94(6), 739–752. [https://doi.org/10.1130/0016-7606\(1983\)94<739:CCIB>2.0.CO;2](https://doi.org/10.1130/0016-7606(1983)94<739:CCIB>2.0.CO;2)
- Humphreys, G. S., & Wilkinson, M. T. (2007). The soil production function: A brief history and its rediscovery. *Geoderma*, 139(1), 73–78. <https://doi.org/10.1016/j.geoderma.2007.01.004>
- IPCC report. (n.d.-a). Chapter 3: Desertification — Special Report on Climate Change and Land. Retrieved October 3, 2022, from <https://www.ipcc.ch/srccl/chapter/chapter-3/>
- IPCC report. (n.d.-b). Chapter 4: Land Degradation — Special Report on Climate Change and Land. Retrieved October 3, 2022, from <https://www.ipcc.ch/srccl/chapter/chapter-4/>
- Jantzi, H., Liébault, F., & Klotz, S. (2017). Sediment residence time in alluvial storage of black marl badlands. *Catena*, 156, 82–91. <https://doi.org/10.1016/j.catena.2017.03.026>
- Jiao, J., Han, L., Jia, Y., Wang, N., Lei, D., & Li, L. (2011). Can seed removal through soil erosion explain the scarcity of vegetation in the Chinese Loess Plateau? *Geomorphology*, 132(1), 35–40. <https://doi.org/10.1016/j.geomorph.2011.04.033>
- Johnstone, S. A., Chadwick, K. D., Frias, M., Tagliaro, G., & Hilley, G. E. (2017). Soil development over mud-rich rocks produces landscape-scale erosional instabilities in the northern Gabilan Mesa, California. *GSA Bulletin*, 129(9–10), 1266–1279. <https://doi.org/10.1130/B31546.1>

- Johnstone, S. A., & Hilley, G. E. (2015). Lithologic control on the form of soil-mantled hillslopes. *Geology*, 43(1), 83–86. <https://doi.org/10.1130/G36052.1>
- Kasanin-Grubin, M. (2013). Clay mineralogy as a crucial factor in badland hillslope processes. *CATENA*, 106, 54–67. <https://doi.org/10.1016/j.catena.2012.08.008>
- Kirchner, J. W., Dietrich, W. E., Iseya, F., & Ikeda, H. (1990). The variability of critical shear stress, friction angle, and grain protrusion in water-worked sediments. *Sedimentology*, 37(4), 647–672. <https://doi.org/10.1111/j.1365-3091.1990.tb00627.x>
- Kirkby, M. (1971). Hillslope Process-Response Models Based on the Continuity Equation. *Inst. Br. Geogr. Spec. Publ.*, 3.
- Klein, M. (1984). Anti clockwise hysteresis in suspended sediment concentration during individual storms: Holbeck catchment; Yorkshire, England. *Catena*, 11(2–3), 251–257. [https://doi.org/10.1016/0341-8162\(84\)90014-6](https://doi.org/10.1016/0341-8162(84)90014-6)
- Kondolf, G. M., Gao, Y., Annandale, G. W., Morris, G. L., Jiang, E., Zhang, J., Cao, Y., Carling, P., Fu, K., Guo, Q., Hotchkiss, R., Peteuil, C., Sumi, T., Wang, H., Wang, Z., Wei, Z., Wu, B., Wu, C., & Yang, C. T. (2014). Sustainable sediment management in reservoirs and regulated rivers: Experiences from five continents. *Earth's Future*, 2(5), 256–280. <https://doi.org/10.1002/2013EF000184>
- Lague, D. (2010). Reduction of long-term bedrock incision efficiency by short-term alluvial cover intermittency. *Journal of Geophysical Research-Earth Surface*, 115, F02011. <https://doi.org/10.1029/2008JF001210>
- Lague, D. (2014). The stream power river incision model: Evidence, theory and beyond. *Earth Surface Processes and Landforms*, 39(1), 38–61. <https://doi.org/10.1002/esp.3462>
- Lague, D., Hovius, N., & Davy, P. (2005). Discharge, discharge variability, and the bedrock channel profile. *Journal of Geophysical Research: Earth Surface*, 110(F4). <https://doi.org/10.1029/2004JF000259>
- Lana-Renault, N., & Regués, D. (2007). Bedload transport under different flow conditions in a human-disturbed catchment in the Central Spanish Pyrenees. *CATENA*, 71(1), 155–163. <https://doi.org/10.1016/j.catena.2006.04.029>
- Langston, A. L., Tucker, G. E., & Anderson, R. S. (2015). Interpreting climate-modulated processes of terrace development along the Colorado Front Range using a landscape evolution model. *Journal of Geophysical Research: Earth Surface*, 120(10), 2121–2138. <https://doi.org/10.1002/2014JF003403>
- Le Bouteiller, C., Chambon, G., Naaim-Bouvet, F., & Mathys, N. (2021). Hydraulics and rheology of natural hyperconcentrated flows from Draix-Bleone observatory, French Alps. *Journal of Hydraulic Research*, 59(2), 181–195. <https://doi.org/10.1080/00221686.2020.1744750>
- Legout, C., Poulenard, J., Nemery, J., Navratil, O., Grangeon, T., Evrard, O., & Esteves, M. (2013). Quantifying suspended sediment sources during flood events in headwater catchments using diffuse reflectance spectroscopy. *EGU2013-2913*. <https://ui.adsabs.harvard.edu/abs/2013EGUGA..15.2913L>
- Lemoine, M., Bas, T., Arnaud-Vanneau, A., Arnaud, H., Dumont, T., Gidon, M., Bourbon, M., de Graciansky, P.-C., Rudkiewicz, J.-L., Megard-Galli, J., & Tricart, P. (1986). The continental margin of the Mesozoic Tethys in the Western Alps. *Marine and Petroleum Geology*, 3(3), 179–199. [https://doi.org/10.1016/0264-8172\(86\)90044-9](https://doi.org/10.1016/0264-8172(86)90044-9)
- Li, D., Overeem, I., Kettner, A. J., Zhou, Y., & Lu, X. (2021). Air temperature regulates erodible landscape, water, and sediment fluxes in the permafrost-dominated catchment on the tibetan

- plateau. Water Resources Research, 57(2), e2020WR028193. <https://doi.org/10.1029/2020WR028193>
- Lickorish, W. H., & Ford, M. (1998). Sequential restoration of the external Alpine Digne thrust system, SE France, constrained by kinematic data and synorogenic sediments. Geological Society Special Publication, 134, 189–211. Scopus. <https://doi.org/10.1144/GSL.SP.1998.134.01.09>
- Liébault, F. (2017). Geomorphology and sediment transport of alpine fluvial systems: From steep-slope torrents to piedmont gravel-bed rivers (p. 150) [HDR]. <https://hal.inrae.fr/tel-02606790>
- Liébault, F., Jantzi, H., Klotz, S., Laronne, J. B., & Recking, A. (2016). Bedload monitoring under conditions of ultra-high suspended sediment concentrations. Journal of Hydrology, 540, 947–958. <https://doi.org/10.1016/j.jhydrol.2016.07.014>
- Liébault, F., Laronne, J. B., Klotz, S., & Bel, C. (2022). Seasonal bedload pulses in a small alpine catchment. Geomorphology, 398, 108055. <https://doi.org/10.1016/j.geomorph.2021.108055>
- Llena, M., Batalla, R. J., Smith, M. W., & Vericat, D. (2021). Do badlands (always) control sediment yield? Evidence from a small intermittent catchment. Catena, 198, 105015. <https://doi.org/10.1016/j.catena.2020.105015>
- Loye, A., Jaboyedoff, M., Theule, J. I., & Liébault, F. (2016). Headwater sediment dynamics in a debris flow catchment constrained by high-resolution topographic surveys. Earth Surface Dynamics, 4(2), 489–513. <https://doi.org/10.5194/esurf-4-489-2016>
- Lukey, B. T., Sheffield, J., Bathurst, J. C., Hiley, R. A., & Mathys, N. (2000). Test of the SHETRAN technology for modelling the impact of reforestation on badlands runoff and sediment yield at Draix, France. Journal of Hydrology, 235(1), 44–62. [https://doi.org/10.1016/S0022-1694\(00\)00260-2](https://doi.org/10.1016/S0022-1694(00)00260-2)
- Malet, J.-P., Auzet, A.-V., Maquaire, O., Ambroise, B., Descroix, L., Esteves, M., Vandervaere, J.-P., & Truchet, E. (2003). Soil surface characteristics influence on infiltration in black marls: Application to the Super-Sauze earthflow (southern Alps, France). Earth Surface Processes and Landforms, 28(5), 547–564. <https://doi.org/10.1002/esp.457>
- Mallet, F. (2018). Spatialisation et modélisation de l'état hydrique des sols pour l'étude des processus de formation des écoulements en contexte torrentiel: Application au bassin versant marneux du Laval (ORE Draix-Bléone, Alpes-De-Haute-Provence, France) [Phdthesis, Université d'Avignon]. <https://tel.archives-ouvertes.fr/tel-01914950>
- Mallet, F., Carrière, S. D., Chalikakis, K., & Marc, V. (2018). Assessing soil water content spatio-temporal variability at the hillslope scale in a headwater catchment using a multi variable interpolation model based on EMI surveys (Draix, South Alps, France). Environmental Earth Sciences, 77(13), 507. <https://doi.org/10.1007/s12665-018-7687-9>
- Mallet, F., Marc, V., Douvinet, J., Rossello, P., Joly, D., & Ruy, S. (2020). Assessing soil water content variation in a small mountainous catchment over different time scales and land covers using geographical variables. Journal of Hydrology, 591, 125593. <https://doi.org/10.1016/j.jhydrol.2020.125593>
- Maquaire, O., Ritzenthaler, A., Fabre, D., Ambroise, B., Thiery, Y., Truchet, E., Malet, J.-P., & Monnet, J. (2002). Caractérisation des profils de formations superficielles par pénétrométrie dynamique à énergie variable: Application aux marnes noires de Draix (Alpes-de-Haute-Provence, France). Comptes Rendus Geoscience, 334(11), 835–841. [https://doi.org/10.1016/S1631-0713\(02\)01788-1](https://doi.org/10.1016/S1631-0713(02)01788-1)

- Martínez-Murillo, J. F., Nadal-Romero, E., Regüés, D., Cerdà, A., & Poesen, J. (2013). Soil erosion and hydrology of the western Mediterranean badlands throughout rainfall simulation experiments: A review. *CATENA*, 106, 101–112. <https://doi.org/10.1016/j.catena.2012.06.001>
- Mathers, K. I., Collins, A. I., England, J., Brierley, B., & Rice, S. p. (2017). The fine sediment conundrum; quantifying, mitigating and managing the issues. *River Research and Applications*, 33(10), 1509–1514. <https://doi.org/10.1002/rra.3228>
- Mathys, N. (2006). Analyse et modélisation à différentes échelles des mécanismes d'érosion et de transport de matériaux solides. Cas des petits bassins versants de montagne sur marne (Draix, Alpes-de-Haute-Provence) (p. 346) [PhD Thesis]. <https://hal.inrae.fr/tel-02588905>
- Mathys, N., Brochot, S., & Meunier, M. (1996). L'érosion des Terres Noires dans les Alpes du sud: Contribution à l'estimation des valeurs annuelles moyennes (bassins versants expérimentaux de Draix, Alpes de Haute Provence, France) / Erosion of the Terres Noires (Black Earth) in the southern French Alps: A contribution to an assessment of mean annual values (Draix experimental catchment areas). *Revue de Géographie Alpine*, 84(2), 17–27. <https://doi.org/10.3406/rga.1996.3855>
- Mathys, N., Brochot, S., Meunier, M., & Richard, D. (2003). Erosion quantification in the small marly experimental catchments of Draix (Alpes de Haute Provence, France). Calibration of the ETC rainfall–runoff–erosion model. *CATENA*, 50(2–4), 527–548. [https://doi.org/10.1016/S0341-8162\(02\)00122-4](https://doi.org/10.1016/S0341-8162(02)00122-4)
- Mathys, N., Klotz, S., Esteves, M., Descroix, L., & Lapetite, J. M. (2005). Runoff and erosion in the black marls of the French Alps: Observations and measurements at the plot scale. *Catena*, 63(2–3), 261–281. <https://doi.org/10.1016/j.catena.2005.06.010>
- Matsuoka, N. (2008). Frost weathering and rockwall erosion in the southeastern Swiss Alps: Long-term (1994–2006) observations. *Geomorphology*, 99(1), 353–368. <https://doi.org/10.1016/j.geomorph.2007.11.013>
- Matsuoka, N., & Murton, J. (2008). Frost weathering: Recent advances and future directions. *Permafrost and Periglacial Processes*, 19(2), 195–210. <https://doi.org/10.1002/ppp.620>
- Michaelides, K., & Martin, G. J. (2012). Sediment transport by runoff on debris-mantled dryland hillslopes. *Journal of Geophysical Research: Earth Surface*, 117(F3). <https://doi.org/10.1029/2012JF002415>
- Misset, C., Recking, A., Legout, C., Poirel, A., Cazilhac, M., Esteves, M., & Bertrand, M. (2019). An attempt to link suspended load hysteresis patterns and sediment sources configuration in alpine catchments. *Journal of Hydrology*, 576, 72–84. <https://doi.org/10.1016/j.jhydrol.2019.06.039>
- Misset, C., Recking, A., Legout, C., Viana-Bandeira, B., & Poirel, A. (2021). Assessment of fine sediment river bed stocks in seven Alpine catchments. *CATENA*, 196, 104916. <https://doi.org/10.1016/j.catena.2020.104916>
- Misset, C., Recking, A., Navratil, O., Legout, C., Poirel, A., Cazilhac, M., Briguet, V., & Esteves, M. (2019). Quantifying bed-related suspended load in gravel bed rivers through an analysis of the bedload-suspended load relationship. *Earth Surface Processes and Landforms*, 44(9), 1722–1733. <https://doi.org/10.1002/esp.4606>
- Nadal-Romero, E., Martínez-Murillo, J. F., & Kuhn, N. J. (2018). Badland dynamics in the context of global change (p. 320). Elsevier.
- Nadal-Romero, E., Martínez-Murillo, J. F., Vanmaercke, M., & Poesen, J. (2011). Scale-dependency of sediment yield from badland areas in Mediterranean environments. *Progress in Physical*

- Geography: Earth and Environment, 35(3), 297–332.
<https://doi.org/10.1177/0309133311400330>
- Nadal-Romero, E., & Regüés, D. (2010). Geomorphological dynamics of subhumid mountain badland areas — weathering, hydrological and suspended sediment transport processes: A case study in the Araguás catchment (Central Pyrenees) and implications for altered hydroclimatic regimes. *Progress in Physical Geography: Earth and Environment*, 34(2), 123–150. <https://doi.org/10.1177/030913309356624>
- Nadal-Romero, E., Regüés, D., & Latron, J. (2008). Relationships among rainfall, runoff, and suspended sediment in a small catchment with badlands. *Catena*, 74(2), 127–136. <https://doi.org/10.1016/j.catena.2008.03.014>
- Nadal-Romero, E., Regüés, D., Martí-Bono, C., & Serrano-Muela, P. (2007). Badland dynamics in the Central Pyrenees: Temporal and spatial patterns of weathering processes. *Earth Surface Processes and Landforms*, 32(6), 888–904. <https://doi.org/10.1002/esp.1458>
- Nadal-Romero, E., Rodríguez-Caballero, E., Chamizo, S., Juez, C., Cantón, Y., & García-Ruiz, J. M. (2021). Mediterranean badlands: Their driving processes and climate change futures. *Earth Surface Processes and Landforms*, in press(n/a). <https://doi.org/10.1002/esp.5088>
- Nasirzadehdizaji, R., & Akyuz, D. E. (2022). Predicting the potential impact of forest fires on runoff and sediment loads using a distributed hydrological modeling approach. *Ecological Modelling*, 468, 109959. <https://doi.org/10.1016/j.ecolmodel.2022.109959>
- Navratil, O., Legout, C., Gateuille, D., Esteves, M., & Liebault, F. (2010). Assessment of intermediate fine sediment storage in a braided river reach (southern French Prealps). *Hydrological Processes*, 24(10), 1318–1332. <https://doi.org/10.1002/hyp.7594>
- Nearing, M. A., Pruski, F. F., & O'Neal, M. R. (2004). Expected climate change impacts on soil erosion rates: A review. *Journal of Soil and Water Conservation*, 59(1), 43–50. Scopus.
- Oostwoud Wijdenes, D. J., & Ergenzinger, P. (1998). Erosion and sediment transport on steep marly hillslopes, Draix, Haute-Provence, France: An experimental field study. *CATENA*, 33(3), 179–200. [https://doi.org/10.1016/S0341-8162\(98\)00076-9](https://doi.org/10.1016/S0341-8162(98)00076-9)
- Osmundson, D. B., Ryel, R. J., Lamarra, V. L., & Pitlick, J. (2002). Flow-sediment-biota relations: Implications for river regulation effects on native fish abundance. *Ecological Applications*, 12(6), 1719–1739. [https://doi.org/10.1890/1051-0761\(2002\)012\[1719:FSBRIF\]2.0.CO;2](https://doi.org/10.1890/1051-0761(2002)012[1719:FSBRIF]2.0.CO;2)
- Pasquet, S., Holbrook, W. S., Carr, B. J., & Sims, K. W. W. (2016). Geophysical imaging of shallow degassing in a Yellowstone hydrothermal system. *Geophysical Research Letters*, 43(23), 12,027-12,035. <https://doi.org/10.1002/2016GL071306>
- Pasquier, C., Cousin, I., Seger, M., Dabas, M., Thiesson, J., & Tabbagh, A. (2013). Comparison between thermal airborne remote sensing, multi-depth electrical resistivity profiling and soil mapping. *Near Surface Geoscience 2013*.
- Pelletier, J. D., Barron-Gafford, G. A., Gutiérrez-Jurado, H., Hinckley, E.-L. S., Istanbulluoglu, E., McGuire, L. A., Niu, G.-Y., Poulos, M. J., Rasmussen, C., Richardson, P., Swetnam, T. L., & Tucker, G. E. (2018). Which way do you lean? Using slope aspect variations to understand Critical Zone processes and feedbacks. *Earth Surface Processes and Landforms*, 43(5), 1133–1154. <https://doi.org/10.1002/esp.4306>
- Pichelli, E., Coppola, E., Sobolowski, S., Ban, N., Giorgi, F., Stocchi, P., Alias, A., Belušić, D., Berthou, S., Caillaud, C., Cardoso, R. M., Chan, S., Christensen, O. B., Dobler, A., de Vries, H., Goergen, K., Kendon, E. J., Keuler, K., Lenderink, G., ... Vergara-Temprado, J. (2021). The first multi-model ensemble of regional climate simulations at kilometer-scale resolution part 2: Historical and

- future simulations of precipitation. *Climate Dynamics*, 56(11–12), 3581–3602. <https://doi.org/10.1007/s00382-021-05657-4>
- Pitlick, J., & Wilcock, P. (2001). Relations between streamflow, sediment transport, and aquatic habitat in regulated rivers. *Geomorphic Processes and Riverine Habitat*, 4, 185–198.
- Piton, G., Recking, A., Le Coz, J., Bellot, H., Hauet, A., & Jodeau, M. (2018). Reconstructing Depth-Averaged Open-Channel Flows Using Image Velocimetry and Photogrammetry. *Water Resources Research*, 54(6), 4164–4179. <https://doi.org/10.1029/2017WR021314>
- Poulenard, J., Legout, C., Némery, J., Bramorski, J., Navratil, O., Douchin, A., Fanget, B., Perrette, Y., Evrard, O., & Esteves, M. (2012). Tracing sediment sources during floods using Diffuse Reflectance Infrared Fourier Transform Spectrometry (DRIFTS): A case study in a highly erosive mountainous catchment (Southern French Alps). *Journal of Hydrology*, 414–415, 452–462. <https://doi.org/10.1016/j.jhydrol.2011.11.022>
- Pye, K., & Miller, J. A. (1990). Chemical and biochemical weathering of pyritic mudrocks in a shale embankment. *Quarterly Journal of Engineering Geology and Hydrogeology*, 23(4), 365–382. <https://doi.org/10.1144/GSL.QJEG.1990.023.04.11>
- Rainato, R., Mao, L., García-Rama, A., Picco, L., Cesca, M., Vianello, A., Preciso, E., Scussel, G. R., & Lenzi, M. A. (2017). Three decades of monitoring in the Rio Cordon instrumented basin: Sediment budget and temporal trend of sediment yield. *Geomorphology*, 291, 45–56. <https://doi.org/10.1016/j.geomorph.2016.03.012>
- Rawling, J. E., Fredlund, G. G., & Mahan, S. (2003). Aeolian cliff-top deposits and buried soils in the White River Badlands, South Dakota, USA. *The Holocene*, 13(1), 121–129. <https://doi.org/10.1191/0959683603hl601rr>
- Regués, D., & Gallart, F. (2004). Seasonal patterns of runoff and erosion responses to simulated rainfall in a badland area in Mediterranean mountain conditions (Vallcebre, southeastern Pyrenees). *Earth Surface Processes and Landforms*, 29(6), 755–767. <https://doi.org/10.1002/esp.1067>
- Regués, D., Guàrdia, R., & Gallart, F. (2000). Geomorphic agents versus vegetation spreading as causes of badland occurrence in a Mediterranean subhumid mountainous area. *CATENA*, 40(2), 173–187. [https://doi.org/10.1016/S0341-8162\(99\)00045-4](https://doi.org/10.1016/S0341-8162(99)00045-4)
- Regués, D., & Nadal-Romero, E. (2013). Uncertainty in the evaluation of sediment yield from badland areas: Suspended sediment transport estimated in the Araguás catchment (central Spanish Pyrenees). *CATENA*, 106, 93–100. <https://doi.org/10.1016/j.catena.2012.05.006>
- Regués, D., Pardini, G., & Gallart, F. (1995). Regolith behaviour and physical weathering of clayey mudrock as dependent on seasonal weather conditions in a badland area at Vallcebre, Eastern Pyrenees. *CATENA*, 25(1–4), 199–212. [https://doi.org/10.1016/0341-8162\(95\)00010-P](https://doi.org/10.1016/0341-8162(95)00010-P)
- Rengers, F. K., Kean, J. W., Reitman, N. G., Smith, J. B., Coe, J. A., & McGuire, L. A. (2020). The Influence of Frost Weathering on Debris Flow Sediment Supply in an Alpine Basin. *Journal of Geophysical Research: Earth Surface*, 125(2), e2019JF005369. <https://doi.org/10.1029/2019JF005369>
- Rengers, F. K., McGuire, L. A., Kean, J. W., Staley, D. M., & Youberg, A. M. (2019). Progress in simplifying hydrologic model parameterization for broad applications to post-wildfire flooding and debris-flow hazards. *Earth Surface Processes and Landforms*, 44(15), 3078–3092. <https://doi.org/10.1002/esp.4697>
- Riebe, C. S., Hahm, W. J., & Brantley, S. L. (2017). Controls on deep critical zone architecture: A historical review and four testable hypotheses. *Earth Surface Processes and Landforms*, 42(1), 128–156. <https://doi.org/10.1002/esp.4052>

- Roering, J. J., Kirchner, J. W., & Dietrich, W. E. (1999). Evidence for nonlinear, diffusive sediment transport on hillslopes and implications for landscape morphology. *Water Resources Research*, 35(3), 853–870. <https://doi.org/10.1029/1998WR900090>
- Rovéra, G., & Robert, Y. (2005). Conditions climatiques hivernales et processus d'érosion périglaciaires dans les bad-lands marneux de Draix (800 m, Alpes du Sud, France). *Geographie Physique et Quaternaire*, 59(1), 31–48. <https://doi.org/10.7202/013735ar>
- Rücker, C., Günther, T., & Wagner, F. M. (2017). pyGIMLi: An open-source library for modelling and inversion in geophysics. *Computers & Geosciences*, 109, 106–123. <https://doi.org/10.1016/j.cageo.2017.07.011>
- Saha, A., Ghosh, M., & Pal, S. C. (2020). Understanding the Morphology and Development of a Rill-Gully: An Empirical Study of Khoai Badland, West Bengal, India. In P. K. Shit, H. R. Pourghasemi, & G. S. Bhunia (Eds.), *Gully Erosion Studies from India and Surrounding Regions* (pp. 147–161). Springer International Publishing. https://doi.org/10.1007/978-3-030-23243-6_9
- Sander, M., Bengtsson, L., Holmquist, B., Wohlfarth, B., & Cato, I. (2002). The relationship between annual varve thickness and maximum annual discharge (1909–1971). *Journal of Hydrology*, 263(1), 23–35. [https://doi.org/10.1016/S0022-1694\(02\)00030-6](https://doi.org/10.1016/S0022-1694(02)00030-6)
- Schoeneberger, P. J., Wysocki, D. A., & Benham, E. C. (2012). Field Book for Describing and Sampling Soils. Government Printing Office.
- Scott, C. P., Lohman, R. B., & Jordan, T. E. (2017). InSAR constraints on soil moisture evolution after the March 2015 extreme precipitation event in Chile. *Scientific Reports*, 7(1), Article 1. <https://doi.org/10.1038/s41598-017-05123-4>
- Shobe, C. M., Braun, J., Yuan, X., Campforts, B., Gailleton, B., Baby, G., Guillocheau, F., & Robin, C. (2022). Inverting passive margin stratigraphy for marine sediment transport dynamics over geologic time. <https://eartharxiv.org/repository/view/3151/>
- Sklar, L. S., Riebe, C. S., Marshall, J. A., Genetti, J., Leclere, S., Lukens, C. L., & Merces, V. (2017). The problem of predicting the size distribution of sediment supplied by hillslopes to rivers. *Geomorphology*, 277, 31–49. <https://doi.org/10.1016/j.geomorph.2016.05.005>
- Small, E. E., Anderson, R. S., & Hancock, G. S. (1999). Estimates of the rate of regolith production using ^{10}Be and ^{26}Al from an alpine hillslope. *Geomorphology*, 27(1), 131–150. [https://doi.org/10.1016/S0169-555X\(98\)00094-4](https://doi.org/10.1016/S0169-555X(98)00094-4)
- Smetanová, A., Le Bissonnais, Y., Raclot, D., Pedro Nunes, J., Licciardello, F., Le Bouteiller, C., Latron, J., Rodríguez Caballero, E., Mathys, N., Klotz, S., Mekki, I., Gallart, F., Solé Benet, A., Pérez Gallego, N., Andrieux, P., Moussa, R., Planchon, O., Santos, J. M., Alshihabi, O., ... Follain, S. (2018). Temporal variability and time compression of sediment yield in small Mediterranean catchments: Impacts for land and water management. *Soil Use and Management*, 34(3), 388–403. <https://doi.org/10.1111/sum.12437>
- Smith, T. R., & Bretherton, F. P. (1972). Stability and the conservation of mass in drainage basin evolution. *Water Resources Research*, 8(6), 1506–1529. <https://doi.org/10.1029/WR008i006p01506>
- Snyder, N. P., Whipple, K. X., Tucker, G. E., & Merritts, D. J. (2003). Channel response to tectonic forcing: Field analysis of stream morphology and hydrology in the Mendocino triple junction region, northern California. *Geomorphology*, 53(1), 97–127. [https://doi.org/10.1016/S0169-555X\(02\)00349-5](https://doi.org/10.1016/S0169-555X(02)00349-5)

- Sole'-Benet, A., Calvo, A., Cerdá, A., La'zaro, R., Pini, R., & Barbero, J. (1997). Influences of micro-relief patterns and plant cover on runoff related processes in badlands from Tabernas (SE Spain). *CATENA*, 31(1), 23–38. [https://doi.org/10.1016/S0341-8162\(97\)00032-5](https://doi.org/10.1016/S0341-8162(97)00032-5)
- Soler, M., Latron, J., & Gallart, F. (2008). Relationships between suspended sediment concentrations and discharge in two small research basins in a mountainous Mediterranean area (Vallcebre, Eastern Pyrenees). *Geomorphology*, 98(1), 143–152. <https://doi.org/10.1016/j.geomorph.2007.02.032>
- Soulet, G., Hilton, R. G., Garnett, M. H., Roylands, T., Klotz, S., Croissant, T., Dellinger, M., & Le Bouteiller, C. (2021). Temperature control on CO₂ emissions from the weathering of sedimentary rocks. *Nature Geoscience*, 14(9), 665–671. <https://doi.org/10.1038/s41561-021-00805-1>
- Sun, L., Yan, M., Cai, Q., & Fang, H. (2016). Suspended sediment dynamics at different time scales in the Loushui River, south-central China. *CATENA*, 136, 152–161. <https://doi.org/10.1016/j.catena.2015.02.014>
- Taccone, F. (2018). Modélisation numérique du transfert sédimentaire en bassin versant montagneux fortement érodable [Phdthesis, Université Paris-Est]. <https://pastel.archives-ouvertes.fr/tel-02138069>
- Tarolli, P. (2014). High-resolution topography for understanding Earth surface processes: Opportunities and challenges. *Geomorphology*, 216, 295–312. <https://doi.org/10.1016/j.geomorph.2014.03.008>
- Tetegan, M., Pasquier, C., Besson, A., Nicoullaud, B., Bouthier, A., Bourennane, H., Desbourdes, C., King, D., & Cousin, I. (2012). Field-scale estimation of the volume percentage of rock fragments in stony soils by electrical resistivity. *Catena*, 92, 67–74. <https://doi.org/10.1016/j.catena.2011.09.005>
- Tolorza, V., Carretier, S., Andermann, C., Ortega-Culaciati, F., Pinto, L., & Mardones, M. (2014). Contrasting mountain and piedmont dynamics of sediment discharge associated with groundwater storage variation in the Biobío River. *Journal of Geophysical Research: Earth Surface*, 119(12), 2730–2753. <https://doi.org/10.1002/2014JF003105>
- Troeh, F. R., & Thompson, L. M. (2005). Soils and soil fertility. Ames, Iowa.
- Tucker, G. E. (2004). Drainage basin sensitivity to tectonic and climatic forcing: Implications of a stochastic model for the role of entrainment and erosion thresholds. *Earth Surface Processes and Landforms*, 29(2), 185–205. <https://doi.org/10.1002/esp.1020>
- Tucker, G. E. (2009). Natural experiments in landscape evolution. *Earth Surface Processes and Landforms*, 34(10), 1450–1460. <https://doi.org/10.1002/esp.1833>
- Tucker, G. E., & Bras, R. L. (1998). Hillslope processes, drainage density, and landscape morphology. *Water Resources Research*, 34(10), 2751–2764. <https://doi.org/10.1029/98WR01474>
- Tucker, G. E., & Bras, R. L. (2000). A stochastic approach to modeling the role of rainfall variability in drainage basin evolution. *Water Resources Research*, 36(7), 1953–1964. <https://doi.org/10.1029/2000WR900065>
- Tucker, G. E., & Hancock, G. R. (2010). Modelling landscape evolution. *Earth Surface Processes and Landforms*, 35(1), 28–50. <https://doi.org/10.1002/esp.1952>
- Tucker, G. E., & Slingerland, R. (1997). Drainage basin responses to climate change. *Water Resources Research*, 33(8), 2031–2047. <https://doi.org/10.1029/97WR00409>

- Tucker, G. E., & Whipple, K. X. (2002). Topographic outcomes predicted by stream erosion models: Sensitivity analysis and intermodel comparison. *Journal of Geophysical Research: Solid Earth*, 107(B9), ETG 1-1-ETG 1-16. <https://doi.org/10.1029/2001JB000162>
- Vallauri, D. (1997). Dynamique de la restauration forestière des substrats marneux avec *Pinus nigra* J.F. Arn. Ssp. *Nigra* dans le secteur haut-provençal. Trajectoires dynamiques, avancement du processus de restauration et diagnostic sur l'intégrité fonctionnelle des écosystèmes recréés (p. 292) [Phdthesis, Doctorat Ecologie, Université Marseille III Saint-Jérôme]. <https://hal.inrae.fr/tel-02577196>
- van der Beek, P. (2013). Modelling Landscape Evolution. In *Environmental Modelling* (pp. 309–331). John Wiley & Sons, Ltd. <https://doi.org/10.1002/9781118351475.ch19>
- van der Beek, P., & Braun, J. (1999). Controls on post-mid-Cretaceous landscape evolution in the southeastern highlands of Australia: Insights from numerical surface process models. *Journal of Geophysical Research: Solid Earth*, 104(B3), 4945–4966. <https://doi.org/10.1029/1998JB900060>
- Vázquez-Tarrío, D., Borgniet, L., Liébault, F., & Recking, A. (2017). Using UAS optical imagery and SfM photogrammetry to characterize the surface grain size of gravel bars in a braided river (Vénéon River, French Alps). *Geomorphology*, 285, 94–105. <https://doi.org/10.1016/j.geomorph.2017.01.039>
- Vicente-Serrano, S. M., Tomas-Burguera, M., Beguería, S., Reig, F., Latorre, B., Peña-Gallardo, M., Luna, M. Y., Morata, A., & González-Hidalgo, J. C. (2017). A High Resolution Dataset of Drought Indices for Spain. *Data*, 2(3), Article 3. <https://doi.org/10.3390/data2030022>
- Wells, T., Binning, P., Willgoose, G., & Hancock, G. (2006). Laboratory simulation of the salt weathering of schist: 1. Weathering of schist blocks in a seasonally wet tropical environment. *Earth Surface Processes and Landforms*, 31(3), 339–354. <https://doi.org/10.1002/esp.1248>
- Whipple, K. X., & Tucker, G. E. (1999). Dynamics of the stream-power river incision model: Implications for height limits of mountain ranges, landscape response timescales, and research needs. *Journal of Geophysical Research: Solid Earth*, 104(B8), 17661–17674. <https://doi.org/10.1029/1999JB900120>
- White, T., Brantley, S., Banwart, S., Chorover, J., Dietrich, W., Derry, L., Lohse, K., Anderson, S., Aufdendkampe, A., Bales, R., Kumar, P., Richter, D., & McDowell, B. (2015). Chapter 2—The Role of Critical Zone Observatories in Critical Zone Science. In J. R. Giardino & C. Houser (Eds.), *Developments in Earth Surface Processes* (Vol. 19, pp. 15–78). Elsevier. <https://doi.org/10.1016/B978-0-444-63369-9.00002-1>
- Wilcock, P. R., & McArdell, B. W. (1997). Partial transport of a sand/gravel sediment. *Water Resources Research*, 33(1), 235–245. <https://doi.org/10.1029/96WR02672>
- Willgoose, G., Bras, R. L., & Rodriguez-Iturbe, I. (1991). A coupled channel network growth and hillslope evolution model: 1. Theory. *Water Resources Research*, 27(7), 1671–1684. <https://doi.org/10.1029/91WR00935>
- Wohl, E., & David, G. C. L. (2008). Consistency of scaling relations among bedrock and alluvial channels. *Journal of Geophysical Research: Earth Surface*, 113(F4). <https://doi.org/10.1029/2008JF000989>
- Yoo, K., & Mudd, S. M. (2008). Discrepancy between mineral residence time and soil age: Implications for the interpretation of chemical weathering rates. *Geology*, 36(1), 35–38. <https://doi.org/10.1130/G24285A.1>

York, D., Evensen, N. M., Martínez, M. L., & De Basabe Delgado, J. (2004). Unified equations for the slope, intercept, and standard errors of the best straight line. *American Journal of Physics*, 72(3), 367–375. <https://doi.org/10.1119/1.1632486>

Zhang, L., Parker, G., Stark, C. P., Inoue, T., Viparelli, E., Fu, X., & Izumi, N. (2015). Macro-roughness model of bedrock–alluvial river morphodynamics. *Earth Surface Dynamics*, 3(1), 113–138. <https://doi.org/10.5194/esurf-3-113-2015>